Universidad de Concepción
Facultad de Ciencias Químicas
Programa de Doctorado en Ciencias Geológicas

# The redox state and metal-volatile budget of primitive arc magmas: implications in the formation of ore-mineralized porphyry systems in the shallow crust

Pablo Antonio Salas Reyes

Tesis para optar al grado de Doctor en Ciencias Geológicas

| | |
|---|---|
| Profesor guía | Dr. Osvaldo Rabbia |
| Comisión evaluadora | Dra. Verónica Oliveros |
| | Dr. Alexandre Corgne |

Agosto de 2020

Concepción, Chile

*“… El artista que hay en él va a ponerse frenético de rabia cada vez que oiga ese remedo de su deseo, de todo lo que quiso decir mientras luchaba tambaleándose y escapándosele la saliva de la boca junto con la música, más que nunca solo frente a lo que persigue, a lo que se le huye mientras más lo persigue...”*

*Julio Cortázar, El Perseguidor, 1959*

# AGRADECIMIENTOS

Agradezco primero a la posibilidad de poder dedicar estos años a desarrollar esta tesis que constituye un anhelo antiguo, buscar en el propio patio para intentar comprender el mundo entero. En esta misma línea, agradezco a mi Profesor Guía, Osvaldo Rabbia, por sintonizar aquellas energías e impulsarme a tomar esta temática, asimismo por su apoyo y pensamiento crítico permanente que me llevaron siempre a un nuevo lugar de búsqueda. Agradezco a Philipp Ruprecht por su confianza y gestión para conseguir acceso a las técnicas microanalíticas que utilizamos; asimismo por su guía durante la preparación de las muestras de inclusiones fundidas y por sus valiosos comentarios y aportes en los alcances del Capítulo 3 de esta tesis. Adicionalmente agradezco a la Profesora Laura Hernández por su excelente trabajo con la microsonda del Instituto GEA con la cual se obtuvieron datos de muy alta calidad que nos permitieron vernos cara a cara con los cristales analizados.

A quienes estuvieron conmigo en terreno, Diego González, Andrés Oyarzún, Javier Espinosa, Paulina Henry, Joaquín Copaja y especialmente a los arraigados del Valle del Melado, Don David en Puente de Piedra, Danilo en Estero Botacura, quienes nos recibieron con brazos abiertos cada vez que los visitamos. A Gerardo Espinoza por su amistad y excelente servicio de vaqueano y caballares que brinda. A Don José Sepúlveda de Las Garzas por su cooperación y buena disposición siempre.

Agradezco a mi primo Tomás Reyes por el tremendo modelado 3D del "*archetypal crystal*", en un proceso largo que se iba actualizando a medida que más íbamos entendiendo.

A María Esperanza que es un soporte esencial para todos los doctorandos, por sus permanentes energías positivas. A la gente que conforma el Taller de Cortes del GEA, Emiliano Navarrete, Miguel Jofré y Pedro Henríquez, por su amistad y cariño permanente, por el trabajo de alta joyería que allí se realiza. Agradecimientos especiales a Miguel que siempre tuvo un tiempo para repasar finamente mis muestras, con calma y buena conversación. Asimismo, agradezco a Gloria Muñoz, Patricia Inostroza, Marcia Vargas, Esteban Otárola, que siempre me ayudaron logísticamente a lograr entrar a alguna de las instalaciones del GEA y me tendieron una mano cuando la necesité.

Por sobre todo agradezco a mi familia, a mi papá y mamá Elsita y Héctor y a mis hermanos Pilar-Pepe y sobrinos David, Daniel y Rafaela; a quienes les debo su paciencia por esperarme y por el ánimo y confianza que me brindaron durante todo este intenso periodo.

Y por supuesto a mi linda compañera de travesía Pamela Castillo, por su apoyo incondicional en esta larga etapa doctoral, con dificultades y alegrías incesantes; y a nuestra Vera, que en sus ojos vemos nuevos horizontes.

# Resumen

A escala global, los sistemas de pórfidos cupríferos de alto tonelaje (>40 Mt de Cu) se ubican exclusivamente a lo largo de segmentos de corteza gruesa (>~40 km) en márgenes continentales activos. Estos sistemas magmáticos-hidrotermales acumulan mena sulfurada que constituye grandes anomalías de Cu, Au y Mo en la corteza somera (<10 km). Los procesos específicos que controlan el transporte a gran escala de azufre (S) y metales (Cu-Au) hacia la corteza somera no se conocen con exactitud, sin embargo, las condiciones redox en los fundidos basálticos primitivos que intruyen la corteza profunda, ejercen un control de primer orden en el comportamiento de dichos metales a través de la especiación de S. La causa basal del carácter más oxidado de los basaltos de arco, comparado con basaltos de otros ambientes tectónicos, se debate entre dos visiones contrastantes. Una de ellas postula que la más alta oxidación refleja las condiciones de la fuente del manto, mientras que la otra atribuye la oxidación a procesos intracorticales durante el ascenso. En el primer caso, la precipitación de sulfuros magmáticos sería eficientemente inhibida debido a que el $S^{6+}$ (sulfato) es la especie de S dominante. Esto permite que el S y los metales sean transportados a niveles corticales más altos. Por el contrario, en el segundo caso, la precipitación de sulfuros magmáticos ($S^{2-}$, sulfuro) en la corteza media-profunda sería el proceso dominante, deprimiendo en metales y S a los magmas residuales que posteriormente alcanzan niveles corticales más altos.

Esta investigación explora las condiciones redox de un magma de arco primitivo en Los Hornitos, un par de volcanes monogenéticos máficos en los Andes Centrales-del Sur (35.5°S), donde olivinos magnesianos (Fo90-92; Ni ~3800 ppm) contienen inclusiones vítreas que fueron analizadas por una combinación de técnicas microanalíticas (μ-XANES, EPMA, SIMS & LA-ICP-MS), permitiendo la determinación de la especiación del Fe ($Fe^{3+}/\Sigma Fe$) y la composición en

elementos mayoritarios, minoritarios y trazas durante las etapas tempranas de estos fundidos de arco, en un segmento andino metalogenéticamente fértil.

Adicionalmente, el análisis de las características texturales y de zonación química a pequeña escala en un gran número de cristales, permitió establecer la evolución textural y volumétrica durante episodios de crecimiento rápido, donde un fenocristal de olivino resulta del crecimiento concéntrico progresivo de estructuras abiertas denominadas "*crystal frames*". Esto implica el desarrollo de capas límites composicionales, lo cual desafía la fiabilidad de las inclusiones de fundido como indicadores de condiciones en equilibrio como una regla implícita.

Los resultados indican que los fundidos basálticos primitivos (1250°C-1GPa) que intruyen la corteza profunda presentan una $fO_2$ equivalente a NNO+1 a +1.7, permitiendo que hasta un ~50% del total de azufre se disuelva como sulfato. Este porcentaje es considerablemente mayor al de otros magmas de arco, que pueden disolver sólo hasta un ~5% de S. Por lo tanto, es posible establecer que la naturaleza metalogenéticamente fértil de los magmas de arco en zonas de subducción maduras, radica en el carácter comparativamente más oxidado de los fundidos que intruyen la corteza desde el manto bajo el arco. Adicionalmente, la contribución en volátiles y metales de aquellos fundidos es 3 wt% de $H_2O$, 4000 ppm de S, 1300 ppm de Cl y 200 ppm de Cu.

# Abstract

At global scale, prominently mineralized porphyry copper systems (>40 Mt Cu) are located exclusively along thick crustal segments (>~40 km) of active continental margins. These magmatic-hydrothermal systems accumulate sulfide ore involving huge anomalies of Cu, Au and Mo in the shallow crust (<10 km depth). The specific processes that allow the large-scale transport of sulfur (S) and metals (Cu-Au) to the upper crust remain unclear, however, the redox conditions in the primitive basaltic melts intruding the deep crust exert a first-order control on the behavior of these metals through the speciation of sulfur. The basic causes of the more oxidized character of arc basalts compared with basalts from other tectonic settings is debated between two contrasting hypotheses. One of these postulates that the higher oxidation reflects the mantle source condition, whereas the other attributes the magma oxidation to intra-crustal processes during the ascent. In the first case, the crystallization of magmatic sulfides would be efficiently inhibited given that $S^{6+}$ (sulfate) is the dominant S specie. This allows to S and metal to be transported to higher crustal levels. Conversely, in the second case, the precipitation of magmatic sulfides in the mid to deep crust would be dominant during the early stages of differentiation ($S^{2-}$, sulfide), depleting in metal and sulfur the residual magmas that later can reach the high crust.

This research explore into the redox conditions of a primitive arc magma at Los Hornitos, a pair of mafic monogenetic vents in the Central-South Andes (35.5°S), where magnesian olivines (Fo90-92; Ni ~3800 ppm) host quenched melt inclusions that were analyzed by a combination of microanalitycal techniques (µ-XANES, EPMA, SIMS & LA-ICP-MS), allowing the determination of Fe speciation ($Fe^{3+}/\Sigma Fe$) and the major, minor and trace element composition during the early stages of this arc melts in a metallogenetic fertile segment of the Andes.

In addition, the examination of textural features and fine-scale zoning of a large amount of crystals, allows to establish the textural and volumetric evolution of

olivine during episodes of rapid growth, where phenocryst-size olivines results of the progressive growth of concentric open structured “crystal frames” that leave behind compositional boundary layers. This challenge the reliability of melt inclusions as indicator of equilibrium conditions as an implicit rule.

Results indicate that the primitive basaltic melts (1250°C-1GPa) intruding the deep crust, present a $fO_2$ equivalent to NNO+1 to +1.7, allowing to dissolve up to ~50% of the sulfur cargo as sulfate. This value is considerably higher compared with other arc magmas that only dissolve as much as ~5% of S. Therefore, it is possible to establish that the metallogenetic fertile nature of arc magmas above mature subduction zones relies in the comparatively more oxidized character of the melts intruding the crust from the subarc mantle. In addition, the contribution in volatile and metal of these melts is 3 wt% of $H_2O$, 4000 ppm of S, 1300 ppm of Cl and 200 ppm of Cu.

# Table of contents

# Capítulo 1: Introducción

## 1.1- Formulación del problema científico

A escala global, la distribución de sistemas tipo pórfido de cobre de alto tonelaje (>40 Mt Cu) ocurre exclusivamente a lo largo de segmentos de gran espesor cortical (>40 km) de márgenes continentales activos. Sin embargo, en un determinado arco, la ocurrencia y distribución espacial de depósitos minerales se restringe a determinados segmentos, donde los procesos de mineralización ocurren durante periodos específicos. Esto sugiere que además del rol fundamental que juegan los magmas de arco en la formación de depósitos tipo pórfido (PCD, por su sigla en inglés), otros procesos deben estar involucrados. Varias líneas de evidencia muestran que un alto *stress* en la placa cabalgante ocurre concomitante al desarrollo del magmatismo que se asocia a los sistemas de tipo pórfido. Por lo tanto, los procesos petrogenéticos y tectónicos que conducen a la formación de PCD's operan sincrónicamente en determinadas longitudes de un arco, resultando en la formación de depósitos relativamente coetáneos agrupados en franjas mineralizadas.

Una característica distintiva observada en magmas de zonas de subducción consiste en el más alto estado de oxidación comparado con magmas de otros ambientes tectónicos. El estado de oxidación de un magma, normalmente expresado como fugacidad de oxígeno ($fO_2$), es definida como la actividad de

oxígeno en un sistema (Carmichael, 1991; Frost, 1991; Kress and Carmichael, 1991), lo cual se expresa utilizando *buffers* de reacciones redox (p.ej., nickel-nickel oxide NNO; fayalita-magnetita-cuarzo FMQ). La fugacidad de oxígeno representa una variable intensiva que proporciona una medida del potencial redox de un sistema en equilibrio, por lo tanto, controla el estado de valencia, y por consiguiente la especiación de elementos sensibles al estado redox (p. ej., Fe, S, As or V) (Lee et al., 2005). Como el hierro es el elemento más abundante sensible al estado redox en sistemas magmáticos, la relación $Fe^{3+}/\Sigma Fe$ es comúnmente utilizada como un *proxy* para constreñir las condiciones redox de un magma.

El carácter más oxidado de los magmas de arco se hace evidente al comparar basaltos emitidos en volcanes de arco con aquellos emitidos en dorsales oceánicas o en cuencas de trasarco (Christie et al., 1986; Wood et al., 1990; Eggins, 1993; Kelley and Cottrell, 2009; Evans et al., 2012; Kelley and Cottrell, 2012; Richards, 2015), sin embargo, las causas fundamentales de aquella diferencia, permanecen abiertas al debate. Una hipótesis propone que la oxidación del manto bajo el arco se debe a fluidos oxidantes provenientes del *slab* subductado, resultando en fundidos parciales oxidados extraídos de la cuña del manto. Esta propuesta es soportada por la correlación positiva entre $Fe^{3+}/\Sigma Fe$ y trazadores de adiciones del slab, como $H_2O$ y la relación Ba/La (Kelley and Cottrell, 2009). Por otra parte, modelos basados en el particionamiento de elementos sensibles al estado redox (p.ej., vanadio en la razón V/Sc; Lee et al.,

2005) sugieren que el estado redox de la fuente del manto no varía entre los diferentes ambientes tectónicos, y que los magmas de arco se hacen más oxidados exclusivamente a medida que se diferencian a lo largo del paso desde el manto a la superficie.

Esas dos contrastantes hipótesis tienen importantes implicancias en la metalogénesis de arco.

De acuerdo a la primera visión, una alta $fO_2$ en la fuente del manto promoverá la ocurrencia de especies de azufre como sulfato ($S^{6+}$), con el consecuente enriquecimiento en metales y $S^{6+}$ en el fundido parcial resultante, debido a la más alta solubilidad de $S^{6+}$ (2 a 5 veces más alta) comparada con $S^{2-}$ en condiciones oxidantes (Carroll and Rutherford, 1987; Luhr, 1990, Masotta and Keppler, 2015). De acuerdo a esta visión, Chambefort et al., 2008, sugieren que los magmas máficos saturados en sulfato, emplazados en niveles corticales profundos, son responsables del transporte eficiente de azufre y metales requeridos para producir grandes sistemas mineralizados en la corteza somera. Tales condiciones oxidadas se registran, por ejemplo, en la amplia presencia de anhidrita ($CaSO_4$) como inclusión en minerales máficos de la secuencia volcánica Yanacocha, genéticamente vinculada al sistema hidrotermal de Cu-Au, que constituye el homónimo depósito epitermal de alta sulfuración (HS) asociado a un PCD más profundo (Chambefort et al., 2008).

Por el contrario, la segunda hipótesis indica que las condiciones más oxidadas observadas en ambiente de arco se generan principalmente en niveles corticales

altos, particularmente durante la exsolución de una fase volátil, sugiriendo que la precipitación de minerales o la desmezcla de una fase sulfurada líquida ocurre masivamente durante las etapas magmáticas tempranas. Los partidarios de esta visión consideran este evento de precipitación de sulfuros magmáticos, previo a una exsolución en volátiles, como un mecanismo de preconcentración de metales favorable para la posterior depositación de mena en sistemas hidrotermales (Jenner et al., 2010; Nadeau et al., 2010; Lee et al., 2012; Sillitoe, 2012; Wilkinson, 2013, Chiaradia, 2014). Esto implica que los fluidos hidrotermales someros derivarían sus metales a partir de la disolución de sulfuros previamente concentrados, en oposición a la primera hipótesis, que considera a los fundidos tempranos oxidados como el contribuidor directo de azufre y metales hacia los niveles corticales someros.

Es importante notar que la transición del campo de sulfuro ($S^{2-}$) a sulfato ($S^{6+}$) en fundidos basálticos a presiones de 1 GPa ocurre a medida que la $fO_2$ aumenta desde NNO+1 a NNO+2, tal que a ~NNO+2,5 la relación $S^{6+}/\Sigma S$ es 0,95 (Matjuschkin et al., 2016) permitiendo altas concentraciones de sulfato disuelto en el fundido y evitando la saturación de fases sulfuradas tempranas (Fig.1.1a). La estrecha transición en la estabilidad de $S^{2-}$ a $S^{6+}$, permite que a $fO_2$'s pertinentes a magmas de arco, sólo una menor fase sulfurada puede ser estable durante la diferenciación magmática. De acuerdo a Richards (2009, 2015), la moderada a mínima presencia de aquella fase sulfurada en comparación a un gran volumen de magma que ha sido sólo parcialmente afectado por la

precipitación de aquella fase, conformará a un magma fértil, teniendo el potencial de formar depósitos de pórfido ricos en Cu en niveles corticales altos.

En el ambiente porfídico, la información derivada de rocas evolucionadas estrechamente vinculadas a depósitos tipo pórfido de clase mundial de varias franjas mineralizadas, muestra que aquellas rocas son más oxidadas que otras rocas estériles distribuidas regionalmente (Dilles et al., 2015; Ballard et al., 2002; Shen et al., 2015). Sin embargo, determinaciones de fugacidad de oxígeno en rocas ígneas evolucionadas, asociadas a procesos de diferenciación tardíos, genera incerteza respecto al origen de la $fO_2$ observada. El más alto estado redox determinado en sistemas porfídicos podría no necesariamente haber sido adquirido en la fuente del manto, sino proceder de la exsolución tardía de una fase volátil enriquecida en $H_2O$ y S. Esto implica que las causas basales del enriquecimiento en metales y azufre observado en magmas formadores de mena, no se conocen con exactitud.

Por lo tanto, para determinar si la “naturaleza fértil” asociada con el estado redox de los magmas de arco es aquella de una alta oxidación en la cuña del manto o bien la precipitación de una fase sulfurada en la transición manto-corteza, es imperativo evitar los efectos producidos por procesos magmáticos e hidrotermales intra-corticales, tales como cristalización, asimilación de roca caja, mezcla de magmas, o alteración por metasomatismo. El hecho que los PCD’s ocurren en segmentos de corteza engrosada, donde las composiciones máficas son prácticamente ausentes a niveles corticales altos o bien se encuentran

potencialmente alteradas por procesos hidrotermales, hace que la consecución de tales composiciones prístinas sea un desafío difícil de conseguir en el ambiente porfídico mismo. Por lo tanto, el análisis de los miembros máficos más cercanos, tanto a escala espacial como temporal, que ocurran a escala de la franja mineralizada, pueden ser alternativamente utilizados para constreñir las etapas tempranas de los magmas de arco. En esta investigación se propone un lugar apropiado en el segmento Andino de la franja mineralizada de edad Mio-Pliocena de Chile Central.

### 1.1.1- Mineralización tipo pórfido en Chile Central.

La franja mineralizada del Mioceno al Plioceno Temprano, ubicada entre los ~31,6° y los ~34,1°S (Deckart et al., 2005, 2014; Stern et al., 2011; Mpodozis y Cornejo, 2012), constituye una de los más grandes enriquecimientos en metales en la corteza somera a nivel mundial, con reservas que alcanzan más de 300 Mt de cobre concentrado en tres depósitos principales (Irarrázaval et al., 2010; Perelló et al., 2009; Cooke et al., 2005). De norte a sur, aquellos corresponden a Los Pelambres-El Pachón (LP-EP; ~12 a 10 Ma), Río Blanco-Los Bronces (RB-LB; ~7 a 4 Ma) y El Teniente (ET; ~6 a 4 Ma) (Fig.1.1b). Adicionalmente, varios prospectos de edades similares se distribuyen a lo largo del segmento y más al sur, extendiéndose la franja magmática-hidrotermal hasta los ~36°S. Aquello indica que los procesos magmáticos e hidrotermales vinculados a la depositación de metales en la corteza alta de este particular segmento Andino, operaron de

manera sincrónica hasta los ~36°S (no implicando necesariamente que exista mineralización económicamente rentable fuera de los depósitos conocidos al presente).

Dos interesantes observaciones de gran escala en la configuración tectono-magmática destacan a esta latitud: (1) El espesor cortical disminuye drásticamente desde >45 km al norte a <45 km al sur de este límite (Fig.1.1b) (Tassara and Echaurren, 2012); y (2) Un considerable cambio en la composición de las rocas volcánicas emitidas desde el frente volcánico, albergando la ocurrencia de basaltos más al norte en el contexto de la Zona Volcánica Sur.

Por lo tanto, aquellas composiciones basálticas, emplazadas en un segmento de corteza gruesa pueden ser un *proxy* cercano para constreñir las condiciones redox de los fundidos menos evolucionados vinculados con la naturaleza fértil de los magmas de arco prospectados a la escala de la franja magmática-hidrotermal de edad Mioceno Tardío a Plioceno Temprano de Chile Central.

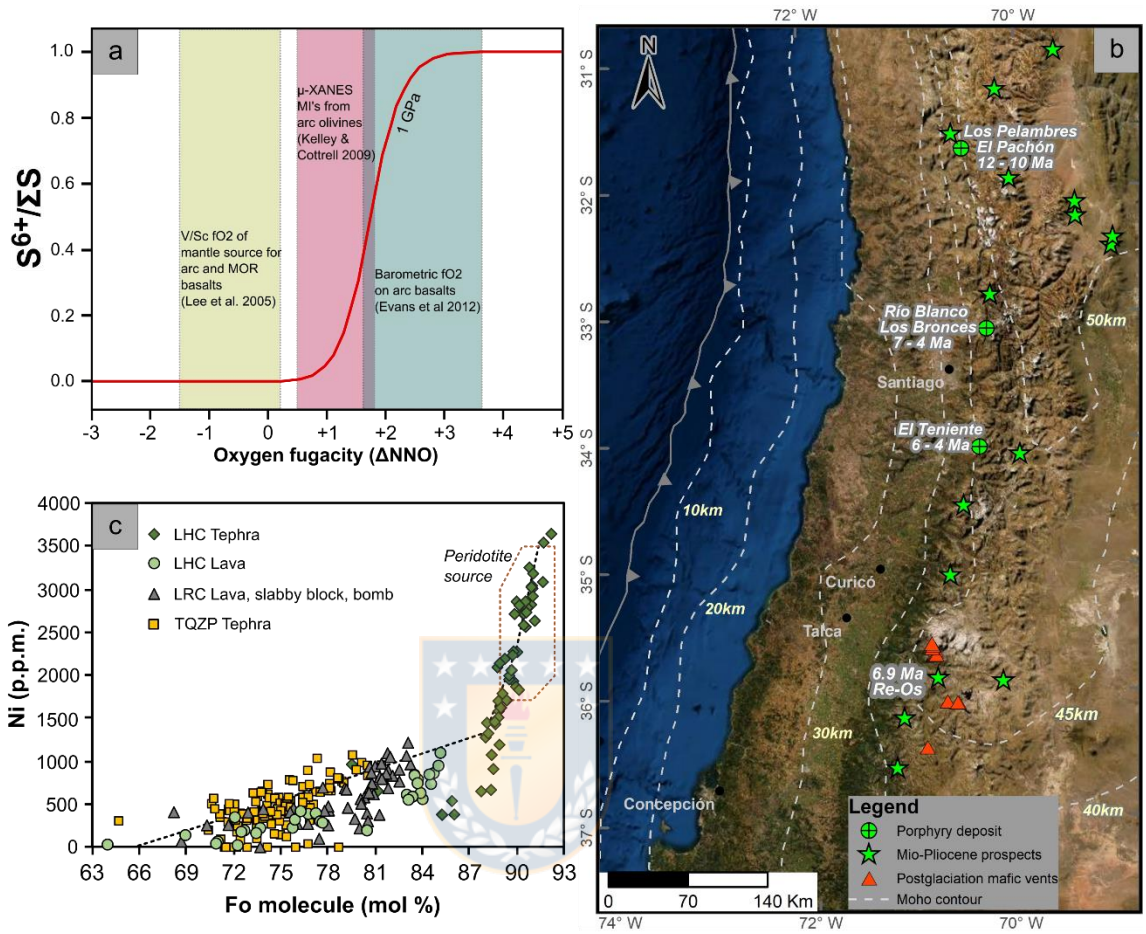


Fig.1.1.- a) Curva de especiación de azufre a 1 GPa modificada de Matjuskin et al., 2016. Se muestran tres aproximaciones diferentes a las condiciones de oxidación: El panel de la izquierda representa la $fO_2$ para la fuente del manto del arco y los basaltos de dorsal oceánica (MORB) modelados con la relación V/Sc (Lee et al., 2005). El panel central representa la $fO_2$ basada en la razón $Fe^{3+}/\Sigma Fe$ medida en inclusiones fundidas, a partir de una colección global de magmas de arco ($n$=7, ninguno de los datos es de Los Andes, $Fo_{host}$ 74-83; Kelley & Cottrell, 2009). El panel de la derecha muestra la $fO_2$ barométrica para basaltos primitivos (Evans et al., 2012). b) Sistemas tipo pórfido, incluyendo depósitos y prospectos de edad Mioceno Tardío-Plioceno Temprano en Chile Central. Adicionalmente, se muestra la distribución de volcanes monogenéticos máficos post-glaciales a los ~36°S. Notar la distribución de las curvas de espesor cortical a lo largo del segmento Andino. c) Variaciones de Fo-Ni entre olivinos de diferentes productos eruptivos que ocurren en el Campo Volcánico del Descabezado Grande.

### 1.1.2.- Prospección de magmas máficos a lo largo de la franja magmática-hidrotermal de Chile Central: los centros eruptivos máficos de edad Plioceno-Reciente a los ~35.5°S.

Estudios previos (Salas 2010; Salas et al., 2014) mostraron la ocurrencia de magmas máficos primitivos en Los Hornitos, un par de conos monogenéticos que ocurren en la vecindad del Campo Volcánico del Descabezado Grande a los 35.5° S. Adicionalmente, la revisión más amplia de la zona del arco, revela la ocurrencia de varios otros volcanes monogenéticos distribuidos entre los 35.5° y los 36.5°S, algunos de ellos de composición desconocida y otros previamente reportados por Hildreth et al., 2010. Por lo tanto, la utilización de la información bibliográfica y campañas de terreno orientadas al reconocimiento y muestreo de volcanes máficos seleccionados, provee la oportunidad de determinar la (s) locación (es) más favorables para prospectar inclusiones de fundido atrapadas en olivino a partir de las composiciones de magma menos evolucionadas.

Por varias razones, el olivino es la fase mineral más adecuada para llevar a cabo estudios de inclusiones de fundido (MI, por su sigla en inglés) en el contexto de composiciones máficas: (1) es la primera fase mineral que cristaliza en la mayoría de las composiciones basálticas en diferentes ambientes tectónicos; (2) su fórmula química sencilla permite un recálculo relativamente sencillo de la composición original de los fundidos atrapados y cualquier potencial contaminación con el *host* puede ser rápidamente detectada. (3) la común ocurrencia de MI's de varios microns de diámetro (>20 µm) y (4) las variaciones de Fo-Ni en olivino permiten una rápida determinación de la posición a lo largo de la línea de cristalización.

El muestreo de capas de tefra que contienen olivino asegura la recolección de MI's enfriadas rápidamente (*quenched*), que ocurre durante la trayectoria aérea de cenizas y fragmentos tamaño lapilli. Este enfriamiento evita cristalización dentro de la inclusión y el fundido atrapado se preserva con cambios mínimos (Danyushevsky et al., 2002; Kent, 2008).

El análisis de MI's hospedadas en olivinos de alta forsterita (i.e. >~Fo88) proporciona el acceso a las etapas más tempranas de la evolución de un magma, cuando olivino (± espinelas) es la única fase cristalizando, potencialmente en equilibrio con la fuente del manto (Fig.1.1c). Análisis previos de MI's hospedadas en Fo90-92 de Los Hornitos, muestran relativamente altos contenidos de S (hasta ~3000 ppm) reflejando la prevalencia de condiciones prácticamente no afectadas por desgasificación durante el atrapamiento de aquellos fundidos primitivos, probablemente en niveles corticales profundos (Salas et al., 2009, 2015; Wehrmann et al., 2014). Por lo tanto, las MI's hospedadas en olivino provenientes de Los Hornitos y potencialmente desde otros volcanes primitivos en el área, serán interrogadas por técnicas microanalíticas (por ej., EPMA, LA-ICPMS, SIMS, µ-XANES) con el fin de constreñir las condiciones redox y la contribución de metales y volátiles desde fundidos primitivos de arco en una zona de subducción madura.

## 1.2.- Preguntas de investigación

1.- ¿La naturaleza fértil de los magmas de arco yace en una alta $fO_2$ (>~NNO+2) de los fundidos primitivos evitando la precipitación de sulfuros, o contrariamente, en condiciones dominantemente reducidas (<~NNO) que permiten la saturación temprana de sulfuros magmáticos, seguida por una posterior re-movilización a la corteza somera?

2.- En cualquiera de aquellas causas básicas, ¿cuál es la relación $S^{6+}/\Sigma S$ en los fundidos primitivos de arco que permite la formación de los más grandes sistemas de pórfido de cobre conocidos, como los son RB-LB y ET en la franja magmática-hidrotermal Mio-Pliocena en Chile Central?

### 1.3.- Objetivo principal

La determinación *in-situ* de la $fO_2$ y la contribución de metales y volátiles asociados a magmas primitivos de arco en la extensión sur de la franja mineralizada Mio-Pliocena de Chile Central, para progresar en la comprensión de los procesos petrogenéticos tempranos vinculados al transporte de metales y azufre que conforman depósitos hidrotermales en niveles corticales altos.

### 1.4.- Objetivos específicos (OE's)

**Objetivo específico 1 (OE1):** Muestreo de volcanes máficos en la extension sur de la franja Mio-Pliocena y la determinación de sus características petro-químicas

con el fin de seleccionar las composiciones más primitivas de los magmas de arco en este segmento.

**Objetivo específico 2 (OE2):** Determinar las características texturales de los cristales de olivino obtenidos a partir de las secuencias de tefra seleccionadas, lo que permitirá orientar la prospección de MI's en cristales texturalmente maduros (i.e. polihedrales).

**Objetivo específico (OE3):** Establecer la composición y la contribución de metales y volátiles a partir de fundidos primitivos a través del estudio de MI's atrapadas en olivinos de alta forsterita.

**Objetivo específico 4 (OE4):** Determinar el estado redox de fundidos primitivos de arco por técnicas microanalíticas a través de la medición de la razón $Fe^{3+}/\Sigma Fe$ en los vidrios atrapados.

**Objetivo específico 5 (OE5):** Integrar los resultados para establecer la influencia de las condiciones magmáticas obtenidas respecto a la formación de PCD's en niveles corticales someros de este segmento Andino.

## 1.5.- Metodología

### Vinculado al OE1

Como se ha mencionado previamente, además de Los Hornitos y los cráteres de La Resolana en el Campo Volcánico del Descabezado Grande (Salas 2010), varios otros volcanes monogenéticos bien preservados se distribuyen en el

segmento andino entre los 35.5° y 36.5°S. Datos preliminares en Los Hornitos (35.5°S) permitieron el reconocimiento de cristales de olivino de alta forsterita (92 ≥ Fo ≥ 88) contenidos en depósitos de tefra, asociados a las etapas iniciales de un evento eruptivo post-glacial. La ocurrencia de MI's rápidamente enfriadas (*quenched*) en algunos de aquellos fenocristales, permite que sean adecuados para un estudio detallado de la química del *host* y los vidrios atrapados. Se realizará revisión bibliográfica y trabajo de terreno dirigido al reconocimiento y muestreo de productos eruptivos en volcanes máficos seleccionados. Se realizarán concentrados de olivino a partir de las muestras de tefra a través del uso de líquidos densos.

**Vinculado al OE2**

A través del uso de lupa binocular, se observarán alícuotas de los concentrados de olivino, de modo de reconocer las características texturales, tamaño y ocurrencia de inclusiones de fundido. Los cristales seleccionados se documentarán con fotografías y un esquema de modo de facilitar el reconocimiento de las inclusiones en etapas posteriores.

El reconocimiento de las características texturales de los cristales hospedantes permitirá *a priori* identificar inclusiones que podrían haber sido atrapadas en condiciones de no-equilibrio. La fidelidad de las MI's como indicador de la composición del fundido desde el cual cristalizo el *host*, depende en gran medida de las condiciones de crecimiento del olivino hospedante durante el atrapamiento

del fundido. Numerosos trabajos muestran que tasas de rápido crecimiento en cristales que conforman morfologías dendríticas y esqueletales, promueven el desarrollo de capas límites composicionales (CBL's, por su sigla en inglés) alrededor del cristal en crecimiento (Milman-Barris et al., 2008; Shea et al., 2015; Welsch et al., 2014; Honour et al., 2018), con lo cual, algunas inclusiones pueden encapsular aquellas composiciones fuera de equilibrio, las cuales estarán deprimidas en elementos compatibles (p.ej., Fo, Ni) y enriquecidas en elementos incompatibles (p.ej., Al, P, Cr).

**Vinculado a OE3**

Alrededor de 70-80 MI's serán seleccionadas para análisis de elementos mayoritarios y minoritarios vía EPMA. Para este propósito, se realizará una etapa previa de exploración y mapeo de cristales a través de microscopía de luz reflejada y transparente, con el objetivo de referenciar las MI's más apropiadas en cada grano. Se medirán los siguientes óxidos mayoritarios y minoritarios: $SiO_2$, $TiO_2$, $Al_2O_3$, $Cr_2O_3$, FeO, MnO, NiO, MgO, CaO, $Na_2O$, $K_2O$, $SO_4$ incluyendo Cl elemental. La composición medida será corregida por cristalización post-atrapamiento (PEC, por su sigla en inglés) de olivino y pérdida difusiva de Fe (Fe-loss) por medio del *software* Petrolog (Danyushevsky and Plechov, 2011). Adicionalmente, $H_2O$, S, Cl, $CO_2$, P y F serán determinados vía SIMS.

Se medirá la composición del olivino hospedante en el área circundante <10 µm alrededor de la MI y se caracterizará por FeO, MgO, NiO, CaO y MnO. Para

acceder al detalle de la metodología respecto al montaje de inclusiones expuestas se debe ver el Capítulo 4.

**Vinculado a OE4**

La relación $Fe^{3+}/\Sigma Fe$ en las inclusiones de fundido será determinado vía µ-XANES. Los valores medidos serán corregidos por modificaciones post-atrapamiento para obtener la razón original. Además, la relación $Fe^{3+}/\Sigma Fe$ será transformada a $fO_2$ usando el algoritmo de Kress and Carmichael (1991) a presiones y temperaturas apropiadas para aquellos fundidos.

**Vinculado al OE5**

Los resultados serán integrados y modelados en las condiciones obtenidas (T, P, $fO_2$, contribución de volátiles y metales) y serán analizadas en el contexto de datos publicados para zonas de arco. De este modo, la fuente del manto bajo la franja magmática-hidrotermal Mio-Pliocena será constreñida, contribuyendo a la comprensión de los procesos metalogenéticos tempranos vinculados a la depositación de mena sulfurada de Cu-Au en niveles corticales altos de márgenes convergentes activos.

# Chapter 1: Introduction

## 1.1- Formulation of the scientific problem

At global scale, prominently mineralized porphyry copper systems (>40 Mt Cu) occur exclusively along thick crustal segments (>40 km) of active continental margins. However, in a given arc, the occurrence and spatial distribution of ore deposits is restricted to certain segments, where mineralization processes take place during specific periods. This suggests that in addition to the fundamental role played by arc magmas in the formation of porphyry copper deposits (PCD), some other processes must also be involved. Several lines of evidence show that high stresses in the overriding plate are ubiquitous during the development of magmatism associated to porphyry copper systems. Therefore, petrogenetic and tectonic processes that lead to the formation of PCD's operate synchronously at certain lengths of an arc, resulting in the formation of relatively coetaneous deposits grouped into mineralized belts.

One distinctive feature observed in subduction zone magmas consists in the higher oxidation state compared with magmas from other tectonic settings. The oxidation state of a magma, normally referred to as oxygen fugacity ($fO_2$), is defined as the activity of oxygen within a system (Carmichael, 1991; Frost, 1991; Kress and Carmichael, 1991), which is also expressed using redox buffers (e.g. nickel-nickel oxide NNO; fayalite-magnetite-quartz FMQ). It represents an

intensive variable that provides a measure of the system's redox potential at equilibrium, therefore, controlling the valence state, and hence speciation, of redox-sensitive elements (e.g. Fe, S, As or V) (Lee et al., 2005). As iron is the more abundant redox-sensitive element in magma systems, the $Fe^{3+}/\Sigma Fe$ ratio is commonly used as a proxy to constraint the redox conditions of a given magma.

The more oxidized character of arc magmas is evidenced by comparing basalts erupted through arc volcanoes with those erupted at mid-ocean ridges or at back-arc basins (Christie et al., 1986; Wood et al., 1990; Eggins, 1993; Kelley and Cottrell, 2009; Evans et al., 2012; Kelley and Cottrell, 2012; Richards, 2015), however, the fundamental causes of that difference, are still open to debate. One hypothesis proposes that oxidation of the subarc mantle is due to oxidized fluids derived from subducted slabs, resulting in oxidized-partial melts extracted from the mantle wedge. This is supported by the positive correlation between $Fe^{3+}/\Sigma Fe$ and tracers of slab additions, as $H_2O$ and Ba/La (Kelley and Cottrell, 2009). On the other hand, models based on redox-sensitive element partitioning (e.g. vanadium in the V/Sc ratio; Lee et al., 2005) suggest that the redox state of mantle source does not vary with tectonic setting, and that arc basalts become oxidized exclusively as they differentiate along the path from mantle to surface.

These two contrasting hypotheses have relevant implications in the arc metallogeny. According to the former view, a high $fO_2$ in the mantle source will promote the occurrence of sulfur species as sulfate ($S^{6+}$), with the consequent enrichment in metal and $S^{6+}$ in the resulting partial melt due to the enhanced

solubility of $S^{6+}$ (2 to 5 times higher) compared with $S^{2-}$ in oxidized conditions (Carroll and Rutherford, 1987; Luhr, 1990, Masotta and Keppler, 2015). In agreement to this, Chambefort et al., 2008, suggest that sulfate-saturated mafic magmas emplaced at deep crustal levels are responsible of the efficient transport of sulfur and metal required to produce large mineralized systems at the shallow crust. Such highly oxidized conditions are recorded, for instance, by the ubiquitous presence of anhydrite as inclusion in mafic minerals from the Yanacocha volcanic sequences, genetically linked to the large Cu-Au hydrothermal system (HS epithermal and deeper PCD).

On the contrary, the latter hypothesis indicates that magmatic oxidation observed in arc environment mostly occurs at high crustal levels, particularly during the exsolution of a volatile phase, suggesting that the precipitation of mineral or unmixing of a liquid sulfide phase is ubiquitous during early magmatic stages. Supporters of this view consider this event of magmatic-sulfide precipitation, before volatile exsolution, as a metal pre-concentration mechanism favorable to later hydrothermal ore formation (Jenner et al., 2010; Nadeau et al., 2010; Lee et al., 2012; Sillitoe, 2012; Wilkinson, 2013, Chiaradia, 2014). This implies that shallow hydrothermal fluids would derive their metals from the dissolution of previously concentrated sulfides, in opposition to the former view that considers the early oxidized melts as the direct contributor of sulfur and metal to higher crustal levels.

It is important to note that the transition of sulfide ($S^{2-}$) to sulfate ($S^{6+}$) stability in basaltic melts at pressures of 1 GPa, occurs as $fO_2$ increase from NNO+1 to NNO+2, such that at ~NNO+2.5 the $S^{6+}/\Sigma S$ ratio is 0.95 (Matjuschkin et al., 2016) allowing high concentrations of dissolved sulfate and precluding the saturation of early sulfide phases (Fig.1.1a). The narrow transition from $S^{2-}$ to $S^{6+}$, allows that at $fO_2$'s pertinent to arc magmas, only a minor sulfide phase can be stable during magmatic differentiation. According to Richards (2009, 2015), the moderate presence of such sulfide phase compared to a large volume of low-depleted silicate melt, will conduct to a fertile magma, having the potential to form Cu-rich porphyry deposits at high crustal levels.

In the porphyry environment, data from evolved rocks closely related to world-class PCD's from several mineralized belts, show that these rocks are more oxidized than other regionally-distributed barren intrusive rocks (Dilles et al., 2015; Ballard et al., 2002; Shen et al., 2014). However, determinations of oxygen fugacity in evolved igneous rocks associated to late-stage differentiation processes generate uncertainties regarding to the origin of the observed $fO_2$. The higher oxidation state recorded in porphyry systems could be not necessarily acquired early in the mantle source but proceeds from the late exsolution of a $H_2O$ and S-rich volatile phase. This implies that the basic causes of metal and sulfur-enrichment in ore-forming magmas is not well constrained yet.

Therefore, to determine if the "fertile nature" associated with the redox-state of arc magmas is that of a high oxidation in the mantle wedge or either the

precipitation of a sulfide phase in the mantle-crust transition, it is imperative to avoid the effects produced by intra-crustal magmatic and hydrothermal processes (i.e. crystallization, assimilation of crustal rocks, magma mixing, rock-alteration). The fact that PCD's occurs in thick-crust segments, where mafic compositions are mostly absent at high crustal levels and/or potentially altered by hydrothermal processes, makes the finding of such pristine compositions a difficult challenge to solve in the porphyry environment itself. Hence, the analysis of the closer mafic members, in temporal and spatial scale, occurring at belt scale can be alternatively used to constraint the early stages of arc magmas. A propitious place in the Andean segment of the Mio-Pliocene PCD belt from Central Chile is proposed for this research.

### 1.1.1- Porphyry-type mineralization in Central Chile

The late Miocene to Early Pliocene mineralized belt of Central Chile, located between ~31,6° and ~34,1°S (Deckart et al., 2014, 2005; Stern et al., 2011; Mpodozis and Cornejo, 2012), constitute one of the world largest known metal endowment and overall ore reserves reach more than 300 Mt of copper concentrated in three main deposits (Irarrázaval et al., 2010; Perelló et al., 2009; Cooke et al., 2005). From north to south those corresponds to Los Pelambres-El Pachón (LP-EP; ~12 to 10 Ma), Río Blanco-Los Bronces (RB-LB; ~7 to 4 Ma) and El Teniente (ET; ~6 to 4 Ma) (Fig.1.1b). Additionally, several prospects of similar

ages are distributed along the segment and further to the south, extending the magmatic/hydrothermal belt towards the ~36°S. These indicate that the magmatic/hydrothermal processes related to metal deposition in the high crust of this particular Andean segment, operated synchronously as far as ~36°S (not implying necessarily economically profitable mineralization out of the present-day known deposits).

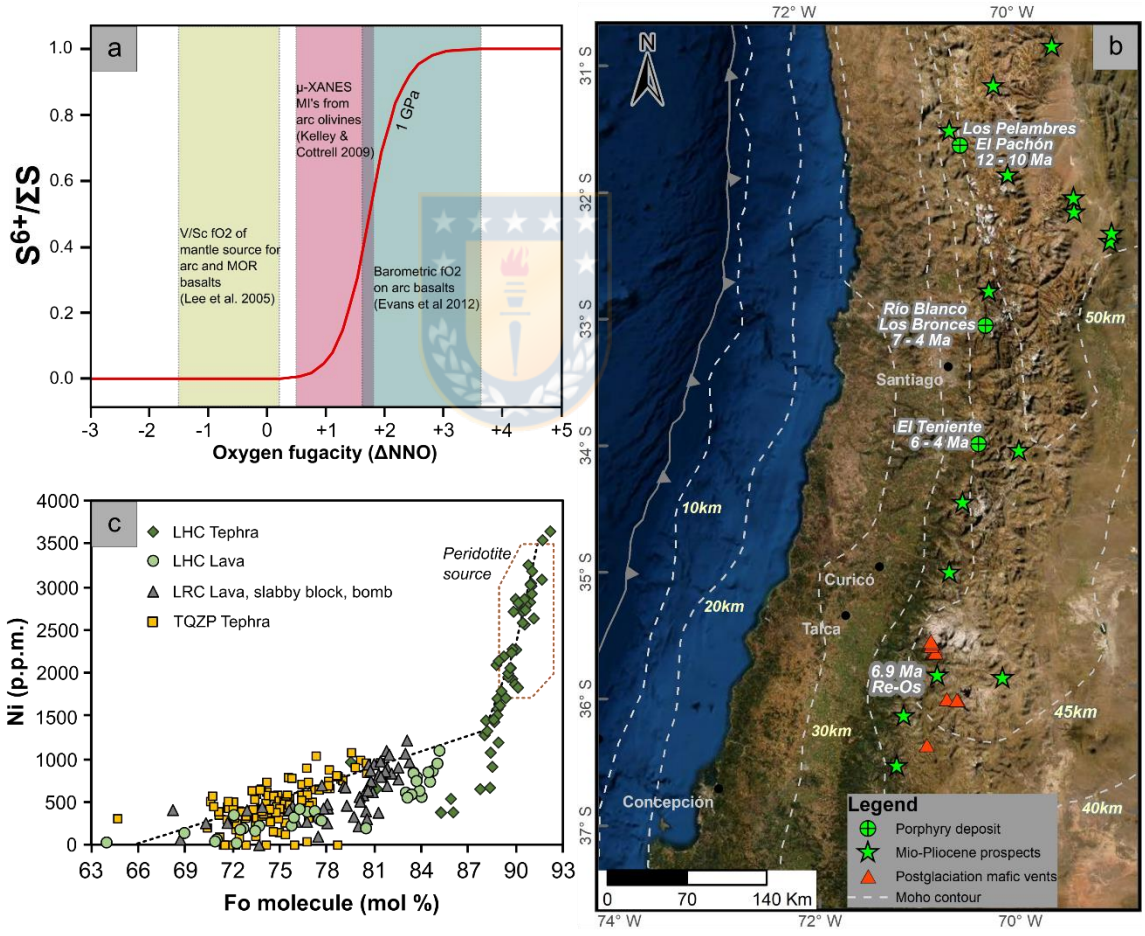


Fig.1.1.- a) Sulfur speciation curve at 1 GPa modified from Matjuskin et al., 2016. Three different approaches to redox conditions are shown. Left box represents the $fO_2$ for the mantle sources at arc and MOR basalts modeled with V/Sc ratios (Lee et al., 2005). Central box represents $fO_2$ based in the $Fe^{3+}/\Sigma Fe$ for melt inclusions from a global collection of arc magmas ($n$=7, no data from the Andes, $Fo_{host}$ 74-83; Kelley and Cottrell, 2009). Right panel show the barometric $fO_2$ calculated for primitive basalts (Evans et al., 2012). b) Porphyry systems, including deposits and

prospects, of Late Miocene-Early Pliocene age in Central Chile. Also, the distribution of post-glacial mafic vents at ~36°S. Note the distribution of crustal thickness along the Andean segment. c) Fo-Ni variations among olivines from different eruptive products occurring in the Descabezado Grande Volcanic Field.

Two interesting large-scale observations in the tectonic-magmatic configuration stand out at this latitude: 1.- The crustal thickness drastically diminish from >45 km at the north to <45 km southward of this boundary (Fig.1.1b) (Tassara and Echaurren, 2012); and 2.- A remarkable shift in the composition of erupted volcanic rocks from the volcanic front, with the northernmost presence of basalt composition in the context of the Southern Volcanic Zone.

Hence, these basaltic compositions, emplaced in a thick-crust segment may be a close proxy to constraint the redox conditions of the less evolved melts related with the fertile nature of arc magmas prospected at the scale of the magmatic/hydrothermal belt of late Miocene to Early Pliocene age in Central Chile.

### 1.1.2.- Prospection of mafic magmas along the magmatic/hydrothermal belt of Central Chile: the Pliocene to recent mafic vents at ~35.5°S.

Previous works (Salas 2010; Salas et al., 2014) shown the occurrence of primitive mafic magmas at Los Hornitos, a pair of monogenetic cones occurring in the vicinity of the Descabezado Grande Volcanic field at 35.5°SL. In addition, a broader examination of the arc region reveals the occurrence of several other

monogenetic volcanoes distributed between 35.5° to 36.5°SL, some of them of unknown composition and others previously reported by Hildreth et al., 2010. Therefore, using bibliographic information, an oriented field-recognizing and sampling of selected mafic vents provide the opportunity to determine the most favorable location(s) to prospect olivine hosted MI's from the less evolved magma compositions.

By several reasons, olivine is the most suitable mineral phase to carry out melt inclusion (MI) studies in the context of mafic compositions: (1) it is the first mineral phase crystallizing at most of basaltic compositions from different tectonic settings; (2) its rather simple composition allows to a relatively simple recalculation of the original trapped melts and any potential contamination with the host may be quickly detected; (3) the common occurrence of several-microns MI's (>20 μm diameter) and (4) Fo-Ni variations in olivine allow a quick determination of the position along the crystallization line.

The sampling of olivine bearing tephra layers ensure the collection of quenched melt inclusions, that results of the rapid cooling experienced during the aerial trajectory of ash and lapilli fragments. This cooling precludes further crystallization inside the inclusion and the trapped melt is preserved with minimal changes (Danyushevsky et al., 2002; Kent, 2008).

The analysis of MI's hosted in high-forsterite olivine (i.e. >~Fo88) provide the access to the earliest stages of magma evolution, when olivine (± spinel) is the only crystallizing phase, potentially in equilibrium with the mantle source

(Fig.1.1c). Previous analysis of MI's hosted by Fo90-92 from Los Hornitos, show relatively high S contents (up to ~3000 ppm) reflecting the prevalence of near undegassed conditions during the trapping of these primitive melts, likely at deep crustal levels (Salas et al., 2009, 2015; Wehrmann et al., 2014). Therefore, the olivine hosted melt inclusions from Los Hornitos and potentially from other primitive vents in the area, will be interrogated by microanalytical techniques (e.g. EPMA, LA-ICPMS, SIMS, μ-XANES) in order to constraint the redox conditions and metal/volatile budget of primitive melts from a mature subduction zone.

## 1.2.- Research questions

1.- Does the metallogenic fertile nature of arc magmas relies on the high $fO_2$ (>~NNO+2) of primitive melts precluding sulfide precipitation, or contrary, within the most reduced conditions (<~NNO) that allow the early saturation of magmatic sulfides followed by a later remobilization to the shallow crust?

2.- At either of those basic causes, what is the $S^{6+}/\Sigma S$ ratio in primitive arc melts that allows the formation of the largest known porphyry Cu-Mo systems like those of RB-LB and ET in the nearby magmatic-hydrothermal belt of Mio-Pliocene age at Central Chile?

## 1.3.- Main goal

Quantitative *in-situ* determination of the $fO_2$ and related metal-volatile budget associated to primitive arc magmas within the southern tip of the Mio-Pliocene mineralized belt of central Chile in order to improve the understanding of the early petrogenetic processes linked to metal and sulfur transport to form hydrothermal deposits at high crustal levels.

### 1.4.- Specific goals (SG's)

**Specific goal 1 (SG1):** Sampling of mafic vents at the southern tip of the Mio-Pliocene belt and determination of its petro-chemical characteristics in order to select the most primitive compositions of arc magmas in this segment.

**Specific goal 2 (SG2):** Determine the textural features of the olivine crystals obtained from the tephra samples, allowing the prospection of MI's in texturally mature crystals (i.e. polyhedrals).

**Specific goal 3 (SG3):** Establish the composition and volatile-metal budget of primitive melts through the study of high-Fo olivine-hosted MI's.

**Specific goal 4 (SG4):** Determine the redox state of primitive arc melts by micro-analytical determination of $Fe^{3+}/\Sigma Fe$ ration in trapped glasses.

**Specific goal 5 (SG5):** Integrate the results to establish the influence of recorded magmatic conditions regarding the formation of PCD's at shallow crustal levels in this segment of the Andes.

## 1.5.- Methodology

### Related to SG1

As mentioned previously, in addition to Los Hornitos and La Resolana Craters in the nearby of Descabezado Grande volcanic field (Salas 2010), several other well-preserved monogenetic mafic vents distribute in the segment 35.5° to 36.5°SL. Preliminary data at Los Hornitos cones (35.5°SL) allowed the recognition of high-Fo ($92 \geq Fo \geq 88$) olivine crystals contained in tephra deposits associated to the initial stages of a post-glacial eruptive event. The occurrence of quenched melt inclusions in some of these crystals makes them suitable for a detailed analysis of mineral chemistry and trapped glasses. Literature revision and field work will be intended for recognition and sampling of eruptive products in selected mafic vents. Olivine separates will be obtained from the tephra samples using heavy liquids.

### Related to SG2

By the use of binocular lenses, aliquots of the olivine separates, will be observed in order to determine textural features, size and occurrence of MI's. The selected crystals will be documented by pictures and sketches that highlight the location of the inclusion, and facilitate the access in further stages.

The recognizing of textural features of crystal hosts will allow a priori to identify inclusions that could be trapped in conditions out of equilibrium. The reliability of melt inclusions as indicator of the composition from which the host crystallized,

largely depends on the growth conditions of the olivine host during the trapping of melts. It is well supported in literature (Milman-Barris et al., 2008; Shea et al., 2015; Welsch et al., 2014; Honour et al., 2018), that fast growth rates conforming dendritic and skeletal textured crystals, promote the development of compositional boundary layers (CBL's) around the emerging crystals, and thus some inclusions may encapsulate such non-equilibrium composition, which will be depleted in compatible (e.g. Fo, Ni) and enriched in incompatible elements (e.g. Al, P, Cr). Therefore, the texturally mature olivines (i.e. near polyhedral) ensure growth conditions such that diffusion take place at the crystal-melt interface, and the entrapped melts are in equilibrium with the far field melt.

**Related to SG3**

About 70-80 MI's will be selected for major and minor element analysis by EPMA. For this purpose, a previous stage of exploration and mapping of crystals by reflected and transparent microscopy will be carried out to reference the most suitable MI's at each olivine grain. Major and minor oxides will be measured: $SiO_2$, $TiO_2$, $Al_2O_3$, $Cr_2O_3$, FeO, MnO, NiO, MgO, CaO, $Na_2O$, $K_2O$, $SO_4$ including the elemental Cl. Melt inclusion data will be corrected for post-entrapment crystallization of olivine (PEC) and diffusive loss of Fe (Fe-loss) by the use of Petrolog software (Danyushevsky and Plechov, 2011). In addition, $H_2O$, S, Cl, $CO_2$, P and F will be determined by SIMS. The composition of the olivine host surrounding the MI at <10 µm will be determined and characterized by FeO, MgO,

NiO, CaO and MnO. Detailed methodology regarding the mounting of exposed melt inclusions can be found in Chapter 4.

**Related to SG4**

The $Fe^{3+}/\Sigma Fe$ ratio in melt inclusions will be determinate by µ-XANES and these measured values will be corrected for post-entrapment modifications to obtain the original ratio. Further, the $Fe^{3+}/\Sigma Fe$ will be transformed to $fO_2$ using the algorithm of Kress and Carmichael (1991) at pressure and temperature appropriated for these magmas.

**Related to SG5**

Results will be integrated and modeled along the obtained variables (T, P, $fO_2$, metal and volatile budget) and analyzed in comparison to published data from arc samples. Thus, the mantle source underneath the magmatic-hydrothermal Mio-Pliocene belt will be constrained, contributing to the understanding of the early metallogenic processes related to Cu-Au ore deposition at high crustal levels in active continental margins.

# Chapter 2: Prospecting the most mafic compositions among the post-glaciation monogenetic vents of the arc region between 35.5° to 36.5°S

Article: Mafic monogenetic vents at the Descabezado Grande volcanic field (35.5°S-70.8°W): the northernmost evidence of regional primitive volcanism in the Southern Volcanic Zone of Chile

**Abstract**

In the Andean Southern Volcanic Zone (SVZ) the broad distribution of mafic compositions along the recent volcanic arc occurs mainly south of 37° S, above a comparatively thin continental crust (≤ ~35 Km) and mostly associated with the dextral strike-slip regime of the Liquiñe-Ofqui Fault Zone (LOFZ). North of 36° S, mafic compositions are scarce. This would be in part related to the effect resulting from protracted periods of trapping of less-evolved ascending magmas beneath a thick Meso-Cenozoic volcano-sedimentary cover that lead to more evolved compositions in volcanic rocks erupted at the surface.

Here, we present whole rock and olivine mineral chemistry data for mafic rocks from four monogenetic vents developed above a SVZ segment of thick crust (~45 Km) in the Descabezado Grande Volcanic Field (~35.5° S). Whole rock chemistry (MgO > 8 wt.%) and compositional variations in olivine (92 ≥ Fo ≥ 88 and Ni up to ~3650 ppm) indicate that some of the basaltic products erupted through these vents (e.g. Los Hornitos monogenetic cones) represent primitive arc magmas reaching high crustal levels.

The combined use of satellite images, regional data analysis and field observations allow to recognize at least 38 mafic monogenetic volcanoes dispersed over an area of about 5000 $km^2$ between 35.5° and 36.5° S. A link between ancient structures inherited from pre-Andean tectonics and the emplacement and distribution of this mafic volcanism is suggested as a first-order structural control that may explain the widespread occurrence of mafic volcanism in this Andean arc segment with thick crust.

**Keywords:** monogenetic volcanism, Andean Southern Volcanic Zone, Descabezado Grande volcanic field, olivine.

Published as: Salas, P. A., Rabbia, O. M., Hernández, L. B., & Ruprecht, P. (2016). Mafic monogenetic vents at the Descabezado Grande volcanic field (35.5 S–70.8 W): the northernmost evidence of regional primitive volcanism in the Southern Volcanic Zone of Chile. *International Journal of Earth Sciences*, *106*(3), 1107-1121.

## 2.1.- Introduction

Mafic monogenetic volcanoes comprise edifices with a small cumulative volume (typically ≤ 1 $km^3$) that have been built up by one continuous, or many discontinuous, small eruptions that occurred over a brief time interval, often with different eruption styles, from highly explosive to effusive regimes leading to different landforms, like spatter and pyroclastic cones, maar-diatremes and tuff rings (e.g. Németh and Kereszturi, 2015, Johnson, 2008; Roberge, 2014; Genareau et al., 2009; Valentine and Gregg, 2008). A common feature of monogenetic volcanoes is the primitive nature of the erupted products suggesting that they represent the composition of deep seated magmas that are able to traverse the crust in short timescales with minimal cooling (e.g. Ruprecht and Plank, 2013) thereby minimizing compositional evolution by shallow crystallization, thus providing key insights into how the mantle produces its partial melts and how that melt rise to the surface (Németh and Kereszturi, 2015). Conversely, long-term differentiation processes commonly associated with stratovolcanoes accounts for modifications of primary magmatic compositions, as evidenced by the scarcity of primitive, non-cumulate, high-MgO (> 8wt.%) magmas potentially in equilibrium with the mantle wedge in volcanic arc suites (Hildreth and Moorbath, 1988; Annen et al., 2006).

Recent magmatism in the Andean SVZ results from subduction of the Nazca Plate beneath South America at a trench normal convergence velocity of ~40 mm/year (e.g. Maloney, et al., 2013). This belt includes volcanoes from the marginal portion

of the Pampean flat slab segment at 33° S to the latitude of the subduction of Chile Ridge at 46° S. The Andean SVZ has been divided into several segments based on petrographic, geochemical and isotopic variations of erupted rocks, spatial volcano distribution and incoming fracture zones (e.g. Völker et al., 2011, Dungan et al., 2001, Hildreth and Moorbath 1988, López-Escobar et al., 1995). According to López-Escobar et al., (1995), four distinctive segments or provinces are recognized in the current arc: northern (NSVZ, 33° - 34.5° S), transitional (TSVZ, 34.5° - 37° S), central (CSVZ, 37° - 41.5° S) and southern (SSVZ, 41.5° - 46° S). Compositional variations of erupted magmas indicate a higher basalt/rhyolite ratio in the CSVZ and SSVZ compared to the NSVZ and TSVZ segments. In addition, andesite and dacite are the dominant rock types erupted in the NSVZ and TSVZ (Stern, 2004).

Crustal thickness beneath the SVZ decreases toward the south, from ~50 km in the NSVZ, ~45 km in the southern part of TSVZ (~36°S) and ~30 km thick at the southern end of the SSVZ (Tassara & Echaurren, 2012).

The distribution of mafic monogenetic volcanoes in the SVZ is mostly restricted to its southern portion (south of ~38° S) in the CSVZ and SSVZ segments (e.g. López-Escobar et al., 1995), where the continental crust is thinner than ~35 km (e.g. Tassara and Echaurren, 2012). Here, this mafic volcanism is structurally related to the main NNE-trending lineaments of the Liquiñe Ofqui fault zone (LOFZ) and/or contained in a subsidiary trend oriented ENE, as it is the case for the Carrán-Los Venados mafic volcanic group (López-Escobar et al., 1995;

Bucchi et al., 2015; Morgado et al., 2015). North of 38° S in a thicker crust environment, mafic monogenetic volcanoes are scarce. Moreover, any basaltic product (lava or pyroclastic deposit) becomes uncommon northward of 36°S, and true basalts (< 52 wt% of $SiO_2$) are not reported north of this latitude. The most mafic lavas (~52 wt% of $SiO_2$) from the Planchón-Peteroa volcano (~35.3°S at the TSVZ; PPV in Fig.2.1b) may represent the northernmost appearance of volcanic products with near-basaltic compositions throughout the entire volcanic belt. Southward, in the TSVZ at about 36°S, mafic products are present in minor proportions at the Tatara-San Pedro volcanic complex (e.g. Dungan et al., 2001; Fig.2.2) and also at Nevado de Longaví volcano (Sellés et al., 2004; Rodríguez et al., 2007; Fig.2.2), located ~36 km towards the southwest of the former volcanic complex (Fig.2.1b, Fig.2.2).

In this contribution we address the conspicuous presence of a dispersed mafic monogenetic volcanic field occurring along a 100 km segment in the TSVZ, between 35.5° and 36.5°S, where crustal thickness reaches up to above 45 km (e.g. Tassara and Echaurren, 2012). Petrography, whole rock and olivine mineral chemistry data from Los Hornitos cones (LHC) and La Resolana craters (LRC), at the southwest flank of Descabezado Grande volcanic field (Maule Region, Fig. 2.1c) are used to support the presence of near-primary basalts in the TSVZ. Results are then discussed in a regional context using published information and implications for the current distribution and long-term record of mafic volcanic products in the area are also provided.

## 2.2.- Distribution of recent mafic monogenetic volcanoes in the TSVZ between 35.5° and 36.5°S

Los Hornitos cones, located 11 km southwest of Quizapu crater (Fig.2.1c, Fig.2.3, Fig.2.4), consist of two twinned pyroclastic cones constituted by pyroclastic fallout deposits, scoria cones and associated lava flows (Fig.2.5a and b). The two cones are named LHC-West and East, referring to their spatial relation. High forsterite (Fo) olivine compositions (up to $Fo_{91}$) hosting sulphur-rich (up to ~3000 ppm) melt inclusions have been reported from Los Hornitos (Salas et al., 2009, 2014, 2015; Wehrmann et al., 2014), reflecting the participation of primitive magmas and the prevalence of near-undegassed conditions during the trapping of melts.

Aside from composition, an obvious difference between Los Hornitos and La Resolana craters, located 8 km apart from each other, is their different eruptive character. LRC represent a cluster of three maar-like vents, here referred to as LRC-North, Central and South. In addition to tephra deposits, lava erupted at LRC-North while only tephra deposits are found associated with LRC-Central and South craters (Fig.2.5c).

Approximately 50 km southeast of the study area, at least three postglacial (<25 ka) mafic units (basalt and mafic andesites) are present in the Laguna del Maule volcanic field (LdM; Fig.2.2) (Hildreth et al., 2010). These include the two pyroclastic cones and associated lava flows of Hoyo Colorado basalt (BHC), the

andesite of Arroyo Cabeceras de Troncoso (MCT) and Crater 2657 andesite (MCP).

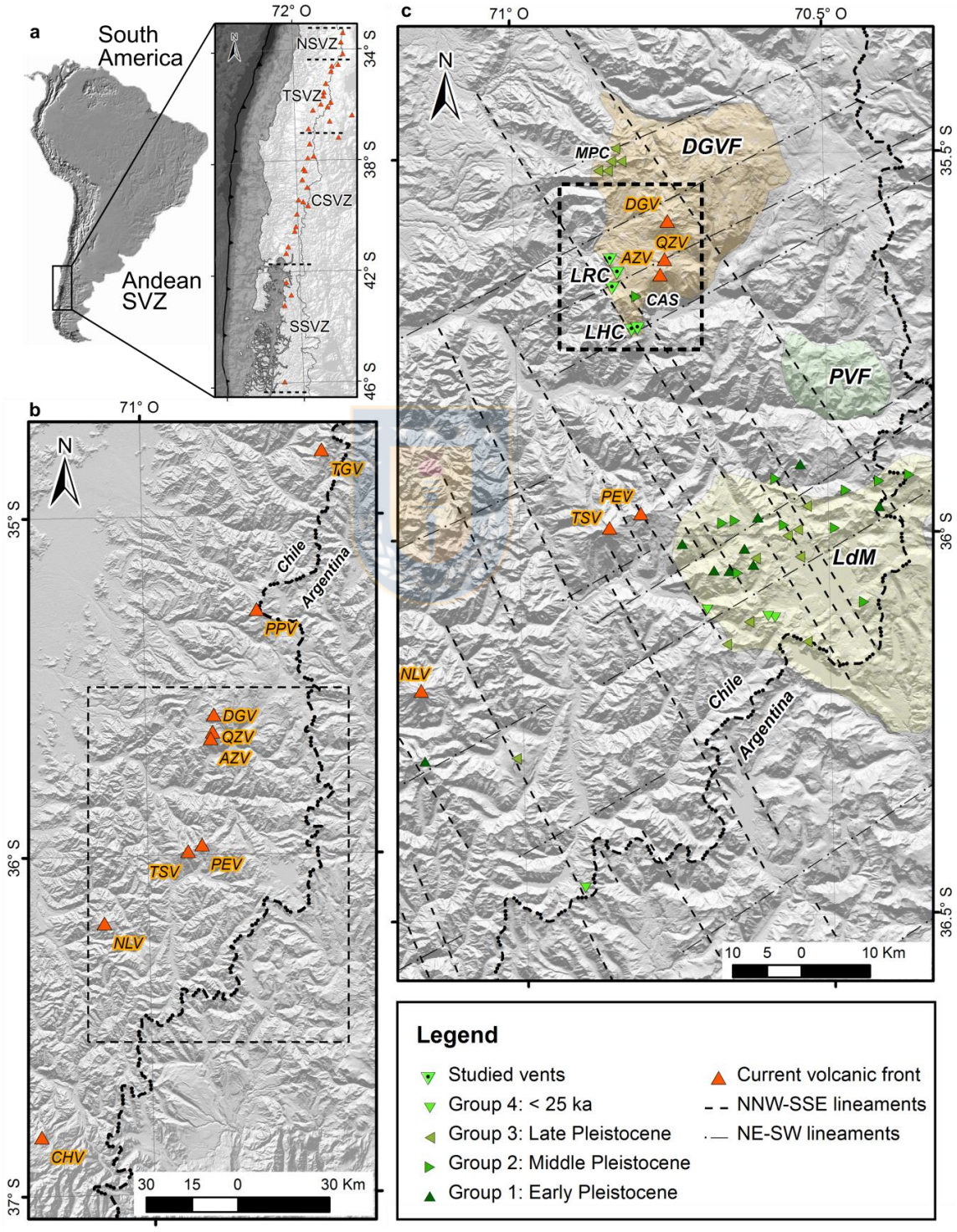

Fig.2.1a. Location of the Andean Southern Volcanic Zone (SVZ) in the context of South America. The segmentation along the arc is shown in the right inset (López-Escobar et al., 1995). b. Distribution of main volcanic centers in the Transitional SVZ. From north to south corresponds to the following volcanoes: Tinguiririca (TGV), Planchón-Peteroa (PPV), Descabezado Grande (DGV), Quizapu (QZV), Azul (AZV), Tatara-San Pedro (TSV), Pellado (PEV), Nevado de Longaví (NLV) and Chillán (CHV). Segmented area corresponds to enlarged area in c. c. Distribution of mafic monogenetic volcanoes in the segment between 35.5° to 36.5° S. Segmented area shows the location of minor vents in the Descabezado Grande volcanic field (DGVF), those are La Resolana craters (LRC), Los Hornitos cones (LHC) and older volcanism of Manantial Pelado cones (MPC) and Las Casitas volcanic field (CAS). Puelche (PVF) and Laguna del Maule (LdM) volcanic fields are also highlighted. Spatial distribution of NNW-SSE and NE-SW lineaments and vents are shown. A detailed classification of groups is shown in Table 2.1.

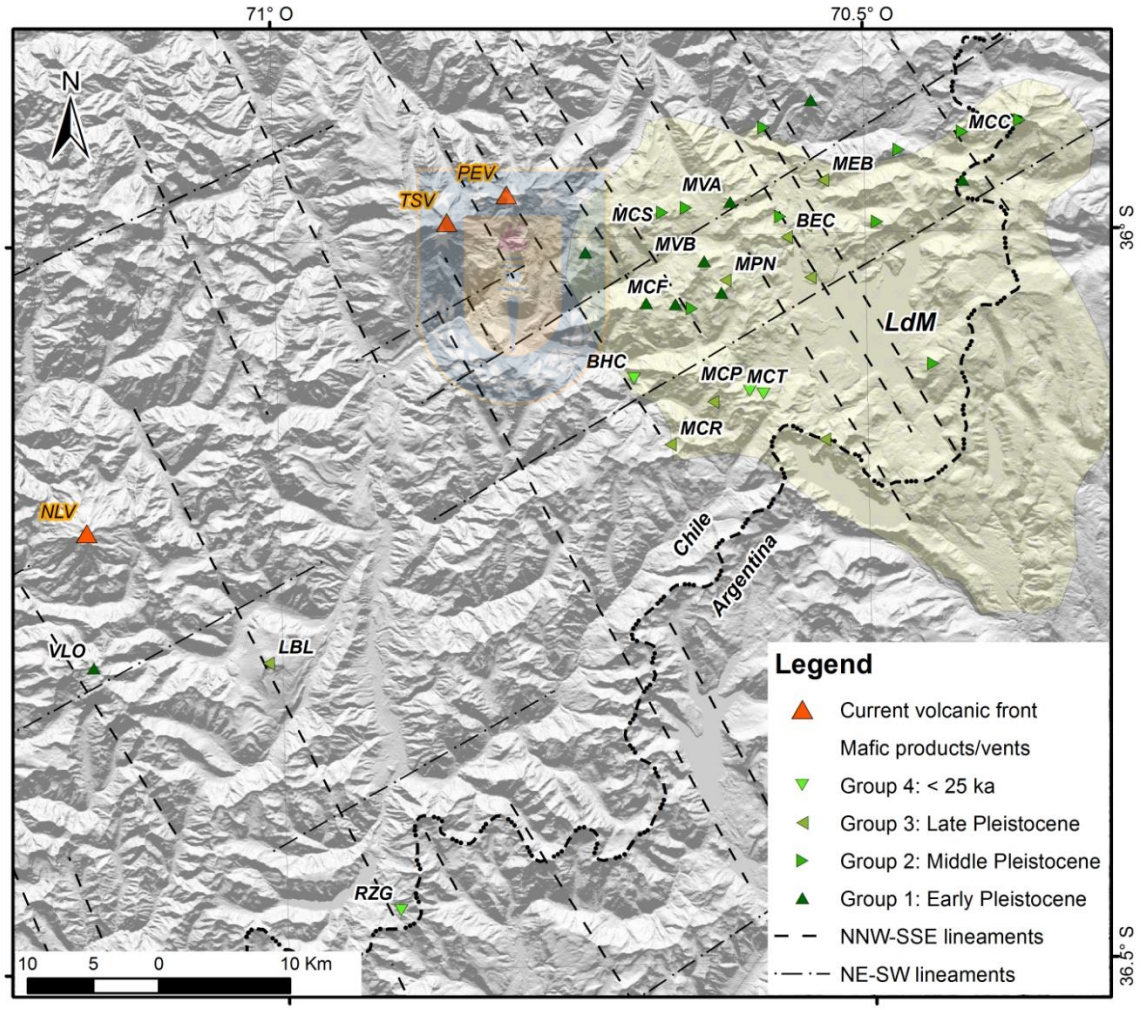


Fig.2.2. Distribution of monogenetic mafic volcanoes in the Laguna del Maule volcanic field (LdM) and the three isolated vents of Loma Blanca (LBL), Rezago (RZG) and Villalobos (VLO) to the southern border. A detailed classification of groups is shown in Table 2.1.

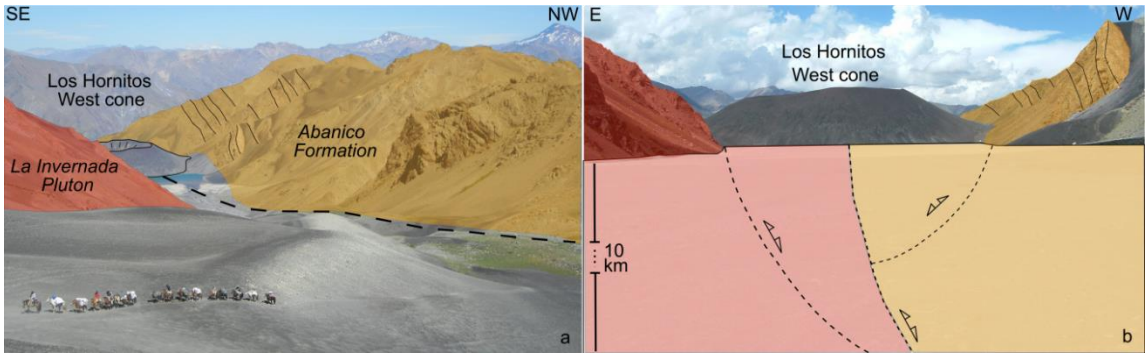


Fig.2.3.a.- Panoramic view looking southward to Los Hornitos valley, showing the position of the cone just on the contact between the folded Abanico Formation and La Invernada Pluton. Segmented line is showing the trace of an inferred fault system along the NNW valley. b.- Conceptual model based in Astaburuaga (2014) representing a schematic motion of blocks during the extensional and contractional Cenozoic events. Note that this structural environment is coherent with the inversion of normal faults that compartmentalized the extensional Abanico Basin during the Mio-Pliocene compressive event (Piquer et al., 2015; Astaburuaga, 2014).

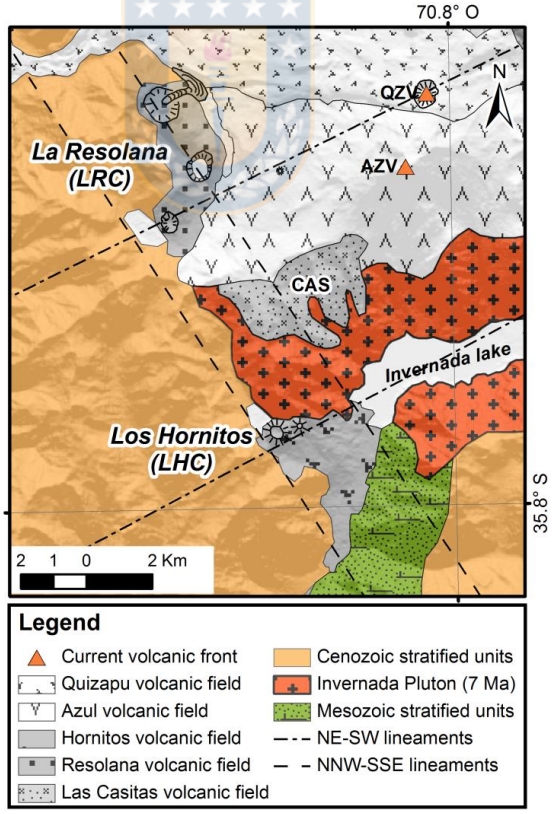


Fig.2.4. Geological map of the surrounding area of Los Hornitos (LHC) and La Resolana (LRC) vents. Regional NNW-SSE and NE-SW lineaments are shown. The age of La Invernada pluton is taken from Hildreth and Drake (1992).

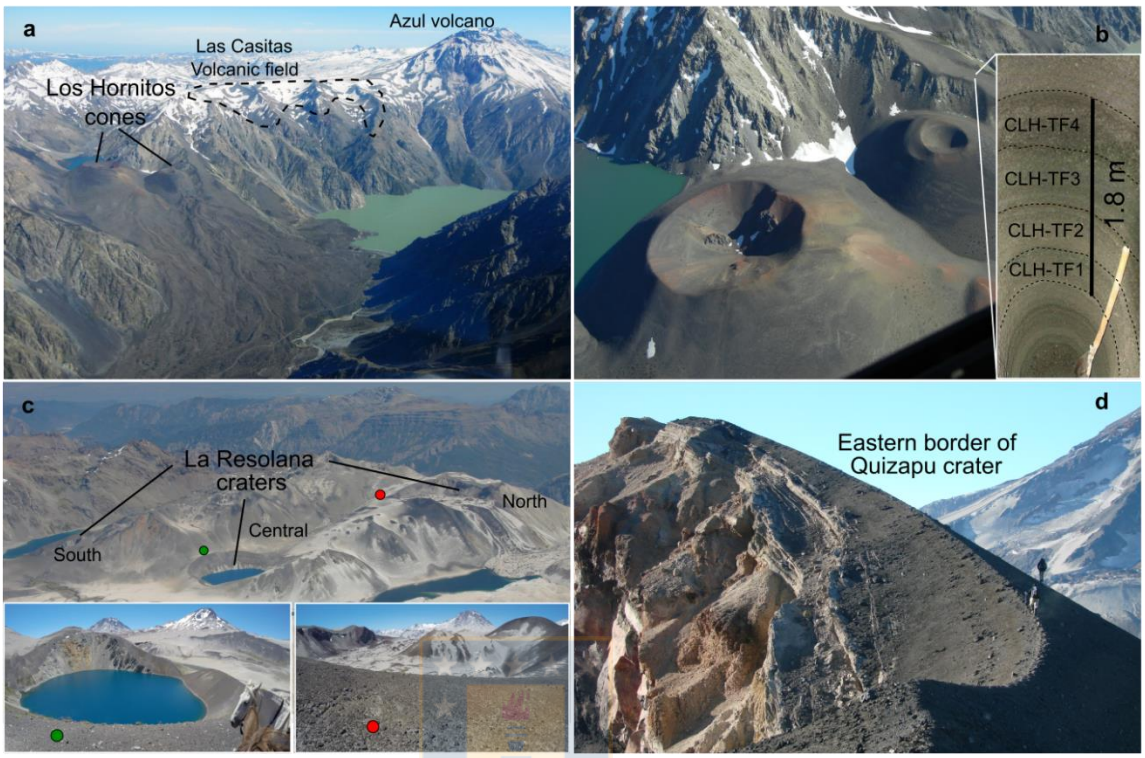


Fig.2.5a. Panoramic view looking northward. In the foreground the two cones of Los Hornitos and its lava field. In the background segmented line is showing the location of Las Casitas volcanic field and Azul volcano. b. Aerial view of the two-cones of Los Hornitos showing the preservation state. Also is shown the inset with the excavated section of the tephra deposit from the initial explosive stage of the younger (eastern) cone. c. Panoramic view looking west showing the distribution of La Resolana craters. The north crater is composed by pyroclastic and lava effusion while only pyroclastic deposits are found associated to the central and south craters. Green and red points show the positions of observer for the lower inset. d. Northward view of the eastern rim of Quizapu crater showing the tephra deposit of mafic scoria emitted in the terminal stage of the plinian event of 1932.

Additionally, eight silicic andesite units are recognized in this volcanic field (not shown in Fig.2.2). The Rezago volcano (RZG) is another scoria cone with associated tephra deposits and lava flows located in the southern end of the TVSZ segment at about 40 km south of LdM (Fig.2.2).

Considering the preservation state of volcanic products, the five vents (LRC-North, Central, South and LHC-West and East) located in the Descabezado

Grande volcanic field (DGVF) together with BHC and RZG appear to be more recent than MCT and MCP, although their precise ages have not been determined yet.

Monogenetic cones from the DGVF are located at 7.5 km west of the Quizapu volcano; a young and voluminous vent which erupted ~10 $km^3$ of andesite to dacite magmas in two eruptive events separated by 86 years (Hildreth and Drake, 1992; Ruprecht et al., 2012; Higgins et al., 2015). The participation of mafic magma is documented in both eruptive episodes; as microgranular mafic enclaves during the effusive event of 1846-1847 and as mafic scoria emission during initial and terminal stages of the plinian event of 1932 (Hildreth and Drake, 1992; Salas et al., 2009; Ruprecht et al., 2012). Considering the young character (<25 ka) of LRC and LHC and the historical eruptions of Quizapu volcano, below we compare a whole rock geochemical and olivine mineral chemistry between these mafic products to discuss how their crustal transit may have varied.

## 2.3.- Regional tectonic features in the area of Descabezado Grande volcanic field

At regional scale, the mafic vents occurring in the western edge of DGVF, including Los Hornitos cones and La Resolana craters, are located in the boundary between two basement domains, the Mesozoic (to the east) and the Cenozoic (to the west). In the study area, these geological domains are

represented by the Mesozoic Río Damas, Baños del Flaco and Colimapu Formations and the Cenozoic Abanico Formation. This major tectonic boundary has been interpreted as the eastern border of Abanico extensional basin (Piquer et al., 2010; Charrier et al., 2002), developed during the Eocene to the Early Miocene (Giambiagi et al., 2015). According to Piquer et al., 2015, the Abanico basin was compartmentalized by previous regional-scale normal fault systems striking NW and NE. Later, during the inversion of Abanico basin, those faults were selectively reactivated by the Mio-Pliocene east-west contraction, with the NW-striking faults showing a composite reverse-sinistral movement and the NE-striking faults showing mainly dextral strike-slip movement. As a consequence of this compressional tectonic event a fault and thrust belt was developed towards the back-arc accommodating different amounts of crustal shortening along the orogen (e.g. Giambiagi et al., 2015; Mescua et al., 2014).

At local scale, LHC are situated in the southern tip of a NNW-valley, which represents the contact between the strongly folded volcano-sedimentary rocks of Abanico Formation to the west and the 12 to 7 Ma La Invernada pluton (Astaburuaga, 2014; Hildreth and Drake, 1992) to the east (Fig.2.3 a, b; Fig.2.4). Therefore, field observations and tectonic interpretations suggest that monogenetic vents occurring at the western border of DGVF (Fig.2.1c) are located over a tectonically weak zone that during Miocene to Early Pliocene time, under a compressive regime, allowed the emplacement of La Invernada pluton and absorbed certain amounts of compressive deformation (e.g. Astaburuaga,

2014), probably facilitated by the thermal gradient provided by the intrusives. Compressive stresses gradually decreased from the Early Pliocene to today (Giambiagi et al., 2015). As a consequence, a thick, mostly mafic volcanic sequence, the Cola de Zorro Formation, was emplaced along the arc region between 36° to 39° S during Late Pliocene to Pleistocene (Sellés, 2006; Muñoz y Niemeyer, 1984; Vergara y Muñoz; 1982).

### 2.4.- Sampling and analytical methodology

Samples for whole rock and mineral chemistry analysis were taken from different eruptive units (tephra, bomb and lava) at LRC and LHC, and from the terminal mafic scoria of 1932 eruption of Quizapu volcano (TQZV). At Los Hornitos cones, stratigraphic relations and preservation state indicate the East cone to be the younger cone. A widely distributed tephra deposit covers the area reaching up to ~1.5 km around the cones. This fallout deposit represents the initial (explosive) eruptive stage of LHC-East and is comprised of layered beds of variable thickness and amounts of lapilli and ash fragments. At the excavation site (~ 400 m E from the vent) individual layers have a maximum thickness of ~50 cm. Samples were collected at four different depths within the section, as shown in the inset of Fig.2.5b. Olivine is the most common mineral phase in the tephra layers and occurs as loose grains, simplifying their separation. The terminal scoria of the 1932 Quizapu eruption ranges from 2 to 6 m (Fig.2.5d) in thickness. It overlies

finely-laminated phreatic ash deposits (Hildreth and Drake, 1992). The contact between phreatic and mafic scoria tephra is gradational suggesting a continuous eruption of these deposits and a progressively larger contribution from mafic magmas. The terminal scoria is generally coarsening upward to lapilli size with the uppermost 2 m mostly composed of glassy, highly vesiculated mafic scoria lacking earlier erupted phreatic components. Some larger mafic bombs (> 20 cm) are found on the crater rim. These deposits are restricted to the east side of the crater. We collected samples from the upper part of the deposit.

Olivine separation was performed at the Laboratory of Sedimentology, Universidad de Concepción, Chile, using a combination of magnetic (Frantz isodynamic magnetic separator) and gravity (2.96 and 3.10 gr/cm$^3$ dense liquids) techniques and mounted in epoxy for chemical analysis, while olivine crystals from the lavas were analyzed in thin sections. At LHC olivine was concentrated from the ash-rich sample (CLHE-TF2; Fig.2.5b). Additionally, a coarse lapilli-rich sample (CLHE-TF4; Fig.2.5b) was selected for whole rock analysis. Thin sections were prepared for olivine analysis from the late effusive stage at LHC (lava sample CLHE-2) and from massive rock samples (i.e. slabby blocks, lava and bombs) from LRC-North and South.

Bulk rock major and trace element analyses were performed by X-ray fluorescence (XRF) at Washington State University following the procedure of Johnson et al., (1999) and results were previously published by Ruprecht et al., (2012). Olivine mineral chemistry was obtained using a JEOL 733 electron

microprobe and a JEOL JXA8600 electron microprobe at the University of Washington (Seattle) and at the Instituto de Geología Económica Aplicada (GEA) from the Universidad de Concepción (Chile), respectively, with similar beam conditions (15 kV accelerating voltage, 20-30 nA beam current and a 5 µm beam diameter). Reference materials for calibration on the JEOL 733 were fayalite (Si, Fe), garnet (Mn), clinopyroxene (Ca), forsterite (Mg), and NiO (Ni) with counting times of 40s/20s (peak/background) for all elements except 100s/50s for Ca. On the JEOL JXA8600 spectrometers were calibrated on diopside USNM 117733 (Si) and fayalite USNM 85276 (Fe) (Jarosewich et al., 1980), and synthetic MnTiO3 (Mn), forsterite (Mg), wollastonite (Ca) and NiO (Ni). Counting times were 20/10 peak/background for Si, Mg and Fe, and 120/60 for Ca, Mn and Ni. Analytical precision was typically better than 1% for Si, Mg and Fe, better than 5% for Mn and Ca, and better than 7% for Ni (20% for JEOL 733). Data reduction was performed using the ZAF correction method.

## 2.5.- Results

### 2.5.1.- Vent distribution and structural controls

At regional scale, the segment between 35.5° and 36.5°S, where mafic volcanism is present, comprises an area of about 5000 $km^2$, bounded by the DGVF to the north and by the Nevado de Longaví and Chillán volcanoes to the south

(Fig.2.1b). The overall distribution of mafic volcanic units in this segment can be organized from north to south as follow:

1.- A cluster of at least 11 vents and volcanic products outcropping in the west flank of DGVF. This includes Manantial Pelado (MPC, 5 vents), LRC (3 maar-like vents), LHC (2 cones) and Las Casitas volcanic field (CAS) (Fig.2.1c).

2.- A cluster of at least 30 vents or volcanic units distributed in the north and west flank of LdM (Fig.2.2). This includes several units accounting since the Early Pleistocene and have been described by Hildreth et al., 2010. Here, several silicic andesite units have been excluded from the analysis and only basaltic and basaltic andesite compositions are considered.

3.- Three isolated and poorly known volcanic centers are dispersed at the southern edge of the segment (Fig.2.2). The Loma Blanca (LBL) and Rezago (RZG) volcanoes are two monogenetic centers located in the southeast area of Nevado de Longaví volcano (NLV). Their state of preservation suggests a Late Pleistocene and post-glacial age, respectively. Additionally, the Villalobos volcano corresponds to a mafic stratocone of Early Pleistocene age located 10 km south of NLV (Sellés, 2006).

Locally the five monogenetic vents in the northern cluster (1) occurring at the southwestern side of DGVF align along a NNW-SSE lineaments (Fig.2.1c, Fig.2.4). Thereby, vents of LRC-North and Central coincide with CAS southward, while the LRC-South aligns with LHC vents southward by the NNW-SSE valley of Los Hornitos. The distribution of these vents seems to be also controlled by NE-

SW lineaments, since most cones occur at these lineament intersections. These two structural trends dominate in the SVZ segment between 35° to 37°S (Fig.2.1b and c, Fig.2.2).

The southward prolongations of NNW-SSE lineaments reach the central portion of LdM and at its northwestern periphery they intersect the locally dominant NE-SW to ENE-WSW lineaments (Fig.2.2). Toward the southwestern margin of LdM the Hoyo Colorado cones (BHC) together with the older Cajón Rodríguez vents (MCR) are emplaced above a lineament that intersects the northern flank of Pellado volcano through the north (Fig.2.2). Several older mafic volcanic units at the western periphery of LdM seem to be grouped in this setting of structures, where a corridor of ENE-WSW lineaments occurs and probably controls the emplacement of these mafic volcanoes (Fig.2.2).

Toward the southern edge of the segment, another NNW-SSE lineament that flanks the eastern border of Nevado de Longaví volcano (NLV) additionally contains the Loma Blanca and Rezago volcanoes through the south. Further, Villalobos volcano (Sellés, 2004; VLO) is emplaced near the intersection of NNW-SSE and NE-SW lineaments (Fig.2.2).

The NNW-SSE lineaments seem to be the main control in the distribution of mafic volcanism between 35.5° and 36.5°S.

### 2.5.2.- Relative age of mafic volcanoes

The relative distribution is divided in four groups based on published ages and preservation state of volcanic landforms.

Table 2.1.- Summarizes the age of 38 mafic monogenetic vents recognized in the segment between 35.5° to 36.5° S. Only basaltic and basaltic andesite ($SiO_2$ < 57 wt %) compositions have been considered. Several silicic andesite compositions from LdM have been excluded of this analysis. Preservation state of volcanic units of Group 4 indicates a post-glacial age, which had been determined to begin at ~25 ka in the area of Laguna del Maule at ~ 36° S in central Chile (Singer et al., 2000).

| Group | Volcanic unit | | Relative age | | |
|---|---|---|---|---|---|
| Group 4 | Los Hornitos | LHC | 0.025 Ma | Holocene | Pleistocene |
| | La Resolana | LRC | | | |
| | Cabecera Troncoso | MCT* | | | |
| | Crater 2657 | MCP* | | | |
| | Hoyo Colorado | BHC* | | | |
| | Rezago | RZG | | | |
| Group 3 | Loma Blanca | LBL | 0.126 Ma | Late | |
| | Manantial Pelado | MNPC | | | |
| | El Candado | BEC* | | | |
| | Vega Piedras Negras | MPN* | | | |
| | Cajón Rodríguez south | MCR* | | | |
| | Laguna Turbia | MLT* | | | |
| | Salto del Maule | MSM* | | | |
| | Estero Bobadilla | MEB* | | | |
| | Puente de la Laguna | MPL* | | | |
| | Las Salinas | MLS* | | | |
| Group 2 | Las Casitas | CAS | 0.9 Ma | Middle | |
| | Volcán de la Calle | MVC* | | | |
| | Cerro Campanario | MCC* | | | |
| | Volcán Pellado | PEV | | | |
| | Cerro San Pedro | MCS* | | | |
| | Cerro Bahamondes | MCB* | | | |
| | La Poza | MLP* | | | |
| | Bobadilla Chico | BBC* | | | |
| | Paso Campanario | MPC* | | | |
| | Río Blanco | MRB* | | | |
| | Oeste Cerro Risco Bayo | MOR* | | | |
| | Cajón Filume | BCF* | | | |
| | Mid El Molino Sequence | MEM | | | |
| Group 1 | Cordón Filume | MCF* | 2.6 Ma | Early | |
| | Volcán Aguirre | MVA* | | | |
| | Volcán Botacura | MVB* | | | |
| | Sin Puerto | MSP* | | | |
| | Volcán Ñirales | MVÑ* | | | |
| | Volcán Munizaga | MVM* | | | |
| | Arroyo Santuario | MAS* | | | |
| | Quebrada Fiera | MQF* | | | |
| | Villalobos | VLO | | | |

*Group 1:* The oldest dated units belong to the Early Pleistocene and correspond to Botacura (MVB; 1,324 ka) and Aguirre (MVA; 1,290 ka) volcanoes (Hildreth et al., 2010) (Fig.2.2). The undated volcanism of Cordón Filume (MCF; Fig.2.2), however, could be even older than 1.5 Ma, as suggested by Hildreth et al., (2010). According to those authors, at least eight mafic volcanic units belong to this period. Further, the mafic Villalobos volcano in the vicinity of NLV has been dated in the range of about 1.7 to 0.9 Ma (Sellés, 2006).

*Group 2:* At least thirteen volcanic units are defined for the Middle Pleistocene, that among others centers include the Cerro San Pedro volcanic shield (MCS; 243 ka), Pellado (PEV; ~188-83 ka) and Cerro Campanario (MCC; ~150 ka) volcanoes (Hildreth et al., 2010). At a broadly similar period, the volcanism was active at Las Casitas (CAS) volcanic field, whose age range between 0.51 to 0.34 Ma (Wolff 2005, Wolff 2008). Further, at the Tatara-San Pedro complex, the Middle El Molino Sequence (MEM; 579 ka) includes three primitive basaltic compositions and an evolved basaltic lava (Dungan et al., 2001).

*Group 3:* During the Late Pleistocene, at least ten mafic units developed in the LdM. Those are represented by Estero Bobadilla mafic andesite (MEB; 86 ka), El Candado basalt (BEC; 62 ka) and Vega Piedras Negras andesite (MPN; 54 ka) (Hildreth et al., 2010). Additionally, the undated units of Manantial Pelado cluster (MPC; Fig.2.1c), at the DGVF, and Loma Blanca vent (LBL), at the southern extreme of the segment, are suggested to have erupted during this period.

*Group 4:* Finally, the distribution of post glaciation vents (< 25 ka) occurs along the whole segment. From north to south, these well-preserved cones include: LRC and LHC at DGVF; the Arroyo Cabeceras de Troncoso (MCT), Crater 2657 (MCP) mafic andesites and the scoria cone of Hoyo Colorado basalt (BHC), all present at the LdM. Lastly, the isolated Rezago volcano (RZG) belongs to this group and is located at the southern limit of this segment.

### 2.5.3.- Petrography

*La Resolana craters (LRC)*

Eruptive products from these vents, including slabby blocks, bombs and lava samples are characterized by a low proportion of phenocrysts (~15-20 vol.%), which consist of olivine (5-8 vol.%) and minor amounts of plagioclase (~4-5 vol.%) and clinopyroxene (3-7 vol.%). The groundmass (~80-85 vol.%) is dominated by plagioclase microlites (~55 vol.%) with minor proportions of clinopyroxene (~7 vol.%), olivine (~6 vol.%), magnetite (~7 vol.%) and glass (~10-30 vol.%) (Table 2.2). The lavas from LRC-North contain orthopyroxene as a fine rim surrounding olivine phenocrysts and also as independent micro-phenocrysts in the groundmass. Those rims may result from the reaction between olivine and melt during a normal basalt-to-andesite crystallization sequence (e.g., Sisson and Grove 1993; Grove et al., 1997).

Table 2.2.- Summary of mineral phases occurring in the sampled volcanic units. Mineral nomenclature as follows: Ol: olivine, Plg: plagioclase, Cpx: clinopyroxene, Opx: orthopyroxene, OxiHbl: oxi-hornblende. All values as volume percent.

| | LHC | | | LRC | | | TQZV |
|---|---|---|---|---|---|---|---|
| | Lava W cone | Lava E cone | Tephra E cone | Bomb N cone | Lava N cone | Bomb S cone | Tephra 1932 |
| *Phenocrysts (%)* | 16 | 15 | 30 | 15 | 20 | 15 | 22 |
| Ol | 10 | 12 | 30 | 8 | 8 | 5 | 7 |
| Plg | 5 | 3 | | 4 | 5 | 3 | 10 |
| Cpx | 3 | 5 | | 3 | 3 | 7 | |
| Opx | | | | | 4 | | 2 |
| OxiHbl | | | | | | | 3 |
| *Groundmass (%)* | 84 | 85 | 70 | 85 | 80 | 85 | 78 |
| Glass | 7 | 5 | 7 | 10 | 10 | 30 | 48 |
| Microlites | 77 | 80 | 63 | 75 | 75 | 55 | 30 |

*Los Hornitos cones (LHC)*

The analyzed lapilli-poor tephra bed (sample CLHE-TF2; Fig.2.5b) is olivine-rich and represents the only phenocryst phase observed in the separates. Olivine phenocrysts are medium to coarse grained (250 to 700 µm), euhedral to subhedral in shape and frequently contain Cr-spinel inclusions. Hand-magnet separation revealed a great proportion of fine-grained (<200 µm) magnetite, however the loose grains are also a mix with other phases. A glassy groundmass with plagioclase microlites and minor olivine crystals usually surround these olivines. In addition, a minor population of small (<150 µm) crystals of clinopyroxene is often observed as loose grains in the separates.

The mineralogical analysis of the sample CLHE-TF4 indicates the presence of forsterite-rich olivine and Cr-spinel inclusions as the dominant phases. Detailed mineral chemistry of olivine is presented below.

The late effusive stage of this vent emitted a voluminous lava flow with variable phenocryst proportions (15 and 20 vol.%) including olivine (~12 vol.%) and a lesser amount of clinopyroxene (~5 vol.%) often clustered in crystal agglomerates. A minor proportion of plagioclase is observed as elongated micro phenocrysts (~3 vol.%). The groundmass is almost holocrystalline (80 to 85 vol.%) with plagioclase (~48 vol.%), clinopyroxene (~28 vol.%), magnetite (~5 vol.%) and a minor amount of glass (~4 vol.%).

*Terminal mafic scoria from Quizapu volcano (TQZV)*

The mafic fallout deposit of Quizapu volcano is mostly composed by ash (75 vol.%) and lapilli fragments (25 vol.%), with a scarce occurrence of bombs (Fig.2.5d). The phase assemblage in the analyzed tephra sample is mainly composed of magnetite (30 vol.%, represent a mix with other phases) and glass (48 vol.%), with minor amounts of plagioclase (10 vol.%), olivine (7 vol.%), orthopyroxene (2 vol.%), oxyhornblende (3 vol.%), and apatite (<1 vol.%) (Table 2.2). Crystals often exhibit a fragmental texture with crystal fragment sizes less than 220 μm.

### 2.5.4.- Whole rock chemistry

Based on geochemical results presented by Ruprecht et al., 2012 (performed on the same samples studied here) and Hildreth and Drake (1992) (Table A.2.1 in

Appendix), the analyzed samples (*n*=16) are mostly basaltic andesite in composition with $SiO_2$ contents ranging between 53.5 and 55.0 wt.%. The only exceptions are the CLHE-TF4 sample, which is of basaltic composition (*n*=1, see below for details), and sample Q-9, corresponding to an andesite composition. Erupted magmas have a sub-alkaline character based on the canonical TAS diagram (Fig.2.6). Besides, the geochemical data yield a modified alkali-lime index (MALI) ranging between -5.32 to -2.64, a mean FeO*/MgO ratio of 1.36 (*n*=15; Fig.2.7) and a $K_2O$ content lower than ~2.07 wt.%, typical of medium-K, calc-alkaline suites.

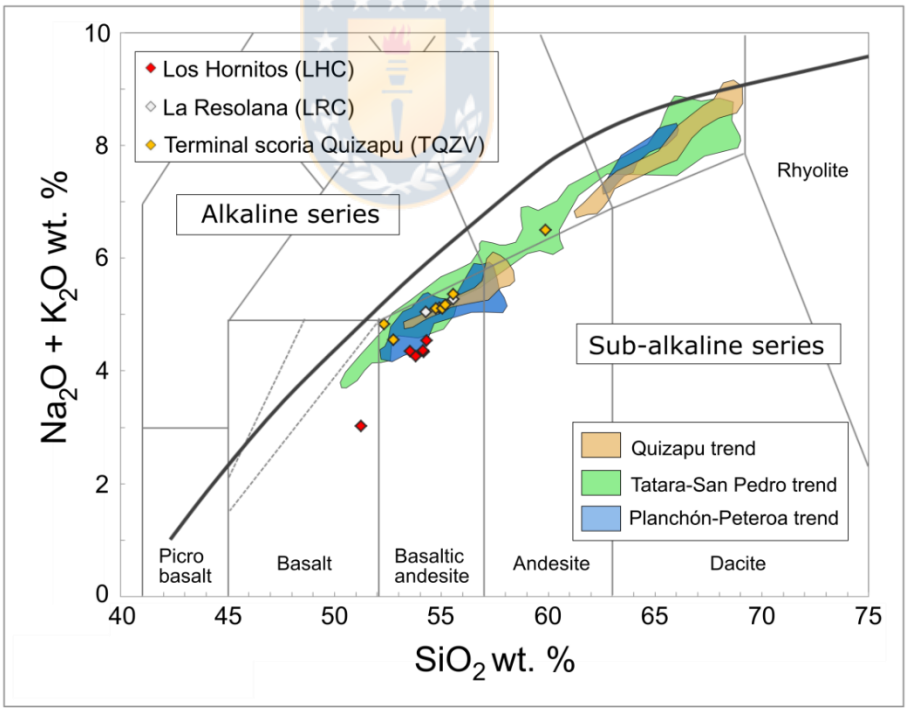


Fig.2.6. TAS diagram showing the whole-rock contents of studied samples compared to chemical trends of neighbor volcanic centers. LHC samples display systematic depletion in alkalis compared to LRC and TQZV samples. Data for neighbor volcanic centers were obtained from EarthChem (October 2015) and complemented with data provided by Ruprecht et al., 2012 and Tormey et al., 1995. Fields were plot using the 95% of samples for Planchón-Peteroa and Tatara-San Pedro volcanic complexes.

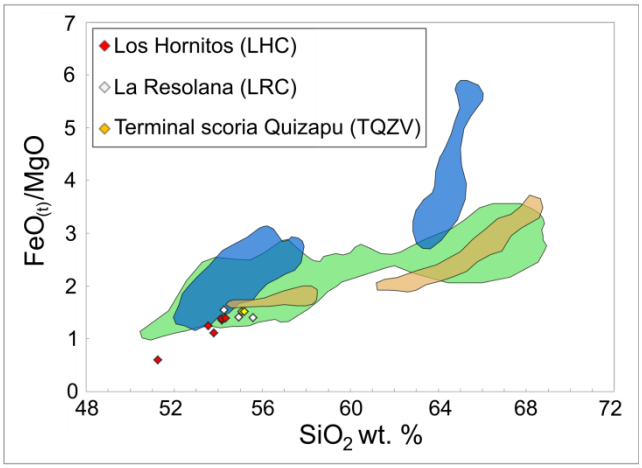


Fig.2.7. FeO(total)/MgO ratio in whole-rock elemental contents in analyzed samples. LHC display a slightly lower ratio compared to TQZV and LRC. Color fields represent the same as in Fig.2.6.

The coarse lapilli-rich tephra (sample CLHE-TF4, Fig.2.5b) from the initial explosive stage at LHC yield highly anomalous values of MgO (13.7 wt.%), Cr (1209 ppm) and Ni (347 ppm), but a relatively evolved character when considering the $SiO_2$ (51.5 wt%) content (Fig.2.7).

Despite the common basaltic andesite composition among the eruptive products, rocks from LHC and LRC are less evolved compared to the terminal scoria at Quizapu volcano (TQZV), where MgO contents are lower for a similar $SiO_2$ content.

### 2.5.5.- Olivine composition

Considering crystal-chemical and textural criteria, magmatic phenocrysts (*sensu stricto*) correspond to large crystals that grew from the melt in which they were

erupted. Nevertheless, in a textural-alone terminology, phenocrysts (*sensu lato*) and microlites refer to crystal sizes, regardless of the origin of crystals. Here, we use the latter meaning, since determine a genetic relation between crystals and co-erupted melts (*sensu stricto*) is often difficult to confirm.

At LHC the olivine populations from the initial (explosive) and late (effusive) stage are compositionally different although both are normally zoned. Olivine phenocrysts from the initial explosive stage are more forsteritic (> ~$Fo_{85}$) than those from the effusive stage (< ~$Fo_{85}$) (Fig.2.8a and b; Table A.2.2 in Appendix). The olivine cores of these two olivine groups exhibit an increasing forsterite range from 2.2 Fo units in the initial tephra ($Fo_{90}$ to $Fo_{92.2}$) to 8 Fo units in the lava flows ($Fo_{77}$ to $Fo_{85}$). The Fo and Ni contents decrease from the initial tephra ($Fo_{90\text{-}92.2}$ and ~1800 - 3642 ppm Ni, respectively) to the late lava flows ($Fo_{77\text{-}85}$ and ~380 - 1095 ppm Ni).

A large fraction of olivine measurements comprise a narrow range from $Fo_{87}$ to $Fo_{92}$ (*n*=50) in the initial stage (tephra) with only a few measurements with lower Fo content ($Fo_{79}$ to $Fo_{87}$; *n*=6). Those lower values correspond to a thin overgrowth present in some olivine phenocrysts. The Ni and Fo contents correlate positively and display a steep variation pattern, with Ni varying from 3642 to 651 ppm for a narrow range of forsterite from ~$Fo_{92}$ to $Fo_{88}$ consistent with olivine-dominated fractional crystallization (Fig.2.8a). Olivine from the initial stage at LHC often contains Cr-spinel inclusions, with Cr# (defined as the atomic ratio of Cr/(Cr+Al)) ranging from 76 to 60 (See Chapter 3, Fig. S.3.6, Table A.3.3).

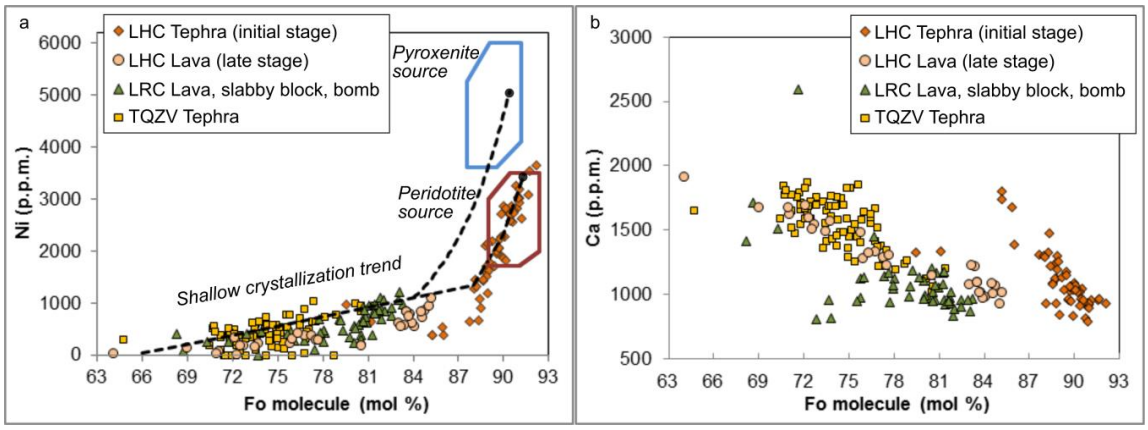


Fig.2.8. a. Forsterite molecule (Fo) versus Ni (ppm) in olivine from the studied eruptive centers. Olivine from the initial tephra at LHC display a narrow range in Fo for a wide variation in Ni contents (from 3642 to ~ 600 ppm) constituting the olivine dominated crystallization trend. A great proportion of these data plots in the calculated olivine composition to be in equilibrium with a peridotite source. Pyroxenite source is also plotted for comparison (Straub et al., 2011). Fractionation curves for two different primary melt compositions are provided (Ruprecht and Plank, 2013). Olivine composition from LHC lavas, LRC and TQZV constitutes the shallow crystallization trend given by a wide range in Fo (Fo < 87) and Ni contents lower than ~1200 ppm. b. Forsterite molecule (Fo) versus Ca (ppm) in olivine showing separated evolution trends for high Fo olivine (Fo > 85) from the initial stage at LHC and the shallow trend crystallization depicted by LHC lavas, LRC and TQZV.

On the other hand, the full compositional range of olivine phenocrysts from the late stage (lava flow) vary from $Fo_{64}$ to $Fo_{85}$ with Ni contents lower than 1095 ppm (*n*=32) (Fig.2.8a).

Fo contents of olivine from LRC are intermediate when compared to those from the effusive stage at LHC and Quizapu volcano (mafic scoria), and range from $Fo_{68}$ to $Fo_{83}$, with Ni contents lower than 1212 ppm (*n*=51) (Fig.2.8 a). Conversely to the case of monogenetic vents, olivine phenocrysts from the terminal mafic scoria of Quizapu volcano (TQZV) exhibit a reversely-zoned core-to-rim pattern, with forsterite values in the range of $Fo_{81}$ to $Fo_{65}$, with Ni contents lower than 1071 ppm (*n*=131) (Fig.2.8a).

The content of Ca in all analyzed olivine crystals varies from about 700 to 1900 ppm and it shows a systematic increase with decreasing forsterite content (Fig.2.8b). The Ca-Fo diagram shows at least two different variation trends, where the high-Fo olivine population displays a steeper Ca enrichment (Fig.2.8b).

## 2.6.- Discussion

*Olivine composition as indicator of parental melt*

Olivine composition can be used as probe of parental melt composition because at most crustal pressures olivine is the first phase to crystallize in almost all mantle-derived magmas (e.g. Weaver et al., 2011). This mineral is also useful because its compositional variation (e.g. Mg/Fe, Ni, Cr, Ca) is suitable for monitoring the degree of fractional crystallization (or differentiation) of the parental magma.

Olivine from the initial explosive stage at LHC displays the highest Fo and Ni contents of all analyzed samples. A few (~6 vol.%) of these olivines can be classified as ultra-magnesian (Fo > 91.5; e.g. Keiding et al., 2011). Primitive magnesian olivine (Fo > 88) are considered to be in equilibrium with the mantle and thus, expected to be associated with primitive mantle-derived melts. As shown in Fig.2.8 a, the bulk composition of most olivine phenocrysts from the initial stage of LHC is in the range of olivines from a peridotitic mantle source (e.g. Straub et al., 2011). The fact that most of the LHC olivines are > $Fo_{88}$ with Ni

contents up to more than 3600 ppm suggests that they are the Mg-rich liquidus phase. Compositional variations in Ca and Ni in such magnesian olivine (Fo > 88; Fig.2.8a and b) are also consistent with olivine-dominated fractional crystallization. The evolution trend defined by lower values (Fo < 88, Ni < 1212 ppm) is consistent with a lower pressure and temperature crystallization where plagioclase and clinopyroxene, seen as microlites in the groundmass, co-crystallize with olivine. Crystallization of plagioclase at high crustal levels increases the $CaO/Al_2O_3$ ratio and alkalis ($Na_2O + K_2O$) content in the melt favoring the Ca incorporation in olivine, as suggested by Libourel (1999).

Following this reasoning, composition of olivine crystals from LRC and Quizapu volcano would indicate a low pressure shallow crustal evolution from a more differentiated melt compared to that associated with LHC. Olivine phenocrysts from the lava flow at LHC, however, share a similar evolution trend with the LRC and Quizapu volcano olivines (Fig.2.8a and b). In this context, three major possibilities arise for LRC and Quizapu volcano melt history: a.- Both volcanic vents could have erupted more forsteritic and Ni-rich olivine during the initial explosive stage, but these were buried by later volcanic products, as the case of LHC. This alternative is particularly relevant for LRC due to a more similar setting to LHC. b.- The magmatic plumbing system of LRC and Quizapu volcano is more complex than LHC and forsteritic olivine did not reach the surface. c.- The magmatic systems of LRC and Quizapu volcano were fed by more evolved melts.

The highly anomalous contents of MgO, Ni and Cr in the coarse lapilli-rich sample (CLHE-TF4) from the initial stage at LHC are interpreted as result of a high proportion of forsterite-rich olivine in the sample. Similar chemical anomalies have been found in lava and dike samples (unaffected by eolian fractionation), but containing high proportions of antecrysts, which are large crystals that according to their chemical composition may not have shared common histories or crystallized from the magma in which they are now hosted, but rather may have grown within the same magmatic system but in a more primitive magma than that from which they are found (Larrea et al., 2012). Thus, although the whole rock composition of the ash-rich level (sample CLHE-TF2; Fig.2.5b) hosting the Mg-rich olivines is not known, the closely related coarse-lapilli deposit has a basaltic composition (~13.7 wt.% MgO and 51 wt.% $SiO_2$; Table A.2.1 in Appendix). Therefore, the primitive character of this tephra deposit from LHC may be a primary feature of a poorly-evolved phyric melt containing about 20 vol.% of high-forsterite olivine, which has experienced limited crystallization at shallow crustal depths involving plagioclase and clinopyroxene. Similar primitive whole rock compositions have been reported for other monogenetic volcanoes such as Jorullo in Mexico (Johnson et al., 2008). Although other volcanic rocks at LHC, mostly lava flows, are basaltic andesites, at the nearby LdM Mg-rich basaltic rocks have also been reported for a couple units (Hildreth et al., 2010).

Furthermore, for primitive olivine like those from LHC, thermal considerations regarding the high-Mg (Fo > 88) compositions and Ni diffusion in olivine would

require a very short crustal residence time -months to few years at most- in order to prevent a re-equilibration toward more evolved compositions (Ruprecht and Plank, 2013). This contrasts with those olivines from the other mafic rocks of the DGVF, where Ni and Fo content are lower than ~1200 ppm and ~85 in olivine crystals, respectively.

*Structural control of mafic volcanism between 35.5° and 36.5°S*

The NNW-SSE set of lineaments is a regional feature observed between ~35° to ~37°S that have also been noted by other authors to dominate over the NS and NE alignments of volcanic centers in the transitional SVZ (e.g. López-Escobar et al., 1995). The pattern defined by NNW-SSE lineaments is broadly in agreement with pre-Andean oblique-slip structures (e.g. high angle faults in the basement) proposed by Cembrano and Lara (2009) to control the position of some volcanic edifices and associated flank vents, as the case of Chillan volcanic chain (~36.8°S).

On the other hand, north of 37° S, the active volcanic front is emplaced above margin parallel, reverse faults developed either within Mesozoic units or at the boundary between Cenozoic and Mesozoic volcano-sedimentary sequences in the westernmost portion of the fold and thrust belt of the back-arc. This is the case of Maipo and Planchón-Peteroa volcanic complexes respectively. Southward, Descabezado Grande-Azul-Quizapu volcanic complex is located at the Meso-

Cenozoic boundary above Cenozoic intrusive basement (e.g. Astaburuaga, 2014).

The segment between 35.5° to 36.5°S is located in a transitional zone where the Meso-Cenozoic cover diminishes toward the south. This cover attenuation may reduce, or even prevent in some cases, the possibility that magmas on route to the surface became trapped at the basement-cover discontinuity, where protracted differentiation processes can take place.

According to Cembrano and Lara (2009), both structural controls (margin parallel and NW-SE structures) are kinematically-uncoupled to the present day tectonic environment and rather the spatial distribution and overall morphology of individual volcanoes and groups of volcanoes are primarily controlled by the inherited basement structures that underlie this arc segment. Therefore, the combination of a reduced Meso-Cenozoic volcano-sedimentary cover and deep inherited structures reaching high-crustal levels, may have contributed for the widespread mafic effusive centers emplacement in the SVZ between 35.5° and 36.5° S.

Further, monogenetic volcanism is favored in extensional settings. In convergent margins, the structural control may vary significantly, involving compressive, strike-slip, extensional and oblique systems (Nakamura, 1977; Acocella, 2014). In the SVZ, the significant degree of strike-slip deformation along the arc, even in the northern (NSVZ) and transitional (TSVZ) segments, allow that compression and extension can occur at same time but in different orientations, both oblique to

the magmatic arc trend (Cembrano and Lara, 2009). In this setting, an additional factor enhancing the dike propagation and eruption is the occurrence of extensional co-seismic and post-seismic deformation triggered by a megathrust earthquake in the forearc (Lupi and Miller, 2014, Bonali et al., 2015). This transient variation of the stress field in the overriding plate may shift from compressive to extensional, as evidenced by the occurrence of normal faulting along a NNW-SSE trend, triggered by the Mw = 8.8 Maule earthquake in 2010 in South-Central Chile (Farías et al., 2011) and the geodetically detected during and immediately after the 2011 Tohoku earthquake, Japan (Ozawa et al., 2011; Takada and Fukushima, 2013). In particular, dike intrusion during these transient conditions may occur along otherwise non-favourable orientations, as arc oblique-NNW-SSE, perpendicular to the oblique convergence vector at the SVZ (Acocella, 2014).

On the other hand, Piquer et al., 2015, propose that the intersection of two conjugates set of regional faults, the NE-striking dextral and the NW-sinistral striking faults can generate a dilatational environment along NW trending structures during the incremental motion of the NE-striking faults under east-west compression; thus explaining the NNW-SSE trend of breccias and ore bodies at Rio Blanco – Los Bronces and El Teniente porphyry deposits (see Piquer et al., 2015 for details).

Finally, as a remarkable fact, the NNW-SSE and ENE-WSW trends are broadly concordant with the ancient structures that controlled the Late Triassic-Early Jurassic rift systems (Ramos, 2009) that were reactivated during the rifting event

associated with the opening of the South Atlantic Ocean in the early Cretaceous (Jacques, 2003; Ramos, 2009). Furthermore, those structural trends have been observed as major features in the entire South American continent, acting as weakness zones which can be repeatedly reactivated, playing a major role in the tectonostratigraphic evolution of the continent (Jacques, 2003). The deep and penetrative character of such structures would explain their effectiveness in channeling and transporting deep seated mafic magmas through the crust.

We speculate that a decrease in the compressional stress regime in the arc region, related to a transient post-seismic relaxation after large subduction earthquakes (e.g. Lupi and Miller, 2014; Bonali et al., 2015), is a possible explanation to link the structural pattern observed in the distribution of mafic volcanoes between 35.5° to 36.5° S.

## 2.7.- Conclusions

The primitive character of olivine phenocrysts from the initial stage at LHC is interpreted to result from the crystallization of a primitive melt in deep crustal or mantle environments, where olivine (± spinel) constitutes the only crystallizing phases. Compositional variations in the more forsteritic (Fo > 88) and Ni-rich olivine phenocrysts (Ni > 650 ppm) suggest equilibrium with a peridotite source. The later joining of shallow crystallization phases, as plagioclase and clinopyroxene, co-crystallizing together with olivine in the groundmass, modify the

olivine-dominated compositional trend (Fig.2.8 a and b). Composition of olivine crystals from LRC and Quizapu volcano would indicate a low pressure shallow crustal evolution from a more differentiated melt compared to that associated with LHC.

Limited residence times in crustal levels are needed in order to preserve the compositional zonation of such forsterite-rich olivine to prevent elemental diffusion at magmatic temperatures. The structural setting where Los Hornitos mafic cones are located suggests that the NNW-striking structures may represent the deep crustal structures that facilitated the rapid ascent of these mafic magmas through crust. These structures, inherited from ancient tectonic regimes, may have also played an important role in the transport of mafic magmas through the Andean crust in the revised segment (35.5° to 36.5°S) during post-Pliocene times, allowing the northernmost presence in the SVZ of near primitive magmas at the surface.

Thus, the widespread emplacement of Pleistocene to Holocene monogenetic mafic vents in the TSVZ, between 35.5° and 36.5°S, is controlled by the occurrence of NNW-SSE and NE-SW deep pre-Andean structures. The combination of a reduced Meso-Cenozoic volcano-sedimentary cover and such structures may have provided a more direct pathway for primitive magma ascent.

# Chapter 3: Textural analysis of olivine hosts: avoiding/noticing growth textures out of equilibrium.

Manuscript title: The early structure of olivine from subduction zones and its missing zoning

**Abstract**

Primitive olivines from Los Hornitos, a pair of monogenetic cones in the Central-South Andes, preserve dendritic, skeletal and polyhedral textures. Those consecutive stages of textural maturation occur along compositional gradients where high Fo-Ni cores of polyhedral olivines ($Fo_{92.5}$, Ni~3,500 ppm) contrast with less mature and compositionally more evolved olivines (dendritic; Fo<91.5, Ni<3,000 ppm), indicating early and late nucleation, respectively. By combining textural and compositional data we develop a growth model that explains complex zoning of Fo-Ni reversals in mature crystals. Here olivine progressively grows via concentric addition of open-structured “crystal frames” during rapid growth episodes, leaving behind compositional boundary layers that subsequently fill in with a Fo-Ni depleted olivine, causing reversals. Elemental diffusion modeling on these reversals reveals timescales of 3.5-40 days between the growth of

individual crystal frames and eruption at the surface, which combined with barometry constraints provide magma ascent rates of 40-500 m/h from the deep crust.



Submitted *to Nature Communications* as: The early structure of olivine from subduction zones and its missing zoning. Salas, P.A.; Ruprecht, P.; Hernández, L.B.; Rabbia, O.M.
The conclusions of this manuscript are beyond its direct application to the proposed melt inclusion study. However, a brief discussion is intended to the direct implications for the further melt inclusion study. See section 3.4.

## 3.1.- Introduction

Crystal forensics (Davidson et al., 2007) or the interpretation of crystal populations and chemical fingerprints in zoned crystals is frequently applied to magmatic systems to infer processes at depth (Hartley et al., 2016; Kahl et al., 2011; Rae et al., 2016; Ruprecht & Plank, 2013; Ruth et al., 2018; Viccaro et al., 2016). For mafic compositions, olivine crystals provide access to events that occur near the liquidus of mantle-derived melts (Mutch et al., 2019; Sobolev et al., 2007). Therefore, olivine can track magmatic processes that may occur near the source regions in the mantle and during transit to the surface. Underlying the use of crystal zoning is the assumption that the events are recorded in a sequential pattern from the oldest in the core to the youngest at the rims. This notion of concentrically growing olivine has been recently challenged in a series of papers that propose a more complex growth history for olivine (Shea et al., 2015; Welsch et al., 2014; Welsch et al., 2013). The presence of distinct dendritic zoning patterns in slow diffusing elements (e.g., P, Al) as well as the rare preservation of their morphologies in some olivine crystals from ocean island basalts argue that an early dendritic olivine growth is followed by an episode of maturation that fills the dendritic network and potentially explains the common occurrence of olivine-hosted melt inclusions. These findings have been tested experimentally on a Hawaiian basalt composition that shows that phenocryst-size (> 100 µm) olivines may form within such two-stage growth for undercooling of 25-40°C, with the

crystal experiencing textural maturation as undercooling diminishes (Mourey & Shea, 2019).

The widespread occurrence in different tectonic settings of olivine with internal dendritic arrangements of slow diffusing elements indicates that the required degrees of undercooling for the development of rapid growth textures may be a common condition among mafic compositions, which can be reached during magma mixing events (Shea et al., 2019) or when magmas experience a high thermal contrast during rapid dike emplacement in cooler crustal rocks or near reservoir edges (Welsch et al., 2013). While the evidence for complex olivine growth in hotspot settings has increasingly mounted, similar observations for arc settings are lacking and arc olivines continue to be interpreted through a paradigm of concentrically grown crystals. This view is driven by the polyhedral habit that dominate arc olivines where evidence for dendritic growth representing remnants of an earlier growth stage is limited to the occasional presence of elevated P and Al zoning (e.g., de Maisonneuve et al., 2016). Such Al and P zoning alone may not be sufficient evidence to support a model of initial dendritic growth followed by crystal maturation as olivines from Shiveluch in the Central Kamchatka Depression were recently interpreted to represent concentric growth (Gordeychik et al., 2018).

Here we present results combining textural analysis with fine-scale olivine chemistry and diffusion modeling to demonstrate the presence of complex growth patterns preserved in samples from Los Hornitos, a pair of Holocene mafic

monogenetic cones in the magmatic arc of the Central-South Andes of Chile. To our knowledge such patterns have not been described in detail for other arc volcanoes. Olivine textures can be classified into different growth stages along maturation. Those stages are partially consistent with the model of Welsch et al. 2013 (Fig.3.1) and correlate with compositional zoning preserved in some of those phenocrysts, allowing to reconstruct the olivine growth history. Moreover, the preservation of internal zoning constraints the time of crystal assembly and magma passage through the crust.

Unlike other volcanoes in the Andean Southern Volcanic Zone that sit on thickened crust (>45 km; Tassara & Echaurren, 2012) and are dominated by magma storage and differentiation in the crust, Los Hornitos erupted primitive magma with olivine phenocrysts in equilibrium with mantle peridotite (up to $Fo_{92.5}$; Salas et al., 2017). Magnesian olivines in arc settings have been interpreted to represent deep crystallization near or below the Moho (Gordeychik et al., 2018; Ruprecht & Plank, 2013) on the grounds of thermal considerations as well as pyroxene-barometry. In the case of Los Hornitos, structural controls may facilitate their uninterrupted ascent to the surface with limited crustal residence despite the thick Andean crust (Salas et al., 2017; Tassara & Echaurren, 2012).

Previous work (Salas et al., 2017) showed that the eruptive events at Los Hornitos occurred along two separated stages for the two cones. Each cone started with an initial explosive stage generating a widely distributed tephra fall deposit (~1.5 km around the vent) that is composed of beds of variable amounts of lapilli and

ash fragments. The eruption transitioned into several lava flows that breached the earlier formed cones at their base. While the tephra of the initial stage erupted primitive compositions (~14 wt% of MgO; >400 ppm of NiO; ~51 wt% of $SiO_2$), the subsequent lava flows comprised more evolved compositions (<7 wt% of MgO; <80 ppm of NiO; ~53 wt% of $SiO_2$). This study focuses on the primitive tephra deposit of the younger eastern cone where magnesian olivine ($Fo_{88-92.5}$ with Ni ~1000 to <4000 ppm) is the dominant phenocryst phase (± Cr-spinel with Cr# up 78) with subordinate clinopyroxene (cpx <5 vol%).

### 3.2.- Results

#### 3.2.1.- Olivine morphologies and growth sequence

Olivines from Los Hornitos tephra are comprised of three groups that are distinguished morphologically, by size, and by their chemical signatures, most notably their Fo-Ni variations. We identified texturally that the majority of the studied olivines (total *n*=455) are characterized by a common polyhedral habit (Group 1 and 2). Group 1 (~27 vol %) and 2 (~54 vol %) are between ~400 to 800 µm in size and we refer to them as mature olivines throughout the text (See histogram and exemplary crystals in Supplementary Fig.S.3.1a, b). They differ in their degree of polyhedral habit, where group 1 olivines are fully polyhedral and group 2 olivines are transitional between polyhedral to skeletal. Furthermore, the euhedral to subhedral group 1 olivines lack open cavities. They are often imperfectly broken along one or two combined poorly-developed cleavages

planes, most commonly parallel to (010) and (001). Group 2 olivines maintain open cavities in the (021) plane and less frequently also in the (010) plane.

Group 3 olivines (~19 vol %) are smaller (~100 to 500 µm) with externally skeletal textures. We refer to these olivines as immature as they also retain visible dendritic features in the innermost part of the crystal. The dendritic pattern of immature olivines occurs as a planar feature in the center of the crystals, along the crystallographic plane *ac* and is given by the occurrence of four interconnected dendrites radiating from the crystal center (Fig.3.1a). Those dendrites are symmetrical and display four apexes shaped as arrow-like tips towards the external part of the emerging crystal. Growth progression in the more advanced olivines leads to full enclosure of the entire external frame along this section (Fig.3.1b). This dendritic arrangement is sharply bounded by four melt pockets systematically distributed along this crystallographic plane. Normal to the *c* axis, the initially *ac* elongated dendritic arms open towards the *b* axis, conforming the typical section of olivine, while leaving two symmetrical cavities that envelope the central crossbar along the *a* axis (Fig.3.1c). As maturation proceeds these cavities eventually form the (021) face, which is well known to remain open even in advanced grown crystals (e.g., Welsch et al., 2013).

According to our observations, the (110) face is always present in the immature crystals and therefore develops early during initial olivine growth. In contrast the (021) face and, less frequently observed the (010) face, remain as skeletal cavities in the most immature olivines. These observations indicate that the

earliest proto crystal is developed as a structure where the faces are limited only to its edges conforming a *"crystal frame"*, a term we will use throughout the text for this ephemeral crystal morphology (Supplementary Fig.S.3.2).

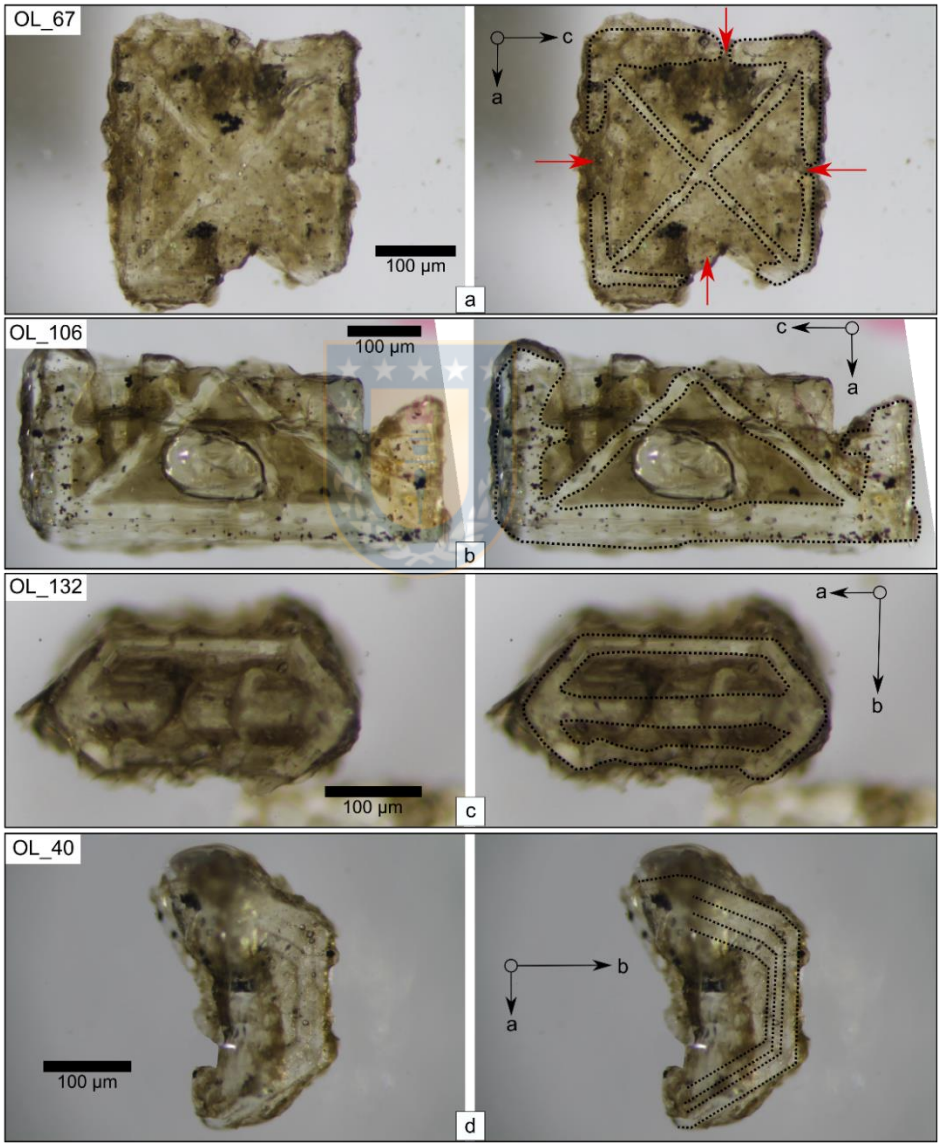


Fig.3.1.- Dendritic and skeletal textures preserved in olivine phenocrysts of Los Hornitos, raw images and their interpretation at left and right, respectively. a) Olivine 67 oriented normal to *b*-axis showing the four dendrites radiating from the central core, partially enclosing the external section, leaving cavities filled with melt (red arrows) connected to the exterior of the crystal. b) Olivine 106 broken along the (100) plane, oriented normal to *b*-axis. This crystal is fully enclosed

along the *c*-direction and shows in detail the morphology of the dendrites and the fully entrapped melt. c) Olivine 132 oriented normal to *c*-axis showing the two cavities enveloping the central crossbar along the *a*-axis. d) Olivine 40 irregularly broken along plane (010) oriented normal to *c*-axis. This crystal denotes the layered texture resultant of the progressive external growth of crystal frames, promoting the occurrence of a thin melt film between two adjacent growth layers.

Larger skeletal olivines emerge through the progressive growth of new crystal frames to the exterior. The repetitive pattern is best observed normal to the *c*-axis, adding a concentric and layered texture to the initial olivine arrangement, preserving the basic structure as crystal growth proceeds. Moreover, the layered framework promotes the presence of a thin melt film between two skeletal growth layers (Fig.3.1d). The small inner frames grow first and can advance towards a more mature texture, while the outer frames lack behind in a purely skeletal stage. Compositionally, the polyhedral crystals of group 1 have the most primitive cores, reaching up to $Fo_{92.5}$ and ~3800 ppm of Ni. Group 2 olivine cores are slightly more evolved at $Fo_{91.5}$ and <~3500 ppm of Ni. The immature olivines of group 3 share a broad similar composition as group 2 ($Fo_{91.3}$ and <~3000 ppm of Ni) with some of the crystals nucleated at ~$Fo_{89}$ (Fig.3.3a). Chemical contrasts among the texturally defined groups hint that the morphology of the three groups represents a sequential record of growth, where the early more primitive olivines advance to greater textural maturation.

### 3.2.2.- Chemical evidence of growth by addition of crystal frames

Selected olivine grains were sectioned to image elemental zoning and its potential relation to olivine growth via crystal frame addition. Detailed EPMA profiles on mature crystals of groups 1 and 2 show a broad normally zoned pattern interrupted by narrow reversals (Fig.3.2). Those olivines express their compositional range as a concentric oscillatory pattern comprised of up to two frames exhibiting elevated Fo and Ni contents separated by zones of lower Fo and Ni contents. These oscillations occur on lengthscales of 10-50 μm and are more pronounced for Ni than for Fo. An analysis of the angles measured in back-scattered electron images reveals that growth of those chemical oscillations reproduce theoretical angles of euhedral olivines (Fig.3.2b-d). Elemental zoning obtained from rim-to-rim profiles along five different olivines (Fig.3.2 and Supplementary Fig.S.3.3) shows qualitative agreement and also similar compositional jumps among the crystals.

The conceptual model consists of four zoning structures (Fig.3.2a): an ***inner core*** of constant composition that is surrounded by an ***outer core*** that is normally zoned (I and II). Rimward, the next zone separated from the core-to-rim sequence consist of a Ni reversal (III) that merges to the central structure by a significant ***Ni depletion*** (IV) ($\Delta$Ni >300 ppm). Major element zoning continues to be normal in this zone. Subsequent zoning continues with ***Ni depletions*** (up to ~900 ppm of $\Delta$Ni; $\Delta$Fo <1) along the profile, usually two, that reverse towards but do not reach contents prior to the depletion (V and VI). Lastly, the ***rims*** consist of significant normal zoning in both Ni and Fo (VII).

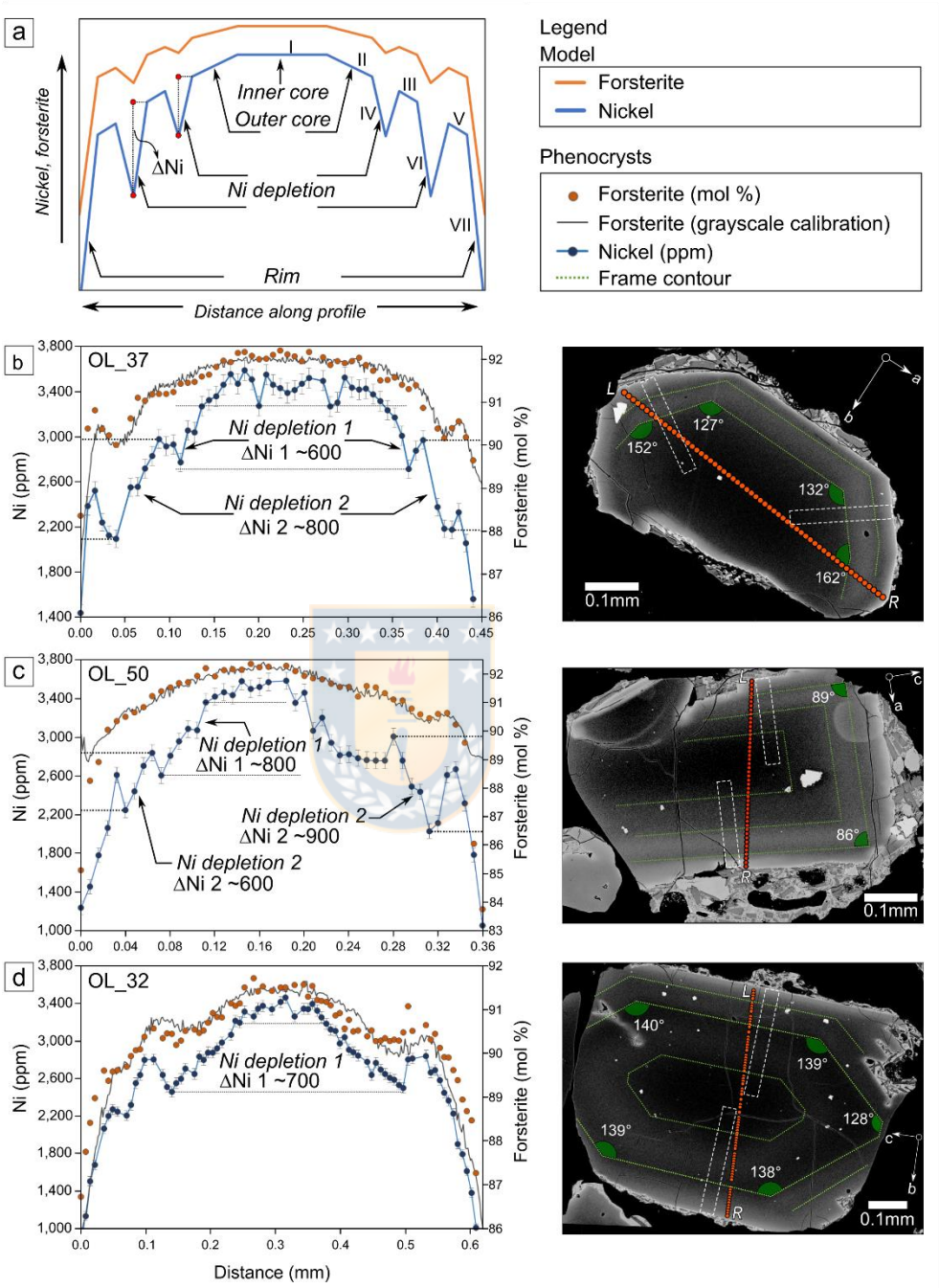


Fig.3.2.- Conceptual illustration of complex zoning preserved in olivine phenocrysts (group 1 and 2) from Los Hornitos. a) schematic model of the Fo and Ni variations explained by four main zoning structures consisting of an inner and outer core, Ni depletions and rim. Roman numerals refer to the growth sequence of the crystal. b-d) Fo (orange; right axis) and Ni (blue; left axis) contents along rim-to-rim traverses along three mature olivines sectioned normal to *c*, *b* and *a*-axis, respectively, with their BSE images and the analyzed traverses. Error bars on Ni data represent 1 sigma. Similar magnitudes of Ni depletions (ΔNi) are observed among the crystals. Segmented

green lines above the images enhance the position of chemical reversals, which reproduce the euhedral olivine morphology, allowing the crystal to be oriented (see raw images and orientation parameters in Supplementary Fig.S.3.4). White segmented blocks show the location of diffusion profiles for timescale calculations. Olivine composition data can be found in Appendix Table A.3.1.

These patterns are symmetrical in these olivines with only minor deviations in compositions (Fig.3.2). Two exemplary mature olivines of group 1 (B: OL_37; C: OL_50) and one of group 2 (D: OL_32) have relatively flat inner cores that range between 3350 ppm of Ni (OL_32) and 3550 ppm of Ni (OL_50) with Fo contents between 91.5 and 92.3, respectively. The normal zoning of the outer cores of OL_37 and OL_50 is of similar magnitude ($\Delta$Fo ~ 0.3 and $\Delta$Ni ~140 ppm). For these crystals, the variations of Ni associated to the inner depletion ($\Delta$Ni-1 ~700 ppm) is smaller than those of the outer depletion ($\Delta$Ni-2 ~ up to 900 ppm). OL_32 shows a more pronounced outer core ($\Delta$Fo ~1 and $\Delta$Ni ~500 ppm) and a change in Ni associated with the depletion of $\Delta$Ni-1 ~700 ppm.

Compositional variations of Fo and Ni for these olivines show a broadly common evolution pattern that outline the described zoning structures (Fig.3.3b). The ***inner core*** Fo-Ni compositions cluster at high contents and grade into a trend with the ***outer core*** characterized by discrete variations of Ni compared to a larger variation in Fo. This trend intersects the generalized olivine crystallization path (Fig.3.3c, segment a) and the shift to lower Fo contents is due to the more advanced diffusion of Fe-Mg-Ni in the cores, compared to the outer zones of the crystals (e.g., ref. (Gordeychik et al., 2018)). In addition, the ***Ni depletions*** represent a drastic decrease of Ni that is inconsistent with olivine crystallization

under equilibrium conditions (Fig.3.3c segment b). Instead, this segment records the secondary effects of an episode of rapid growth where Ni is quickly depleted in the surrounding melt given the high partitioning in olivine ($Kd_{Ni}$ ol/melt > ~10 in basaltic compositions (Beattie et al., 1991; Hart & Davis, 1978; Kinzler et al., 1990; Matzen et al., 2017; Straub et al., 2008) and the subsequent development of a compositional boundary layer (CBL*) around the crystal, which is depleted in compatible element and enriched in incompatible elements (e.g., Honour et al., 2019; Shea et al., 2019; Zellmer et al., 2016). Comparatively, Fo is less sensitive to variations in the CBL environment given the higher initial concentrations of Mg and Fe in the melt and its comparatively lower partition coefficients (Beattie et al., 1991) (Supplementary Fig.S.3.5). Ni reversals deviate from a broadly common value of ~2700 ppm (Fig.3.3b). This segment represents the growth of a crystal frame out of the CBL environment, where near-equilibrium compositions can be resumed since the melt has not been affected by accumulation/fractionation of elements out of equilibrium. By this reason, increments are more developed for Ni than for Fo (Fig.3.3c, segment c). Slight positive variations in Fo, as for OL_37, indicate that the new attained equilibrium out of the CBL is comparatively less fractionated in MgO than previously in the CBL. However, these variations are <0.6 Fo unit, whereas variations in Ni are >200 ppm. Rimward, another Ni depletion may occur, as for the case of OL_37 and OL_50, followed by a frame that detaches from a common background value of ~2200 ppm of Ni (Fig.3.3b).

*Note: transient CBL's form associated to rapid crystal growth, since the compatible components are strongly fractionated and incompatibles are rejected in the crystal-melt interface. Thus, compatibles will be depleted and incompatibles will be enriched in the CBL environment. For details see Land et al., 1999; Watson and Müller, 2009 and Shea et al., 2019.

Finally, the ***rims*** follow a trend that is more consistent with olivine crystallization, and transit toward the shallow crystallization trend, as does OL_50 and OL_39 (Fig.3.3b). Fo-Ni variations are more complex in OL_32 and the core of this crystal is comparatively more evolved that the other crystals, however, in agreement with the other crystals, two major perturbations occur at ~2500 and ~2200 ppm of Ni, sharing a common growth history with the less evolved crystals.

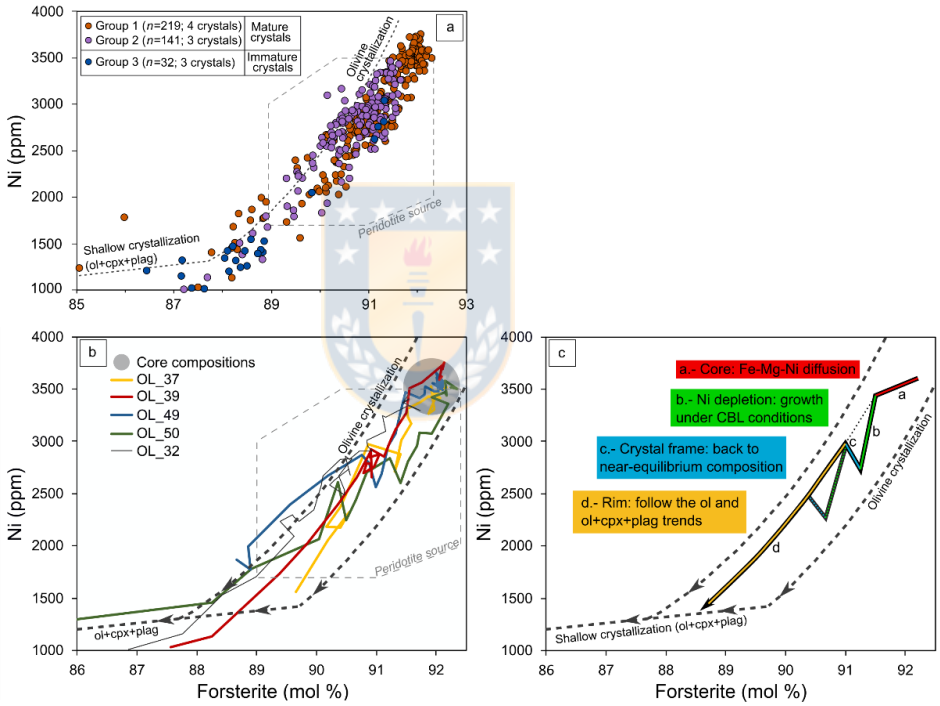


Fig.3.3.- Distribution of Fo-Ni contents among the different crystal groups and variations along selected crystal profiles. a) Olivine groups separated by color show that the texturally mature crystals tend to be more primitive whereas the immature olivines are compositionally more evolved. b) Core to rim profiles of selected crystals. Note the core compositions falling in a restricted Fo-Ni space (gray circle). Rimward, the color-coded crystals share a common evolution pattern, characterized by a sharp Ni decrease accompanied by only a slight variation of Fo, followed by abrupt increments of Ni-only variations at approximately constant Fo. Close to the margins, the crystals chemistry is consistent with co-crystallization of olivine + clinopyroxene ± plagioclase along the crystallization path. c) Schematic illustration of the evolution pattern of a -core to rim- section of a model crystal. Labels indicate the crystallization conditions of the different slopes of segments (a to d). The alternative path in segment d shows that some crystals may experience multiple sequences of externally developed crystal frames and Ni depletions followed by a return to equilibrium crystallization, e.g., Olivine 50. Crystallization lines after Ruprecht and Plank (2013) and mantle peridotite field after Straub et al., (2011).

The magnitudes of Fo-Ni increments associated with the growth of crystal frames (∆Fo <0.6 and ∆Ni >200 ppm) contrast with known examples of chemical variations in olivine induced by magma mixing, as those reported for a ring tuff of Shiveluch volcano in Kamchatka (Gordeychik et al., 2018) and Llaima volcano (de Maisonneuve et al., 2016) in the Andean Southern Volcanic Zone of Chile. At Shiveluch, primitive compositions of olivine present increments of up to ~300 ppm of Ni accompanied by increments of Fo greater than two forsterite units (∆Fo >2), whereas at Llaima volcano, evolved olivine crystals (~$Fo_{74}$) present increments of Ni on the order of ~150 ppm accompanied by increments of Fo greater than 3 Fo units (∆Fo >3). On the other hand, chemical variations induced by the entrainment of primitive melts of distinct composition accounted for Ni reversals >~800 ppm for mostly invariant Fo, as the case of Irazú volcano in Costa Rica (Ruprecht & Plank, 2013).

All these observations indicate that: 1.- The early structure of these olivines represent rapid growth of crystal frames disrupting a core-to-rim sequence. Those frames, composed by high Fo-Ni merge each other by zones of lower Fo-Ni composition. Diffusion of Fe-Mg-Ni may erase such compositional gradients. 2.- The cores of mature olivines of group 1 share a similar source and maintain a trend of diffusion that was acquired early during its development. 3.- Zoning structures within the frames are minimally affected by diffusion compared to the core of the crystals of group 1, and therefore they represent a recent stage of growth.

### 3.2.3.- Clinopyroxene-liquid thermobarometry

Clinopyroxene (cpx) and spinel are the other two early crystallizing phases. Cpx occurs exclusively as microphenocryst (<300 µm) and grades into smaller sizes in the groundmass with Mg# (molar Mg/[Mg+Fe]) ranging from 81 to 86 (Supplementary Table A.3.2). Sector zoning is commonly observed in cpx, consistent with rapid growth and development of dendritic and skeletal textures induced by a pronounced undercooling (Welsch et al., 2016). Spinels that co-crystallized in equilibrium with cpx are systematically lower in Mg# (<42) compared to the spinels that equilibrated with magnesian olivines (45<Mg#<76) (Supplementary Fig.S.3.6 and Table A.3.3).

We applied the cpx-liquid barometer (*n*=24) using the model of Al partitioning between cpx and melt (eq. 32c of Putirka, 2008) and the jadeite-diopside/hedenbergite (Jd-Di/Hd) exchange model (eq. 31 of Putirka, 2008). The models yield a pressure range of 4 to 7 kbar (14-24km) and 3 to 5 kbar (12-18km), respectively. Crystallization temperatures of 1140° to 1167°C are calculated for the cpx-melt equilibrium using eq. 33 of Putirka 2008 (Appendix Table A.3.4). Clinopyroxene crystallized from a more evolved melt under potentially lower pressure conditions when compared to magnesian olivine because it is in equilibrium with lower Mg# spinels. Thus, the pressure and temperature estimates derived from cpx provide minimum depth and minimum temperature constraints for the assembling conditions of primitive olivines.

### 3.2.4.- Timescales

The detailed textural investigation of the Los Hornitos olivines suggests a complex growth history where zones are not simply recording time along a continuous core-to-rim traverse. Conventionally the reversals would be interpreted to represent mixing events (Gordeychik et al., 2018; Kahl et al., 2011). In the case of Los Hornitos, we disregard that option as olivines show multiple reversals within single crystals requiring a complex magma assembly history for this primitive magma. Furthermore, unlike other systems that show mixing of diverse mantle melts (e.g., Ruprecht & Plank, 2013), these olivines stay on a very restricted differentiation path with respect to Fo-Ni systematics. Therefore, we interpret the zoning patterns representing the out-of-sequence assembly, where the crystals grow quickly in an evolving liquid from $Fo_{92}$ in the core to $Fo_{88}$ rimward (excluding the outermost rims that evolve beyond $Fo_{88}$). The growth history can then be extracted by linking up zones of decreasing Fo. As the outer frames have grown after any inner frame, they preserve more pronounced reversals. We focus our diffusion timescale calculations on these last reversals as they provide time information about two processes: 1) time between skeletal growth and eruption, where growth occurred deep in the crust (>24 km depth) and 2) given that the olivines track differentiation that has yet to be erased within the crystal zoning, the timescales also provide a unique constraint on the timing of melt differentiation in this primitive system.

Given our growth model for these olivines it is inappropriate to develop a sequential growth and diffusion model (e.g., Kahl et al., 2011; Oeser et al., 2018; Shea et al., 2015), the exact initial conditions are unknown. However, the systematic stepwise lowering of each individual high Fo frame from core to rim suggests that initial Fo contents of these zones were not significantly higher than what is preserved in individual frames. It should be noted though that while growth is still faster in these olivines than diffusion (Shea et al., 2015), here these olivines are approaching a Peclet number of 1 (Ruprecht & Cooper, 2012). This is substantially different than olivine examples presented for Kilauea (Shea et al., 2015) where growth is instantaneous relative to diffusion.

We limit our timescale calculations to the short lengthscale reversals in three crystals for which we have good control on the orientation of the crystal section (those of Fig.3.2b, c, d). All three crystals show reversals that are <20 μm. The calculated diffusion timescales for these crystals range from 3.5-40 days (Supplementary Fig.S.3.7). These provide minimum rates of magma ascent on the order of 25 to 300 meters per hour (assuming a minimum depth of 24 km constrained by cpx barometry), although those can be considerably higher if the locus of olivine assembly is deeper. Using 40 km as a conservative depth provide magma ascent rates of 40 to 500 meters per hour (see discussions below).

### 3.2.5.- Dendritic/skeletal morphologies and frozen Fo-Ni zoning testifying rapid growth regimes: an update to the olivine growth model

Linking textural and compositional data presented above allow us to determine that Ni depletions in these crystals develop in the course of episodes of rapid growth that is followed by a slow-down of crystal growth due to the effects of a CBL depleted in compatible components and enriched in elements rejected by olivine (e.g., Honour et al., 2019; Land et al., 1999; Sleutel et al., 2018; Welsch et al., 2013). In addition, we interpret the development of olivine-euhedral morphologies of elevated Fo-Ni contents that result in multiple reversals as seen in BSE images (Fig.S.3.4a, b, c) as spatial out-of-sequence growth where crystal frames form just beyond the CBL environment in order to reestablish near-equilibrium crystallization conditions. Thus, each frame represents an event of rapid growth that is quicker than growth rates under the CBL environment. The result is an external frame emplaced prior to the full closure of the gap between the two successive crystal structures. The out of sequence growth leaves behind a compositional suture that is represented by the minimum of the Ni depletions (Fig.3.2 and Fig.3.3). These compositional gradients may be quickly obliterated by diffusion due to their short lengthscales. Thus, only the outermost, younger frames may be preserved in pronounced profiles. Similar growth features in the crystal interior get erased by diffusion. In particular, the smaller differences in Fo content are only visible in the Los Hornitos olivines as flat shoulders, while higher amplitude Ni reversals may still be preserved.

Using the findings in these natural crystals we propose an updated olivine growth model that is consistent with our textural observations and chemical zoning

features. This model complements existing interpretation for zoning and textural parameters retrieved from natural and experimental samples observed elsewhere (Faure et al., 2007; Milman-Barris et al., 2008; Mourey & Shea, 2019; Shea et al., 2015; Welsch et al., 2013; Welsch et al., 2014).

In this model, the formation of a polyhedral normal zoned crystal occurs through five main stages (Fig.3.4):

***Stage 1:*** Four dendritic extensions radiate from a crystal nucleus (Fig.3.4a). During this stage, growth occurs mostly as a planar feature along the crystallographic plane *ac*. Those dendritic extensions enclose the entire perimeter of the crystal section leaving four pockets of melt symmetrically distributed (Fig.3.4b). The particular morphology along this section is the first evidence that growth develops along preferential directions (anisotropic growth) at the expense of the whole plane of a given face, consistent with the so called “Berg effect” (Berg & Bragg, 1938). Experimental growth rate constraints (Faure et al., 2007; Jambon et al., 1992; Mourey & Shea, 2019) suggest that dendritic extensions like those described here grow on the order of minutes (~1.5 minutes for a ~100 microns dendrite). The crystal shape that emerges during this stage is similar to that described for high cooling rate experiments (1890°C/h; -$\Delta$T=118°C) in Faure & Schiano (2005) (their Fig.11, photomicrography B2).

Two-dimensional (tabular) morphologies (e.g., Faure et al., 2003) as well as preferential initial growth along the plane *ac* has been also observed in

experiments (Mourey & Shea, 2019). However, a distinctive elongation along the *a* axis described in these experiments was not observed in our natural samples.

***Stage 2:*** A 3D structure begins to form when crystal growth expands along the crystallographic axis *b*. This growth episode initiates simultaneously from the four crystal corners, along the convergent edges of face (021) and split to conform the edges of face (010) (Fig.3.4c). The advanced morphology of this stage constitutes a crystal frame and the emergence of a euhedral proto-crystal with hollow faces (Fig.3.4d). As the size of the emerging crystal is limited during the initial stages (< 100 µm) and by applying experimentally determined growth rates associated with the development of skeletal textures (Mourey & Shea, 2019), we estimate that this morphology emerges on timescales of minutes to hours. The immature olivines of group 3 described above represent a textural maturation analogous to morphologies that develop during stage 1 and 2. Crystals of similar morphology have been experimentally obtained by Faure and Tissandier (2014).

If saturation decreases in the silicate melt, the growth mechanism may shift to slow-growth and filling-in of cavities proceeds, thus favoring textural maturation (Fig.3.4e). This is the case of the cores of mature crystals of group 1, that additionally experienced Fo-Ni diffusion.

***Stage 3:*** Growth continues along the four dendritic extensions along *ac* plane (Fig.3.4f) and successively, the growth of a new frame, rooted in the four recently grown corners (Fig.3.4g). As consequence of this rapid growth stage, a CBL is left behind between the recently formed frame and the internal arrangement.

Here, growth rates are comparatively slower and the melt strongly decreased in Ni (e.g., Supplementary Fig.S.3.5), resulting in a Ni depletion segment (pale green color in Fig.3.4h). Based on measurements on the rim-to-rim profiles of mature olivines of group 1 (Appendix Table A.3.1), the mean distance between two successive frames is ~35 µm.

***Stage 4:*** As undercooling continues, e.g., during magma ascent into progressively cooler crust, new crystal frames can grows surrounding the previous crystal structure (Fig.3.4i) with the development of contemporary Ni depletions in response to the rapidly grown frames (Fig.3.4j). Some of the zones of Ni depletions are not totally filled and that explain the occurrence of elongated cavities that parallel the external crystal faces and ultimately may conform elongated melt inclusions; as frequently observed in natural and experimental crystals of olivine (e.g., Faure & Tissandier, 2014; Mourey & Shea, 2019; Shea et al., 2015; Welsch et al., 2013).

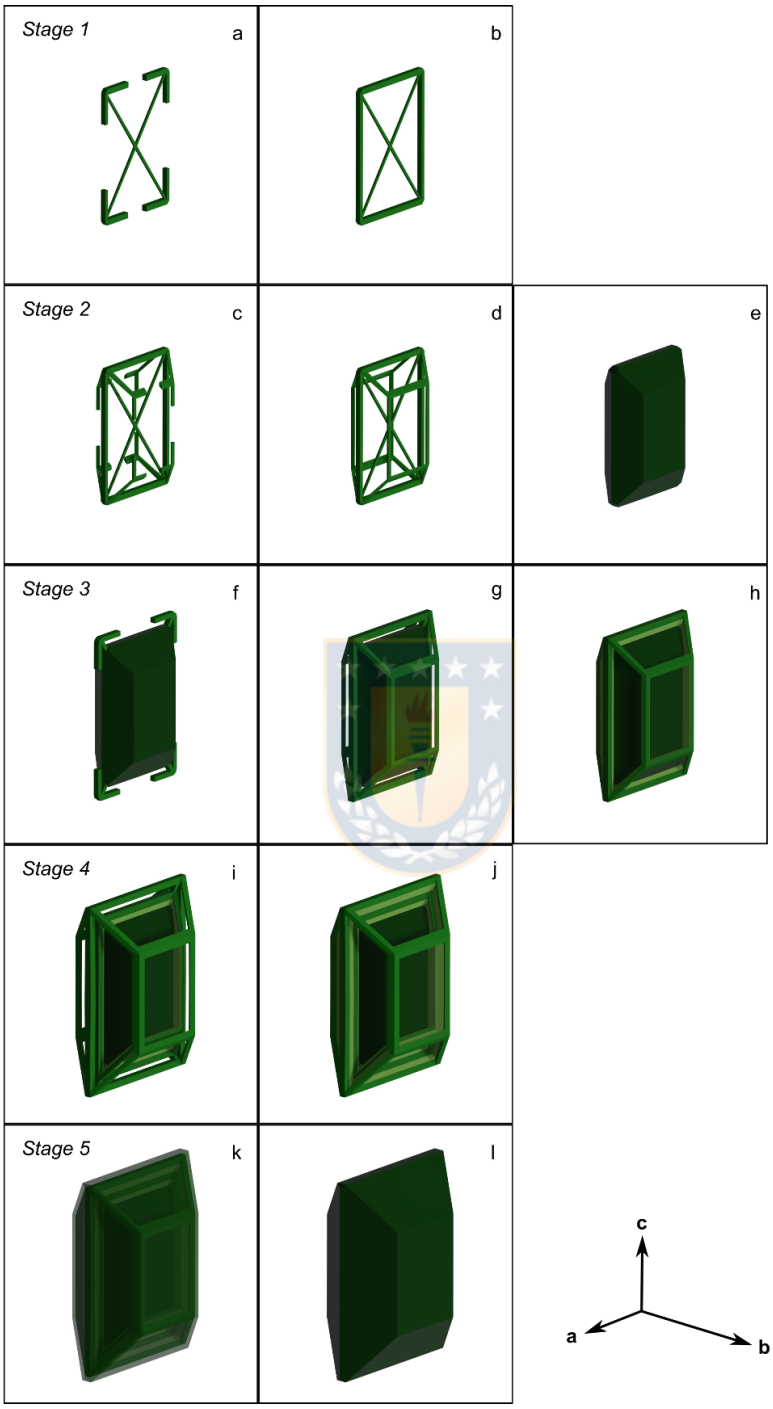


Fig.3.4.- Three-dimensional model of growth for the mature olivines found in Los Hornitos separated in five stages: a-b) four dendrites simultaneously radiate from a central *nucleus* along the *ac* plane and enclose the external section. c-e) growth detaches along the *b*-axis simultaneously from the four corners, conforming a crystal frame, where the olivine morphology is restricted to the edges of the crystal faces. Subsequently, the recently formed inner-frame is filled as maturation proceeds and a small olivine core is conformed. f-h) crystal growth continues at

rapid rates and the initial dendrites grow again along the *ac* plane. A new crystal frame grows separated from the internal structure leaving behind a compositional boundary layer, which is responsible for the so-called *Ni depletion* structure in the studied olivines (pale green structure between two successive frames in Fig.3.4h). i-j) the process repeats and a new frame and associated Ni depletion is externally developed in the emerging crystal. k-l) Maturation proceeds from the most internal to the outer frame and the skeletal texture transit towards a polyhedral morphology. Zoning structures may be partially or fully erased depending of the timescales and storage conditions of the host magma.

***Stage 5:*** Continued textural maturation leaves the innermost structures texturally more evolved. The resultant morphology corresponds to a crystal in the skeletal to polyhedral transition, as those mature olivines of group 1 and 2 (Fig.3.4k). The culmination of this stage consists of a polyhedral crystal avoiding cavities, and depending of the elapsed time in the hot magmatic environment, the olivine may (or may not) record the differential composition of frames and Ni depletions (Fig.3.4l).

### 3.3.- Discussion and Conclusions

Integrating textural data with fine-scale olivine chemistry allows us to illuminate the history of crystallization, from the earliest to the advanced stages of growth and maturation. At Los Hornitos those stages of growth and maturation are preserved, in contrast to other arc volcanoes where they are commonly not observed. Our model defines a concentric growth of discontinuous *crystal frames*, out of the core-to-rim sequence and contemporary, but slower, infill of Ni depletion zones. While frames represent structures of rapid growth, the depletions are a

response to secondary effects of such rapid growth, where out of equilibrium conditions cause concentric zones remarkably depleted in Ni and Fo in a less degree. Therefore, the extent of Ni depletions in the rim-to-rim profiles (Fig.3.2 and Fig.S.3.3), is directly linked to the potential thickness of the involved CBL's. Our observations in mature olivines of group 1 (Appendix Table A.3.1), indicate that the thickness of these boundary layers is between 20 to 50 µm. Using a medium value of 35 µm and applying it to the model of Watson & Müller (2009), allows us to estimate olivine growth rates on the order of $5x10^{-8}$ to $7x10^{-8}$ m $s^{-1}$ (Supplementary Fig.S.3.5). Those values are about one order of magnitude higher than the growth rates estimated by Jambon et al., (1992) and Donaldson (1976) but are consistent with the 3D estimates of Mourey & Shea (2019) in experiments carried out with an undercooling of 40°C.

Since cpx barometry represent the evolution of olivine at Fo<~88 and Ni<~1500 ppm, the depth at which most of the olivine crystallization occurs, from $Fo_{92.5}$ to $Fo_{88}$, is deeper and hotter than the cpx constraints. On the other hand, the polyhedral and high Fo-Ni olivines of group 1 maintain in the core remarkable diffusion profiles (Fig.3.3b, c), that are absent in the cores of olivines of groups 2 and 3. Thus, we suggest that based on compositional and thermal considerations (e.g., Gordeychik et al., 2018) group 1 olivines nucleated and later experienced diffusion in the nominally hotter subarc mantle, whereas olivines of group 2 and 3 nucleated in the deep to mid crust (Fig.3.5).

In addition, given that the immature olivines share a similar textural maturation, preserving visible dendritic features along a considerable Fo spectra of 91 to 89, we argue that rapid growth associated to magma ascent and cooling occurred early in the deep crust and continued at mid crustal levels (~20 km depth) evidenced by the rapid-growth textures preserved also in clinopyroxene in the form of sector zoning.

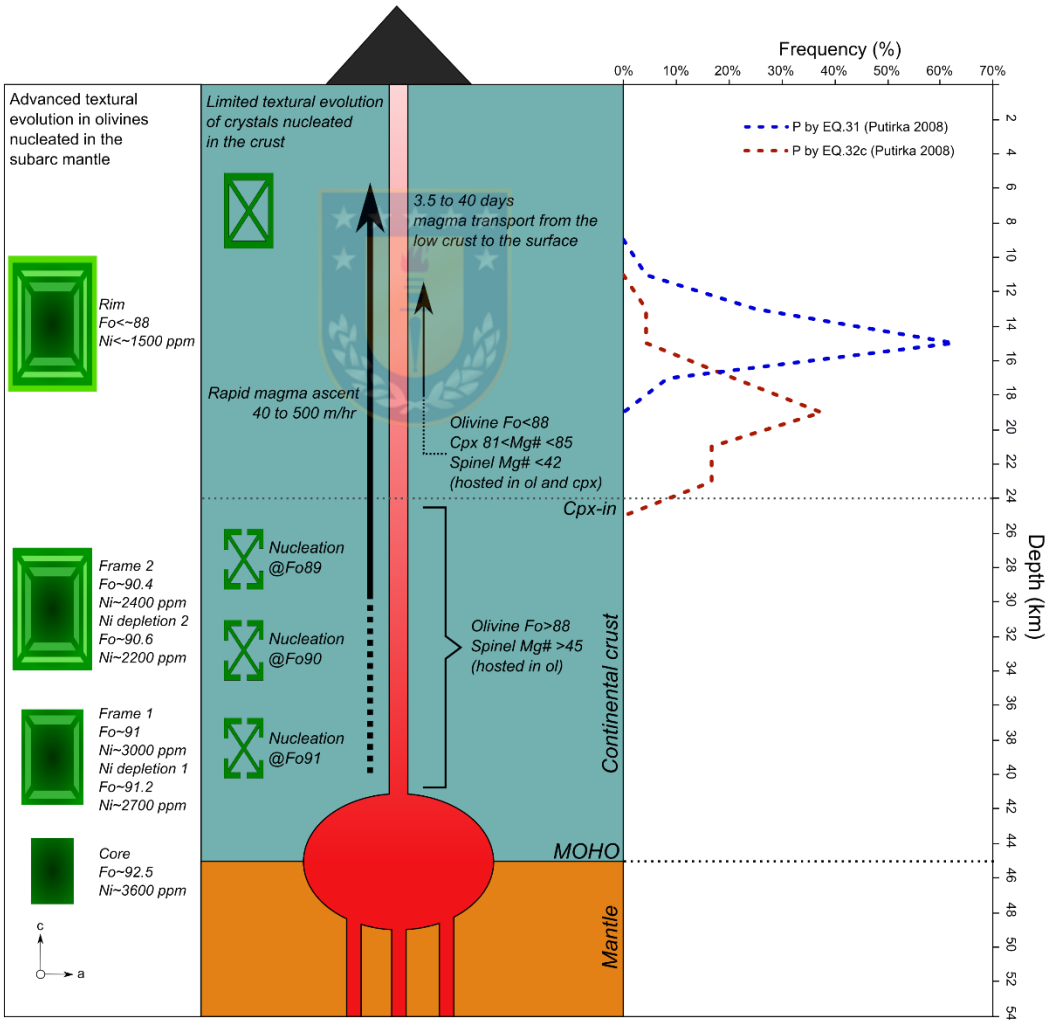


Fig.3.5.- Schematic illustration of the magmatic system of Los Hornitos. Mature olivines of Group 1, likely nucleated at mantle conditions, reach advanced textural maturity and preserve zoning structures of crystal frames and Ni depletions. Mature olivines of Group 2 and immature olivines

of Group 1, nucleated in the low to mid crust, preserve skeletal and dendritic textures, and are compositionally more evolved. Diffusion calculations in the most external frame of mature olivines indicate timescales of magma transport from the deep crust to the surface on the order of 3.5 to 40 days.

These observations indicate that the host magma experienced a continuous and increasing degree of undercooling as it advanced through the cooler crust, enhancing conditions for nucleation at the expense of those more appropriated for maturation of the crystals. In this scenario the skeletal assembly of frames around the cores occurred in the lower crust as magma moved towards the surface with nucleation and subtle textural maturation of olivines of group 3 also operating closely in time and depth (Fig.3.5). Therefore, the outer frame at Fo~90.5 and ~2400 ppm of Ni, where we developed diffusion calculations (3.5 to 40 days), have grown and ascended from a broad depth estimate of 40 km implying magma ascent rates on the order of 40 to 500 m/h. Our timescale calculations are of similar magnitude to those recently published for Los Hornitos (13 to 63 days, excluding three outlier values <102 days) (Tassara et al., 2020). Also, the retrieved ascent rates are more conservative than those reported by Gordeychik et al., 2018 for Shiveluch (80 to 1200 m/hr), and is orders of magnitude higher than those reported for andesitic stratovolcanoes (e.g., 55 to 80 m/day) (Ruprecht & Plank, 2013) that underwent also cumulate mobilization on ascent (Oeser et al., 2018).

Our findings suggest that the presence of reversed zoning in olivine may not always reflect magma recharge and mixing. Instead, complex growth histories that lead to out-of-sequence growth can lead to reversed zoning in a system that does not experience substantial interaction with another less evolved magma. In the case of Los Hornitos and presumably other monogenetic cones, such reversals are better explained by closed-system processes such as cooling and fractionation during ascent combined with out-of-sequence growth and boundary layer effects. The result is a simplified magma assembly history for Los Hornitos and potentially other systems that show similar systematics. Small, individual batches of primitive arc basalt can reach mid to high crustal levels over short timescales. The presence of multiple magma batches stored in the crust to account for several compositional reversals recorded in olivine phenocrysts are not required. However, with the exception of small monogenetic systems those rarely erupt since they often intersect crustal magma reservoirs of prolonged residence, as those underneath stratovolcanoes or in the mid to lower crust (Hildreth & Moorbath, 1988). There, the early morphology and the complex zoning of olivine is erased by overgrowth and diffusion, respectively, resulting in slower rates of magma ascent, as in the cases of Irazú (Ruprecht & Plank, 2013) and Llaima (Ruth et al., 2018) volcanoes. Moreover, Los Hornitos is part of the Southern Volcanic Zone (Lopez-Escobar et al., 1995) that is the type locality for MASH processes. The occurrence of monogenetic cones like Los Hornitos suggests that lower crustal MASH zones are not pervasive throughout the arc,

but crustal regions that lack zones of prolonged storage where magmas can ascent uninterruptedly to the shallow crust and eventually erupt at the surface co-exist in thick arc crust.



See the Method section at Appendix A.3.

The following section do not conform part of the submitted manuscript, and is only intended to introduce the reader into the melt inclusion study to answer the research questions.

### 3.4.- Implications for the proposed melt inclusions study

The main implications derived from the proposed crystal growth model for the additional study of melt inclusions are:

1.- A considerable percentage (73 vol %) of the total olivine population found in Los Hornitos tephra, retain evidence of rapid growth, expressed as dendritic and skeletal textures. As shown above, rapid growth rates promote the development of CBL surrounding the crystal, therefore if a melt inclusion is trapped during such episodes of growth, the composition of the trapped melt will represent conditions out of equilibrium, where compatible components are depleted and incompatible components are enriched, as the crystal consume and reject those elements respectively. On the other hand, polyhedral textured crystals, grown at comparatively slower growth-rates at least during the more advanced stages of its textural maturation, are able to trap melt in equilibrium, since the elements can diffuse and re-equilibrate in the crystal-melt interface. According to Faure 2007, growth mechanisms like dendritic or skeletal are relevant for melt inclusion formation, but those will represent the parental melt only if the sealing of such inclusions occurs during slow-growth regimes, when the skeletal crystal transits towards polyhedral morphology.

As $Fe^{3+}$ is incompatible in olivine, it may be concentrated in the CBL's, as $Al^{3+}$, $P^{5+}$ and $Cr^{3+}$ does (Milman-Barris et al., 2008; Shea et al., 2015; Welsch et al.,

2014; Shea et al., 2019), and so, $Fe^{3+}/\Sigma Fe$ determinated by μ-XANES in such inclusions will derive high anomalous values, not representative of the melt in equilibrium with the host crystal.

2.- According to cpx-barometry, cpx became the liquidus phase at ~24 km depth. As cpx postdate the crystallization of Fo>~88, this indicates that the locus of crystallization of the high Fo-Ni olivines (Fo92.5 to Fo88) occurs deeper than the cpx constraints. By the other hand, the mature olivines of group 1, present a remarkable diffusion profile in the core. Based on thermal and compositional criteria, those cores have been grown and underwent diffusion in the nominally hotter subarc mantle, whereas the olivines of groups 2 and 3 have grown later in the deep to the mid crust. Therefore, the crystal structures depicting Fo-Ni reversals, where we performed diffusion calculations (@Fo~90.5), have been grown at a broad depth of 40 km and rapidly ascended through the crust in the order of 3.5 to 40 days. As the melt inclusions devoted to the next chapter are hosted in olivine crystals in the range of Fo90 to Fo92, this indicates that these inclusions were trapped in the deep crust and quickly transported to the surface where they quenched during the eruptive event. Thus, the cooling path of this particularly simple basaltic magma system allows a good preservation of the trapped melts, and hence can be positively subject to further microanalytical research.

## Supplementary Figures

## Chapter 3: Textural analysis of olivine hosts: avoiding/noticing growth textures out of equilibrium.

Manuscript title: The early structure of olivine from subduction zones and its missing zoning

Fig.S.3.1a

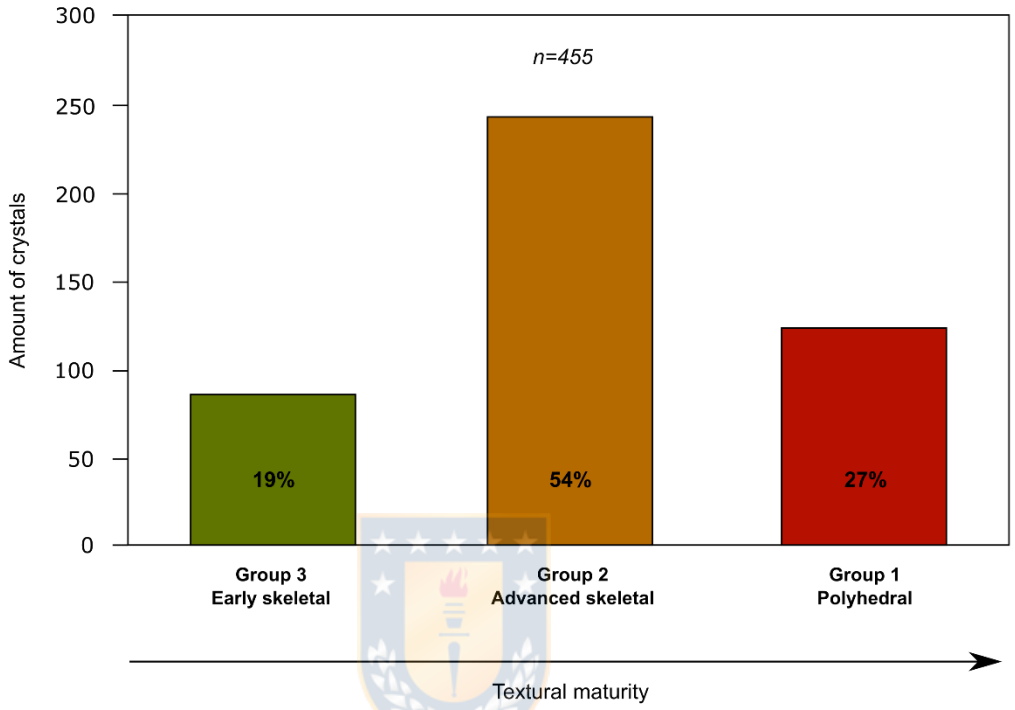


Fig.S.3.1a.- Histogram showing the modal distribution of crystals categorized according to their textural maturation in early skeletal, advanced skeletal and polyhedral.

Fig.S.3.1b

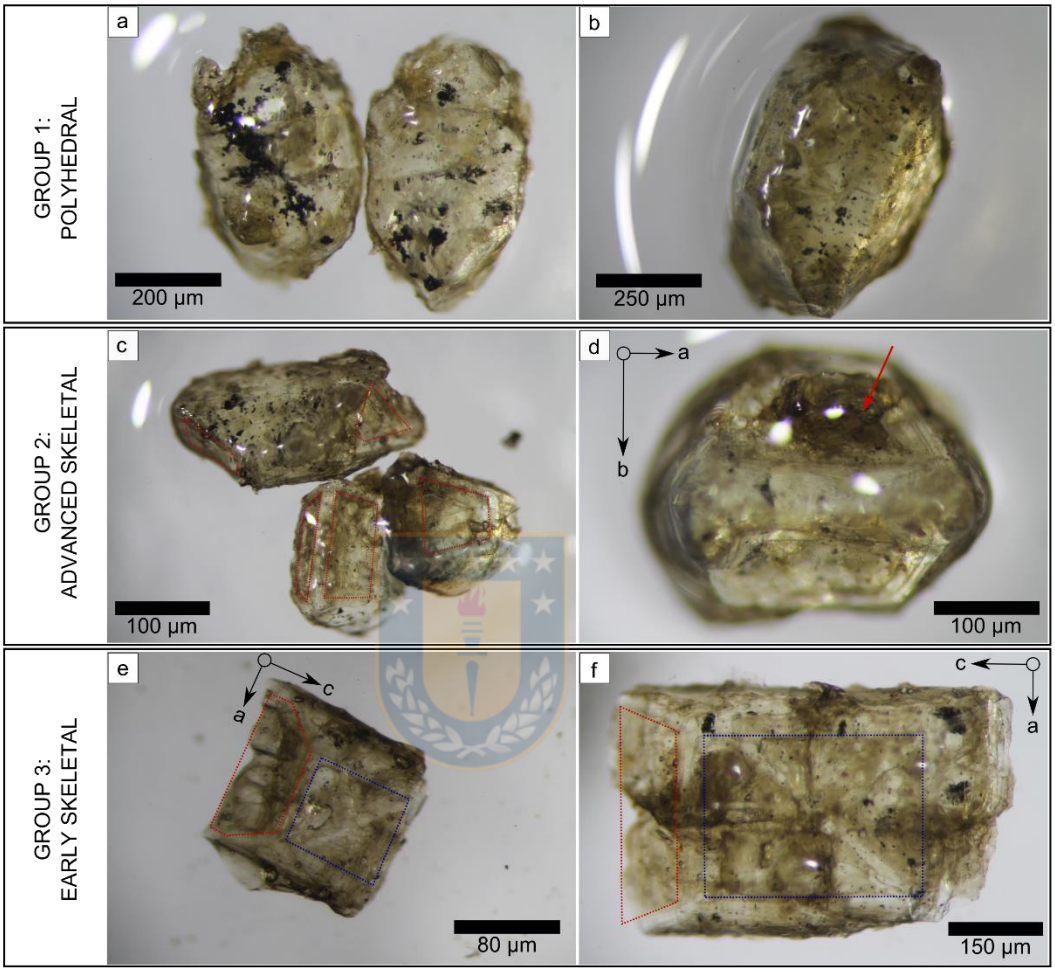


Fig.S.3.1b.- Examples of crystals observed under the binocular lenses by category. a) two euhedral to subhedral olivines with well-developed external faces. b) euhedral olivine with a fully polyhedral habit. Note the absence of internal cavities in crystals of a and b. c) three near-polyhedral olivines retaining skeletal features in the (021) face (segmented red lines). d) detail of a skeletal crystal oriented normal to *c*-axis, showing a prominent pocket of glass trapped in the upper cavity (red arrow). These crystals maintain the typical morphology of olivine while leaving open cavities along the (021) planes. e) and f) two olivines oriented normal to the *b*-axis showing an externally skeletal texture but retaining dendritic features in the innermost part along plane *ac.* These immature crystals maintain open cavities along the (021) and (010) faces (red and blue segmented lines, respectively), allowing to observe the four internal dendrites that symmetrically radiate from the central core along the *ac* plane.

Fig.S.3.2

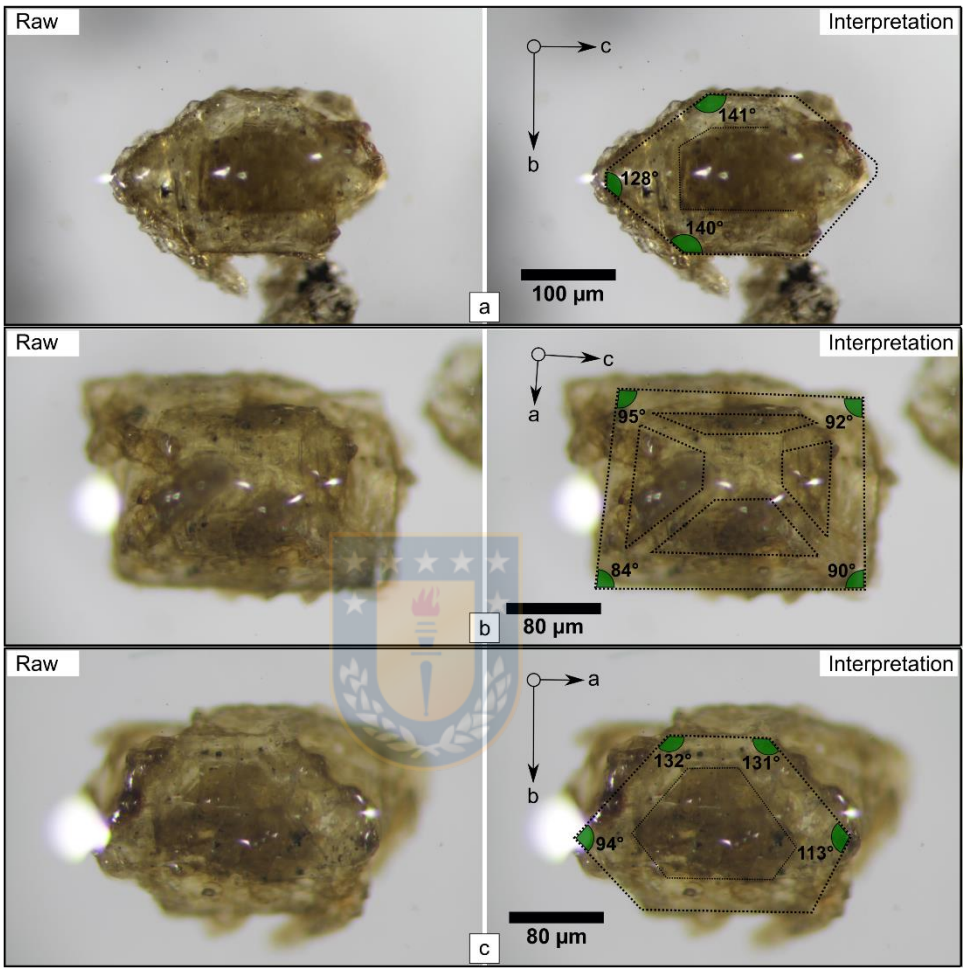


Fig.S.3.2.- OL-62 observed under the binocular lenses showing the early structure of an immature olivine. Left side shows raw images of three different orientations of the same crystal whereas the interpreted crystal morphology, enhanced by segmented lines, is shown on the right side. The interfacial angles for the three positions allow to identify the crystallographic orientation for a) normal to *a*, b) normal to *b* and c) normal to *c*. Note the sharp contacts between the crystal (pale green) with the adjacent glass (greenish brown). See theoretical interfacial angles of olivine in Fig. S.3.4 a, b and c.

Fig.S.3.3

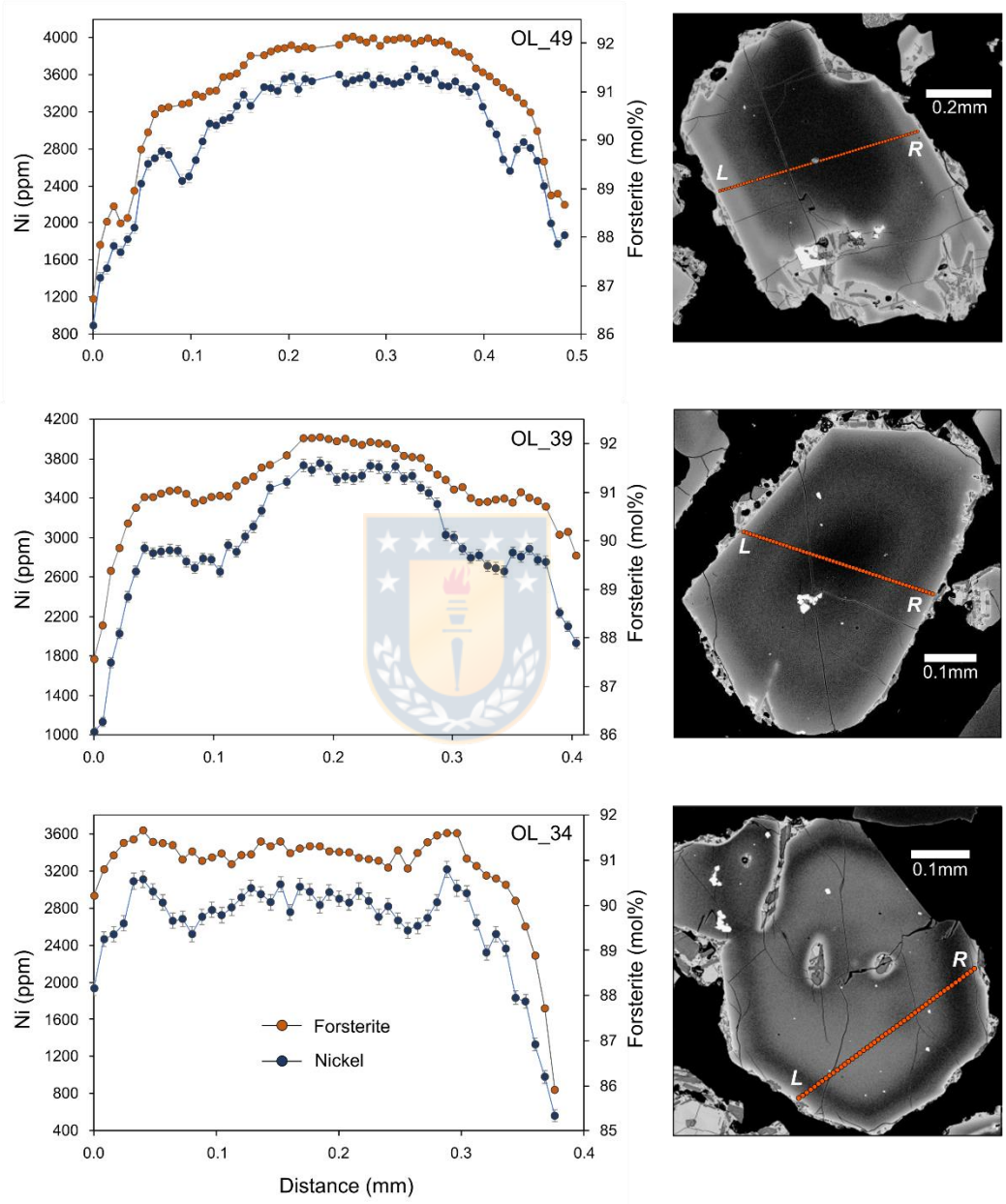


Rim to rim profiles in three additional examples of mature olivines (OL_49, OL_39 and OL_34) depicting *Ni depletions* and successive reversals. The absence of a high Fo-Ni inner core in OL_34 indicate that this section does not intersect the center. The crystal orientation is not certain and thus these crystals are not used for diffusion timescale calculations.

Fig.S.3.4a

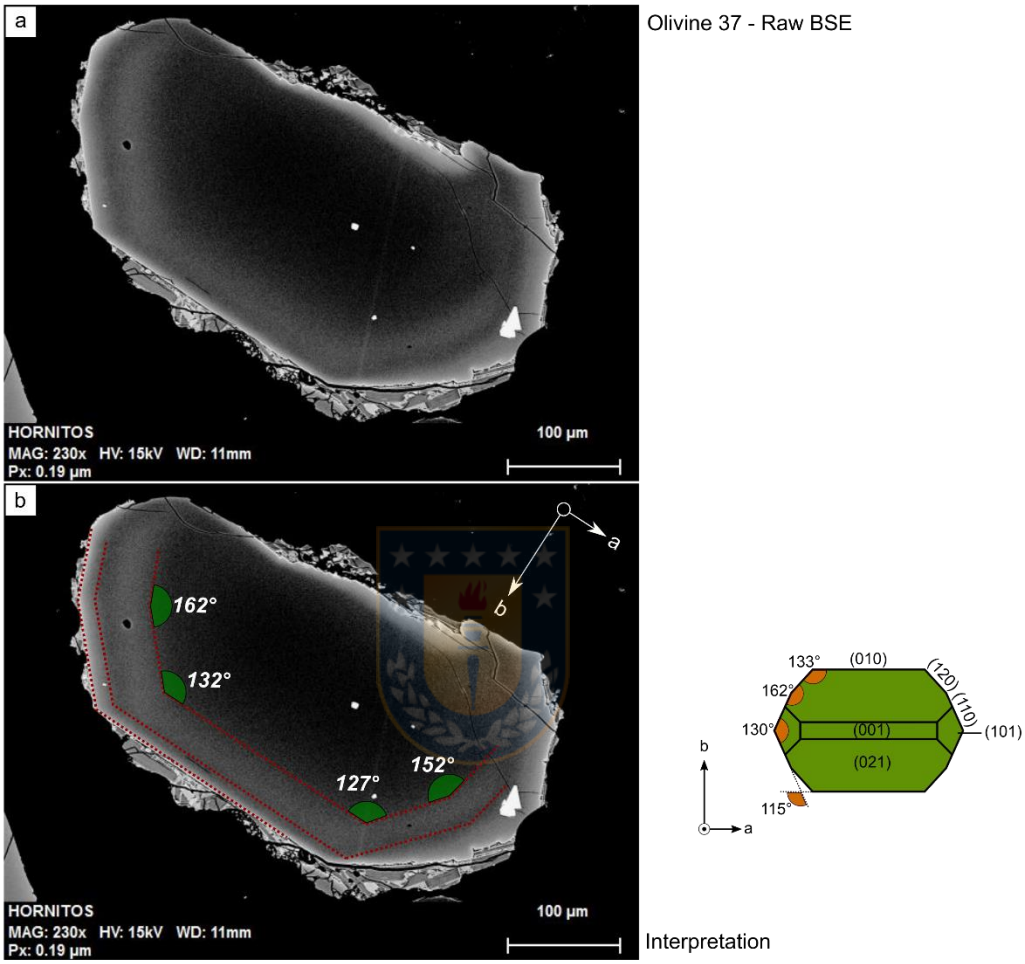
a
Olivine 37 - Raw BSE
HORNITOS
MAG: 230x HV: 15kV WD: 11mm
Px: 0.19 µm
100 µm
b
a
b
162°
132°
152°
127°
HORNITOS
MAG: 230x HV: 15kV WD: 11mm
Px: 0.19 µm
100 µm
Interpretation
133°
(010)
(120)
(110)
162°
130°
(001)
(101)
(021)
115°
b
a

Fig.S.3.4b

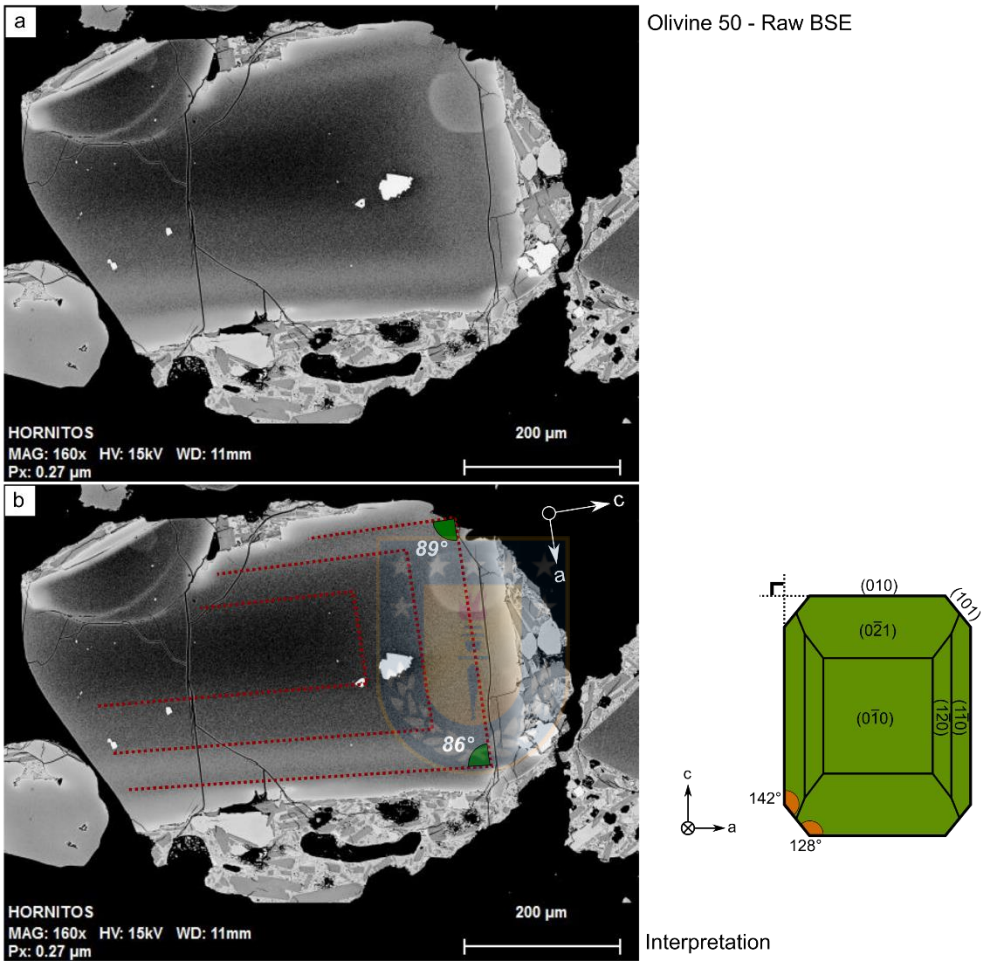
a
Olivine 50 - Raw BSE
HORNITOS
MAG: 160x HV: 15kV WD: 11mm
Px: 0.27 µm
200 µm
b
c
a
89°
86°
HORNITOS
MAG: 160x HV: 15kV WD: 11mm
Px: 0.27 µm
200 µm
Interpretation
(010)
(101)
(0$\bar{2}$1)
(0$\bar{1}$0)
(110)
(120)
c
a
142°
128°

Fig.S.3.4c

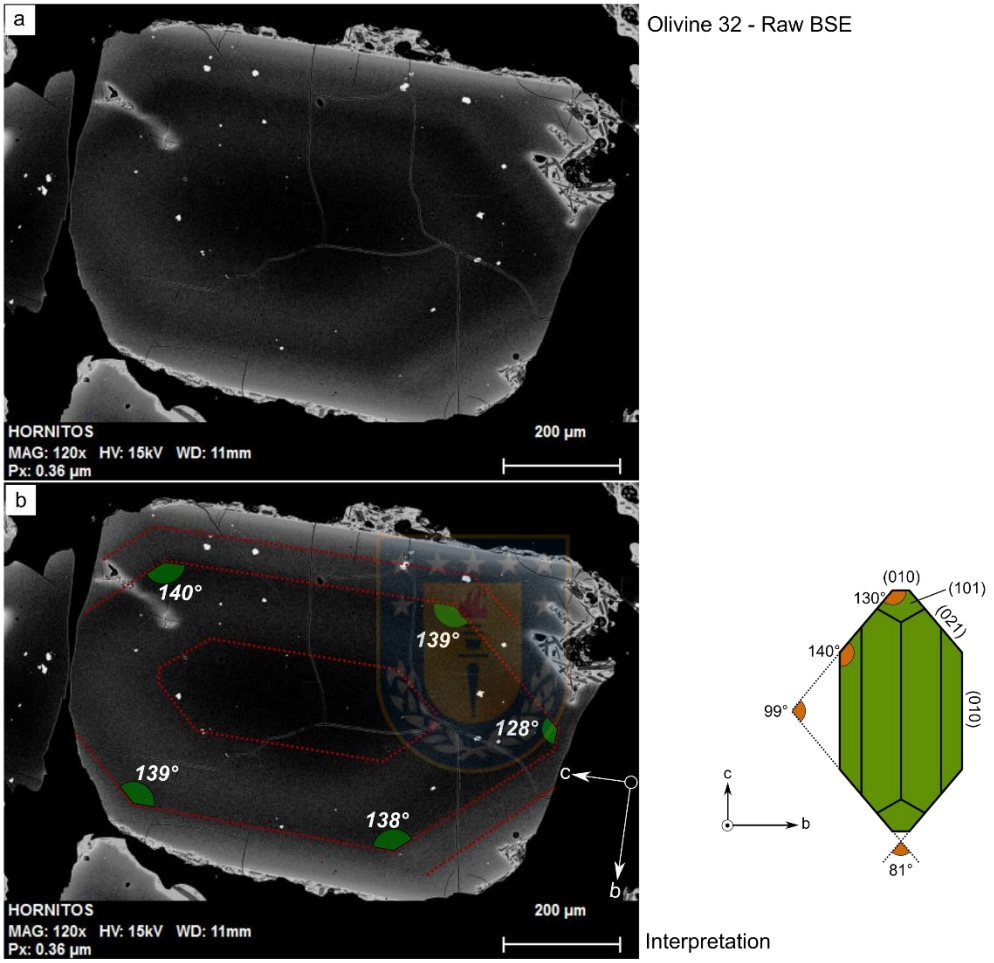


Fig.S.3.4.- Interfacial angles denoting the crystallographic orientation of the section: a) Olivine 37 closely normal to *c*-axis, b) Olivine 50 closely normal to *b*-axis and c) Olivine 32 closely normal to *a*-axis (mineralogical data taken from Welsch et al.,2013).

Fig.S.3.5

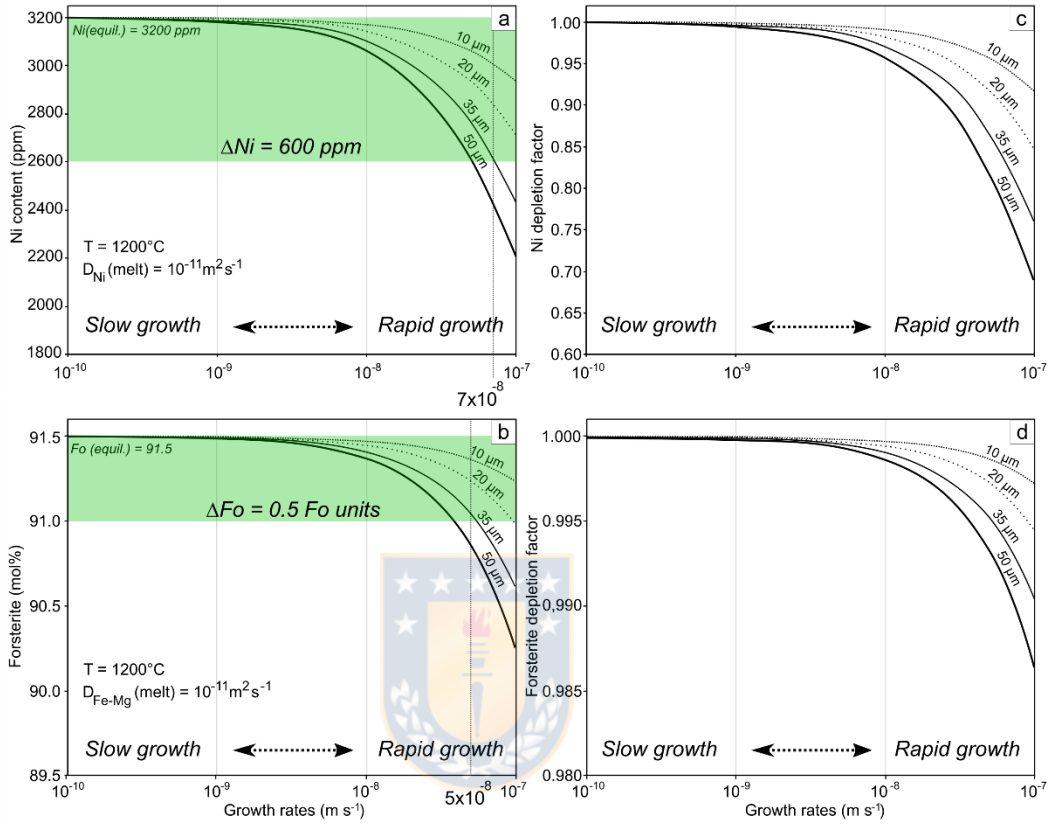


Fig.S.3.5.- Modeling the depletion of compatible components using the equation of Watson and Müller (2009) for an olivine growing under the effects of a compositional boundary layer (CBL) using different thicknesses (segmented and continuous curves) along with slow to rapid growth rates. Green fields in a and b represent broad compositional ranges observed in natural samples from Los Hornitos. a) Ni and b) Fo variations from an initial equilibrium composition of $Fo_{91.5}$ and 3200 ppm of Ni. Depletion factors of c) Ni and d) Fo, determined as the ratio of the calculated disequilibrium concentration over the initial equilibrium condition, show the considerable larger impact on Ni compared to minor variations in Fo.

As *Ni depletions* in olivine represent growth under a CBL, the thickness of those structures measured in the rim-to-rim profiles indicate the potential extent of the layer. Based on the measuring of the five imaged olivines (Fig.3.2 and Fig.S.3.3), we determined the thickness to be between 20 to 50 µm. Using a mean value of 35 µm along with the broad values of ΔFo and ΔNi observed in the depletions of the imaged crystals (see Fig.3.2 and Fig.S.3.3), we obtain growth rates on the order of $5x10^{-8}$ to $7x10^{-8}$ (m $s^{-1}$) (as shown in Fig.S.3.5 a and c).

For calculations in our model we used average distribution coefficients for Mg, Fe ($Kd_{Mg}^{ol\text{-}melt}$ = 5, $Kd_{Fe}^{ol\text{-}melt}$ = 1.65; e.g., Beattie et al., 1991) and Ni ($Kd_{Ni}^{ol\text{-}melt}$ = 10; e.g., Beattie et al., 1991; Hart & Davis, 1978; Kinzler et al., 1990; Straub et al., 2008). At 1200°C the diffusivities of Fe and Mg in the melt are of similar magnitude in basaltic melts (Zhang et al., 2010) so we used a common value of $D_{Fe\text{-}Mg}^{melt}$ = 1 x $10^{-11}$ ($m^2$/s) (Zhang et al., 2010). The diffusivity of Ni in the melt was approximated to the values reported by Zhang et al., 2010 for a haploandesitic melt with values identical to the ones used for Fe and Mg.

Fig.S.3.6

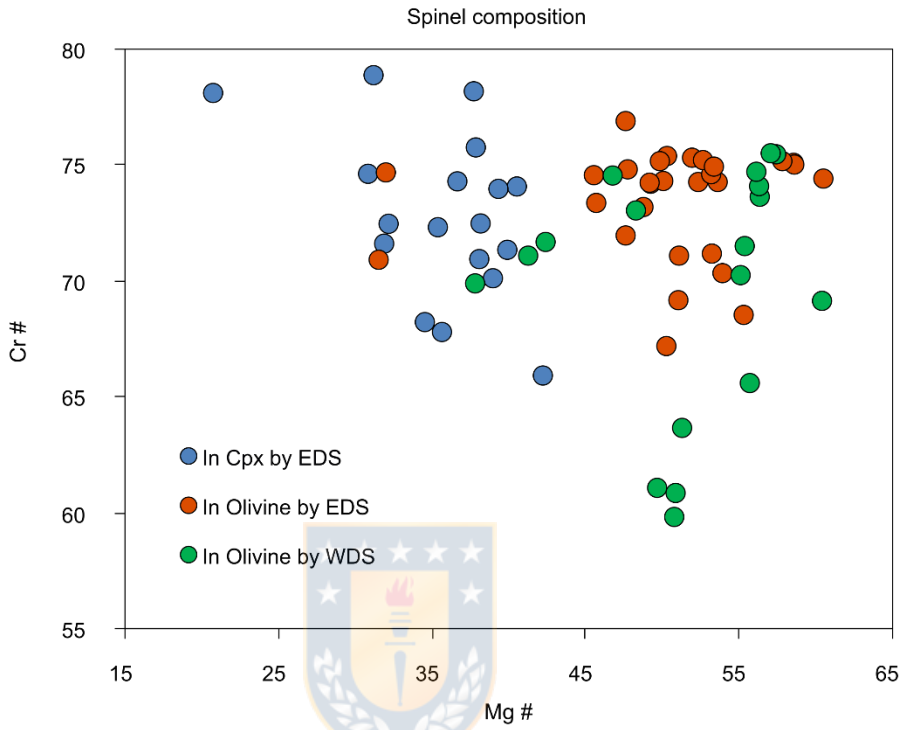


Fig.S.3.6.- Composition of clinopyroxene and olivine hosted spinels determined by EDS (blue and orange circles) and by WDS (green circles). Most of the olivine hosted spinels plot at Mg# >45. Five exceptions plots at Mg# ≤42 and those are spinels located in the outermost rim of olivine (where Fo ≤~88), in equilibrium with clinopyroxene. By contrast, spinels hosted in clinopyroxene are more iron rich with Mg# <42.

Fig.S.3.7

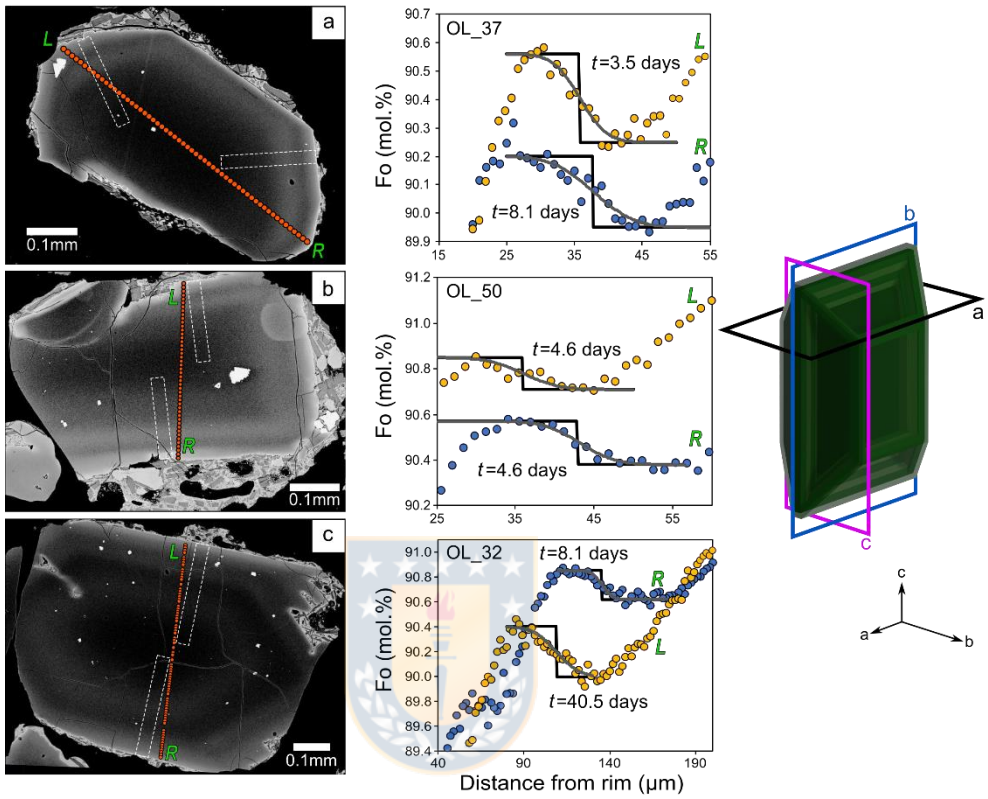


Fig.S.3.7.- Timescale calculations at 1150°C for three mature olivines with a good control on the orientation of the crystal section. a) Olivine 37, b) Olivine 50 and c) Olivine 32 oriented closely normal to the crystallographic axis *c*, *b* and *a*, respectively. Five of the six analyzed traverses provide timescales of <10 days and only one traverse provides a timescale of 40.5 days.

# Chapter 4: The redox state and metal/volatile budget of primitive arc magmas

## 4.1.- Introduction

Melt inclusions (MI's) contained in high-forsterite olivine crystals were interrogated by combined microanalytical techniques (SIMS, EPMA, µ-XANES & LA-ICPMS) in order to investigate the volatile/metal endowment as well as the redox conditions of primitive arc magmas in a base-metal fertile segment of the Andes. Olivine crystals were taken from ash layers where olivine occurs as loose grains, thereby minimizing chemical modifications of trapped melts given the high thermal gradient during its cooling (Lloyd et al., 2013). Consequently, all the analyzed inclusions correspond to "quenched glasses" avoiding the crystallization of daughter phases inside the MI.

As typically observed in melt inclusion assemblages, the analyzed MI's consist of the volumetrically dominant silicate glass and the associated shrinkage bubble, but also visible carbonate phases were frequently observed in the bubble-glass transition, readily distinguishable under the microscope.

In the following sub-chapters, I briefly describe the methodology for sample preparation and microanalysis on MI samples, and also the results on physical

and chemical properties of the analyzed samples. Major discussions and conclusions will be incorporated in a final section.

## 4.2.- Methodology

### 4.2.1.- Sample preparation

The full steps of sample preparation can be shortly summarized as follow:

**1.- Sampling in the field:** independent layers of tephra were sampled from fallout deposits in the proximities of the studied mafic vents.

**2.- Sieving and mineral separation:** after collection in the field, tephra samples were sieved, and olivine separates were obtained by the use of heavy liquids. I used LST liquid (lithium heteropolytungstate) at the Sernageomin facilities in Santiago, at a room temperature of ~25°C.

**3.- Prospection of olivine-melt inclusion pairs:** olivine separates embedded in mineral oil were observed under the binocular lenses in order to prospect for melt inclusion bearing crystals. The selected candidates were pictured and sketched to document the occurrence and estimated depth of MI's inside the crystals (Fig.4.1a).

**4.- Mounting in dental resin:** individual crystals were strategically placed in a dental resin mount in order to polish out the crystal host and expose the best

section of each MI. Polishing can be separated in two stages: Stage 1 corresponds to the “coarse polishing”, by the use of silica carbide based polishing discs (600 to 1200 grit). This stage is oriented to take out most of the host that is far from the MI. Stage 2 correspond to the “fine polishing”, which is carefully developed by the use of diamond paste suspensions (four steps from 9 to 1 µm suspensions). This stage ends with flat surfaces of hosts and outcropped inclusions. Profuse ultrasonic cleaning with DI water is key to remove all possible C-residue from the samples (essential for accurate $CO_2$ determinations) (Fig.4.1b, c, d).

**5.- Unmounting from the dental resin:** once the olivine-MI samples are well polished and documented under the microscope, the crystals are carefully unmounted from the dental resin by the use of a hand solder machine. The remaining dental resin around the crystal was carefully dissolved using acetone.

**6.- Mounting in Indium:** the loose polished crystals with outcropping inclusions were placed in an indium filled aluminum sample holder. The very low hardness of Indium allows to softly indent the crystal samples. During this stage, the crystals were individually mounted, avoiding “flower patterns” among the crystals, in order to obtain a final mount where every individual is recognizable. Crystal samples ordered in columns/rows accompanied by a sketch map is the best way to control the identity of the samples (Fig.4.1e).

**7.- Final polishing:** the crystal samples placed in the Indium mount were carefully polished by the use of alumina suspension 0,05 µm, in order to avoid any irregularity in the flat morphology of the final mount.

### 4.2.2.- Analytical procedures

The different microanalytical techniques developed on the melt inclusion suite and the olivine hosts, are contemporary listed as follow:

#### 4.2.2.1.- Collection of data by Secondary Ionization Mass Spectrometry (SIMS)

SIMS data were collected with a Cameca IMS 7f-Geo at the Institute of Materials Science and Engineering (IMSE) in the Washington University of St. Louis (WUSTL), Louisiana, United States (Fig.4.1f).

A single SIMS session were devoted to volatile and halogen abundance measurements. The sample holder with the olivine-MI's pairs were coated with a 40 nm thick-layer of gold, to provide an electrically conductive surface. The $Cs^+$ ion beam configured using a 5-10 nA current and 10kV of acceleration voltage was used to create a 15 µm beam size. Measured species were $CO_2$, $H_2O$, F, P, S and Cl. Mafic glasses standards were used for all standardizations. Detection limits is 30 ppm $H_2O$, 3 ppm $CO_2$, and 1 ppm F, S and Cl.

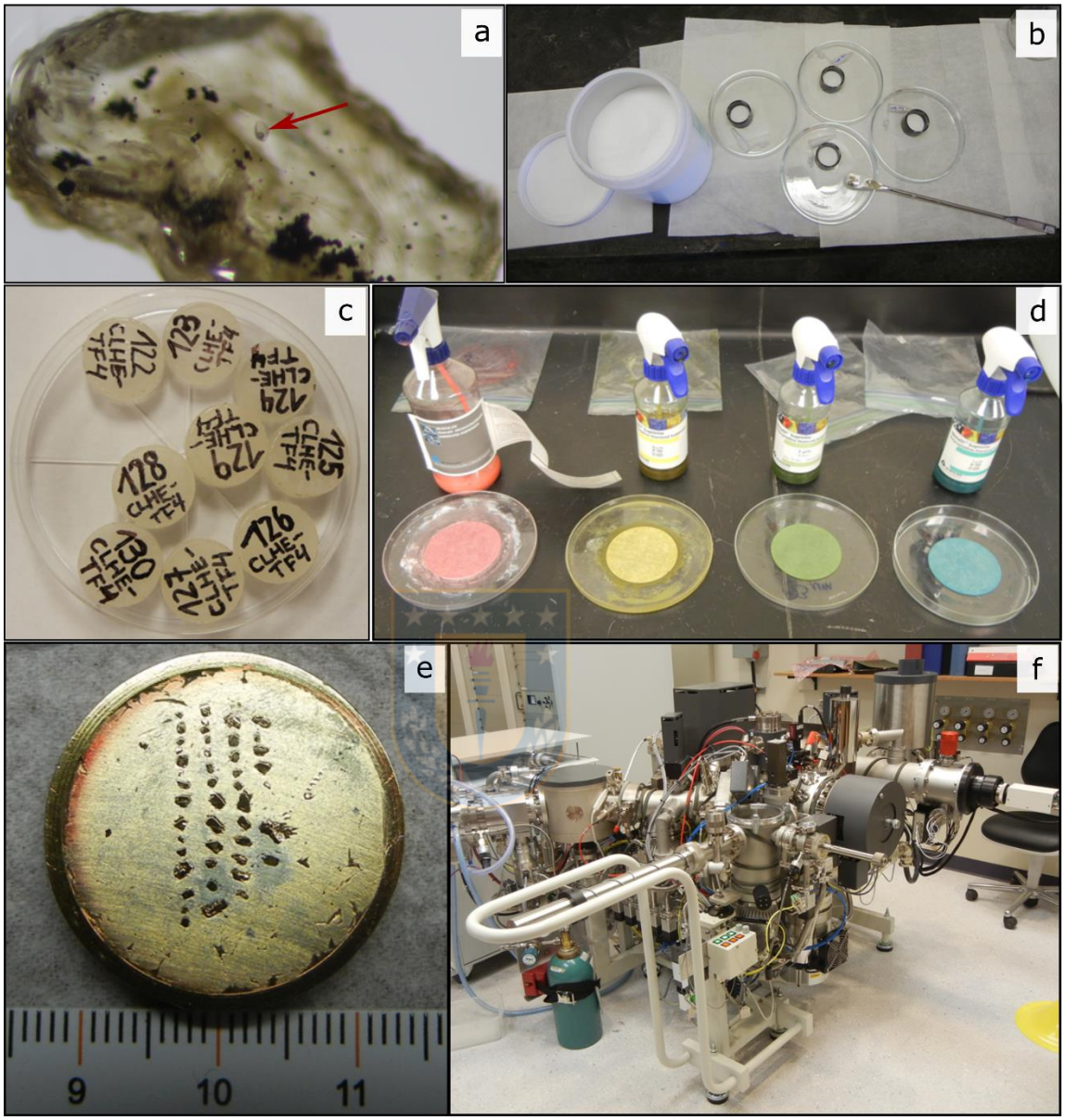


Fig.4.1.- Selected pictures of steps along sample preparation for further analysis. a.- Prospection of inclusions under the binocular lenses (red arrow shows an inclusion). b.- Mounting of crystal grains with dental resin for polishing. c.- Individual mounts of crystal-host pairs for later coarse polishing. d.- Fine polishing setting for diamond suspensions. e.- Gold coated final mount holding 44 crystal grains for microanalysis (scale in cm). f.- SIMS facilities at Washington University of St. Louis (WUSTL).

#### 4.2.2.2.- Collection of data by Electron Probe Micro Analysis (EPMA)

EPMA data were collected with a Jeol Superprobe JXA-8600M in the Instituto de Geología Económica Aplicada (GEA) at Universidad de Concepción, Chile.

Two separates sessions were devoted for melt inclusion and crystal host characterizations. The sample holder with the olivine-MI pairs was carefully polished to remove the gold coating and successively was carbon coated. Melt inclusions were analyzed with a defocused electron beam of 10 microns, 15 kV of acceleration voltage and 10 nA of current. The analyzed major and minor elements in the MI's were as follow: $SiO_2$, $TiO_2$, $Al_2O_3$, FeO, MnO, MgO, CaO, $Na_2O$, $K_2O$, $P_2O_5$, S and Cl. Detection limits for K, P and Cl is 160 ppm, and for Na and Cl is 600 and 130 ppm, respectively. Crystal hosts were analyzed with a focused electron beam of 1 µm, 15 kV of acceleration voltage and 10 nA of current. The analyzed major and minor oxides were as follow: $SiO_2$, MgO, FeO, NiO, CaO.

#### 4.2.2.3.- Collection of data by Micro X-ray Absorption Near Edge Structure (µ-XANES)

Micro-XANES data were collected at the Advanced Photon Source (APS) at the Argonne National Laboratory, Chicago, Illinois, United States.

A single session was devoted to the determination of the Fe K-edge, from 7020-7220 eV, using a 2 x 2 µm x-ray beam, on silicate glasses, including melt

inclusions and external glass of the groundmass. Analytical conditions were the same as those of Fiege et al. (2017) for their analytical sessions on APS.

The full µ-XANES spectrum of each unknown sample was carefully examined to assess the potential presence of olivine crystals in the beam path.

#### 4.2.2.4.- Collection of data by Laser Ablation Induced Coupled Plasma Mass Spectrometry (LA-ICP-MS)

Melt inclusions were analyzed at the W.M. Keck Collaboratory for Plasma Spectrometry hosted in the College of Earth, Ocean, and Atmospheric Sciences at Oregon State University, Corvallis, Oregon, United States.

The following elements were measured: Sc, Ti, Ni, Cu, Zn, Rb, Sr, Y, Zr, Nb, Ba, La, Ce, Pr, Nd, Sm, Eu, Gd, Dy, Er, Yb, Hf, Pb, Th and U. Details of the technique and analytical conditions used here were the same as those of Kent et al. (2004).

## 4.3.- Results

### 4.3.1.- Morphology, sizes and volumetric analysis of MI's

The sizes of observed MI's (*n*=47) range between 25 and 220 µm, with most of the inclusions (*n*=41) falling in the range between 25 to 90 µm. In polished samples, the shape of analyzed MI's varies from rounded to rounded-elongated morphologies. A minor group of inclusions (< 5%) presents morphologies different to rounded edges (e.g. straight angular margins), likely due to crepitation or

associated fractures of the host. Low volatile and magnesium contents on those inclusions were indicative of extensive degassing and diffusion, and so, they were discarded from further analysis.

According to literature (Moore et al., 2015 and references therein), melt inclusions maintain a volumetric relation within the associated shrinkage bubble. Their analysis on samples from Kilauea, Fuego and Seguam volcanoes, revealed that most of the inclusions cluster along a line where ~3% of total volume of the inclusion is occupied by the associated bubbles. Robidoux et al. (2018) in samples from San Cristóbal volcano found that bubbles occupied a range between 0.7 to 9 vol%. Our samples show a more scattered data, with most MI-bubble pairs falling between ~2 and ~10 vol% (Fig.4.2). Only 11 MI's exceeded that range, reaching up to 32% in a pair of isolated values. The inclusions that host such high values are not rounded, and so, either relevant post entrapment processes have occurred or they just represent rare inclusions, where vapor and melt were separately trapped.

The broad constant volume proportion of vapor in the MI's as shown in Fig.4.2 indicates that gas bubbles represent volatiles that were originally dissolved in the melt and later exsolved as the inclusion isolates. The isolation and cooling of the inclusion induce decompression due to the differential thermal contraction between the host (almost null) and the glass (comparatively higher); but also emphasized by the post-entrapment crystallization (PEC) of olivine at the

inclusion rim, due to the minor molar volume of olivine components in the crystal compared to the molar volume in the glass (Moore et al., 2015).

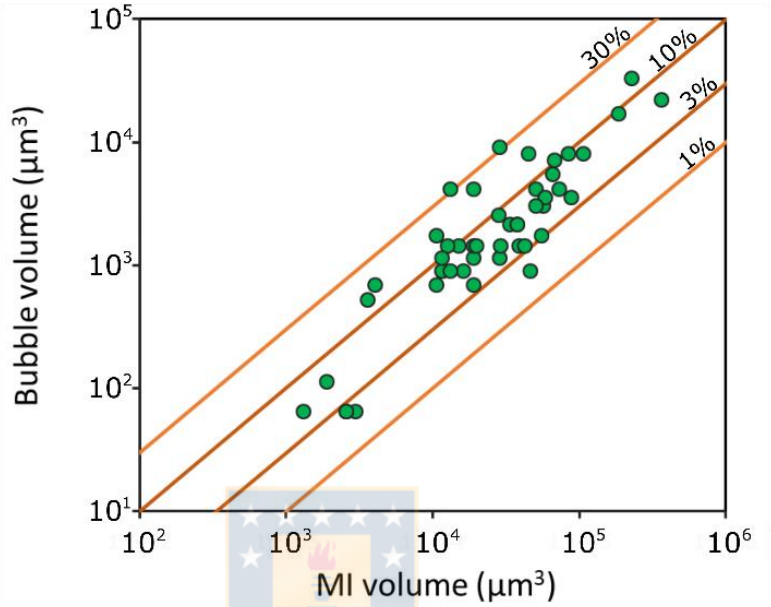


Fig.4.2.- Volumetric relationship between MI and gas bubble with contours of volume percent gas for all the analyzed inclusions of Los Hornitos. Original data of this figure can be found in Table A.4.1.

### 4.3.2.- Volatile contents of glasses determined by SIMS

Twenty-five MI's and twenty-four non-trapped glasses were measured. Included in the last category are melts occurring as channels inside the crystals, reentrants and groundmass. Replicate analysis of two glass check standards FRND-6001 (11) and MRND-7001 (19) yielded analytical uncertainties of 27% for C, 12% for OH, 8% for S, 7% for Cl, 2% for P and 17% for F (respective number of analysis of glass standards in parenthesis; uncertainties calculated from the Variation Coefficient = [standard deviation/average] x 100. Data for standardization curves can be found in Table A.4.2 and A.4.3. Standardization curves for all analyzed

species can be found in Appendix Fig.A.4.1. Measured values on MI's and external glasses can be found in Table A.4.4 and A.4.5, respectively.

**a.- $CO_2$ and $H_2O$:** the two standards glasses used during the analytical session contain 10 and 80 ppm of $CO_2$, which are lower contents compared to those normally observed in melt inclusion suites from arc or MORB tectonic environments (e.g. Wallace et al., 2005). Consequently, retrieved results must be used with caution and only as broad values.

The use of distribution histograms, allow to observe that for both, the MI and external glasses groups, most of the data cluster below 540 ppm of $CO_2$. Additionally, eight MI's and two non-trapped glasses reported values above this limit. These anomalous values observed in MI's scatters between ~1800 to ~26000 ppm. According to the minimum $CO_2$ content estimated for arc magmas of ~3000 ppm (Hilton et al., 2002; Wallace, 2005), I consider the measured values below that limit as geologically meaningful ($n$=20), whereas those higher are interpreted as result of the partial incorporation of C from carbonates precipitated along the bubble-glass transition during the ionization ($n$=5; in the range of ~5700 to 26000 ppm of $CO_2$). By the other hand, the two anomalous values on non-trapped glasses (~4000 and 16000 ppm) could be explained by C contamination from residual diamond suspension used during polishing, and deposited in glass cavities around or inside the crystal due the comparatively softer hardness of glass. Those extremely high values for both MI's and external glasses were considered outliers and discarded from further analysis.

After these considerations, and as expected, the bulk data of MI's distributes towards comparatively higher contents than the external glasses (Fig.4.3). However, the two highest isolated values of external glasses are similar or even slightly higher regarding to $CO_2$ than the top values of MI's. The $CO_2$ contents in MI's ranges between 38 to 2885 ppm, although most of the data contains < 402 ppm of $CO_2$, with a median value of 251 ppm. By the other hand, the median on $CO_2$ contents on external glasses is 90 ppm (*n*=22) with values between 4 to 540 ppm. Excluding the two highest isolated values, the median on external glasses decrease to 76 ppm.

Regarding to $H_2O$, five standards were utilized to construct the calibration curve, obtaining a good correlation line ($R^2$ = 0,95). The highest concentration of $H_2O$ in those standards is 1,98%. Measured contents of $H_2O$ in MI's are systematically higher compared to external glasses. The first group of samples lies between 1,63 and 3,47 wt%, with an average value of 2,60 wt% of $H_2O$ (*n*=25). By the other hand, external glasses range between 0,29 to 0,76 wt%, with an average of 0,58 wt% of $H_2O$ (*n*=24). The variations of $H_2O$-$CO_2$ are shown in Fig.4.3. Note that the $CO_2$ data is shown for values < 600 ppm. A typical degassing curve is fitted for the melt inclusion data, showing that for values > ~3 wt% $H_2O$, the variation of $CO_2$ is considerably larger than does below that limit. This trend is explained by the much lower solubility of $CO_2$ compared to that of $H_2O$ in silicate melts, which results in profuse degassing of $CO_2$ without significant degassing of $H_2O$ (Dixon and Stolper, 1995; Newman et al., 2000). Both species degass progressively

below ~500 ppm $CO_2$. Using the fitted curve allows to calculate that this magma system may have contained 1318 ppm of $CO_2$ at 5 wt% of $H_2O$. Those values are consistent with published data of arc MI's (Wallace, 2005). Regarding the external glasses, there are two different trends. One of these is consistent with the degassing trend of the MI's whereas the different trend, encircled by the ellipse, is characterized by a rapid decrease from 540 to 101 ppm of $CO_2$ at relatively fixed content of 0,7 wt% $H_2O$. The origin of this latter trend is not clear, but it may be related to compositional profiles in embayments, where higher volatile concentrations ($H_2O$, $CO_2$ and S) occur towards the most internal zones of the embayments. This type of features had been described in olivine from Fuego volcano (Lloyd et al., 2014).

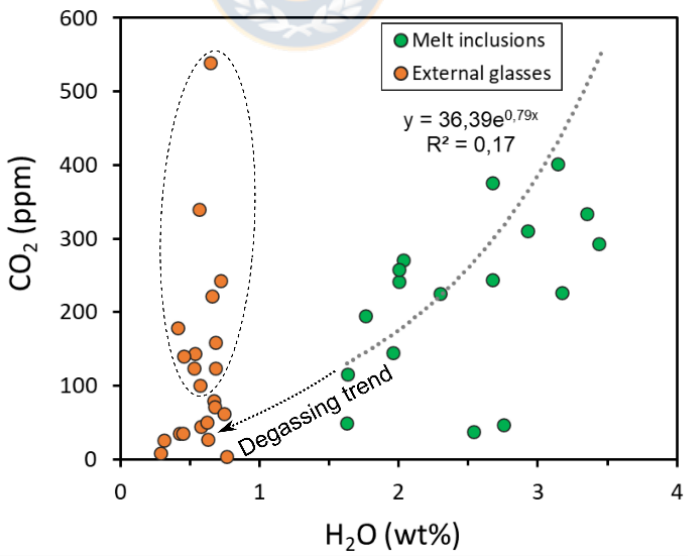


Fig.4.3.- $H_2O$ plotted against $CO_2$ contents obtained by SIMS in both melt inclusions and external glasses. Data from Table A.4.4 and A.4.5. Analytical uncertainties for $H_2O$ and $CO_2$ were 12% and 27%, respectively.

**b.- S and Cl:** Five standards were utilized to construct the calibration curve for S and Cl, reaching a very high correlation for both curves ($R^2$=0,99). The highest concentration of S and Cl in the standards is 950 and 747 ppm, respectively (Fig.A.4.1). Measured values in MI's scatters between 1645 and 5305 ppm of S, with an average value of 3341 ppm (*n*=25), with only five values lower than 3000 ppm (Fig.4.4). Contrastingly, S contents in the external glasses are very low, with values between 4 and 518 ppm (Fig.4.4), with an average of 102 ppm (*n*=24). Regarding Cl, retrieved results on the MI samples report values between 1002 and 1488 ppm of Cl, with an average of 1253 ppm (*n*=25). By the other hand, the external glasses present Cl contents between 272 to 1092 ppm (Fig.4.4), with an average of 790 ppm of Cl (*n*=24).

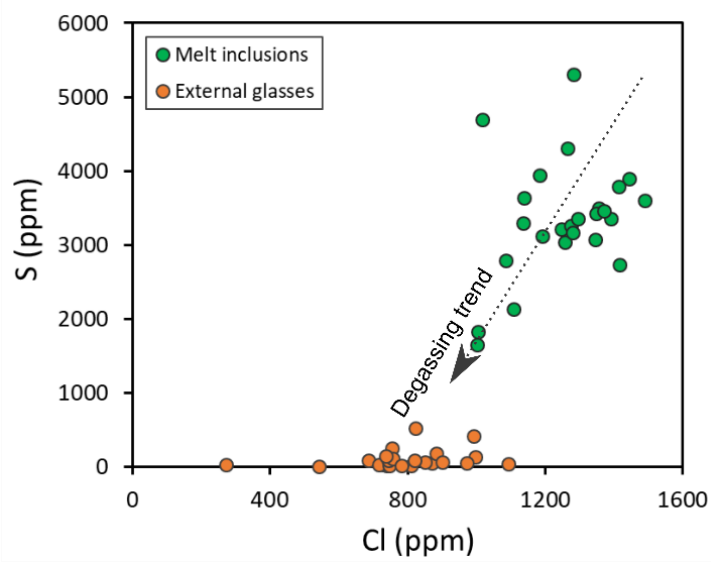


Fig.4.4.- Cl versus S contents obtained by SIMS in both melt inclusions and external glasses. Data from Table A.4.4 and A.4.5. Analytical uncertainties for Cl and S were 7% and 8%, respectively.

The S-Cl variation in the MI's indicates a degassing trend, where high contents of S and Cl (~5000 ppm of S and 1400 ppm of Cl) progressively decrease to lower contents as the host magma ascend from the deep to the mid crust (e.g. barometry results in Chapter 3) and inclusions are trapped at different pressures. By the other hand, the external glasses represent a late stage of evolution, with most of the S degassed from the melt and with a significant amount of Cl remaining in the melt.

**e.- P and F:** Calibration curves for both, P and F, were constructed with 6 glass standards, and yielded $R^2$ values of 0,93 and 0,89, respectively (Fig.A.4.1).

Contents of P and F are broadly similar for both type of glasses (MI's and external glasses). The median value of P in MI's is 683 ppm (*n*=25), for a range of contents between 571 to 870 ppm. In addition, the median value in external glasses is 765 ppm (*n*=24), for a range of contents between 413 to 965 ppm of P (Fig.4.5).

On the other hand, F presents higher contents in MI's (341 to 806 ppm) compared to external glasses (162 to 515 ppm), with median values of 429 and 397, respectively (Fig.4.5).

Compared to the previously described components $CO_2$, $H_2O$, S and Cl, contents of P and F seem unaffected by degassing. In addition, the fact that the broad contents of P in MI's and external glasses are constrained in a limited range of ~600 to 1000 ppm, may indicate that P behaves as mildly compatible, since it is not enriched (i.e. incompatible behavior) or either depleted (i.e. compatible

behavior) in the external glass. This observation is also valid for F variations in MI's and external glasses, with the exception of 6 values of MI's that show higher contents of F and slightly decreased contents of P. This subgroup of MI's may record the crystallization of apatite. Results for all analyzed species can be found in Appendix, Table A.4.4 and A.4.5.

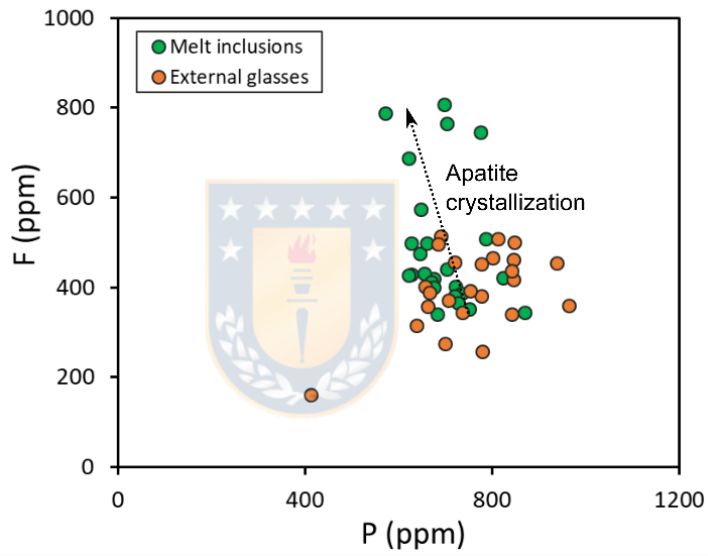


Fig.4.5.- P plotted against F contents obtained by SIMS in both melt inclusions and external glasses. Data from Table A.4.4 and A.4.5. Analytical uncertainties for P and F were 2% and 17%, respectively.

### 4.3.3.- Major and minor elements on silicate glasses and olivine hosts by EPMA

In total, 27 MI's and respective olivine pairs were analyzed (Table A.4.6 in Appendix). Additionally, 27 spots in the matrix glass were executed (Table A.4.7 in Appendix). Averaged internal errors for major and minor elements was less

than 5%, with the exceptions of Ti (5,34%), Mn (53,15%), P (24,07%) and Cl (7,82%). The internal error associated to host olivine measurements, reported averaged values of ~1% for Si, Fe and Mg, 5,0% for Ni and 4,8% for Ca. Replicate analysis (3) of standard glass FRND6001 allowed to determine uncertainties through variations coefficients of <6% for most of the oxides, with the exceptions of $TiO_2$ (11,6%), MnO (15,3%), $Na_2O$ (5,6%) and $P_2O_5$ (19,1%).

The measured (uncorrected) compositions of trapped and non-trapped glasses are sharply distinguishable in different diagrams of major element distribution, as for example those of $SiO_2$, MgO, $K_2O$ (Fig.4.6). While melt inclusions range in a restricted field of silica of 46 to 50 wt% of $SiO_2$, the external glasses encompass a range between ~51 to ~56 wt % of $SiO_2$. The MgO-$SiO_2$ variations in external glasses distribute consistently in values constrained between ~5 to ~6 wt%. Meanwhile, MgO contents in MI's are more scattered, ranging from 4,5 to 8,5 wt% (Fig.4.6a). Some of these data are anomalously low in MgO (< 6% wt%), falling out of the general trend defined by the bulk distributions in trapped and non-trapped glasses (6 MI's outlined by dashed line in Fig.4.6a). Images of the host crystal-melt inclusion pairs of such anomalous values, indicate that they correspond to inclusions with rare shapes, frequently with non-rounded rims, likely due to crepitation, which lately may conduct to Mg diffusion out of the MI, and thus record non-equilibrium compositions. For this reason, such inclusions were discarded of further analysis, leading to a database of 21 MI's that will be corrected for post-trapping modifications in the Section 4.4.1.b.

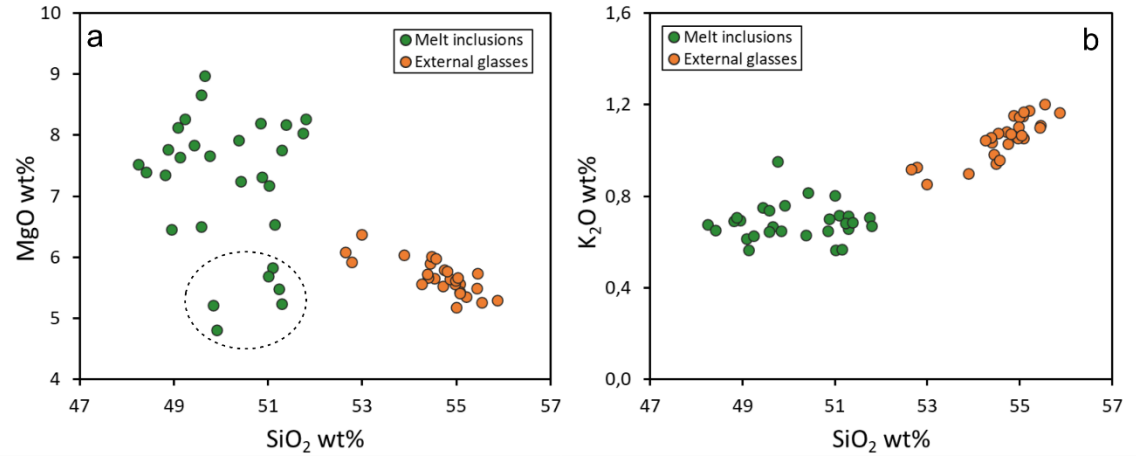


Fig.4.6.- Normalized measured (uncorrected) data on melt inclusions and external glasses. a.- 6 MI's with anomalous low contents of MgO. Those MI's were not considered in the analysis of the data and discussions. b.- $K_2O$ contents higher in the external glasses as expected for incompatibles elements. Measured data can be found in Table A.4.6.

The broad composition of olivine hosts reported Mg and Fe proportions, expressed as forsterite contents, ranging from $Fo_{88}$ to $Fo_{92}$, positively correlated with Ni contents between 990 to 3664 ppm. Compositional data of melt inclusions and olivine pairs, as well as reconstituted MI compositions are reported in Table 4.2 in Section 4.4.1.

Sulfur was measured on the sulphate peak position and was standardized on $CaSO_4$. Both S and Cl were measured by EPMA and SIMS, with excellent correlation for S ($R^2$ value of 0.99) and with a moderate correspondence for Cl ($R^2$ value of 0,54) but a consistent slope offset of 1,5 for S and 0,87 for Cl (Figure 4.7).

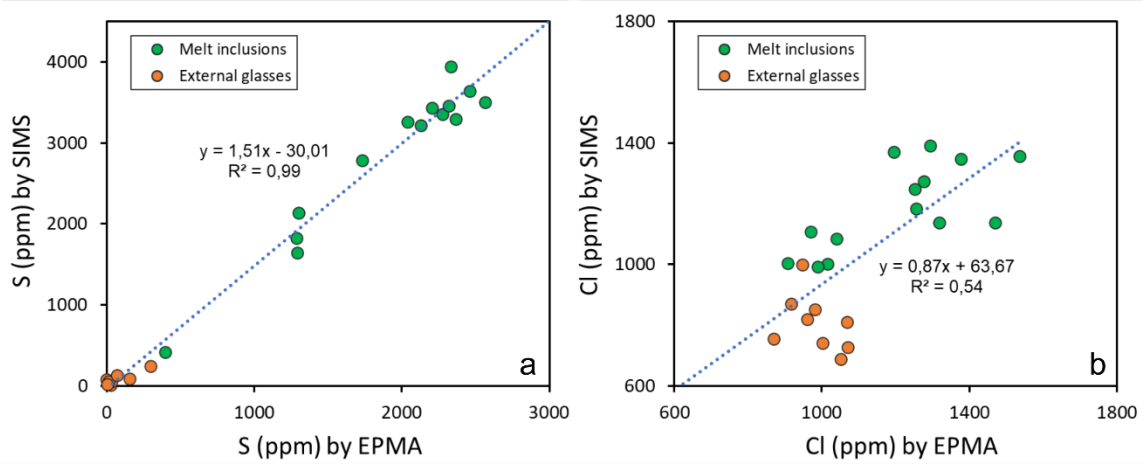


Fig.4.7.- Comparison of S (a) and Cl (b) measured by EPMA versus SIMS. Data from Tables A.4.4, A.4.5, A.4.6 and A.4.7.

### 4.3.4.- $Fe^{3+}/\Sigma Fe$ on silicate glasses by μ-XANES

In total, 118 spots of data were collected, including 65 on MI's and 53 in the external glass of the groundmass. During the analytical session 12 standard glasses were measured in duplicates. For all duplicates, the standard deviation reported excellent reproducibility with the exceptions of standards REV-1 and REV-3 (Table A.4.8 in Appendix) and were discarded for calibrations. The accuracy of determined centroid positions present a systematic overestimation of ~0.1078 eV regarding the centroid positions reported by Fiege et al. (2017) for all the same standard glasses measured in the same synchrotron line. By this reason, data were corrected by subtracting 0.1078 eV. Consecutively, the Equation 6 of Fiege et al. (2017), which is specific for basaltic glasses, was applied to the centroid positions in order to obtain the $Fe^{3+}/\Sigma Fe$ of the samples. That equation consists of a polynomial arrange that includes determinations of centroid positions of basaltic glasses in four different syncrothron lines, including

ANKA (Germany), APS (United States), DESY (Germany) and ESRF (France) (Fiege et al., 2017; Giuli et al., 2011; Wilke et al., 2004).

The full µ-XANES spectrum of each unknown sample was carefully examined to assess the potential presence of olivine crystals in the beam path. The broad plateau of Fe absorption at high energy develops significant structure when crystals are in the beam path, and the influence of olivine in the spectra is readily identified. After the evaluation of olivine contamination in retrieved spectra, only 13 melt inclusions reported clean data, which correspond to the 20% of the initial data. Regarding external glasses, 22 spots reported clear beam paths, which correspond to 42% of the initial data. The values for both the MI's and external glasses can be found in Table A.4.9 Appendix.

Complete µ-XANES spectra and close-up views of the pre-edge region for selected MI's are shown in Figure 8.

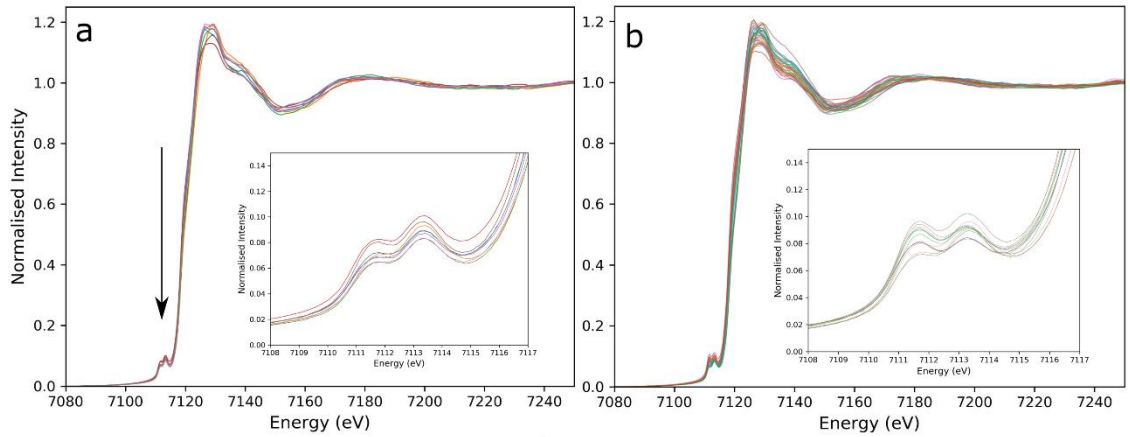


Fig.4.8.- Full spectra and close-up to the pre-edge region for a.- selected melt inclusions uncontaminated with olivine host (*n*=8) and discussed through the text. b.- all spectra uncontaminated by crystal along the beam path (*n*=35). Black arrow in (a) indicate the pre-edge region. Centroid position for MI's and external glasses can be found in Table A.4.9.

For melt inclusions, the averaged measured value ($n$=13) of $Fe^{3+}/\Sigma Fe$ is 0,34, within an entire range from 0,28 to 0,40. By the other hand, external glasses reported comparatively lower values, with $Fe^{3+}/\Sigma Fe$ in the range of 0,21 to 0,33, and an average value of 0,25 ($n$=22). Results for reconstructed MI's can be found in Table 4.2 (Section 4.4.1).

### 4.3.5.- Trace elements in melt inclusions by LA-ICP-MS

In total, 73 melt inclusions were analyzed, and duplicated measurements were carried out on three selected MI's. During the analytical session, the standard glasses BHVO-2G (5) and GSE-1G (12) were measured in replicates. Determination of analytic error ($E_A$) in standard glasses by Equation 1, retrieved uncertainties <12,6% for all the analyzed elements. Duplicates in MI's retrieved uncertainties of 93% for Ni and 44% for Zn. Considering the respective high and moderate partitioning of these elements in olivine (e.g. Straub et al., 2008; Ewart and Griffin, 1994), such high uncertainties values are due the partial incorporation of the olivine host during the ablation. Uncertainties were <15% for the elements Sc, Cu, Rb, Sr, Y, Zr, Ba, La, Ce, Pr, Nd, Gd, Er, Pb, Th and U. In addition, Nb, Sm, Eu, Dy, Yb and Hf have uncertainties between 18% and 34%. These moderately high values are explained by the low concentrations of these elements in the sample (< 4 ppm), which cause larger uncertainties when the standard deviation reaches values close to the average.

Trace element contents for reconstructed MI's can be found in Appendix Table A.4.10.

$$E_A = \sqrt{\frac{CV_{std1}^2 + CV_{std2}^2}{2}}$$ Equation 1;

where CV corresponds to the variation coefficient given by StdDev/Average.

Among the total analyzed MI's (*n*=73), a subgroup of 15 MI's were also analyzed by EPMA, and therefore the trace element composition of these MI's was internally standardized with the CaO content of each inclusion measured by EPMA. Those inclusions are listed in Table A.4.10. The other 58 spots of laser were sampled in MI's that were not analyzed by EPMA, and therefore, I used the measured averaged value of CaO to provide a mean to estimate the trace element component (Table A.4.11).

The trace element composition normalized to the primitive mantle (McDonough and Sun, 1995) of MI's and 9 whole-rock analysis of tephras (Appendix Table A.4.12) is shown in Fig.4.9. All the analyzed MI's display distribution patterns that are consistent with the whole-rock composition. These variations are typical of arc magmas and differ systematically with the normalized N-MORB distribution patterns. The most significative features of the trace element patterns are made up by the strong positive anomalies of Pb and Sr, and the negative Nb anomalies, similar to those reported by Schmidt and Jagoutz 2017 for primitive arc basalts.

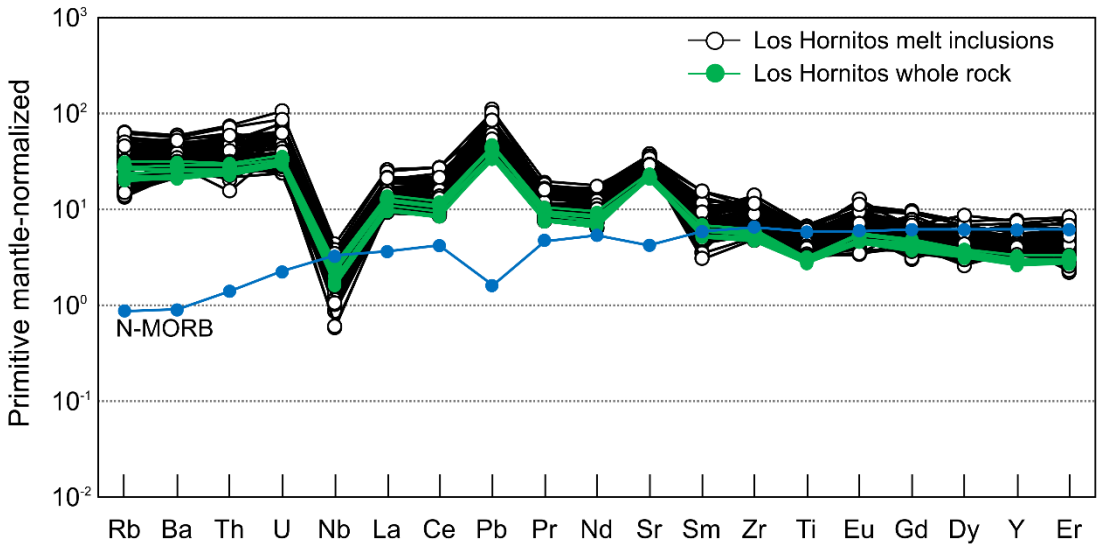


Fig.4.9.- Trace element composition normalized to the primitive mantle for all analyzed melt inclusions (*n*=73) and whole-rock analysis of tephra from Los Hornitos. In addition, the distribution patterns of N-MORB normalized to the primitive mantle is shown as reference.

Finally, note that despite of the relatively large amount of individual analyses per microanalytical technique (25 by SIMS, 27 by EPMA, 65 by µ-XANES and 73 by LA-ICP-MS), the filtering of the data and the crossing of different data sources, reduces significantly the amount of multi-sourced results for a single melt inclusion. In the incoming chapter, I describe the correction of measured values in MI's and integrate the different sources of data.

## 4.4.- Data treatment to reconstruct the original composition of melt inclusions

Corrected compositions of MI's are listed in Table 4.2. For clarity the measured compositions of MI's and the forsterite content of the hosts are included in the same table. The correction procedure is detailed next.

The correction procedure begins with the test of equilibrium between the MI and its respective host (Fig.4.11). This equilibrium test helps to identify the more modified compositions of MI's, affected by post-entrapment modifications (PEC and/or Fe loss) and allow a broad estimation of the degree of olivine addition to reach-back equilibrium (Fig.4.11a). By the other hand, including the whole-rock data into the analysis allow to determine the degree of Fe-loss from the inclusion to the host olivine (Fig.4.11b). See details below.

### 4.4.1.- Testing the equilibrium between trapped melts and its olivine host

Melt inclusions are trapped in olivine phenocrysts at high temperatures, so as the MI and host cool down during the magmatic ascent and eruption, olivine may crystallize along the rim of the inclusion during post-entrapment crystallization. Additionally, the residual melt may be prone to experience diffusion of $Fe^{+2}$ out of the inclusion in a process referred to as "Fe-loss" (Danyushevsky et al., 2000).

Testing the equilibrium between MI and its olivine host is necessary to proceed as follow. According to Roeder & Emslie (1970) the molar relation (Fe/Mg) on olivine divided by (Fe/Mg) on the melt equals to 0,3 for an olivine in equilibrium with its parental melt ($Kd_{ol/melt} = (Fe/Mg)_m$ Ol/$(Fe/Mg)_m$ Melt = 0.3). Establishing this relation requires separating the FeOt measured by EPMA (where FeOt

corresponds to FeO total = $Fe_2O_3$ + FeO; expressed as FeO) into $Fe_2O_3$ and FeO in each inclusion using the $Fe^{3+}/\Sigma Fe$ measured by µ-XANES.

Among the suitable MI's analyzed by EPMA (*n*=21), only eight of those reported robust $Fe^{3+}/\Sigma Fe$ determinations (Fig.4.8a and Table 4.1). In order to provide a mean to estimate the "measured" redox conditions for inclusions only analyzed by EPMA, a statistical analysis of that paired data (i.e. $Fe^{3+}/\Sigma Fe$ versus EPMA data) allowed to determine that $SO_3$ and MgO presented the highest correlation values with $Fe^{3+}/\Sigma Fe$ (Pearson coefficients of 0,63 and 0,62, respectively, Table A.4.13).

Table 4.1: Measured $Fe^{3+}/\Sigma Fe$ and $SO_3$/MgO ratio on the 8 inclusions analyzed by µ-XANES and EPMA. Complete measured and corrected data for melt inclusion composition can be found in Table 2.

| Olivine – MI pair | Measured $Fe^{+3}/\Sigma Fe$ | $SO_3$/MgO |
|---|---|---|
| OL_82inc.1 | 0.34 ± 0.029 | 0,065 ± 0.0016 |
| OL_82inc.2 | 0.34 ± 0.029 | 0,070 ± 0.0017 |
| OL_100inc.1 | 0.33 ± 0.032 | 0,041 ± 0.0010 |
| OL_107inc.1 | 0.32 ± 0.036 | 0,046 ± 0.0011 |
| OL_122inc.1 | 0.32 ± 0.035 | 0,042 ± 0.0010 |
| OL_125inc.1 | 0.39 ± 0.016 | 0,076 ± 0.0018 |
| OL_133inc.1 | 0.31 ± 0.037 | 0,051 ± 0.0012 |
| OL_137inc.1 | 0,37 ± 0.022 | 0,062 ± 0.0015 |

Thus, the incorporation of the $SO_3$/MgO ratio (Table 4.1) provide a way to determine an estimated value of $Fe^{3+}/\Sigma Fe$ for inclusions not analyzed via µ-XANES, through the equation $Fe^{3+}/\Sigma Fe = 1,57 \times SO_3/MgO + 0,25$ (Fig.4.10; $R^2$= 0,62). Fig.4.10b show the relation between calculated versus measured Fe speciation. Points falling above the 1:1 line evidence a subestimation of the calculated $Fe^{3+}/\Sigma Fe$, whereas those falling below overestimate the Fe ratio.

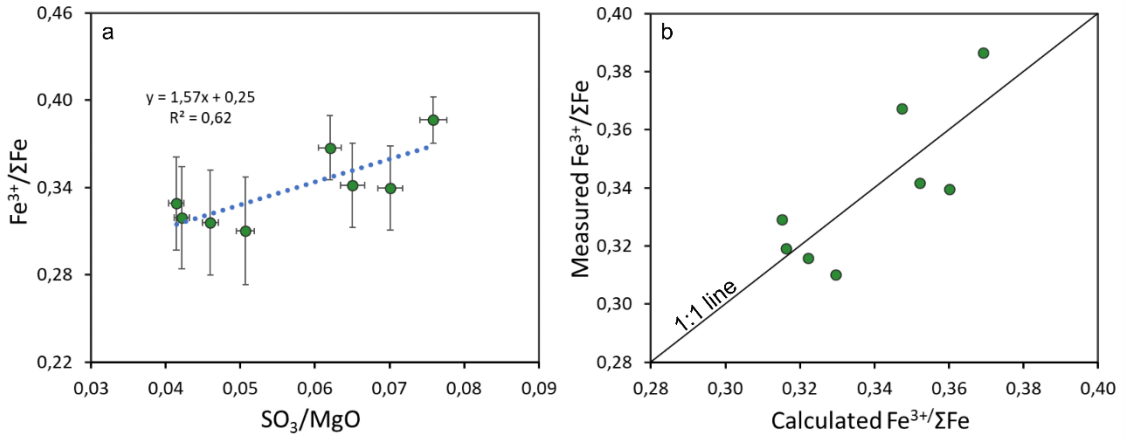


Fig.4.10.- a.- Lineal arrange between $SO_3$/MgO determined by EPMA versus $Fe^{3+}/\Sigma Fe$ determined by µ-XANES, allowing to estimate the Fe speciation for inclusions not analyzed by µ-XANES. Data from Table 4.1. b.- Calculated $Fe^{3+}/\Sigma Fe$ from the lineal arrange versus the measured $Fe^{3+}/\Sigma Fe$. For reference, the 1:1 line is shown. For all the inclusions, the difference between the measured and the calculated value of $Fe^{3+}/\Sigma Fe$ is < ± 0.002.

The application of this model allows to estimate a value of $Fe^{3+}/\Sigma Fe$ to inclusions not analyzed by µ-XANES, and thus establishing the equilibrium test for 21 inclusions in total (Table A.4.6 Appendix), showed in Fig.4.11a. This diagram shows the relation between the composition of the olivine host and the olivine that is in equilibrium with the measured composition of the MI. Note that this relation should be 1:1 when equilibrium between the MI and the host occurs. Calculated values of Fo from the MI composition that plots above the 1:1 line are interpreted to result due diffusion of $Fe^{+2}$ out of the inclusion, yielding increased calculated Fo. By the other hand, calculated values of Fo that fall below the 1:1 line represent crystallization of olivine inside the inclusion rim (PEC), although additional partial re-equilibration of $Fe^{+2}$ cannot be discarded.

Furthermore, given the highly magnesian character of the studied olivine hosts, the composition of the trapped glasses is prone to experience $Fe^{+2}$ re-

equilibration. This can be observed in Fig.4.11b, where the melts trapped in the most magnesian crystals are the more depleted in FeOt, conforming a trend of progressive enrichment in FeO as Fo of the host decreases. Importantly, this trend is not coherent with FeOt evolution in calc-alkaline magmas, where early it behaves as compatible. The observed trend is comparable to those described by Danyushevsky et al. (2000) for different suites of MI's hosted in magnesian hosts, where the term "Fe-loss" was introduced. According to Danyushevsky and Plechov (2011), the Fe-loss process can be reversed through the determination of proper FeOt contents, provided by the whole-rock data (blue line in Fig.4.11.b).

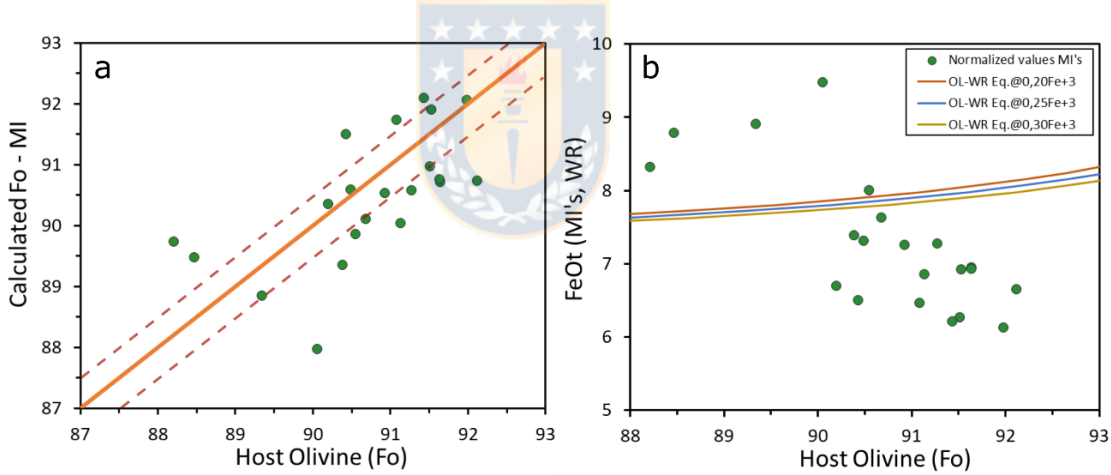


Fig.4.11. a.- Equilibrium test between Fo (host) compared with calculated Fo from MI's. Note that the 1:1 line correspond to the equilibrium. Red dashed lines represent the propagation of error on Mg# from uncertainties on EPMA measurement of FeO and MgO. b.- Different degrees of $Fe^{+2}$ re-equilibrium during Fe-loss experienced by MI's. Note the broad trend of higher degrees of re-equilibrium of inclusions hosted by the more forsteritic crystals. Data from Table 4.2.

Thus, the inclusions will be corrected by PEC and Fe-loss, providing the FeOt contents of the whole rock data from lava and tephra compositions published in Salas et al. (2016). Some of the inclusions indicate approximate equilibrium with their olivine hosts (Fig.4.11) and the magnitude of post-entrapment modifications

will be small. Four samples that falls above the equilibrium line described by the whole-rock data (upper data points in Fig.4.11b) were excluded for further analysis given the anomalous high contents of FeOt, yielding a database conformed by 17 inclusions for further corrections. Those inclusions are listed in Table 4.2.

### 4.4.2.- Post-entrapment corrections of melt inclusion compositions

Measured composition of MI's were normalized including S and Cl measured by EPMA and $H_2O$ via SIMS. The averaged measured $H_2O$ content was used for inclusions that were not analyzed by SIMS. The PEC and Fe-loss corrections were determined using Petrolog 3 (Danyushevsky and Plechov 2011), which incorporates increments of 0,01% of calculated olivine back to the MI until equilibrium between the host and the melt is achieved. During the calculations, a $Kd_{ol/melt}$ equals to 0,3 (Roeder and Emslie, 1970) and the olivine model of Putirka (2005) were considered. Additionally, the system was considered closed for oxygen, and thus $Fe^{3+}$ behaves as an incompatible element.

Fig.4.11b shows that the higher the Fo content of the host, the larger the degree of $Fe^{+2}$ disequilibrium in the MI. Then, inclusions were corrected accordingly by the addition of $Fe^{+2}$ (reported as FeO in Table 2). By the other hand, the 6 inclusions falling closer to the equilibrium line (Fig.4.11b) are modelled as only experiencing PEC, and correction proceed by the addition of olivine (See Danyushevsky et al., 2000 and Danyushevsky and Plechov, 2011 for details on correction process).

Table 4.2: Measured EPMA and corrected compositions of 17 MI's analyzed. (1)$H_2O$ by SIMS; (c)calculated; (m)measured

| *Measured glass inclusion* | | OL_58 inc.1 | OL_82 inc.1 | OL_82 inc.2 | OL_86 inc.1 | OL_87 inc.1b | OL_100 inc.1 | OL_106 inc.1 | OL_107 inc.1 | OL_110 inc.2 |
|---|---|---|---|---|---|---|---|---|---|---|
| $SiO_2$ | wt% | 46,83 | 48,55 | 47,78 | 47,34 | 47,53 | 49,94 | 46,86 | 48,77 | 46,04 |
| $TiO_2$ | wt% | 0,74 | 0,76 | 0,71 | 0,77 | 0,72 | 0,72 | 0,74 | 0,79 | 0,71 |
| $Al_2O_3$ | wt% | 15,93 | 16,04 | 15,58 | 17,21 | 15,25 | 15,87 | 16,35 | 16,77 | 17,29 |
| FeO* | wt% | 6,70 | 6,36 | 7,03 | 7,20 | 6,38 | 7,18 | 7,86 | 6,73 | 5,93 |
| FeO | wt% | 4,28 | 4,19 | 4,64 | 4,40 | 3,68 | 4,82 | 4,99 | 4,60 | 3,60 |
| $Fe_2O_3$ | wt% | 2,69 | 2,41 | 2,65 | 3,11 | 3,00 | 2,63 | 3,19 | 2,36 | 2,59 |
| MnO | wt% | 0,07 | 0,09 | 0,05 | 0,08 | 0,13 | 0,07 | 0,14 | 0,11 | 0,06 |
| MgO | wt% | 8,18 | 7,82 | 7,51 | 6,21 | 6,07 | 7,75 | 7,45 | 7,01 | 7,03 |
| CaO | wt% | 12,18 | 11,91 | 12,40 | 12,62 | 13,07 | 11,33 | 12,18 | 12,20 | 13,94 |
| $Na_2O$ | wt% | 2,42 | 2,56 | 2,40 | 2,49 | 2,32 | 2,48 | 2,86 | 3,00 | 2,55 |
| $K_2O$ | wt% | 0,61 | 0,62 | 0,60 | 0,71 | 0,53 | 0,68 | 0,68 | 0,79 | 0,62 |
| $P_2O_5$ | wt% | 0,11 | 0,15 | 0,15 | 0,16 | 0,13 | 0,07 | 0,10 | 0,13 | 0,14 |
| $SO_3$ | wt% | 0,58 | 0,51 | 0,53 | 0,55 | 0,67 | 0,32 | 0,55 | 0,32 | 0,64 |
| Cl | wt% | 0,12 | 0,13 | 0,12 | 0,14 | 0,13 | 0,09 | 0,13 | 0,10 | 0,15 |
| Total | wt% | 94,46 | 95,49 | 94,86 | 95,48 | 92,94 | 96,51 | 95,89 | 96,73 | 95,11 |
| $H_2O^{(1)}$ | wt% | 2,68 | 3,17 | 2,00 | 2,29 | 3,35 | 2,54 | 2,60 | 1,63 | 2,03 |
| $Fe^{3+}/\Sigma Fe$ | | 0,36(c) | 0,34(m) | 0,34(m) | 0,39(c) | 0,42(c) | 0,33(m) | 0,36(c) | 0,32(m) | 0,39(c) |
| Equil. Fo | | 91,91 | 91,73 | 90,58 | 89,35 | 90,73 | 90,53 | 89,87 | 90,05 | 92,07 |
| Host Fo | | 91,53 | 91,08 | 91,27 | 90,38 | 92,11 | 90,92 | 90,55 | 91,13 | 91,98 |
| *Post-entrapment corrected glass* | | | | | | | | | | |
| *Olivine added (%)* | | | | 6,07 | 4,52 | | 4,89 | -0,67 | | |
| *$Fe^{+2}$ added (wt% FeO)* | | 1,05 | 1,44 | | | 1,41 | | | 1,06 | 1,91 |
| $SiO_2$ | wt% | 47,75 | 48,49 | 48,87 | 48,17 | 48,25 | 49,95 | 47,73 | 48,73 | 46,43 |
| $TiO_2$ | wt% | 0,71 | 0,71 | 0,69 | 0,75 | 0,65 | 0,69 | 0,75 | 0,74 | 0,64 |
| $Al_2O_3$ | wt% | 15,46 | 15,08 | 15,18 | 16,87 | 13,87 | 15,26 | 16,56 | 15,54 | 15,59 |
| FeO* | wt% | 7,96 | 7,91 | 7,93 | 7,83 | 8,05 | 7,89 | 7,85 | 7,92 | 8,03 |
| FeO | wt% | 5,61 | 5,87 | 5,60 | 5,07 | 5,60 | 5,62 | 4,95 | 5,95 | 5,92 |
| $Fe_2O_3$ | wt% | 2,61 | 2,27 | 2,59 | 3,06 | 2,73 | 2,53 | 3,23 | 2,19 | 2,34 |
| MnO | wt% | 0,07 | 0,08 | 0,05 | 0,08 | 0,12 | 0,07 | 0,14 | 0,10 | 0,05 |
| MgO | wt% | 10,20 | 10,08 | 9,85 | 8,02 | 10,99 | 9,46 | 7,98 | 10,29 | 11,43 |
| CaO | wt% | 11,82 | 11,20 | 12,07 | 12,37 | 11,89 | 10,90 | 12,33 | 11,31 | 12,57 |
| $Na_2O$ | wt% | 2,35 | 2,40 | 2,34 | 2,45 | 2,11 | 2,39 | 2,89 | 2,78 | 2,30 |
| $K_2O$ | wt% | 0,59 | 0,58 | 0,58 | 0,69 | 0,48 | 0,66 | 0,69 | 0,73 | 0,56 |
| $P_2O_5$ | wt% | 0,11 | 0,14 | 0,15 | 0,16 | 0,12 | 0,07 | 0,10 | 0,12 | 0,13 |
| $H_2O$ | wt% | 2,6 | 2,98 | 1,95 | 2,24 | 3,04 | 2,44 | 2,63 | 1,51 | 1,83 |
| S | ppm | 2397 | 2071 | 2183 | 2264 | 2787 | 1301 | 2223 | 1315 | 2648 |
| Cl | ppm | 1235 | 1298 | 1243 | 1413 | 1356 | 917 | 1341 | 1034 | 1587 |
| $Fe^{3+}/\Sigma Fe$ | | 0,30 | 0,26 | 0,29 | 0,35 | 0,31 | 0,29 | 0,37 | 0,25 | 0,26 |
| T° C | | 1228 | 1223 | 1234 | 1183 | 1235 | 1242 | 1179 | 1256 | 1268 |
| ΔNNO@T° & 1 GPa | | 1,59 | 1,22 | 1,56 | 2,09 | 1,69 | 1,58 | 2,19 | 1,08 | 1,22 |
| ΔNNO@1250°C & 1 GPa | | 1,60 | 1,23 | 1,57 | 2,13 | 1,70 | 1,59 | 2,24 | 1,07 | 1,21 |
| ΔNNO@1000°C & 0,5 GPa | | 1,00 | 0,62 | 0,96 | 1,53 | 1,09 | 0,98 | 1,63 | 0,46 | 0,60 |

Continued Table 4.2

| *Measured glass inclusion* | | OL_115 inc.1 | OL_119 inc.1 | OL_120 inc.1 | OL_122 inc.1 | OL_124 inc.3 | OL_125 inc.1 | OL_130 inc.1 | OL_135 inc.1 |
|---|---|---|---|---|---|---|---|---|---|
| $SiO_2$ | wt% | 46,56 | 48,50 | 47,66 | 48,45 | 47,04 | 48,75 | 46,92 | 47,32 |
| $TiO_2$ | wt% | 0,76 | 0,74 | 0,79 | 0,64 | 0,70 | 0,67 | 0,78 | 0,73 |
| $Al_2O_3$ | wt% | 16,79 | 16,58 | 17,36 | 15,26 | 16,54 | 15,84 | 17,82 | 17,90 |
| FeO* | wt% | 6,77 | 6,59 | 6,12 | 7,39 | 7,17 | 6,80 | 6,43 | 6,20 |
| FeO | wt% | 4,24 | 4,42 | 3,85 | 5,03 | 4,51 | 4,17 | 4,04 | 3,68 |
| $Fe_2O_3$ | wt% | 2,81 | 2,41 | 2,52 | 2,62 | 2,95 | 2,92 | 2,66 | 2,80 |
| MnO | wt% | 0,13 | 0,05 | 0,05 | 0,14 | 0,12 | 0,12 | 0,14 | 0,07 |
| MgO | wt% | 7,01 | 6,97 | 7,55 | 7,71 | 7,31 | 6,86 | 7,32 | 6,24 |
| CaO | wt% | 12,94 | 11,87 | 12,41 | 11,00 | 13,02 | 12,94 | 13,62 | 13,77 |
| $Na_2O$ | wt% | 2,95 | 2,78 | 2,93 | 2,49 | 2,51 | 2,26 | 2,74 | 2,90 |
| $K_2O$ | wt% | 0,66 | 0,67 | 0,72 | 0,65 | 0,54 | 0,54 | 0,66 | 0,67 |
| $P_2O_5$ | wt% | 0,17 | 0,13 | 0,11 | 0,14 | 0,12 | 0,13 | 0,12 | 0,12 |
| $SO_3$ | wt% | 0,55 | 0,35 | 0,58 | 0,33 | 0,56 | 0,52 | 0,57 | 0,62 |
| Cl | wt% | 0,10 | 0,11 | 0,13 | 0,10 | 0,12 | 0,12 | 0,13 | 0,14 |
| Total | wt% | 95,39 | 95,35 | 96,41 | 94,29 | 95,76 | 95,55 | 97,25 | 96,68 |
| $H_2O^{(1)}$ | wt% | 2,60 | 3,23 | 2,35 | 2,76 | 2,93 | 2,60 | 2,00 | 2,60 |
| $Fe^{3+}/\Sigma Fe$ | | $0,37^{(c)}$ | $0,33^{(c)}$ | $0,37^{(c)}$ | $0,32^{(m)}$ | $0,37^{(c)}$ | $0,39^{(m)}$ | $0,37^{(c)}$ | $0,41^{(c)}$ |
| Equil. Fo | | 90,76 | 90,35 | 92,10 | 90,10 | 90,59 | 90,71 | 91,50 | 90,97 |
| Host Fo | | 91,64 | 90,19 | 91,43 | 90,68 | 90,48 | 91,64 | 90,43 | 91,51 |
| *Post-entrapment corrected glass* | | | | | | | | | |
| *Olivine added (%)* | | | | | 2,83 | 2,82 | | | |
| *$Fe^{+2}$ added (wt% FeO)* | | 1,05 | 1,11 | 1,74 | | | 1,03 | 1,33 | 1,70 |
| $SiO_2$ | wt% | 46,89 | 48,61 | 47,43 | 49,72 | 47,70 | 48,85 | 46,85 | 46,75 |
| $TiO_2$ | wt% | 0,71 | 0,71 | 0,72 | 0,64 | 0,70 | 0,63 | 0,75 | 0,64 |
| $Al_2O_3$ | wt% | 15,62 | 15,83 | 15,94 | 15,31 | 16,37 | 14,72 | 17,01 | 15,95 |
| FeO* | wt% | 7,98 | 7,81 | 7,95 | 7,86 | 7,84 | 7,98 | 7,82 | 7,96 |
| FeO | wt% | 5,62 | 5,74 | 5,87 | 5,49 | 5,21 | 5,54 | 5,54 | 5,72 |
| $Fe_2O_3$ | wt% | 2,62 | 2,30 | 2,31 | 2,63 | 2,92 | 2,71 | 2,54 | 2,49 |
| MnO | wt% | 0,12 | 0,06 | 0,05 | 0,14 | 0,12 | 0,12 | 0,13 | 0,06 |
| MgO | wt% | 10,37 | 8,89 | 10,53 | 8,99 | 8,33 | 10,22 | 8,81 | 10,37 |
| CaO | wt% | 12,04 | 11,34 | 11,40 | 11,04 | 12,89 | 12,02 | 13,00 | 12,26 |
| $Na_2O$ | wt% | 2,75 | 2,65 | 2,68 | 2,51 | 2,48 | 2,10 | 2,62 | 2,58 |
| $K_2O$ | wt% | 0,61 | 0,64 | 0,66 | 0,65 | 0,53 | 0,50 | 0,62 | 0,60 |
| $P_2O_5$ | wt% | 0,16 | 0,13 | 0,10 | 0,14 | 0,12 | 0,12 | 0,11 | 0,11 |
| $H_2O^{(2)}$ | wt% | 2,42 | 3,08 | 2,16 | 2,77 | 2,57 | 2,42 | 1,91 | 2,32 |
| S | ppm | 2261 | 1425 | 2368 | 1344 | 2297 | 2129 | 2299 | 2518 |
| Cl | ppm | 1067 | 1083 | 1275 | 1001 | 1230 | 1197 | 1307 | 1465 |
| $Fe^{3+}/\Sigma Fe$ | | 0,30 | 0,26 | 0,26 | 0,30 | 0,34 | 0,31 | 0,29 | 0,28 |
| T° C | | 1237 | 1196 | 1248 | 1201 | 1185 | 1230 | 1209 | 1237 |
| ΔNNO@T° & 1 GPa | | 1,54 | 1,24 | 1,24 | 1,66 | 1,89 | 1,71 | 1,44 | 1,40 |
| ΔNNO@1250°C & 1 GPa | | 1,54 | 1,27 | 1,24 | 1,69 | 1,93 | 1,72 | 1,47 | 1,41 |
| ΔNNO@1000°C & 0,5 GPa | | 0,93 | 0,66 | 0,63 | 1,08 | 1,32 | 1,11 | 0,86 | 0,80 |

Results after PEC correction shows that MI's required less than ~6% of olivine back to the inclusions to achieve equilibrium (Table 4.2). By the other hand, inclusions experiencing Fe-loss needed < 1,9 wt% of FeO to be added and reach equilibrium (Table 4.2). Those values are comparable to correction values reported by other authors (Kelley and Cottrell, 2009; Lloyd et al., 2012; Brounce et al., 2014; Robidoux et al., 2017). The magnitude of post-entrapment modifications produced a difference of less than ~30% with respect to the measured $Fe^{3+}/\Sigma Fe$.

### 4.4.3.- Corrected compositions of melt inclusions

The $Fe^{3+}/\Sigma Fe$ ratios of Los Hornitos melt inclusions present a mostly invariant to a slightly increasing pattern along the differentiation segment between ~9 to ~11 wt% of MgO, within a $Fe^{3+}/\Sigma Fe$ range of 0,25 to 0,31. However, three more oxidized inclusions occurs at MgO < 9 wt%, covering a range of $Fe^{3+}/\Sigma Fe$ of 0,34 to 0,37, conforming a separated trend (Fig.4.12a). The related co-variation of FeO ($Fe^{+2}$ expressed as FeO) with MgO during differentiation results of olivine fractionation (Fig.4.12b). Magnetite saturation were not reached by the magma, as noted by the incompatible behavior of $Fe^{3+}$, as well as $TiO_2$ (Fig.4.12c and d). Note the subset at <9 wt% of MgO presenting depleted and enriched contents of FeO and $Fe_2O_3$, respectively in Fig.4.12 b and c. The incompatible character of $Al_2O_3$ indicate that plagioclase has not reached saturation (Fig.4.12e), however, note that the incompatible trend is highly controlled by two extreme values at MgO

~11 and ~9 wt% with comparatively lower and higher values of $Al_2O_3$ (black arrows in Fig.4.12e), respectively. Excluding that values, the aluminum contents are nearly invariant along differentiation. A mildly compatible behavior of this oxide may result of co-crystallizing Cr-Spinels that contain ~16 to 20 wt% of $Al_2O_3$ (Table A.3.3 Appendix of Chapter 3). The $CaO/Al_2O_3$ ratio remains nearly constant between 0,7 and 0,8 along differentiation and is mostly shifted by the scattered data of CaO (Fig.4.12f and g), however a minor precipitation of clinopyroxene cannot be discarded. $K_2O$ and $Na_2O$ slightly increases along the restricted differentiation window recorded by the trapped melts, showing its incompatible character (Fig.4.12h and i). $P_2O_5$ remains nearly constant along the differentiation (Fig.4.12j).

Note that the subset of 3 MI's with the higher $Fe^{3+}/\Sigma Fe$ are depleted in FeO and enriched in $Fe_2O_3$, but also present higher anomalous contents of $Al_2O_3$ and CaO. Fig.4.13a show the variation of MgO along $SiO_2$ as a proxy of differentiation, and reveals that for ~48% $SiO_2$ the subset of MI's is > ~1 wt% lower compared to the trend displayed by the broader group of MI's. In adittion, the variation of $Fe^{3+}/\Sigma Fe$, MgO and FeO ($Fe^{2+}$) along temperature is plotted in Fig.4.13 b, c, d, respectively, and show that the low Mg-Fe subset of MI's were trapped at relatively low temperatures (T° C < 1185) whereas the others were trapped in the range 1196 to 1268°C. Therefore, the former subgroup will be referred to as the "low temperature subset".

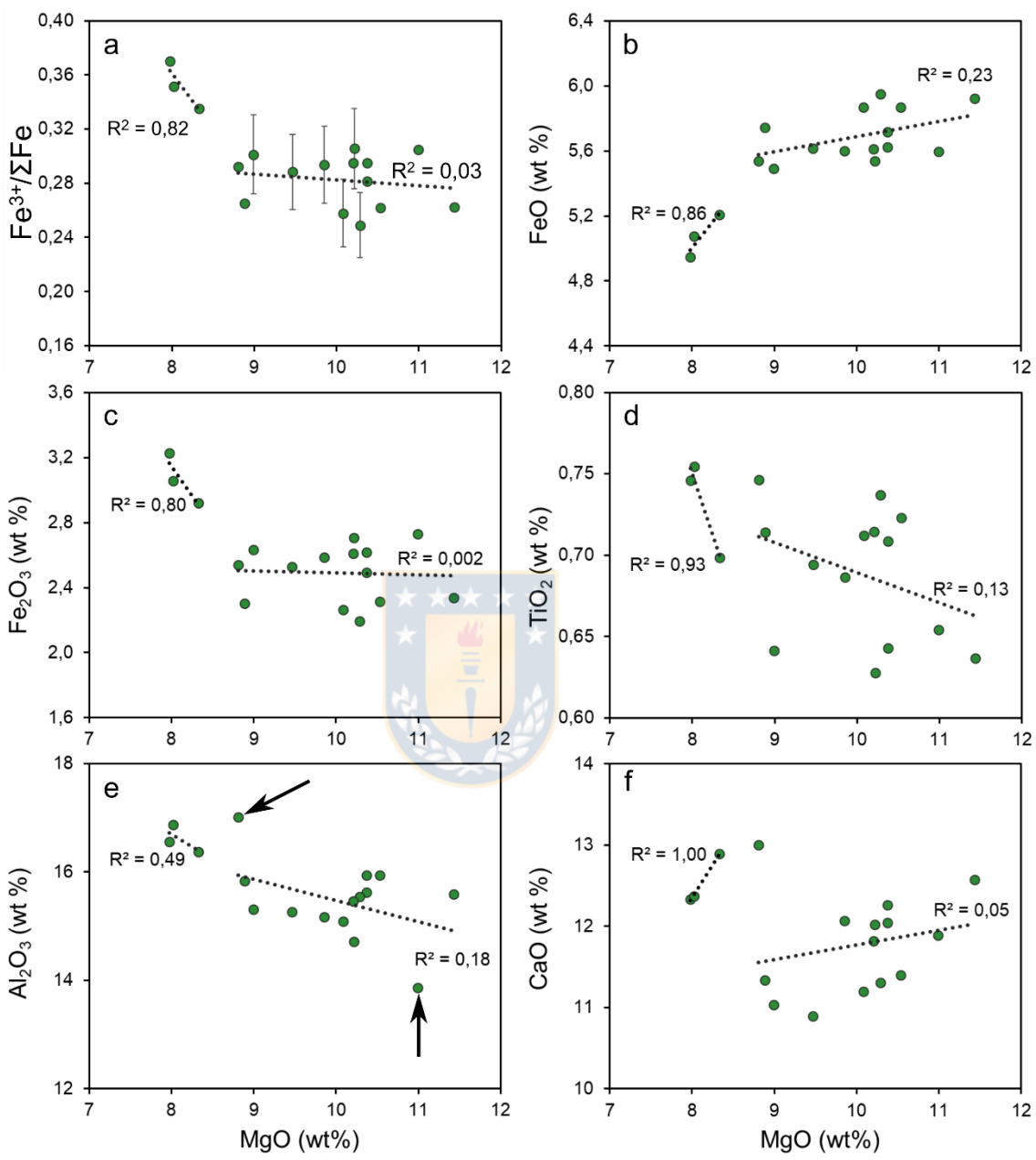


Fig.4.12.- Compositional variations of selected elements along the differentiation recorded by MI's from Los Hornitos. a.- $Fe^{3+}/\Sigma Fe$, b.- FeO, c.- $Fe_2O_3$, d.- $TiO_2$, e.- $Al_2O_3$, f.- CaO. See text for discussions. Data from Table 4.2.

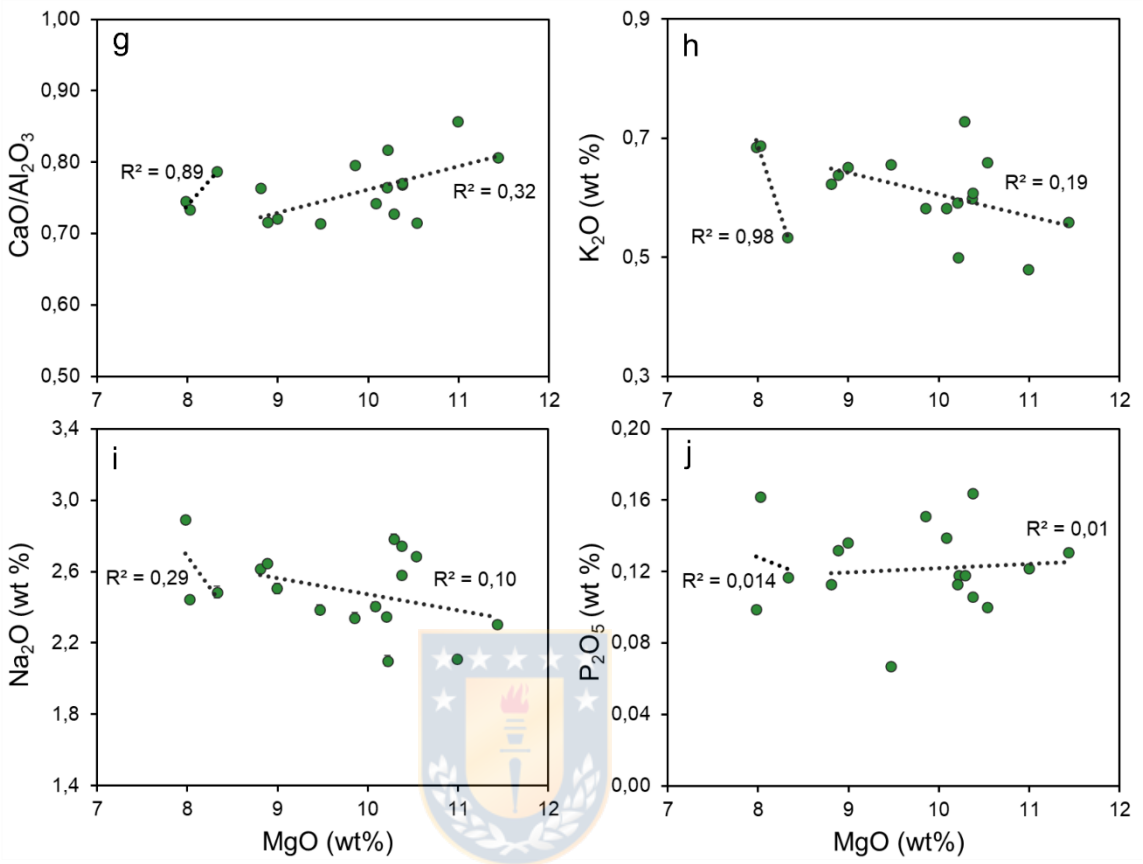


Fig.4.12.- continued.- g.- $CaO/Al_2O_3$. h.- $K_2O$. i.- $Na_2O$, j.- $P_2O_5$. See text for discussions. For all reported oxides and ratios, the source data can be found in Table 4.2.

The chemical anomalies described for the “low temperature” subset of MI’s could indicate that these inclusions are not representative of equilibrium with the bulk magma system, and thus, these will be discussed separately of the main group of data. Discussion regarding the origin of these chemical differences can be found in pag. 150.

With the exception of the low-temperature high-oxidation sub-set of MI’s, the compositional variations showed by most MI data indicate that olivine was the main crystallizing phase during the entrapment of analyzed MI’s. This is

corroborated by Fo-Ni variations on a large mineral data (Salas et al., 2016), which expands the olivine-alone trend towards ~$Fo_{88}$.

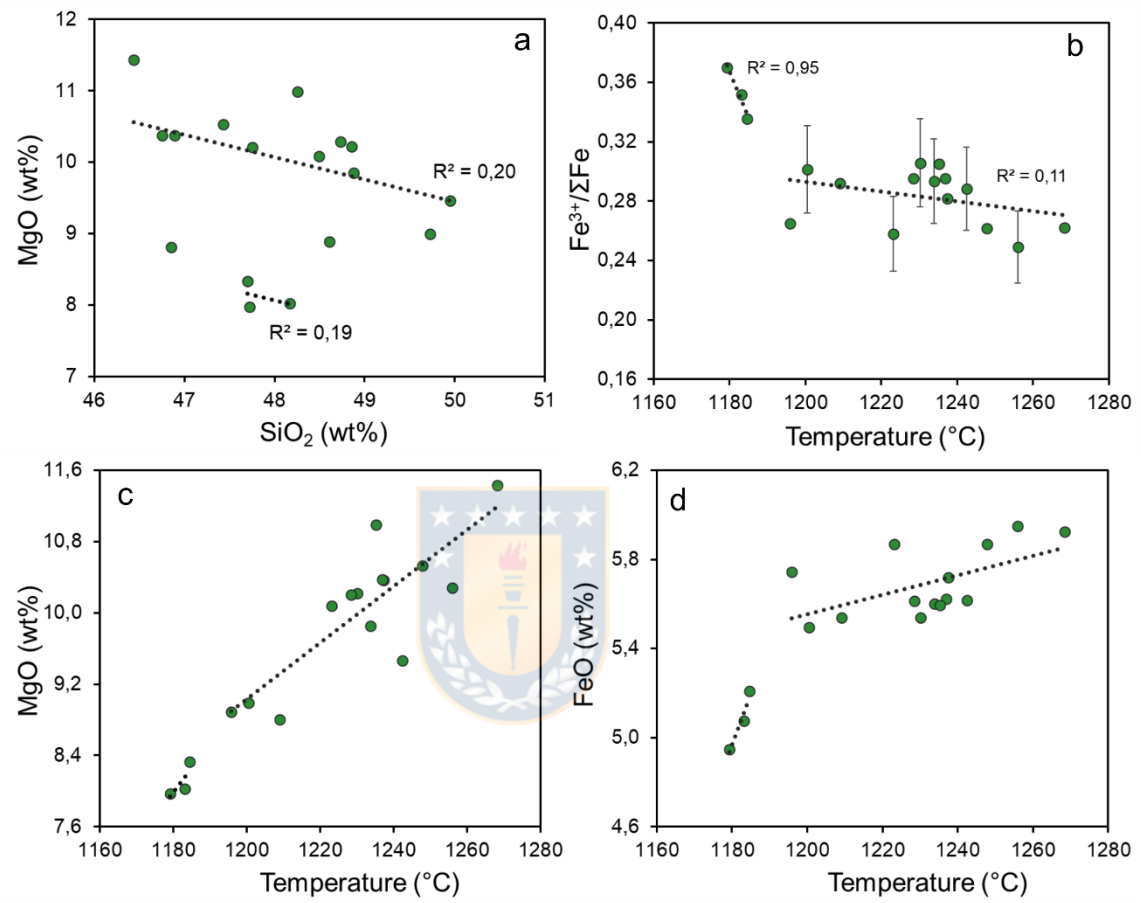


Fig.4.13.- Harker diagrams using $SiO_2$ and temperature as proxies of differentiation. a.- The subset of MI's with comparatively depleted MgO contents (~8 wt% MgO) for ~48 wt% $SiO_2$. b.- the subset of low temperature MI's showing its higher Fe speciation. c and d.- MgO and FeO depleted in the low temperature subset of MI's compared to the trend conformed by the broader group of MI's. Source data can be found in Table 4.2.

To translate the compositions of melt inclusions into oxygen fugacities, the temperature of each MI was determined using olivine-liquid thermometry (Putirka, 2007) and the algorithm of Kress and Carmichael (1991), to calculate $fO_2$ in log units relative to the nickel-nickel-oxide (NNO) buffer (Table 4.2). Considering the

full dataset, these calculations indicate that magmatic $fO_2$ conditions increased from ΔNNO+1,08 to +1,71 (excluding the higher values of the low temperature subset) during the differentiation range preserved by the MI's (considering modeled temperatures for each inclusion and pressure of 1GPa). At these conditions, the $fO_2$ range determined for Los Hornitos is comparatively higher than those reported for other arc basalts determined by the same approach. In the next section, results obtained at Los Hornitos will be compared with published data from other arc volcanoes.

## 4.5.- Discussions

### 4.5.1.- Oxygen fugacity determined in basaltic arc volcanoes

Because composition, pressure and temperature of magmas influence the direct translation of magmatic $Fe^{3+}/\Sigma Fe$ into oxygen fugacity (Kress and Carmichael, 1991), fundamental differences in primary melt composition or P-T conditions that vary with tectonic setting, could potentially offset the relationships between $fO_2$ and $Fe^{3+}/\Sigma Fe$ ratios of magmas. Therefore, oxygen fugacities, referenced to the NNO buffer, will be calculated for published $Fe^{3+}/\Sigma Fe$ data, at common P-T conditions relevant for arc environment, for Los Hornitos and other volcanoes. The effect of composition is avoided by comparing MI's similarly evolved.

There are only a few places on Earth, where arc redox conditions have been established by melt inclusion studies. In the case of Mariana arc, a database of 102 points from Sarigan, Alamagan, Guguan and Agrigan volcanoes is available from the contributions of Kelley and Cottrell, 2009; Kelley and Cottrell, 2012; and Brounce et al., 2014. Additionally, isolated data points had been locally determined for other arc volcanoes, as for the case of Augustine (Alaska), Paricutín (Mexico), Barren Island (India) and Galunggung (Java) (Fig.4.14). The data of Jalopy Cone, in the Basin and Range Province, California, USA, is also included given the contributions of subduction components (e.g., up to 3 wt% $H_2O$, Pb and Nb anomalies, $Fe^{3+}/\Sigma Fe$ up to 0,3; Gazel et al., 2012) that have been reported in the erupted magmas of that otherwise extensional setting (Fig.4.14). Additionally, the data (*n*= 10 MI's) of a recent melt inclusion study at Los Hornitos is included (Tassara et al., 2020) (Fig.4.14). The database of Erebus Volcano in North Antarctica was discarded since it was not corrected for post-entrapment modifications (Moussalam et al., 2014).

One of the main principles behind melt inclusion works states that the composition of the olivine host (i.e. forsterite content) remains invariant from the time of entrapment of inclusions to the time of eruption and cooling of the system (Danyushevsky et al., 2000), allowing to constraint the differentiation of the melt from a fixed position, which ultimately is a more robust monitor than the early compatible elements recorded by the inclusions (e.g. MgO, NiO, FeO).

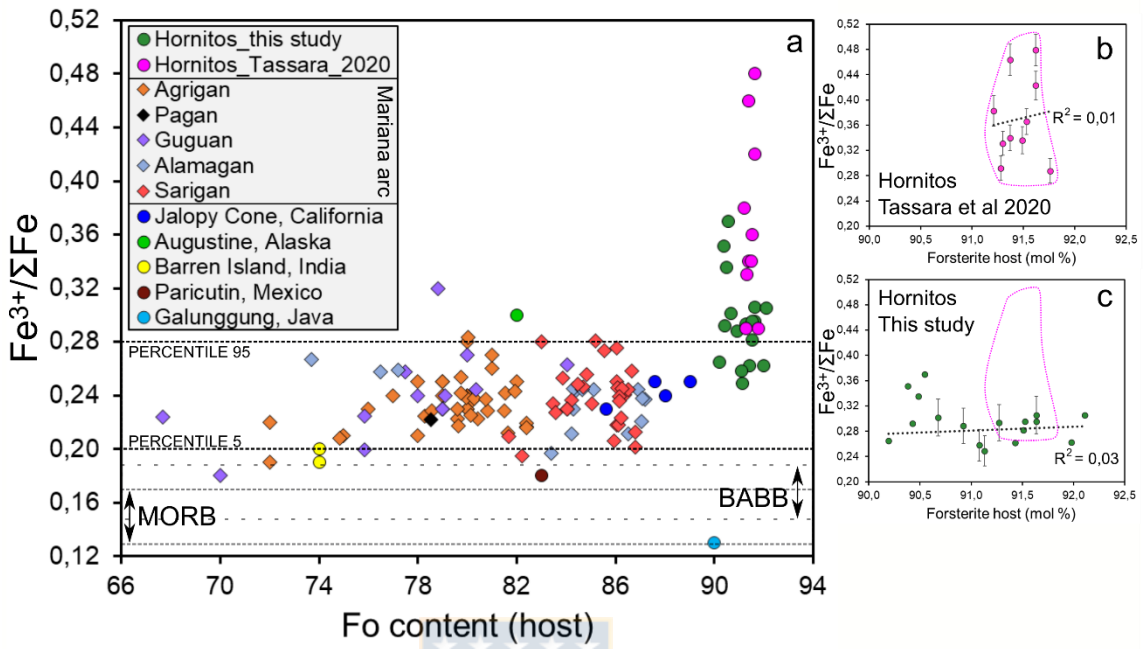


Fig.4.14.- Summary of Fe speciation plotted against forsterite content of the host for arc magmas. a.- Excluding the samples from Los Hornitos (*n*=111), and by applying the percentile 5 and percentile 95, it is clear that the 90% of the data plots in the window of Fe speciation of 0,2 to 0,28, irrespective of the Fo host. Note the three more oxidized samples of Los Hornitos from this study, conform a consistent trend with the five moderately oxidized samples of Tassara et al. (2020). b and c.- Blow up of the differentiation segment recorded by Los Hornitos inclusions measured by Tassara et al. (2020) and by this study, respectively. For comparison, irrespective to the equilibrium forsterite, the $Fe^{3+}/\Sigma Fe$ range measured for BABB (Back Arc Basin Basalts) and MORB (Mid Ocean Ridge Basalt) glasses are plotted (Kelley and Cottrell, 2009). Data for arc magmas, except Hornitos (this study), are from Kelley and Cottrell (2009); Kelley and Cottrell (2012); Brounce et al. (2014); Tassara et al. (2020).

The following observations arise from Fig.4.14a-c:

- The bulk of arc samples are significantly more oxidized than MORB and BABB samples. An isolated sample from Galunggung, Java, trapped in a $Fo_{90}$ host record a comparatively more reduced condition (although this inclusion required a large correction of post-entrapment modifications; Kelley and Cottrell 2009). Additionally, an isolated sample of Paricutín and Barren Island, as those of Agrigan and Guguan volcanoes, lies in the boundary region of BABB.

- The $Fe^{3+}/\Sigma Fe$ recorded at Los Hornitos constitute the most primitive samples yet analyzed by µ-XANES in arc environment. The lower $Fe^{3+}/\Sigma Fe$ values determined at Los Hornitos are higher than the global average for arcs (0,24 ± 0,02; 1 sigma) but broadly similar to those preserved at Jalopy cone, whereas the intermediate $Fe^{3+}/\Sigma Fe$ values from Los Hornitos are consistent with the higher values obtained at Agrigan and Sarigan volcanoes in Mariana arc, and Augustine volcano in Alaska. Lastly, the highest range of values obtained in Los Hornitos has no counterpart among published data.

- The broad and singular trends developed by samples of Mariana arc show mostly invariant redox conditions along the differentiation segment of $Fo_{87}$ to $Fo_{75}$, with a $Fe^{3+}/\Sigma Fe$ range of 0,20 to 0,28 (90 % of the data). The samples of Jalopy cone describe a slightly reducing trend, but it is partially controlled by a single sample at ~$Fo_{85}$ with a lower redox condition. Los Hornitos samples from this study also show a constant redox condition along the restricted segment of magma evolution, but occupying a comparatively more restricted $Fe^{3+}/\Sigma Fe$ range of 0,25 to 0,31. If the low temperature subset is included, these range reach up to 0,37. In addition, the MI's data provided by Tassara et al. (2020) show an extremely large range of $Fe^{3+}/\Sigma Fe$, encompassing 0.28 to 0.48 for a very limited range of Fo (i.e. $Fo_{91.2}$ to $Fo_{91.8}$, Fig.4.14b, c). According to those authors, such abrupt oxidation cannot be explained by the crystallization of olivine and Cr-spinel nor by S degassing.

It is important to mention that the reconstruction of original compositions at Mariana arc is supported by whole-rock data which indicated an incompatible behavior of FeO*, and consequently the inclusions were mostly corrected by PEC (Kelley and Cottrell, 2009; Kelley and Cottrell, 2012; Brounce et al., 2014). However, it is not clear whether the whole-rock pattern of FeO* at Jalopy cone behaves as compatible or incompatible, since no published data is available. As the olivine hosts at this volcano are comparatively forsterite-rich ($Fo_{83}$ to $Fo_{89}$), those are more prone to experience Fe-loss, and post-entrapment corrections should consider such modification. Measured and corrected data of this volcano could indicate different degrees of Fe-loss (Kelley and Cottrell, 2012; their Table S5). Then, if the whole-rock trend of FeO* is compatible, inclusion data would display an oxidizing trend (not reducing as show in Fig.4.14a).

By the other hand, it is interesting to note that according with the bulk Fe speciation data, the primitive parental melts of Augustine volcano, may have evolved from a more reduced member along an oxidizing trend or either be as oxidized as Los Hornitos, however, the lack of additional data does not allow to do farther observations.

Finally, independent if magmatic processes induced oxidation or reduction during differentiation, any effort in determining the oxygen fugacity of the subarc mantle requires focusing in the least evolved samples of a given suite of MI's. Table 4.3 provide a summary of $fO_2$ calculations for selected MI's trapped by forsteritic hosts (Fo ≥ 87). This subset of MI's includes samples from Alamagan, Jalopy cone and

Galunggung volcanoes. Additionally, 18 reconstructed primary melt compositions (Kelley and Cottrell, 2012) for samples from Agrigan volcano equilibrated with $Fo_{90}$, $Fo_{91,5}$ and $Fo_{93}$ are also included (not shown in Fig.4.14) and the data of Tassara et al. (2020) for Los Hornitos. These results and calculations performed on the 17 samples of this study at Los Hornitos are compared to common P-T conditions, set as 1 GPa-1250°C and 0,5 GPa-1000°C (Fig.4.15) (see Table 4.2 for Los Hornitos MI's of this study and Table 4.3 for the other samples).

According to the Fe speciation of inclusions, the oxygen fugacity determined for Los Hornitos is systematically higher than the reconstructed compositions of Agrigan, for a similar forsterite range. By the other hand, excluding the least evolved sample from Jalopy cone (hosted by $Fo_{82}$), the trendline adopts an oxidizing tendency, but as previously discussed, retrieved trendlines may not represent the proper corrected value if Fe-loss occurred and were not accounted for. Alamagan samples does not show a clear evolution trend since the trapping hosts are stationary at ~$Fo_{87}$.

Referenced to 1250°C and 1GPa, Los Hornitos MI's indicates $fO_2$ conditions from 1,07 to 1,72 log units above the nickel-nickel-oxide buffer (NNO), whereas Agrigan and Jalopy do from 0,19 to 1,07 and 0,71 to 0,92, respectively (Fig.4.15a).

Table 4.3.- Forsterite contents of the host, Fe speciation and $fO_2$ calculated for selected primitive arc samples. Note that the samples of Agrigan are modeled from more evolved MI compositions instead of directly measured (Kelly and Cottrell, 2012).

| Location/Samples | Fo host | $Fe^{3+}/\Sigma Fe$ | ΔNNO@1250°C 1 GPa | ΔNNO@1000°C 0,5 GPa |
|---|---|---|---|---|
| *Agrigan volcano, Mariana* | | | | |
| AGR19-02-01 | 90,0 | 0,22 | 1,07 | 0,46 |
| AGR19-02-08 | 90,0 | 0,18 | 0,48 | -0,13 |
| AGR19-02-10 | 90,0 | 0,21 | 0,89 | 0,28 |
| AGR19-02-11 | 90,0 | 0,18 | 0,52 | -0,09 |
| AGR19-02-14 | 90,0 | 0,19 | 0,65 | 0,04 |
| AGR19-02-16 | 90,0 | 0,18 | 0,57 | -0,04 |
| AGR19-02-01 | 91,5 | 0,21 | 0,92 | 0,31 |
| AGR19-02-08 | 91,5 | 0,17 | 0,34 | -0,27 |
| AGR19-02-10 | 91,5 | 0,20 | 0,75 | 0,14 |
| AGR19-02-11 | 91,5 | 0,17 | 0,38 | -0,23 |
| AGR19-02-14 | 91,5 | 0,16 | 0,50 | -0,11 |
| AGR19-02-16 | 91,5 | 0,17 | 0,43 | -0,18 |
| AGR19-02-01 | 93,0 | 0,19 | 0,77 | 0,16 |
| AGR19-02-08 | 93,0 | 0,16 | 0,19 | -0,41 |
| AGR19-02-10 | 93,0 | 0,18 | 0,60 | -0,01 |
| AGR19-02-11 | 93,0 | 0,16 | 0,23 | -0,38 |
| AGR19-02-14 | 93,0 | 0,16 | 0,36 | -0,25 |
| AGR19-02-16 | 93,0 | 0,16 | 0,28 | -0,33 |
| *Alamagan volcano, Mariana* | | | | |
| ALA-02-12 | 87,0 | 0,24 | 0,92 | 0,32 |
| ALA-02-15 | 87,2 | 0,24 | 0,90 | 0,30 |
| ALA-03-1 | 87,3 | 0,21 | 0,59 | -0,02 |
| *Jalopy cone, California* | | | | |
| DF-BP-08-19b-01 | 89,0 | 0,25 | 0,71 | 0,10 |
| DF-BP-08-19b-02 | 87,6 | 0,25 | 0,92 | 0,31 |
| DF-BP-08-19b-04 | 87,9 | 0,24 | 0,84 | 0,23 |
| *Galunggung, Java* | | | | |
| G98-02 | 90,0 | 0,13 | -0,45 | -1,05 |
| *Los Hornitos (Tassara et al)* | | | | |
| 3 | 91,4 | 0,46 | 3,19 | 2,58 |
| 4 | 91,6 | 0,42 | 2,87 | 2,26 |
| 5 | 91,6 | 0,48 | 3,33 | 2,72 |
| 6 | 91,4 | 0,34 | 2,05 | 1,44 |
| 7 | 91,5 | 0,37 | 2,26 | 1,65 |
| 21 | 91,3 | 0,33 | 1,91 | 1,31 |
| 28 | 91,8 | 0,29 | 1,48 | 0,87 |
| 34 | 91,2 | 0,38 | 2,41 | 1,80 |
| 37 | 91,3 | 0,29 | 1,52 | 0,92 |
| 38 | 91,5 | 0,34 | 2,03 | 1,42 |
| *East Pacific Rise* | | | | |
| EN113_13D-1B | 88,0 | 0,15 | -0,25 | -0,86 |

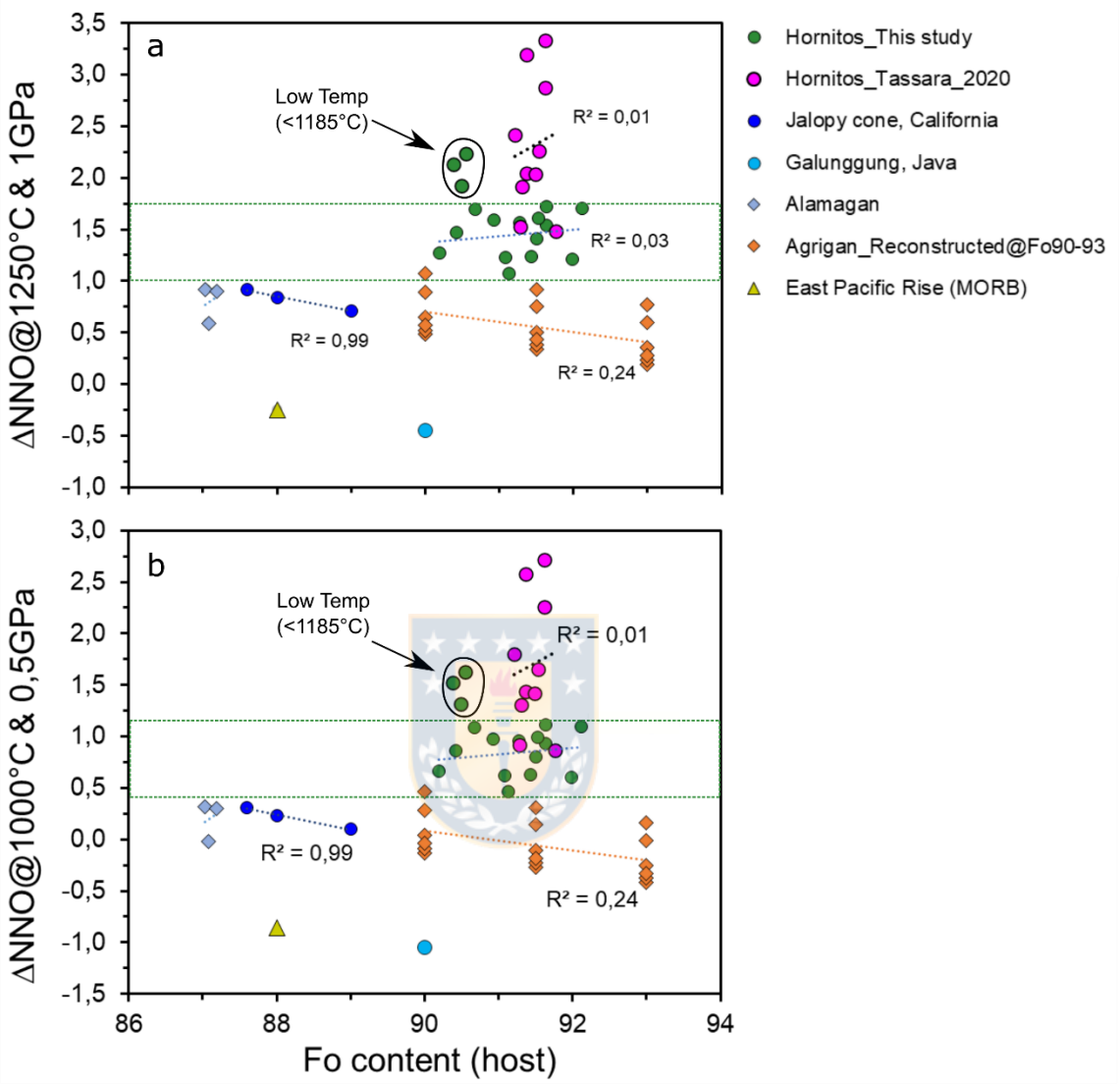


Fig.4.15.- Fo content versus $fO_2$ for selected MI's. a.- P-T conditions fixed at 1250°C and 1 GPa and b.- 1000°C and 0,5 GPa.

The subset of low temperature MI's from Los Hornitos (this study, encircled by a black line in Fig.4.15a) occupy an $fO_2$ range between 1,93 to 2,24 log units above the NNO buffer. By the other hand, the $fO_2$ reported by the data of Tassara et al. (2020) provide a segment between 1,48 to 3,33 log units above the NNO buffer, corresponding to a variation of 1,85 log units along only 0,6 forsterite units. Only

2 of the 10 MI's provided by this recent publication are consistent with our data. However, it is interesting to note that the higher $fO_2$ conditions reported by Tassara et al. (2020) conform a trend similar to that developed by the subset of 3 more oxidized MI's of this study. This means that a process affecting those MI's may be the common cause for such elevated redox conditions, documented in both studies. This issue will be discussed further (See page 150).

The range of variation of $fO_2$ for a given forsterite content is about 0,7 log units for both Los Hornitos and Agrigan (Fig.4.15).

The data presented above, indicate that compared to other arc magmas, inclusions from Los Hornitos record redox conditions by about 1 log unit more oxidized at roughly similar melt evolution (e.g. Agrigan volcano).

Contrasting the $fO_2$ conditions of Los Hornitos (this study) with those of Agrigan volcano at $Fo_{92}$ allows to observe the data in terms of S speciation, in order to explore into the early behavior of sulfur and implications in its solubility, transport and availability in primitive basaltic melts (see next section). For Agrigan, I use the composition of extreme MI's to calculate the range of $fO_2$, whereas at Los Hornitos (this work), given the very low $R^2$ value, I prefer to consider a constant value of $fO_2$ along differentiation, and hence, I use the entire range of redox conditions (green rectangle in Fig.4.15a). The subset of more oxidized MI's is shown separately. I include the calculation for Jalopy cone, that given the scarcity of data is represented by a point instead of a segment of $fO_2$ (see Fig.4.16).

### 4.5.2.- Sulfur speciation determined in melt inclusions from Los Hornitos, Agrigan and Jalopy volcanoes

The calculated oxygen fugacity for the melt at the evolution stage of Fo92, can be found in Table 4.4. Those results allow to determine the sulfur speciation in the melt, based in cumulative experimental data (Matjuschkin et al., 2016; Jugo, 2009; Jugo et al., 2010; Botcharnikov et al., 2011). In particular, results are plotted into the curves determined by Matjuschkin et al., 2016 (Fig.4.16).

Table 4.4.- Calculated $fO_2$ window for a fixed position of melt evolution at $Fo_{92}$

| Location | ΔNNO@1 GPa-1250°C | | | | ΔNNO@0,5 GPa-1000°C | | | |
|---|---|---|---|---|---|---|---|---|
| | Min $fO2$ | Min $S^{6+}/\Sigma S$ | Max $fO_2$ | Max $S^{6+}/\Sigma S$ | Min $fO_2$ | Min $S^{6+}/\Sigma S$ | Max $fO_2$ | Max $S^{6+}/\Sigma S$ |
| Los Hornitos high T° | 1,07 | 0,08 | 1,72 | 0,53 | 0,46 | 0,30 | 1,11 | 0,82 |
| Los Hornitos low T° | 1,93 | 0,66 | 2,24 | 0,87 | 1,32 | 0,90 | 1,63 | 0,96 |
| Agrigan | 0,27 | 0,00 | 0,88 | 0,04 | -0,30 | 0,03 | 0,25 | 0,15 |
| Jalopy | -0,09 | 0,00 | - | - | -0,70 | 0,01 | - | - |

Curves of S speciation are useful to observe the variation in the proportion of sulfur species (sulfide $S^{2-}$ and sulphate $S^{6+}$) along changes in the oxygen fugacity of the silicate melt. For relatively reducing conditions (≤~NNO) and high pressure (1 GPa) most of sulfur is present as sulfide whereas at slightly more oxidizing conditions, the proportion of sulfur as sulphate drastically increases, such that converts in the only stable specie at >~ΔNNO+2.

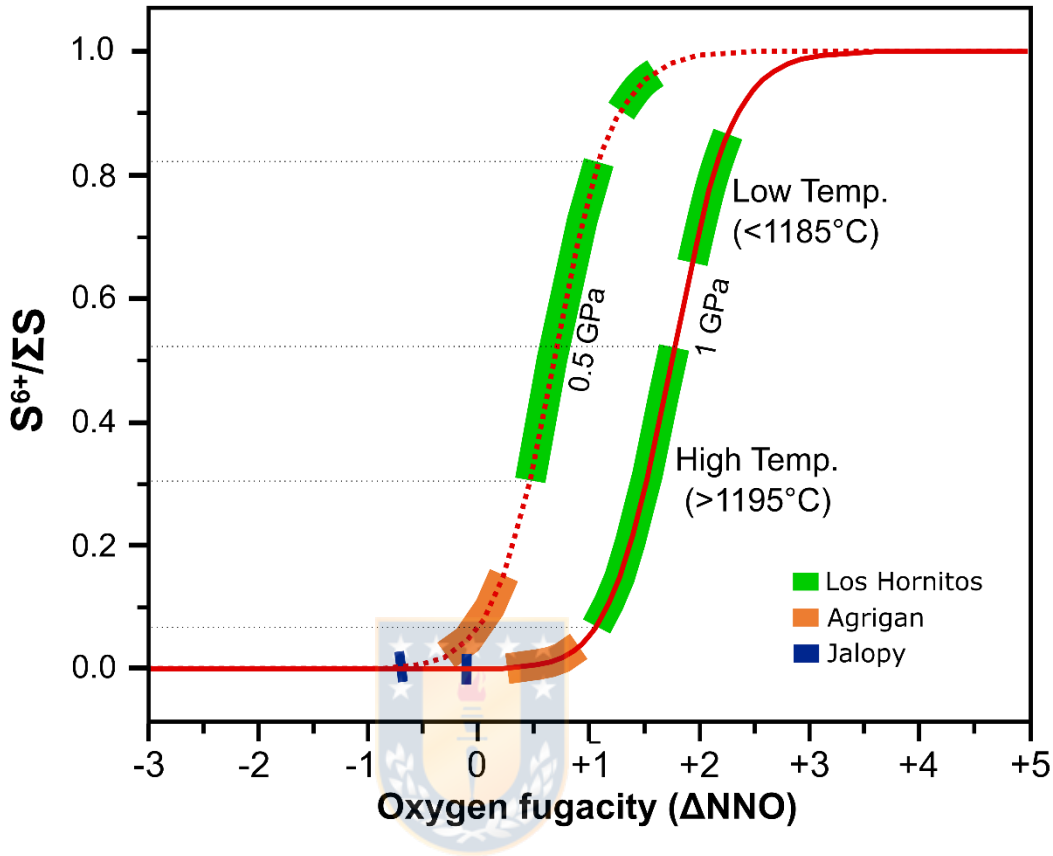


Fig.4.16.- Sulfur speciation for selected arc volcanoes at common P-T conditions and at fixed composition of $Fo_{92}$. Data from Table 4.4.

Four major observations arise from Fig.4.16 and previous analysis:

1.- The $fO_2$ recorded at Jalopy cone, either at 1 GPa-1250°C or 0,5GPa-1000°C, indicate that the total amount of sulfur occurs as sulfide, and so $S^{6+}/\Sigma S$ is 0. Agrigan $fO_2$ ranging between ΔNNO +0.27 to +0.88 for the high-pressure model account for a maximum $S^{6+}/\Sigma S$ of 0,04 whereas the low-pressure model indicates a $S^{6+}/\Sigma S$ of 0,03 to 0,15, therefore prevailing sulfur as sulfide, with less than 15% of sulfate.

2.- Comparatively, the longer paths described by Los Hornitos, at high and low pressures, are located at the mid to upper segment where $S^{2-}$ transit to $S^{6+}$, respectively. At conditions of 1 GPa-1250°C, the $fO_2$ range determined is between ΔNNO +1,07 to +1,72 and account for a $S^{6+}/\Sigma S$ of 0.08 to 0,53. Such redox conditions calculated at 0,5GPa-1000°C provide a $fO_2$ range of ΔNNO +0,46 to +1,11, corresponding to a $S^{6+}/\Sigma S$ 0,30 to 0,82. By the other hand, the low-temperature subset of MI's of Los Hornitos, provide a $fO_2$ range of ΔNNO 1,93 to 2,24 (1 GPa-1250°C), corresponding with a $S^{6+}/\Sigma S$ 0,66 to 0,87. At 0,5 GPa-1000°C these MI's describe a $fO_2$ of ΔNNO +1,32 to +1,63 which account for a $S^{6+}/\Sigma S$ of 0,90 to 0,96.

3.- Based in Fig.4.15a, most of the $fO_2$ values at 1 GPa-1250°C falls above ΔNNO +1,4, and therefore, a representative sulfur speciation value of $S^{6+}/\Sigma S$ is >~0,2. In the same way, based in Fig.4.15b, the low-pressure model indicate that most of MI's have a $fO_2$ of ΔNNO > +0,75 and therefore a more representative value of the sulfur speciation, expressed as $S^{6+}/\Sigma S$, is > 0,50. In both of these scenarios, the more oxidizing conditions recorded at Los Hornitos have a large impact in the speciation of sulfur; and ultimately those redox conditions promote the transport of sulfur and metals to shallow crustal levels, more efficiently than in Jalopy and Agrigan cases, where sulfide saturation, early in the magma evolution, may be relevant or just massive.

4.- The compositional features of the low temperature subset of MI's (*n*=3) diverge of the trends that follow most of the data (*n*=14) on different harker diagrams

(Fig.4.12 and 4.13). The anomalous patterns consist of low FeO and MgO and higher contents of $Al_2O_3$, and are better observed using $SiO_2$ as a proxy for differentiation (Fig.4.17). These MI's may not be representative of equilibrium conditions. Rather, these MI's may represent the entrapment of melts from a compositional boundary layer environment (CBL). Thus, the depleted contents of MgO and FeO in such conditions is explained by the rapid uptake of olivine compatible components from the adjacent environment surrounding the growing crystal. Conversely, olivine incompatible components are enriched in the surrounding environment. In particular, the contents of $Al_2O_3$ may be increased in the CBL given its slow diffusivity in basaltic melts (Zhang et al., 2010; Shea et al., 2015; Welsch et al., 2014). As the diffusivity of $SiO_2$ is roughly half of that of $Al_2O_3$ (Zhang et al., 2010), it may also be accumulated in the CBL environment. Therefore, as observed in Fig.4.17a, b, c it is likely that the compositions of MgO, FeO and $Al_2O_3$ are influenced by a CBL, but also $SiO_2$ is controlled by this effect. Besides, an examination of images of the crystal hosts, reveals that OL_106 and OL_124 retain remarkable dendritic and skeletal textures, respectively, and thus, the scenario of entrapment of MI's during rapid growth rates is possible. In particular, OL_106 is the less texturally evolved crystal found in this study (Fig.3.1c, Chapter 3) and thus, the MI's trapped in that particular crystals, are very likely affected by a CBL. As $Fe^{3+}$ is incompatible in olivine, its accumulation in the CBL environment will induce overestimated $Fe^{3+}/\Sigma Fe$ determinations. The same process is proposed to be affecting to the bulk of MI's analyzed by Tassara et al.

(2020) (with exceptions of MI's #37 and #28). Consequently, the $Al_2O_3$ contents measured by those authors is considerably more elevated that those measured by this study (Fig.A.4.2 Appendix).

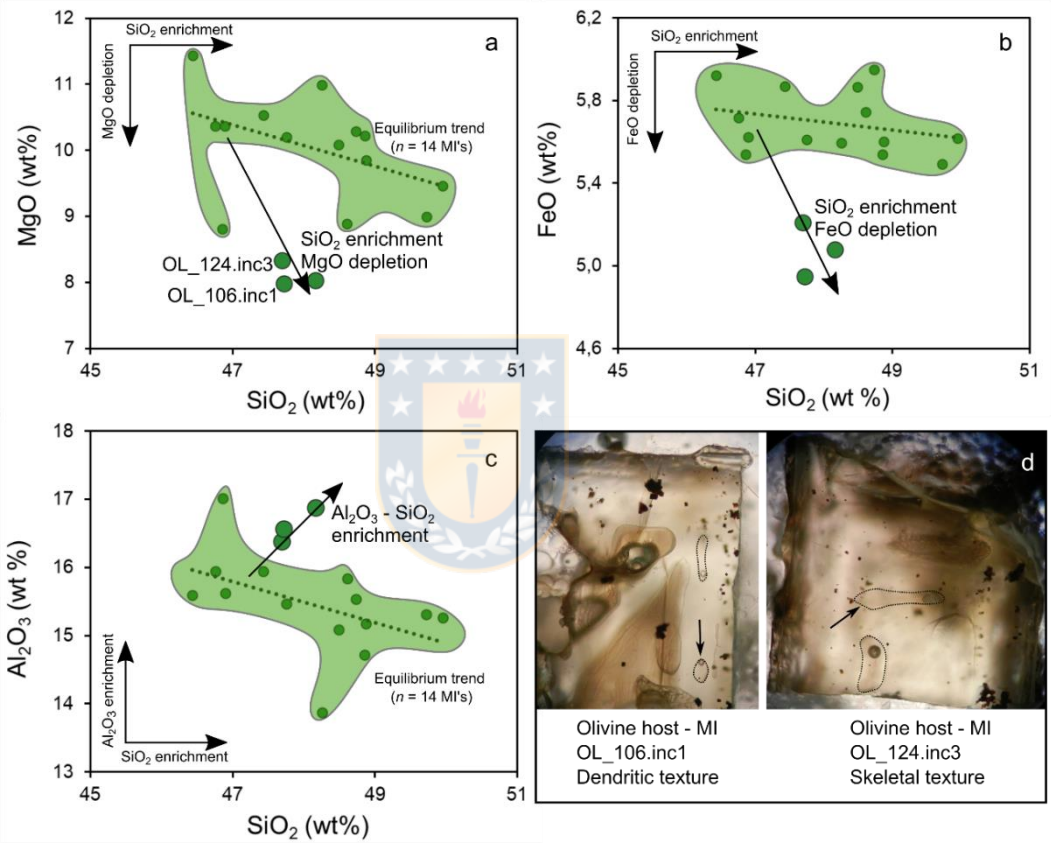


Fig.4.17.- Compositional variations between the low temperature subset of MI's (*n*=3; green bigger points in a, b, c) and the dominant trend conformed by most of the data (*n*=14; encircled in a greenish field in a, b, c). a and b.- Note the compositional variation that result of $SiO_2$ accumulation and MgO and FeO depletions. c.- $Al_2O_3$ and $SiO_2$ accumulation in a hypothetical CBL. d.- Images under the binocular lenses showing the dendritic texture of OL_106 and the skeletal texture in OL_124, visible as a marked crystal frame in the backround. The anomalous measured MI's are labeled in a, and are marked with an arrow at each crystal in d.

Also, results of $fO_2$ found in Los Hornitos have implications in the SCAS (Sulfur Content at Anhydrite Saturation), as basaltic melts oxidized above ΔNNO+2 (@1

GPa; Matjuschkin et al., 2016) enhance significatively the total carrying capacity of sulfur. Cumulative experimental data show that SCAS strongly decrease with increasing $SiO_2$ and increase along CaO increases (Chowdhury and Dasgupta 2019, and references therein), therefore, basaltic magmas with silica contents below 50 wt% $SiO_2$ and CaO between 11 to 13%, as those recorded in the MI's from Los Hornitos, are excellent carriers of sulfur as sulfate (e.g. Fig.6 Chowdhury and Dasgupta 2019). Additionally, the SCAS increases linearly with increasing pressure and exponentially with increasing temperature (Jugo et al., 2010). These observations reinforce the role of oxidized basaltic magmas as key transporters of sulfur towards high crustal levels.

Recent findings, based in 1 atm experiments, suggest that temperature have a strong effect in the sulfur speciation, shifting the position of the curves of Fig.4.16 towards less oxidizing conditions as temperature increases (Nash et al., 2019). However, it is not clear the net effects of cumulative high temperature and pressure, since the shifting of both effects is counterpart (Matjuschkin et al., 2016; Nash et al., 2019).

Figure 4.18 show the chlorine (Cl) and sulfur (S) contents determined in melt inclusions hosted in olivine along the Andean Southern Volcanic Zone of Chile (SVZ), compiled from published data of Werhman et al. (2014) and Weller and Stern (2018). Additionally, the bulk data for Mariana arc (Brounce et al., 2014) and Jalopy cone is incorporated (Kelley and Cottrell 2012). Finally, the data

measured in this study for Los Hornitos, in both melt inclusions (MI's) and external glasses (EG's), obtained by EPMA and SIMS, is included.

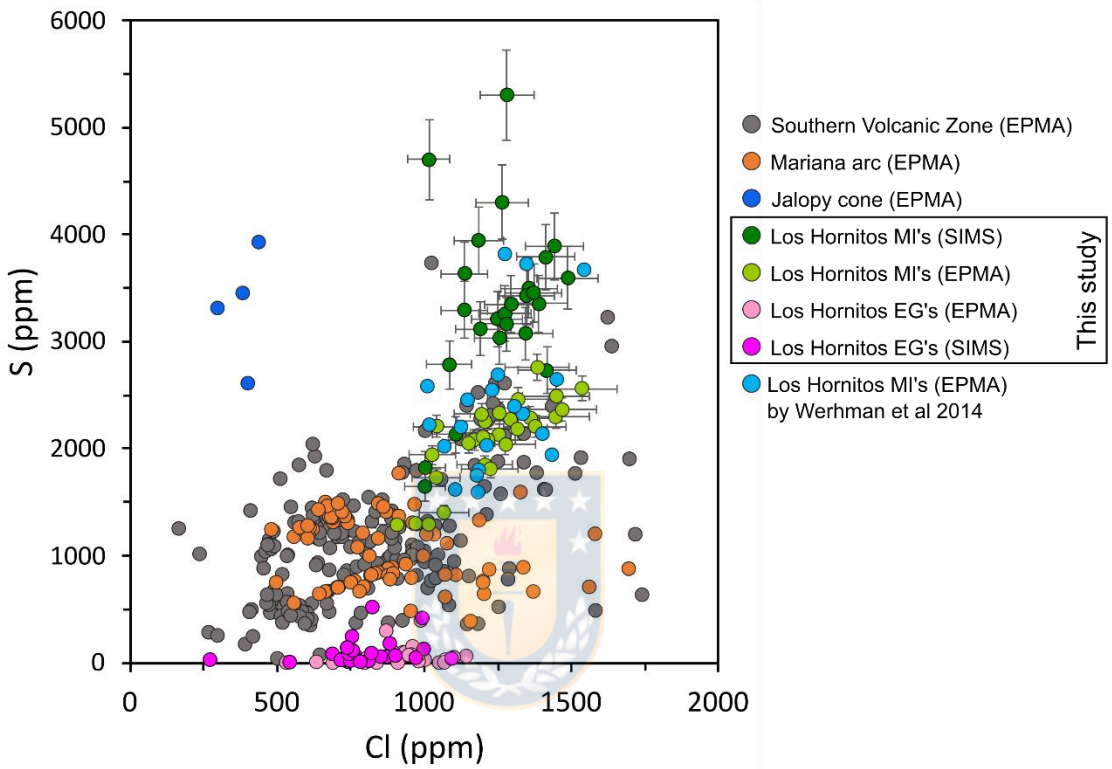


Fig.4.18.- Chlorine versus sulfur in melt inclusions (MI's) and external glasses (EG's). Note that for Los Hornitos, volatile data measured by EPMA and SIMS is shown. Data for Los Hornitos (this study) can be found in Tables A.4.4, A.4.5, A.4.6 and A.4.7. Data of Jalopy, Mariana and Southern Volcanic Zone from Kelley and Cottrell (2012); Brounce et al. (2014); Wehrmann et al. (2014) and Weller and Stern (2017).

Disregarding the evolution degree of the magma (i.e. the forsterite host) it is clear that sulfur and in a great extension chlorine, measured at Los Hornitos, correspond to the highest reported values along the entire SVZ, with the bulk of the sulfur data above ~3000 ppm and reaching up ~5300 ppm of S. Inclusions from Mariana arc, by the other hand, reported values that encompass a segment between ~500 to ~1500 ppm of S. It is interesting to note that the S and Cl range

occupied by Mariana samples correlates well with a significant amount of data from the SVZ. Instead of redox conditions, this may indicate comparable storage conditions for magma reservoirs underneath the stratovolcanoes.

Jalopy cone develop a unique trend with high S contents but comparatively low Cl contents, likely induced by the particular magma source therein, which only partially obey the subduction fingerprint (see Gazel et al., 2012).

Finally, external glass measured at Los Hornitos are strongly degassed in S but still containing Cl contents comparable to the cluster conformed by Mariana and part of the SVZ (Fig.4.18).

Despite the highly oxidizing conditions preserved at inclusions from Los Hornitos, trace element data provided by LA-ICP-MS (Fig.4.19), indicate that the contents of copper decrease drastically from ~200 ppm, at $Fe^{3+}/\Sigma Fe$ ~0,25 to values of ~90 ppm at $Fe^{3+}/\Sigma Fe$ ~0,3, suggesting that copper is being fractionated from the melt. Two main hypotheses may explain this observation:

1.- A minor proportion of sulfide is present, and pyrrotite or other sulfide phase is sequestering chalcophile elements. This is corroborated by a similar trend depicted by Pb and the positive co-variation of both elements (Fig.4.20a, b).

2.- A volatile phase has been exsolved and elements like $Fe^{+2}$, $Cu^{+2}$ partition to it, leaving the silicate melt comparatively decreased in such elements.

The second scenario is more difficult to occur, given that at the high pressures where these MI's have been trapped (> 7kbar), the $H_2O$ saturation is unlikely. The

first scenario is likely to occur given the recorded $S^{6+}/\Sigma S$ at Los Hornitos, however no sulfides were observed in the analyzed samples.

The samples at Jalopy cone remains stationary at $Fe^{3+}/\Sigma Fe$ ~0,25 and ~100 ppm of Cu (Fig.4.18). The Mariana samples display different patterns. Sarigan samples indicate Cu depletion along magma reduction, whereas Cu contents decrease along a wide redox condition at Agrigan and Alamagan. Sulfide saturation is very likely to occur in the early melts of Mariana arc given the comparatively more reduced conditions recorded in the MI's.

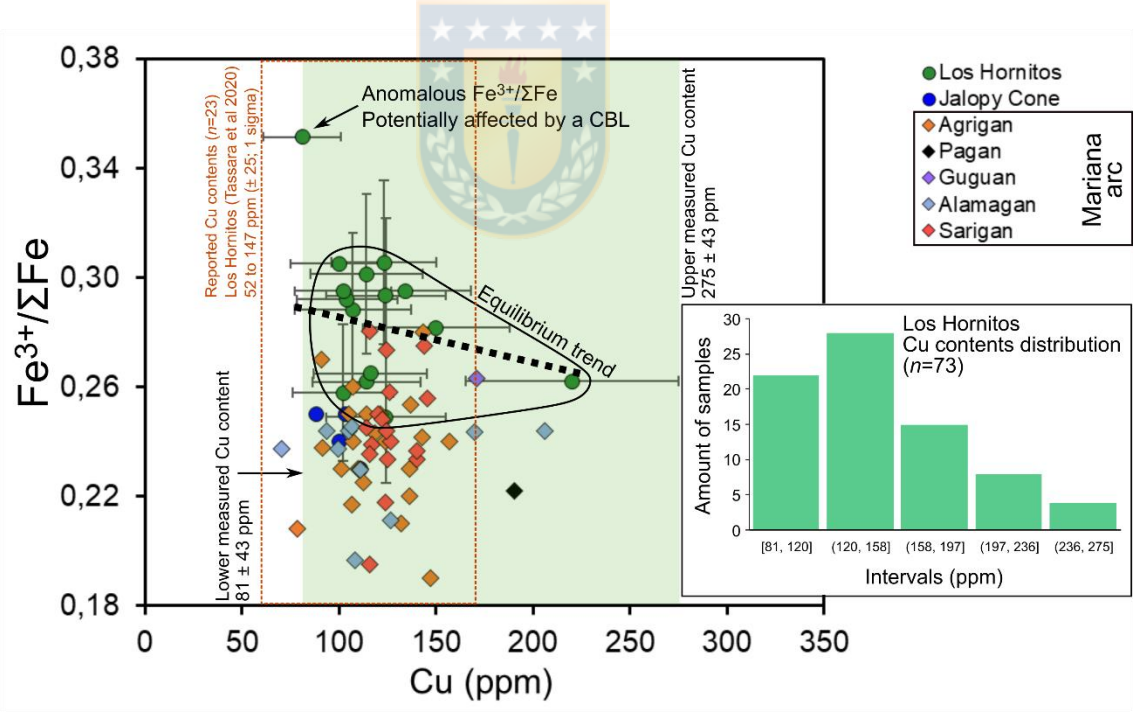


Fig.4.19.- Cu contents versus $Fe^{3+}/\Sigma Fe$ for samples from Mariana, Andes and Basin and Range. Data of Fe speciation from Table 4.2 and trace element from Table A.4.10 and A.4.11.

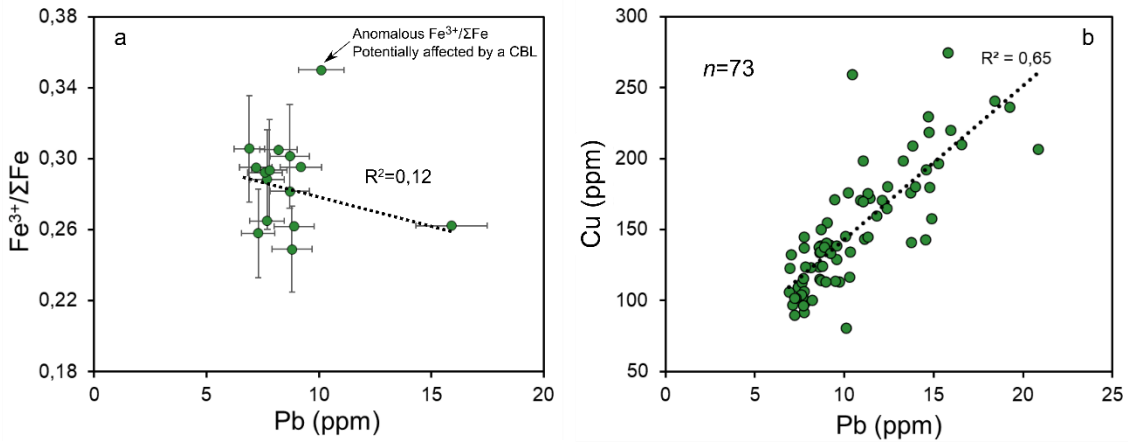


Fig.4.20.- a.- Pb contents versus $Fe^{3+}/\Sigma Fe$ recorded in melt inclusions from Los Hornitos. Most of the data plots below 10 ppm of Pb and therefore the trendline is not a robust. b.- Cu and Pb contents in melt inclusions showing a positive covariation, describing a similar behavior of these two chalcophile elements.

Finally, it is interesting to note the uniform Cu content (tight cluster between ~80 to 150 ppm; Fig.4.19) within the melt inclusions from three contrasting mantle sources as those of Andes, Mariana and that from the Basin and Range Province, corresponding to different members of arc magmas. The broad similar copper enrichment in different primitive magmas, suggest that anomalous metal endowments of the mantle source may not be a prerequisite to generate large ore mineralized provinces at shallow upper-crust levels. This observation further suggests that the main mechanism behind the accumulation of metals in the upper crust of certain continental segments may be controlled by the availability of sulfur, pumped as sulphate by oxidized basaltic magmas that episodically deliver volatile-metal charges to mid-upper crustal levels.

## 4.6.- Conclusions

Melt inclusions preserved at forsterite-rich olivine hosts of Los Hornitos record variations in major, minor and trace elements, as well as redox conditions that make possibly get insights into the early compositions of deep emplaced primitive basaltic melts in the Andean arc at 35,5°S.

The main conclusions of this chapter are:

1.- The MI compositions found at Los Hornitos, compared to other arc compositions captured in melt inclusions hosted in olivine (e.g. Mariana arc, Augustine in Alaska, Paricutín in Mexico, Barren Island in India, Galuggung in Java and Jalopy cone in USA), record the highest $Fe^{3+}/\Sigma Fe$ conditions yet measured in basaltic arc melts. Additionally, the mid to lower $Fe^{3+}/\Sigma Fe$ ratios retrieved in Los Hornitos are similar to those known for other arc magmas, but the latter reach such higher redox conditions at a later stage in the evolution of magma.

2.- The $Fe^{3+}/\Sigma Fe$ values at Los Hornitos distribute between 0,25 to 0,31, along a nearly constant to slightly increasing trend, as the melt evolve from 11,5 to 8,5 wt % of MgO (Fig.4.12a) and cools from 1268° to 1196°C (Fig.4.13b). A subset of MI's record $Fe^{3+}/\Sigma Fe$ between 0,34 to 0,37, but those may not represent equilibrium conditions. Rather, those more oxidized values may obey to the

entrapment of melts chemically influenced by transient CBL's, that are enriched in slow diffusing incompatible (e.g. $Al_2O_3$, $SiO_2$) and depleted in compatible components (FeO, MgO) (Fig.4.17).

3.- Transformed to oxygen fugacity, the redox conditions measured in equilibrium at Los Hornitos ($\Delta$NNO +1,07 to +1,72), locate right where the transition of sulfide to sulfate occurs (1 GPa-1250°C), and hence those basaltic melts can conservatively dissolve 20 to 50% of the total sulfur cargo as sulfate. However, a minor sulfide precipitation may occur, as shown by the copper systematics. At lower pressures (0,5 GPa-1000°C), the redox conditions measured at Los Hornitos can transport even larger amounts of sulfur, as the $S^{6+}/\Sigma S$ ratio reaches values of 0,30 to 0,82.

4.- The volatile-metal composition of an archetypal primitive melt of this Andean segment is: $H_2O$ 3 wt %, 4000 ppm of S, 1300 ppm of Cl and 200 ppm of Cu.

5.- The redox condition preserved in melt inclusions contained in olivine hosts equilibrated with the sub-Andean mantle source reveals the capacity of these oxidized basaltic melts to dissolve large amounts of sulfate that can subsequently be transported to shallower levels of the crust.

6.- The tight range of Cu contents observed in primitive melt inclusions from different magmatic arc systems in the Earth, reveals that the availability of metals is rather uniform in the mantle source, and therefore, the key to form porphyry copper deposits in mature subduction zones, like the Andes, consist in the enhanced capacity of primitive melts to transport sulfur as sulphate under oxidizing conditions, rather than anomalous Cu contents.

# Chapter 5: Discussion & Final Conclusions

As explained in Chapter 1, the more oxidized character of arc basalts, compared with basalts of other tectonic setting constitutes the first line of research to explain the efficient transport and accumulation of metal and sulfur that make up the conformation of huge anomalies of sulfide-ore in porphyry systems emplaced in the shallow crust of continental margins above subduction zones.

However, it is not clear whether the oxidation in these magmas reflect the oxidation condition of the mantle source or either, the arc magmas become oxidized by intra crustal processes. These two different approaches have relevant implications in the understanding of the fundamental processes that govern the transport at high-scale of metals and sulfur through the crust. Given the pervasive hydrothermal alteration and the scarcity of mafic rocks, the evaluation of the early redox conditions of magmas is not possible to directly measure in the porphyry environment.

By exploring the redox conditions and metal-volatile endowment in the more primitive arc basalts occurring in a thick-crust segment of the central-south Andes (35.5°S), I addressed these basic conditions and link them to the occurrence of the Mio-Pliocene mineralized belt of Central Chile, since the close scales in time and space.

In Chapter 2, based in the analysis of bibliography and samples collected during field work, I demonstrated that Los Hornitos constitutes the northernmost

occurrence of primitive basalts in the arc region of the Southern Volcanic Zone. Here, olivine of forsterite contents ranging between Fo88 to Fo92.5 are in equilibrium with a peridotitic mantle source and contain quenched melt inclusions that are suitable for the interrogation by micro-analytical techniques.

In addition, results of Chapter 3 indicate that the high forsterite crystals hosting melt inclusions have crystallized deep in the crust (~40 km) at temperatures > 1170°C and rapidly ascended to the surface in timescales of 3.5 to 40 days. Even though, the core of the most forsteritic-rich olivines crystallized at mantle conditions and experienced diffusion.

The bulk population of olivine crystals of Los Hornitos experienced periods of rapid growth evidenced by different degrees of textural maturity but also because the concentric Fo-Ni zoning reflect the operation of transient compositional boundary layers (CBL's) surrounding the emerging crystals. These CBL's are depleted in olivine compatible (Ni-Fo) and enriched in incompatible components, especially in those of slow diffusion as P, Cr, Al, Si, $Fe^{3+}$. The recognition of the effects of such CBL's during the growth history of a given crystal and the potential trapping of melts during these transient periods, challenge the notion of melt inclusions as indicators of equilibrium as an implicit rule.

After this consideration, the data indicate that only few melt inclusions (3 of 17 inclusions) of this study evidenced the effects of CBL's, noticeable in anomalous high $Fe^{3+}/\Sigma Fe$, depletion in MgO-FeO and $Al_2O_3$-$SiO_2$ enrichment.

For the melt inclusions in conditions of equilibrium, the main conclusions that response to the questions that guide this research, are listed below:

1.- The MI analyzed in Los Hornitos, compared to other arc compositions measured in melt inclusions hosted in olivine (e.g. Mariana arc, Augustine in Alaska, Paricutín in Mexico, Barren Island in India, Galuggung in Java and Jalopy cone in USA), record the highest $Fe^{3+}/\Sigma Fe$ conditions yet measured in basaltic arc melts.

2.- The compositional features of an archetypal primitive melt entrained to the deep crust of this arc segment is constrained by a $Fe^{3+}/\Sigma Fe$ in the range 0,25 to 0,31 (average 0,28 ± 0,02; 1 sigma) which is equivalent to a $\Delta$NNO window of +1,07 to +1,72 and correspond to a $S^{6+}/\Sigma S$ of ~0,1 to 0,5. The volatile-metal composition of this primitive melt is ~3 wt % of $H_2O$, 4000 ppm of S, 1300 ppm of Cl and 200 ppm of Cu.

3.- Despite such high $fO_2$, it does not overpass the limit of $\Delta$NNO+2, where most of the sulfur occurs as sulfate. However, the determined $fO_2$ allow to a melt equilibrated at $Fo_{92}$ to dissolve a minimum of 8% to more than 50% of the total sulfur cargo as sulfate ($S^{6+}$) (at 1 GPa-1250°C). This magma system, rapidly emplaced at mid crustal levels (0,5 GPa-1000°C), may even increase their sulfur

carrying capacity, as $S^{6+}/\Sigma S$ expands to 0,3 to 0,82, allowing to dissolve 30 to more than 80 % of sulfur as sulfate.

4.- The primitive basaltic melts from Los Hornitos are 1.4 to 2 log units more oxidized than the modeled $fO_2$ proposed by Lee et al. (2012) for the mantle source of arc magmas. Therefore, our results are consistent with the findings of Kelley and Cottrell 2009, that the oxidation state of arc basalts reflect the oxidized conditions of the mantle source, and thus, are already oxidized when entrain into the continent crust.

5.- Contrary to the claims of advocates of similar $fO_2$ at MORB and arc mantle sources around FMQ (which is equivalent to ~$\Delta$NNO-0.3) and the consequently massive precipitation of sulfide in the early stages of melt evolution as a prerequisite for the generation of ore related magmas (Nadeau et al., 2010; Lee et al., 2012, Sillitoe, 2012; Wilkilson, 2013; Chiaradia, 2014), this research show that at the $fO_2$ conditions recorded in Los Hornitos, a minor sulfide precipitation is also possible to occur, however no sulfide was observed during petrographic or EPMA exploration of the samples. The moderate to low occurrence of such sulfide phase compared to a large volume of silicate melt only slightly affected by the precipitation of sulfide, will conduct to a metallogenic fertile magma.

6.- The tight range of Cu contents observed in primitive melt inclusions from different magmatic arc systems in the Earth, reveals that the availability of metals is rather uniform in the mantle source, and therefore, the key to form porphyry copper deposits in mature subduction zones, like the Andes, consist in the enhanced capacity of primitive melts to transport sulfur as sulphate under oxidizing conditions, rather than anomalous Cu contents.

7.- Unlike to the conclusions of Tassara et al. (2020), the melt inclusions of Los Hornitos record a mostly invariant redox evolution along the differentiation segment between $Fo_{92}$ to $Fo_{90}$. The elevated and extremely anomalous values reported by those authors in 8 of 10 of their MI's, as well as the "low-Temperature subset" of this study, owes its highly oxidized character to the anomalous concentration of incompatible elements (e.g. $Fe_2O_3$) in the transient CBL that surround to olivine crystals experiencing rapid-growth regimes. The textural arrangement resulting of such rapid growth episodes was systematically observed (under the binocular lenses) as dendritic and skeletal crystals, that ultimately provide the opportunity to avoid or notice, previous to the analytical stage, key textural aspects to alert about non-equilibrium conditions captured in MI's. This observation implies that petrographic and textural analysis under the binocular lenses is key to obtain a more complete understanding of the validity of analytical results and finally appraisal the full meaning of trapped melts.

Finally, based in the extended analysis of melt inclusions from different arc localities and contrasted with the samples of this study, it is possible to say that the metallogenic fertile nature of arc magmas above mature subduction zones, like the Central-South Andes, relies in the comparatively more oxidized character of the primitive melts that entrain into the crust from the subarc mantle.

However, the formation of highly-mineralized porphyry systems will only occur if a consecutive scale of processes or features conduce to an optimization of normal ore-forming processes (Richards 2013). Therefore, such high oxidizing condition recorded in these melt inclusions constitute the first and more relevant condition to extract and dissolve metal and sulfur from the mantle wedge, but as melt entrains into the crust, has to be encompassed by periods of high compressive tectonics. Further, at the mid to shallow crust, other optimal circumstances for the development of ore deposition are i) temporal-spatial focusing of Cu-rich fluids, ii) succession of multiple ore forming events and iii) reactive host rocks (Richards 2013).

The succession of optimized processes can be distinguishable in the two world-largest deposits emplaced in the Mio-Pliocene belt of Central Chile. It has been suggested that El Teniente and Río Blanco-Los Bronces deposits, owe its unusually large sizes due a prolongated magmatic-hydrothermal activity as long as ~3 Ma (Stern et al., 2011; Deckart et al., 2014). In addition, at El Teniente, the key feature in its large size, consist of the presence of particularly receptive mafic wallrocks that chemically trapped over 80% of the sulfide mineralization of the

deposit (Richards 2013). Other authors have pointed out that the magmatic activity vinculated to these porphyry systems occurred at the end of a protracted period of compressive deformation, producing shortening and crustal thickening (Giambiagi et al., 2015). The change in the type of deformation south of 35°S (Tapia, 2015) may be the first-order cause of the occurrence of several Mio-Pliocene prospects south of this latitude, for which at present days, has not been reported economically relevant sulfide deposition, despite several efforts of advanced prospection by core-drilling, developed in the recent years, as for instance in Arcángel (35.1°S), Alondra (35.8°S), Brahma-Austral (35.6) and Ventana Cura (36.3°S) prospects.

# REFERENCES


Acocella, V. 2014. Structural control on magmatism along divergent and convergent plate boundaries: Overview, model, problems. Earth-Science Reviews, 136, 226-288.

Annen, C., Blundy, J. D., & Sparks, R. S. J. 2006. The genesis of intermediate and silicic magmas in deep crustal hot zones. Journal of Petrology, 47 (3), 505-539.

Astaburuaga, D. 2014. Evolución estructural del límite Mesozoico-Cenozoico de la Cordillera Principal entre los 35°30' y 36° S, Región del Maule, Chile. Master thesis. Universidad de Chile.

Bacon, C. R., & Druitt, T. H. 1988. Compositional evolution of the zoned calc-alkaline magma chamber of Mount Mazama, Crater Lake, Oregon.Contributions to Mineralogy and Petrology, 98(2), 224-256.

Baedecker, P. A. 1987. Methods for geochemical analysis. US Geological Survey Bulletin 1770. 184 p.

Ballard, J. R., Palin, M. J., & Campbell, I. H. (2002). Relative oxidation states of magmas inferred from Ce (IV)/Ce (III) in zircon: application to porphyry copper deposits of northern Chile. Contributions to Mineralogy and Petrology, 144(3), 347-364.

Beattie, P., Ford, C., & Russell, D. (1991). Partition coefficients for olivine-melt and orthopyroxene-melt systems. Contributions to Mineralogy and Petrology, 109(2), 212-224.

Berg, W. F., & Bragg, W. L. (1938). Crystal growth from solutions. Proceedings of the Royal Society of London. Series A - Mathematical and Physical Sciences, 164(916), 79-95.

Bonali, F. L., Tibaldi, A., & Corazzato, C. 2015. Sensitivity analysis of earthquake-induced static stress changes on volcanoes: the 2010 Mw 8.8 Chile earthquake. Geophysical Journal International, 201(3), 1868-1890.

Botcharnikov, R. E., Linnen, R. L., Wilke, M., Holtz, F., Jugo, P. J., & Berndt, J. (2011). High gold concentrations in sulphide-bearing magma under oxidizing conditions. Nature Geoscience, 4(2), 112-115.

Brounce, M. N., Kelley, K. A., & Cottrell, E. (2014). Variations in Fe3+/∑Fe of Mariana Arc Basalts and Mantle Wedge fO2. Journal of Petrology, 55(12), 2513-2536.

Bucchi, F., Lara, L. E., & Gutiérrez, F. 2015. The Carrán - Los Venados volcanic field and its relationship with coeval and nearby polygenetic volcanism in an intra-arc setting. Journal of Volcanology and Geothermal Research, 308, 70-81.

Carmichael, I. S. (1991). The redox states of basic and silicic magmas: a reflection of their source regions? Contributions to Mineralogy and Petrology, 106(2), 129-141.

Chowdhury, P., & Dasgupta, R. (2019). Effect of sulfate on the basaltic liquidus and sulfur Concentration at Anhydrite Saturation (SCAS) of hydrous basalts–Implications for sulfur cycle in subduction zones. Chemical Geology, 522, 162-174.

Carrol, M. R., & Rutherford, M. J. (1987). The stability of igneous anhydrite: experimental results and implications for sulfur behavior in the 1982 El Chichón trachyandesite and other evolved magmas. J Petrol, 28, 781-801.

Cembrano, J., & Lara, L. 2009. The link between volcanism and tectonics in the southern volcanic zone of the Chilean Andes: a review. Tectonophysics, 471(1), 96-113.

Christie, D. M., Carmichael, I. S., & Langmuir, C. H. (1986). Oxidation states of mid-ocean ridge basalt glasses. Earth and Planetary Science Letters, 79(3-4), 397-411.

Chambefort, I., Dilles, J. H., & Kent, A. J. (2008). Anhydrite-bearing andesite and dacite as a source for sulfur in magmatic-hydrothermal mineral deposits. Geology, 36(9), 719-722.

Chiaradia, M. (2014). Copper enrichment in arc magmas controlled by overriding plate thickness. Nature Geoscience, 7(1), 43-46.

Cooke, D. R., Hollings, P., & Walshe, J. L. (2005). Giant porphyry deposits: characteristics, distribution, and tectonic controls. Economic geology, 100(5), 801-818.

Danyushevsky, L. V., Della-Pasqua, F. N., & Sokolov, S. (2000). Re-equilibration of melt inclusions trapped by magnesian olivine phenocrysts from subduction-related magmas: petrological implications. Contributions to Mineralogy and Petrology, 138(1), 68-83.

Danyushevsky, L. V., McNeill, A. W., & Sobolev, A. V. (2002). Experimental and petrological studies of melt inclusions in phenocrysts from mantle-derived magmas: an overview of techniques, advantages and complications. Chemical Geology, 183(1-4), 5-24.

Danyushevsky, L. V., & Plechov, P. (2011). Petrolog3: Integrated software for modeling crystallization processes. Geochemistry, Geophysics, Geosystems, 12(7).

Davidson, J. P., Morgan, D. J., Charlier, B. L. A., Harlou, R., & Hora, J. M. (2007). Microsampling and Isotopic Analysis of Igneous Rocks: Implications for the Study of Magmatic Systems. Annual Review of Earth and Planetary Sciences, 35(1), 273-311.

de Maisonneuve, C. B., Costa, F., Huber, C., Vonlanthen, P., Bachmann, O., & Dungan, M. A. (2016). How do olivines record magmatic events? Insights from major and trace element zoning. Contributions to Mineralogy and Petrology, 171(6), 56.

Deckart, K., Clark, A. H., Celso, A. A., Ricardo, V. R., Bertens, A. N., Mortensen, J. K., & Fanning, M. (2005). Magmatic and hydrothermal chronology of the giant Río Blanco porphyry copper deposit, central Chile: Implications of an integrated U-Pb and 40Ar/39Ar database. Economic Geology, 100(5), 905-934.

Deckart, K., Silva, W., Spröhnle, C., & Vela, I. (2014). Timing and duration of hydrothermal activity at the Los Bronces porphyry cluster: An update. Mineralium Deposita, 49(5), 535-546.

Dilles, J. H., Kent, A. J., Wooden, J. L., Tosdal, R. M., Koleszar, A., Lee, R. G., & Farmer, L. P. (2015). Zircon compositional evidence for sulfur-degassing from ore-forming arc magmas. Economic Geology, 110(1), 241-251.

Dixon, J. E., & Stolper, E. M. (1995). An experimental study of water and carbon dioxide solubilities in mid-ocean ridge basaltic liquids. Part II: applications to degassing. Journal of Petrology, 36(6), 1633-1646.

Dohmen, R., & Chakraborty, S. (2007). Fe–Mg diffusion in olivine II: Point defect chemistry, change of diffusion mechanisms and a model for calculation of diffusion coefficients in natural olivine. Physics and Chemistry of Minerals, 34(6), 409-430. https://doi.org/10.1007/s00269-007-0158-6

Donaldson, C. H. (1976). An experimental investigation of olivine morphology. Contributions to Mineralogy and Petrology, 57(2), 187-213. https://doi.org/10.1007/BF00405225

Dungan, M. A., Wulff, A., & Thompson, R. 2001. Eruptive stratigraphy of the Tatara–San Pedro complex, 36° S, Southern Volcanic Zone, Chilean Andes: reconstruction method and implications for magma evolution at long-lived arc volcanic centers. Journal of Petrology, 42(3), 555-626.

Eggins, S. M. (1993). Origin and differentiation of picritic arc magmas, Ambae (Aoba), Vanuatu. Contributions to Mineralogy and Petrology, 114(1), 79-100.

Evans, K. A., Elburg, M. A., & Kamenetsky, V. S. (2012). Oxidation state of subarc mantle. Geology, 40(9), 783-786.

Ewart, A., & Griffin, W. L. (1994). Application of proton-microprobe data to trace-element partitioning in volcanic rocks. Chemical Geology, 117(1-4), 251-284.

Farías, M., Comte, D., Roecker, S., Carrizo, D., & Pardo, M. 2011. Crustal extensional faulting triggered by the 2010 Chilean earthquake: The Pichilemu Seismic Sequence. Tectonics, 30(6).

Faure, F., Trolliard, G., Nicollet, C., & Montel, J.-M. (2003). A developmental model of olivine morphology as a function of the cooling rate and the degree of undercooling. Contributions to Mineralogy and Petrology, 145(2), 251-263.

Faure, F, & Schiano, P. (2005). Experimental investigation of equilibration conditions during forsterite growth and melt inclusion formation. Earth and Planetary Science Letters, 236(3-4), 882-898.

Faure, François, Schiano, P., Trolliard, G., Nicollet, C., & Soulestin, B. (2007). Textural evolution of polyhedral olivine experiencing rapid cooling rates. Contributions to Mineralogy and Petrology, 153(4), 405-416.

Faure, F., & Tissandier, L. (2014). Contrasted Liquid Lines of Descent Revealed by Olivine-hosted Melt Inclusions and the External Magma. Journal of Petrology, 55(9), 1779-1798.

Fiege, A., Ruprecht, P., Simon, A. C., Bell, A. S., Göttlicher, J., Newville, M., ... & Moore, G. (2017). Calibration of Fe XANES for high-precision determination of Fe oxidation state in glasses: Comparison of new and existing results obtained at different synchrotron radiation sources. American Mineralogist, 102(2), 369-380.

Frost, B. R. (1991). Introduction to oxygen fugacity and its petrologic importance. Reviews in Mineralogy and Geochemistry, 25, 1-9.

Gazel, E., Plank, T., Forsyth, D. W., Bendersky, C., Lee, C. T. A., & Hauri, E. H. (2012). Lithosphere versus asthenosphere mantle sources at the Big Pine Volcanic Field, California. Geochemistry, Geophysics, Geosystems, 13(6).

Genareau, K., Valentine, G. A., Moore, G., & Hervig, R. L. 2010. Mechanisms for transition in eruptive style at a monogenetic scoria cone revealed by microtextural analyses (Lathrop Wells volcano, Nevada, USA). Bulletin of Volcanology, 72 (5), 593-607.

Giambiagi, L., Tassara, A., Mescua, J., Tunik, M., Alvarez, P. P., Godoy, E., & Tapia, F. 2015. Evolution of shallow and deep structures along the Maipo–Tunuyán transect (33° 40′ S): from the Pacific coast to the Andean foreland. Geological Society, London, Special Publications, 399(1), 63-82.

Giuli, G., Paris, E., Hess, K. U., Dingwell, D. B., Cicconi, M. R., Eeckhout, S. G., ... & Valenti, P. (2011). XAS determination of the Fe local environment and oxidation state in phonolite glasses. American Mineralogist, 96(4), 631-636.

Gordeychik, B., Churikova, T., Kronz, A., Sundermeyer, C., Simakin, A., & Wörner, G. (2018). Growth of, and diffusion in, olivine in ultra-fast ascending basalt magmas from Shiveluch volcano. Scientific Reports, 8(1), 11775.

Grove, T. L., Donnelly-Nolan, J. M., & Housh, T. 1997. Magmatic processes that generated the rhyolite of Glass Mountain, Medicine Lake volcano, N. California. Contributions to Mineralogy and Petrology, 127(3), 205-223.

Hart, S. R., & Davis, K. E. (1978). Nickel partitioning between olivine and silicate melt. Earth and Planetary Science Letters, 40(2), 203-219.

Hartley, M. E., Morgan, D. J., Maclennan, J., Edmonds, M., & Thordarson, T. (2016). Tracking timescales of short-term precursors to large basaltic fissure eruptions through Fe–Mg diffusion in olivine. Earth and Planetary Science Letters, 439, 58-70. https://doi.org/10.1016/j.epsl.2016.01.018

Higgins, M. D., Voos, S., & Vander Auwera, J. 2015. Magmatic processes under Quizapu volcano, Chile, identified from geochemical and textural studies. Contributions to Mineralogy and Petrology, 170(5-6), 1-16.

Hildreth, W., & Moorbath, S. 1988. Crustal contributions to arc magmatism in the Andes of central Chile. Contributions to mineralogy and petrology, 98(4), 455-489.

Hildreth, W., & Drake, R. E. 1992. Volcán Quizapu, Chilean Andes. Bulletin of Volcanology, 54 (2), 93-125.

Hildreth, W., Godoy, E., Fierstein, J., & Singer, B. 2010. Laguna del Maule Volcanic field: eruptive history of a Quaternary basalt-to-rhyolite distributed volcanic field on the Andean range crest in central Chile. Servicio Nacional de Geología y Minería–Chile, Boletin, 63, 142.

Hilton, D. R., Fischer, T. P., & Marty, B. (2002). Noble gases and volatile recycling at subduction zones. Reviews in mineralogy and geochemistry, 47(1), 319-370.

Honour, V. C., Holness, M. B., Charlier, B., Piazolo, S. C., Namur, O., Prosa, T. J., ... & Jean, M. M. (2019). Compositional boundary layers trigger liquid unmixing in a basaltic crystal mush. Nature communications, 10(1), 1-8.

Humphreys, M. C. S., Kearns, S. L., & Blundy, J. D. (2006). SIMS investigation of electron-beam damage to hydrous, rhyolitic glasses: Implications for melt inclusion analysis. American Mineralogist, 91(4), 667-679.

Irarrazaval, V., Sillitoe, R. H., Wilson, A., Toro, J. C., Robles, W., Lyall, G., ... & Monecke, T. (2010). Discovery history of a giant, high-grade, hypogene porphyry copper-molybdenum deposit at Los Sulfatos, Los Bronces-Río Blanco district, central Chile. Society of Economic Geologists Special Publication, 15(14), 253-269.

Jacques, J. 2003. A tectonostratigraphic synthesis of the Sub-Andean basins: implications for the geotectonic segmentation of the Andean Belt. Journal of the Geological Society, 160 (5), 687-701.

Jambon, A., Lussiez, P., Clocchiatti, R., Weisz, J., & Hernandez, J. (1992). Olivine growth rates in a tholeiitic basalt: An experimental study of melt inclusions in plagioclase. Chemical Geology, 96(3-4), 277-287.

Jarosewich, E., Nelen, J. A., & Norberg, J. A. (1980). Reference Samples for Electron Microprobe Analysis*. Geostandards Newsletter, 4(1), 43-47.

Jenner, F. E., O'Neill, H. S. C., Arculus, R. J., & Mavrogenes, J. A. (2010). The magnetite crisis in the evolution of arc-related magmas and the initial concentration of Au, Ag and Cu. Journal of Petrology, 51(12), 2445-2464.

Johnson, D. M., Hooper, P. R., & Conrey, R. M. 1999. XRF analysis of rocks and minerals for major and trace elements on a single low dilution Li-tetraborate fused bead. Advances in X-ray Analysis, 41(843867), 1988.

Johnson, E.; Wallace, P.; Delgado Granados, H., Kent, A. 2008. Magmatic volatile contents and degassing-induced crystallization at Volcán Jorullo, Mexico: Implications for melt evolution and the plumbing systems of monogenetic volcanoes. Earth and Planetary Science Letters 269, 478-487.

Jugo, P. J. (2009). Sulfur content at sulfide saturation in oxidized magmas. Geology, 37(5), 415-418.

Jugo, P. J., Wilke, M., & Botcharnikov, R. E. (2010). Sulfur K-edge XANES analysis of natural and synthetic basaltic glasses: Implications for S speciation and S content as function of oxygen fugacity. Geochimica et Cosmochimica Acta, 74(20), 5926-5938.

Kahl, M., Chakraborty, S., Costa, F., & Pompilio, M. (2011). Dynamic plumbing system beneath volcanoes revealed by kinetic modeling, and the connection to monitoring data: An example from Mt. Etna. Earth and Planetary Science Letters, 308(1-2), 11-22. https://doi.org/10.1016/j.epsl.2011.05.008

Keiding, J. K., Trumbull, R. B., Veksler, I. V., & Jerram, D. A. 2011. On the significance of ultra-magnesian olivines in basaltic rocks. Geology, 39(12), 1095-1098.

Kelley, K. A., & Cottrell, E. (2009). Water and the Oxidation State of Subduction Zone Magmas. Science, 325(5940), 605-607.

Kelley, Katherine A., & Cottrell, E. (2012). The influence of magmatic differentiation on the oxidation state of Fe in a basaltic arc magma. Earth and Planetary Science Letters, 329-330, 109-121.

Kent, A. J., Jacobsen, B., Peate, D. W., Waight, T. E., & Baker, J. A. (2004). Isotope Dilution MC-ICP-MS Rare Earth Element Analysis of Geochemical Reference Materials NIST SRM 610, NIST SRM 612, NIST SRM 614, BHVO-2G, BHVO-2, BCR-2G, JB-2, WS-E, W-2, AGV-1 and AGV-2. Geostandards and Geoanalytical Research, 28(3), 417-429.

Kent, A. J. (2008). Melt inclusions in basaltic and related volcanic rocks. Reviews in Mineralogy and Geochemistry, 69(1), 273-331.

Kinzler, R. J., Grove, T. L., & Recca, S. I. (1990). An experimental study on the effect of temperature and melt composition on the partitioning of nickel between olivine and silicate melt. Geochimica et Cosmochimica Acta, 54(5), 1255-1265.

Kress, V. C., & Carmichael, I. S. (1991). The compressibility of silicate liquids containing Fe2O3 and the effect of composition, temperature, oxygen fugacity and pressure on their redox states. Contributions to Mineralogy and Petrology, 108(1-2), 82-92.

Land, T. A., Martin, T. L., Potapenko, S., Palmore, G. T., & De Yoreo, J. J. (1999). Recovery of surfaces from impurity poisoning during crystal growth. Nature, 399(6735), 442-445. https://doi.org/10.1038/20886

Larrea, P., França, Z., Lago, M., Widom, E., Galé, C., & Ubide, T. 2013. Magmatic processes and the role of antecrysts in the genesis of Corvo Island (Azores Archipelago, Portugal). Journal of Petrology, 54(4), 769-793.

Lee, C. T., Leeman, W. P., Canil, D., & Li, Z. X. A. (2005). Similar V/Sc systematics in MORB and arc basalts: implications for the oxygen fugacities of their mantle source regions. Journal of Petrology, 46(11), 2313-2336.

Lee, C. T. A., Luffi, P., Chin, E. J., Bouchet, R., Dasgupta, R., Morton, D. M., ... & Jin, D. (2012). Copper systematics in arc magmas and implications for crust-mantle differentiation. Science, 336(6077), 64-68.

Libourel, G. 1999. Systematics of calcium partitioning between olivine and silicate melt: implications for melt structure and calcium content of magmatic olivines. Contributions to Mineralogy and Petrology, 136 (1-2), 63-80.

Lloyd, A. S., Plank, T., Ruprecht, P., Hauri, E. H., & Rose, W. (2013). Volatile loss from melt inclusions in pyroclasts of differing sizes. Contributions to Mineralogy and Petrology, 165(1), 129-153.

Lloyd, A. S., Ruprecht, P., Hauri, E. H., Rose, W., Gonnermann, H. M., & Plank, T. (2014). NanoSIMS results from olivine-hosted melt embayments: magma ascent rate during explosive basaltic eruptions. Journal of Volcanology and Geothermal Research, 283, 1-18.

López-Escobar, L., Cembrano, J., & Moreno, H. 1995. Geochemistry and tectonics of the Chilean Southern Andes basaltic Quaternary volcanism (37-46 S). Andean Geology, 22(2), 219-234.

Luhr, J. F. (1990). Experimental phase relations of water-and sulfur-saturated arc magmas and the 1982 eruptions of El Chichón volcano. Journal of Petrology, 31(5), 1071-1114.

Maloney, K.T., Clarke, G.L., Klepeis, K.A. and Quevedo, L., 2013. The Late Jurassic to present evolution of the Andean margin: Drivers and the geological record. Tectonics, 32, 1049-1065.

Masotta, M., & Keppler, H. (2015). Anhydrite solubility in differentiated arc magmas. Geochimica et Cosmochimica Acta, 158, 79-102.

Matjuschkin, V., Blundy, J. D., & Brooker, R. A. (2016). The effect of pressure on sulphur speciation in mid- to deep-crustal arc magmas and implications for the formation of porphyry copper deposits. Contributions to Mineralogy and Petrology, 171(7), 66.

Matzen, A. K., Baker, M. B., Beckett, J. R., Wood, B. J., & Stolper, E. M. (2017). The effect of liquid composition on the partitioning of Ni between olivine and silicate melt. Contributions to Mineralogy and Petrology, 172(1), 3. https://doi.org/10.1007/s00410-016-1319-8

McDonough, W. F., & Sun, S. S. (1995). The composition of the Earth. Chemical geology, 120(3-4), 223-253.

Mescua, J. F., Giambiagi, L. B., Tassara, A., Gimenez, M., & Ramos, V. A. 2014. Influence of pre-Andean history over Cenozoic foreland deformation: Structural styles in the Malargüe fold-and-thrust belt at 35° S, Andes of Argentina. Geosphere, 10(3), 585-609.

Milman-Barris, M. S., Beckett, J. R., Baker, M. B., Hofmann, A. E., Morgan, Z., Crowley, M. R., Vielzeuf, D., & Stolper, E. (2008). Zoning of phosphorus in igneous olivine. Contributions to Mineralogy and Petrology, 155(6), 739-765. https://doi.org/10.1007/s00410-007-0268-7

Moore, L. R., Gazel, E., Tuohy, R., Lloyd, A. S., Esposito, R., Steele-MacInnis, M., ... & Bodnar, R. J. (2015). Bubbles matter: An assessment of the contribution of vapor bubbles to melt inclusion volatile budgets. American Mineralogist, 100(4), 806-823.

Mourey, A. J., & Shea, T. (2019). Forming Olivine Phenocrysts in Basalt: A 3D Characterization of Growth Rates in Laboratory Experiments. Frontiers in Earth Science, 7, 300.

Morgado, E., Parada, M. A., Contreras, C., Castruccio, A., Gutiérrez, F., & McGee, L. E. 2015. Contrasting records from mantle to surface of Holocene lavas of two nearby arc volcanic complexes: Caburgua-Huelemolle Small Eruptive Centers and Villarrica Volcano, Southern Chile. Journal of Volcanology and Geothermal Research, 306, 1-16.

Moussallam, Y., Oppenheimer, C., Scaillet, B., Gaillard, F., Kyle, P., Peters, N., ... & Donovan, A. (2014). Tracking the changing oxidation state of Erebus magmas, from mantle to surface, driven by magma ascent and degassing. Earth and Planetary Science Letters, 393, 200-209.

Mpodozis, C., & Cornejo, P. (2012). Cenozoic tectonics and porphyry copper systems of the Chilean Andes. Society of Economic Geologists Special Publication, 16, 329-360.

Muñoz, J., & Niemeyer, H. 1984. Hoja 64 Laguna del Maule, Regiones del Maule y Bio-Bio. Carta Geológica de Chile, Servicio Nacional de Geologıa y Mineria de Chile, scale, 1:250.000.

Mutch, E. J. F., Maclennan, J., Shorttle, O., Edmonds, M., & Rudge, J. F. (2019). Rapid transcrustal magma movement under Iceland. Nature Geoscience, 12(7), 569-574.

Nakamura, K. 1977. Volcanoes as possible indicators of tectonic stress orientation—principle and proposal. Journal of Volcanology and Geothermal Research, 2(1), 1-16.

Nadeau, O., Williams-Jones, A. E., & Stix, J. (2010). Sulphide magma as a source of metals in arc-related magmatic hydrothermal ore fluids. Nature Geoscience, 3(7), 501-505.

Nash, W. M., Smythe, D. J., & Wood, B. J. (2019). Compositional and temperature effects on sulfur speciation and solubility in silicate melts. Earth and Planetary Science Letters, 507, 187-198.

Németh, K. 2010. Monogenetic volcanic fields: origin, sedimentary record, and relationship with polygenetic volcanism. Geological Society of America Special Papers, 470, 43-66.

Németh, K., & Kereszturi, G. 2015. Monogenetic volcanism: personal views and discussion. International Journal of Earth Sciences, 104(8), 2131-2146.

Newman, S., Stolper, E., & Stern, R. (2000). H2O and CO2 in magmas from the Mariana arc and back arc systems. Geochemistry, Geophysics, Geosystems, 1(5).

Oeser, M., Ruprecht, P., & Weyer, S. (2018). Combined Fe-Mg chemical and isotopic zoning in olivine constraining magma mixing-to-eruption timescales for the continental arc volcano Irazú (Costa Rica) and Cr diffusion in olivine. American Mineralogist, 103(4), 582-599.

Ozawa, S., Nishimura, T., Suito, H., Kobayashi, T., Tobita, M., & Imakiire, T. 2011. Coseismic and postseismic slip of the 2011 magnitude-9 Tohoku-Oki earthquake. Nature, 475(7356), 373-376.

Perelló, J., Sillitoe, R. H., Brockway, H., Posso, H., & Mpodozis, C. (2009). Contiguous porphyry Cu-Mo and Cu-Au mineralization at Los Pelambres, central Chile. Santiago, 22, S11_026.

Piquer, J., Castelli, J. C., Charrier, R., & Yáñez, G. 2010. El Cenozoico del alto río Teno, Cordillera Principal, Chile central: estratigrafía, plutonismo y su relación con estructuras profundas. Andean geology, 37(1), 32-53.

Piquer, J., Skarmeta, J., & Cooke, D. R. 2015. Structural Evolution of the Rio Blanco-Los Bronces District, Andes of Central Chile: Controls on Stratigraphy, Magmatism, and Mineralization. Economic Geology, 110(8), 1995-2023.

Putirka, Keith D., Mikaelian, H., Ryerson, F., & Shaw, H. (2003). New clinopyroxene-liquid thermobarometers for mafic, evolved, and volatile-bearing lava compositions, with applications to lavas from Tibet and the Snake River Plain, Idaho. American Mineralogist, 88(10), 1542-1554.

Putirka, K. D. (2005). Mantle potential temperatures at Hawaii, Iceland, and the mid-ocean ridge system, as inferred from olivine phenocrysts: Evidence for thermally driven mantle plumes. Geochemistry, Geophysics, Geosystems, 6(5).

Putirka, K. D. (2008). Thermometers and Barometers for Volcanic Systems. Reviews in Mineralogy and Geochemistry, 69(1), 61-120.

Rae, A. S. P., Edmonds, M., Maclennan, J., Morgan, D., Houghton, B., Hartley, M. E., & Sides, I. (2016). Time scales of magma transport and mixing at Kīlauea Volcano, Hawai'i. Geology, 44(6), 463-466.

Richards, J. P. (2009). Postsubduction porphyry Cu-Au and epithermal Au deposits: Products of remelting of subduction-modified lithosphere. Geology, 37(3), 247-250.

Richards, J. P. (2013). Giant ore deposits formed by optimal alignments and combinations of geological processes. Nature geoscience, 6(11), 911-916.

Richards, J. P. (2015). The oxidation state, and sulfur and Cu contents of arc magmas: implications for metallogeny. Lithos, 233, 27-45.

Roberge, J., Guilbaud, M. N., Mercer, C. N., & Reyes-Luna, P. C. 2015. Insight into monogenetic eruption processes at Pelagatos volcano, Sierra Chichinautzin, Mexico: a combined melt inclusion and physical volcanology study. Geological Society, London, Special Publications, 410(1), 179-198.

Robidoux, P., Aiuppa, A., Rotolo, S. G., Rizzo, A. L., Hauri, E. H., & Frezzotti, M. L. (2017). Volatile contents of mafic-to-intermediate magmas at San Cristóbal volcano in Nicaragua. Lithos, 272, 147-163.

Robidoux, P., Frezzotti, M. L., Hauri, E. H., & Aiuppa, A. (2018). Shrinkage Bubbles: The C–O–H–S Magmatic Fluid System at San Cristóbal Volcano. Journal of Petrology, 59(11), 2093-2122.

Rodríguez, C., Sellés, D., Dungan, M., Langmuir, C., & Leeman, W. 2007. Adakitic dacites formed by intracrustal crystal fractionation of water-rich parent magmas at Nevado de Longavi volcano (36.2° S; Andean Southern Volcanic Zone, Central Chile). Journal of Petrology, 48(11), 2033-2061.

Roeder, P. L., & Emslie, R. (1970). Olivine-liquid equilibrium. Contributions to mineralogy and petrology, 29(4), 275-289.

Ruprecht, P., Bergantz, G. W., Cooper, K. M., & Hildreth, W. 2012. The crustal magma storage system of Volcán Quizapu, Chile, and the effects of magma mixing on magma diversity. Journal of Petrology, 53 (4): 801-840.

Ruprecht, P., & Cooper, K. M. (2012). Integrating the Uranium-Series and Elemental Diffusion Geochronometers in Mixed Magmas from Volcán Quizapu, Central Chile. Journal of Petrology, 53(4), 841-871.

Ruprecht, P., & Plank, T. 2013. Feeding andesitic eruptions with a high-speed connection from the mantle. Nature, 500(7460), 68-72.

Ruth, D. C. S., Costa, F., Bouvet de Maisonneuve, C., Franco, L., Cortés, J. A., & Calder, E. S. (2018). Crystal and melt inclusion timescales reveal the evolution of magma migration before eruption. Nature Communications, 9(1), 2657. https://doi.org/10.1038/s41467-018-05086-8

Salas, P., Rabbia, O., Ruprecht, P., Bergantz, G. 2009. Geoquímica de los centros eruptivos menores y escoria máfica de la erupción de 1932 del volcán Quizapu, Región del Maule, Chile. XII Congreso Geológico Chileno, Santiago, S8_027, 1-3.

Salas, P. (2010). Geoquímica de los centros eruptivos menores y de la escoria máfica de la erupción pliniana de 1932 del Volcán Quizapu, Región del Maule, Chile. Memoria de título. Universidad de Concepción.

Salas, P., Rabbia, O.M., Hernández L., 2014. High magnesium olivine in basaltic andesites from minor vents of Quizapu volcano, Southern Volcanic Zone, Chile. XIX Congreso Geológico Argentino, Córdoba, S24,1-4.

Salas, P., Rabbia, O.M., Hernández, L. 2015. Compositional evolution of Los Hornitos mafic cones: Insights from whole rock chemistry and high-resolution EMPA profiles in high-forsterite olivine phenocrysts. XIV Congreso Geológico Chileno, At1St3_026.

Salas, P. A., Rabbia, O. M., Hernández, L. B., & Ruprecht, P. (2017). Mafic monogenetic vents at the Descabezado Grande volcanic field (35.5°S–70.8°W): The northernmost evidence of regional primitive volcanism in the Southern Volcanic Zone of Chile. International Journal of Earth Sciences, 106(3), 1107-1121.

Sellés, D., Rodriguez, A., Dungan, M. A., Naranjo, J. A., & Gardeweg, M. 2004. Geochemistry of Nevado de Longaví Volcano (36.2°S): a compositionally atypical arc volcano in the Southern Volcanic Zone of the Andes. Revista geológica de Chile, 31(2), 293-315.

Sellés, D. 2006. Stratigraphy, Petrology, and Geochemistry of Nevado de Longaví Volcano, Chilean Andes (36.2°S). Dissertation, University of Geneve.

Shea, T., Lynn, K. J., & Garcia, M. O. (2015). Cracking the olivine zoning code: Distinguishing between crystal growth and diffusion. Geology, 43(10), 935-938.

Shea, T., Hammer, J. E., Hellebrand, E., Mourey, A. J., Costa, F., First, E. C., Lynn, K. J., & Melnik, O. (2019). Phosphorus and aluminum zoning in olivine: Contrasting behavior of two nominally incompatible trace elements. Contributions to Mineralogy and Petrology, 174(10), 85.

Shen, P., Hattori, K., Pan, H., Jackson, S., & Seitmuratova, E. (2015). Oxidation condition and metal fertility of granitic magmas: zircon trace-element data from porphyry Cu deposits in the Central Asian Orogenic Belt. Economic Geology, 110(7), 1861-1878.

Sillitoe, R. H. (2012). Copper provinces. Society of Economic Geologists Special Publication, 16, 1-18.

Sisson, T. W., & Grove, T. L. 1993. Experimental investigations of the role of H2O in calc-alkaline differentiation and subduction zone magmatism. Contributions to Mineralogy and Petrology, 113(2), 143-166.

Sleutel, M., Lutsko, J., & Van Driessche, A. E. S. (2018). Mineral Growth beyond the Limits of Impurity Poisoning. Crystal Growth & Design, 18(1), 171-178.

Sobolev, A. V., Hofmann, A. W., Kuzmin, D. V., Yaxley, G. M., Arndt, N. T., Chung, S.-L., Danyushevsky, L. V., Elliott, T., Frey, F. A., Garcia, M. O., Gurenko, A. A., Kamenetsky, V. S., Kerr, A. C., Krivolutskaya, N. A., Matvienkov, V. V., Nikogosian, I. K., Rocholl, A., Sigurdsson, I. A., Sushchevskaya, N. M., & Teklay, M. (2007). The Amount of Recycled Crust in Sources of Mantle-Derived Melts. Science, 316(5823), 412-417.

Stern, C. R. 2004. Active Andean volcanism: its geologic and tectonic setting. Revista geológica de Chile, 31(2), 161-206.

Stern, C. R., Skewes, M. A., & Arévalo, A. (2011). Magmatic evolution of the giant El Teniente Cu–Mo deposit, central Chile. Journal of Petrology, 52(7-8), 1591-1617.

Straub, S. M., LaGatta, A. B., Martin-Del Pozzo, A. L., & Langmuir, C. H. (2008). Evidence from high-Ni olivines for a hybridized peridotite/pyroxenite source for orogenic andesites from the central Mexican Volcanic Belt: Andesite petrogenesis in Central MVB. Geochemistry, Geophysics, Geosystems, 9(3).

Straub, S. M., Gomez-Tuena, A., Stuart, F. M., Zellmer, G. F., Espinasa-Perena, R., Cai, Y., & Iizuka, Y. (2011). Formation of hybrid arc andesites beneath thick continental crust. Earth and Planetary Science Letters, 303(3), 337-347.

Takada, Y., & Fukushima, Y. 2013. Volcanic subsidence triggered by the 2011 Tohoku earthquake in Japan. Nature Geoscience, 6(8), 637-641.

Tapia, F. 2015. Evolución tectónica y configuración actual de los Andes Centrales del Sur (34°45'-35°30'S). Tesis para optar al grado de Doctor en Ciencias, Mención Geología. Universidad de Chile.

Tassara, A., Götze, H.-J., Schmidt, S., & Hackney, R. (2006). Three-dimensional density model of the Nazca plate and the Andean continental margin. Journal of Geophysical Research, 111(B9), B09404.

Tassara, A., & Echaurren, A. (2012). Anatomy of the Andean subduction zone: Three-dimensional density model upgraded and compared against global-scale models: Anatomy of the Andean subduction zone. Geophysical Journal International, 189(1), 161-168.

Tassara, S., Reich, M., Cannatelli, C., Konecke, B. A., Kausel, D., Morata, D., Barra, F., Simon, A. C., Fiege, A., Morgado, E., & Leisen, M. (2020). Post-melting oxidation of highly primitive basalts from the southern Andes. Geochimica et Cosmochimica Acta, 273, 291-312.

Ubide, T., Mollo, S., Zhao, J., Nazzari, M., & Scarlato, P. (2019). Sector-zoned clinopyroxene as a recorder of magma history, eruption triggers, and ascent rates. Geochimica et Cosmochimica Acta, 251, 265-283.

Valentine, G. A., & Gregg, T. K. P. 2008. Continental basaltic volcanoes-processes and problems. Journal of Volcanology and Geothermal Research, 177 (4), 857-873.

Vergara, M., & Munoz, J. 2010. La Formación Cola de Zorro en la alta cordillera andina chilena (36°-39° Lat. S), sus características petrográficas y petrológicas: una revisión. Andean Geology, (17).

Viccaro, M., Giuffrida, M., Nicotra, E., & Cristofolini, R. (2016). Timescales of magma storage and migration recorded by olivine crystals in basalts of the March–April 2010 eruption at Eyjafjallajökull volcano, Iceland. American Mineralogist, 101(1), 222-230.

Völker, D., Kutterolf, S., & Wehrmann, H. 2011. Comparative mass balance of volcanic edifices at the southern volcanic zone of the Andes between 33° S and 46° S. Journal of Volcanology and Geothermal Research, 205(3), 114-129.

Wallace, P. J. (2005). Volatiles in subduction zone magmas: concentrations and fluxes based on melt inclusion and volcanic gas data. Journal of volcanology and Geothermal Research, 140(1-3), 217-240.

Watson, E. B., & Müller, T. (2009). Non-equilibrium isotopic and elemental fractionation during diffusion-controlled crystal growth under static and dynamic conditions. Chemical Geology, 267(3-4), 111-124.

Weaver, S. L., Wallace, P. J., & Johnston, A. D. 2011. A comparative study of continental vs. intraoceanic arc mantle melting: Experimentally determined phase relations of hydrous primitive melts. Earth and Planetary Science Letters, 308(1), 97-106.

Wehrmann, H., Hoernle, K., Jacques, G., Garbe-Schönberg, D., Schumann, K., Mahlke, J., & Lara, L. E. 2014. Volatile (sulphur and chlorine), major, and trace element geochemistry of mafic to intermediate tephras from the Chilean Southern Volcanic Zone (33–43 S). International Journal of Earth Sciences,103(7), 1945-1962.

Weller, D. J., & Stern, C. R. (2018). Along-strike variability of primitive magmas (major and volatile elements) inferred from olivine-hosted melt inclusions, southernmost Andean Southern Volcanic Zone, Chile. Lithos, 296, 233-244.

Welsch, B., Faure, F., Famin, V., Baronnet, A., & Bachèlery, P. (2013). Dendritic Crystallization: A Single Process for all the Textures of Olivine in Basalts? Journal of Petrology, 54(3), 539-574.

Welsch, B., Hammer, J., & Hellebrand, E. (2014). Phosphorus zoning reveals dendritic architecture of olivine. Geology, 42(10), 867-870.

Welsch, B., Hammer, J., Baronnet, A., Jacob, S., Hellebrand, E., & Sinton, J. (2016). Clinopyroxene in postshield Haleakala ankaramite: 2. Texture, compositional zoning and supersaturation in the magma. Contributions to Mineralogy and Petrology, 171(1), 6.

Wilke, M., Partzsch, G. M., Bernhardt, R., & Lattard, D. (2004). Determination of the iron oxidation state in basaltic glasses using XANES at the K-edge. Chemical Geology, 213(1-3), 71-87.

Wilkinson, J. J. (2013). Triggers for the formation of porphyry ore deposits in magmatic arcs. Nature Geoscience, 6(11), 917-925.

Wolff, A. 2005. Age and petrogenesis of lavas from the Casitas shield, Descabezado Grande-Cerro Azul volcanic complex, Chilean Andes. In 2005 Salt Lake City Annual Meeting.

Wolff, A. 2008. Chemical stratigraphy of lavas from the Casitas Shield, Descabezado Grande-cerro Azul volcanic complex, Chilean Andes. Goldschmidt Conference

Wood, B. J., Bryndzia, L. T., & Johnson, K. E. (1990). Mantle oxidation state and its relationship to tectonic environment and fluid speciation. Science, 248(4953), 337-345.

Zhang, Y., Ni, H., & Chen, Y. (2010). Diffusion data in silicate melts. Reviews in Mineralogy and Geochemistry, 72(1), 311-408.

Zellmer, G. F., Sakamoto, N., Hwang, S.-L., Matsuda, N., Iizuka, Y., Moebis, A., & Yurimoto, H. (2016). Inferring the Effects of Compositional Boundary Layers on Crystal Nucleation, Growth Textures, and Mineral Chemistry in Natural Volcanic Tephras through Submicron-Resolution Imaging. Frontiers in Earth Science.

# Appendix Chapter 2

## Prospecting the most mafic compositions among the post-glaciation monogenetic vents of the arc region between 35.5° to 36.5°.

Article title: Mafic monogenetic vents at the Descabezado Grande volcanic field (35.5°S-70.8°W): the northernmost evidence of regional primitive volcanism in the Southern Volcanic Zone of Chile

Pablo Salas[1]*, Osvaldo Rabbia[2*], Laura Hernández[2], Philipp Ruprecht[3]

[1]Departamento de Ciencias de la Tierra, Universidad de Concepción, Chile.

[2]Instituto de Geología Económica Aplicada GEA, Universidad de Concepción, Chile.

*E-mail: rabbia@udec.cl

[3]Lamont-Doherty Earth Observatory of Columbia University, 61 Route 9W, Palisades, NY 10964, USA.

Table A.2.1: Major element plus Ni and Cr composition of eruptive products from Holocene monogenetic vents and the terminal scoria of Quizapu 1932 event.

| Sample | $SiO_2$ wt % | $TiO_2$ wt % | $Al_2O_3$ wt % | FeO wt % | MnO wt % | MgO wt % | CaO wt % | $Na_2O$ wt % | $K_2O$ wt % | $P_2O_5$ wt % | Total wt % | Ni ppm | Cr ppm |
|---|---|---|---|---|---|---|---|---|---|---|---|---|---|
| ***Los Hornitos (LHMC)*** | | | | | | | | | | | | | |
| HOR-06-01 | 53.55 | 0.81 | 17.42 | 7.48 | 0.14 | 5.55 | 9.46 | 3.30 | 0.98 | 0.17 | 98.86 | 32 | 109<br>120 |
| CLHE-TF4 | 51.51 | 0.64 | 13.99 | 8.13 | 0.15 | 13.66 | 9.26 | 2.38 | 0.65 | 0.12 | 100.49 | 347 | 9 |
| CLHE1 | 54.35 | 0.83 | 17.76 | 7.56 | 0.14 | 5.49 | 9.70 | 3.38 | 1.00 | 0.17 | 100.37 | 26 | 105 |
| CLHE2 | 54.08 | 0.79 | 17.02 | 7.67 | 0.14 | 6.92 | 9.45 | 3.30 | 0.99 | 0.17 | 100.50 | 60 | 199 |
| CLHW1 | 53.73 | 0.88 | 17.91 | 7.51 | 0.14 | 6.06 | 9.58 | 3.38 | 0.98 | 0.18 | 100.35 | 31 | 122 |
| CLHW4 | 54.17 | 0.83 | 17.66 | 7.39 | 0.13 | 5.34 | 9.47 | 3.46 | 1.07 | 0.18 | 99.71 | 48 | 139 |
| ***La Resolana (LRMC)*** | | | | | | | | | | | | | |
| RES-06-01 | 54.94 | 0.89 | 17.38 | 7.13 | 0.13 | 5.10 | 7.85 | 3.84 | 1.37 | 0.21 | 98.85 | 43 | 84 |
| CLRN2 | 55.01 | 0.92 | 17.80 | 7.39 | 0.14 | 5.24 | 8.31 | 3.83 | 1.30 | 0.22 | 100.15 | 32 | 65 |
| CLRS2 | 54.44 | 0.99 | 18.35 | 7.38 | 0.14 | 4.79 | 8.93 | 3.83 | 1.22 | 0.24 | 100.31 | 19 | 57 |
| ***Quizapu terminal scoria 1932 (TQZP)*** | | | | | | | | | | | | | |
| VQ-18 | 54.27 | 0.97 | 17.91 | 7.21 | 0.13 | 4.77 | 8.03 | 3.75 | 1.29 | 0.21 | 98.50 | 67 | 110 |
| VQ-42 | 54.42 | 0.97 | 17.91 | 7.14 | 0.13 | 4.72 | 8.02 | 3.77 | 1.33 | 0.21 | 98.60 | 38 | 63 |
| Q-9* | 59.65 | 0.80 | 17.39 | 5.82 | 0.11 | 3.29 | 5.90 | 4.40 | 2.07 | 0.19 | 100.10 | - | - |
| Q-16* | 54.50 | 1.00 | 17.95 | 7.55 | 0.13 | 4.86 | 8.26 | 3.80 | 1.29 | 0.22 | 100.50 | - | - |
| Q-18* | 55.30 | 0.96 | 17.95 | 7.21 | 0.12 | 4.50 | 7.96 | 3.92 | 1.42 | 0.22 | 99.90 | - | - |
| Q-17* | 52.60 | 1.04 | 18.62 | 8.03 | 0.13 | 5.35 | 9.12 | 3.55 | 0.98 | 0.23 | 100.70 | - | - |
| Q-89* | 52.10 | 1.05 | 18.71 | 8.11 | 0.13 | 5.43 | 9.01 | 3.82 | 0.99 | 0.22 | 99.60 | - | - |

Measurement uncertainties are as reported by Baedecker (1987), Bacon and Druitt (1988) and Johnson et al. (1999). *Data from Hildreth and Drake, 1992.

Table A.2.2: Olivine major and minor element composition expressed as wt %.

| | $SiO_2$ | FeO | MnO | CaO | MgO | NiO | Total | Fo |
|---|---|---|---|---|---|---|---|---|
| | wt % | wt % | wt % | wt % | wt % | wt % | wt % | % |
| ***LHMC – Tephra*** | | | | | | | | |
| CLH_OL1 | 40.83 | 10.69 | 0.16 | 0.16 | 47.37 | 0.266 | 99.47 | 88.76 |
| CLH_OL10.1 | 40.79 | 11.35 | 0.19 | 0.18 | 46.76 | 0.162 | 99.43 | 88.01 |
| CLH_OL12 | 41.26 | 8.91 | 0.12 | 0.13 | 48.61 | 0.354 | 99.38 | 90.67 |
| CLH_OL1 | 40.76 | 10.33 | 0.15 | 0.16 | 48.07 | 0.278 | 99.74 | 89.24 |
| CLH_OL10.1 | 40.83 | 11.37 | 0.19 | 0.18 | 47.21 | 0.184 | 99.98 | 88.10 |
| CLH_OL12 | 41.08 | 9.17 | 0.13 | 0.14 | 49.19 | 0.363 | 100.07 | 90.53 |
| CLH_OL15 | 41.01 | 9.33 | 0.14 | 0.14 | 48.78 | 0.347 | 99.75 | 90.31 |
| CLH_OL16 | 41.03 | 9.29 | 0.14 | 0.13 | 49.24 | 0.345 | 100.18 | 90.43 |
| CLH_OL18 | 40.91 | 10.12 | 0.17 | 0.16 | 48.43 | 0.254 | 100.05 | 89.51 |
| CLH_OL19 | 41.34 | 8.06 | 0.11 | 0.14 | 50.00 | 0.451 | 100.09 | 91.71 |
| CLH_OL20 | 41.07 | 10.68 | 0.17 | 0.17 | 48.07 | 0.272 | 100.42 | 88.92 |
| CLH_OL23 | 41.46 | 7.62 | 0.11 | 0.13 | 50.45 | 0.464 | 100.22 | 92.19 |
| CLH_OL25.1 | 40.27 | 13.32 | 0.22 | 0.24 | 45.44 | 0.068 | 99.55 | 85.88 |
| CLH_OL25.2 | 41.03 | 10.49 | 0.17 | 0.12 | 48.08 | 0.227 | 100.12 | 89.09 |
| CLH_OL26 | 40.93 | 9.96 | 0.17 | 0.14 | 48.40 | 0.262 | 99.85 | 89.65 |
| CLH_OL27 | 41.02 | 9.47 | 0.13 | 0.15 | 48.66 | 0.358 | 99.78 | 90.16 |
| CLH_OL28 | 40.96 | 9.79 | 0.15 | 0.13 | 48.62 | 0.345 | 100.00 | 89.85 |
| CLH_OL35 | 40.75 | 10.89 | 0.14 | 0.15 | 47.52 | 0.185 | 99.65 | 88.61 |
| CLH_OL36-1 | 39.36 | 18.89 | 0.30 | 0.19 | 41.13 | 0.123 | 100.00 | 79.51 |
| CLH_OL36-2 | 41.00 | 9.12 | 0.14 | 0.13 | 49.43 | 0.347 | 100.18 | 90.62 |
| CLH_OL37 | 40.82 | 9.93 | 0.16 | 0.15 | 48.70 | 0.284 | 100.04 | 89.73 |
| CLH_OL38.1 | 39.42 | 17.37 | 0.30 | 0.19 | 41.98 | 0.083 | 99.34 | 81.16 |
| CLH_OL38.2 | 41.11 | 8.78 | 0.14 | 0.11 | 49.42 | 0.385 | 99.94 | 90.94 |
| CLH_OL39 | 38.05 | 24.83 | 0.41 | 0.23 | 36.43 | 0.038 | 99.99 | 72.34 |
| CLH_OL40 | 40.74 | 10.20 | 0.15 | 0.14 | 48.12 | 0.217 | 99.57 | 89.37 |
| CLH_OL41 | 40.60 | 11.34 | 0.16 | 0.13 | 47.54 | 0.169 | 99.94 | 88.20 |
| CLHE_OL7_1 | 40.94 | 8.87 | 0.11 | 0.11 | 49.14 | 0.414 | 99.59 | 90.80 |
| CLHE_OL10.1 | 41.08 | 9.76 | 0.16 | 0.14 | 48.02 | 0.246 | 99.42 | 89.76 |
| CLHE_OL10.2 | 40.69 | 9.87 | 0.13 | 0.13 | 48.15 | 0.262 | 99.24 | 89.69 |
| CLHE_OL11.1 | 40.95 | 9.65 | 0.17 | 0.14 | 48.39 | 0.238 | 99.54 | 89.94 |
| CLHE_OL12.1 | 41.03 | 8.69 | 0.14 | 0.13 | 49.17 | 0.387 | 99.55 | 90.98 |
| CLHE_OL13.2.1 | 39.92 | 13.92 | 0.24 | 0.25 | 45.08 | 0.048 | 99.47 | 85.23 |
| CLHE_OL13.2.2 | 40.57 | 10.64 | 0.18 | 0.17 | 47.44 | 0.216 | 99.21 | 88.82 |
| CLHE_OL15.1 | 41.11 | 8.06 | 0.12 | 0.13 | 49.70 | 0.392 | 99.51 | 91.66 |
| CLHE_OL16.1.1 | 40.55 | 9.55 | 0.15 | 0.15 | 48.32 | 0.288 | 99.01 | 90.02 |
| CLHE_OL16.1.2 | 40.83 | 9.08 | 0.14 | 0.15 | 48.85 | 0.326 | 99.37 | 90.56 |
| CLHE_OL16.2.1 | 40.77 | 8.68 | 0.14 | 0.13 | 48.76 | 0.359 | 98.84 | 90.92 |
| CLHE_OL17.1 | 40.52 | 11.64 | 0.20 | 0.18 | 46.68 | 0.083 | 99.30 | 87.73 |
| CLHE_OL18.1 | 40.71 | 9.89 | 0.16 | 0.16 | 47.36 | 0.248 | 98.54 | 89.51 |
| CLHE_OL19.1 | 40.75 | 8.62 | 0.14 | 0.13 | 49.81 | 0.335 | 99.79 | 91.15 |
| CLHE_OL19.2.1 | 40.88 | 8.62 | 0.11 | 0.13 | 48.88 | 0.383 | 99.00 | 91.00 |
| CLHE_OL20.1 | 39.91 | 13.22 | 0.21 | 0.19 | 45.67 | 0.049 | 99.26 | 86.03 |
| CLHE_OL20.2 | 40.90 | 8.62 | 0.13 | 0.13 | 49.10 | 0.405 | 99.27 | 91.03 |
| CLHE_OL21.2 | 40.63 | 10.61 | 0.16 | 0.13 | 47.49 | 0.202 | 99.22 | 88.86 |
| CLHE_OL22.1 | 40.58 | 11.11 | 0.18 | 0.21 | 47.53 | 0.137 | 99.76 | 88.41 |
| CLHE_OL22.2 | 40.83 | 9.83 | 0.15 | 0.15 | 48.56 | 0.290 | 99.82 | 89.80 |
| CLHE_OL23.1 | 40.49 | 10.64 | 0.18 | 0.18 | 47.81 | 0.151 | 99.45 | 88.90 |
| CLHE_OL24.1 | 40.47 | 10.52 | 0.18 | 0.18 | 47.81 | 0.206 | 99.36 | 89.01 |
| CLHE_OL25.1 | 40.80 | 9.46 | 0.14 | 0.15 | 48.49 | 0.233 | 99.28 | 90.13 |
| CLHE_OL3.1 | 40.64 | 9.60 | 0.14 | 0.12 | 48.45 | 0.363 | 99.32 | 89.99 |
| CLHE_OL4.1 | 40.24 | 10.92 | 0.19 | 0.17 | 47.15 | 0.116 | 98.79 | 88.50 |
| CLHE_OL4.2 | 41.09 | 8.69 | 0.14 | 0.13 | 49.35 | 0.371 | 99.77 | 91.01 |
| CLHE_OL5.1 | 40.12 | 13.91 | 0.24 | 0.24 | 45.12 | 0.048 | 99.68 | 85.25 |
| CLHE_OL5.2 | 41.08 | 9.20 | 0.15 | 0.14 | 48.85 | 0.328 | 99.75 | 90.44 |

| | $SiO_2$ | FeO | MnO | CaO | MgO | NiO | Total | Fo |
|---|---|---|---|---|---|---|---|---|
| | wt % | wt % | wt % | wt % | wt % | wt % | wt % | % |
| CLHE_OL7.2 | 40.58 | 11.15 | 0.18 | 0.19 | 47.48 | 0.085 | 99.67 | 88.36 |
| CLHE_OL9.1 | 40.43 | 10.67 | 0.17 | 0.16 | 47.57 | 0.192 | 99.18 | 88.82 |
| CLHE_OL9.2 | 40.52 | 10.73 | 0.17 | 0.15 | 47.01 | 0.182 | 98.76 | 88.65 |
| | | | | | | | | |
| ***LHMC - Lava*** | | | | | | | | |
| CLHE-2(1)-1 | 39.59 | 14.63 | 0.21 | 0.15 | 45.50 | 0.110 | 100.20 | 84.72 |
| CLHE-2(1)-2 | 37.46 | 25.91 | 0.44 | 0.23 | 35.61 | 0.009 | 99.69 | 71.01 |
| CLHE-2(2)-1 | 39.84 | 15.67 | 0.23 | 0.14 | 45.17 | 0.100 | 101.17 | 83.71 |
| CLHE-2(2)-2 | 38.40 | 24.77 | 0.42 | 0.22 | 36.99 | 0.025 | 100.84 | 72.69 |
| CLHE-2(3)-1 | 39.68 | 15.40 | 0.14 | 0.14 | 45.40 | 0.071 | 100.91 | 84.01 |
| CLHE-2(3)-3 | 38.36 | 21.59 | 0.35 | 0.19 | 40.02 | 0.050 | 100.56 | 76.76 |
| CLHE-2(4)-1 | 40.00 | 14.83 | 0.20 | 0.14 | 45.55 | 0.093 | 100.83 | 84.55 |
| CLHE-2(4)-2 | 38.25 | 22.41 | 0.40 | 0.21 | 39.31 | 0.029 | 100.61 | 75.76 |
| CLHE-2(10)-1 | 38.84 | 21.25 | 0.34 | 0.18 | 40.42 | 0.050 | 101.11 | 77.22 |
| CLHE-2(10)-2 | 36.62 | 31.46 | 0.54 | 0.27 | 31.40 | 0.004 | 100.33 | 64.01 |
| CLHE-2(7)-1 | 39.83 | 15.47 | 0.22 | 0.14 | 45.19 | 0.080 | 100.94 | 83.89 |
| CLHE-2(7)-2 | 38.53 | 22.10 | 0.38 | 0.18 | 39.07 | 0.041 | 100.31 | 75.91 |
| CLHE-2(6)-1 | 39.83 | 16.18 | 0.22 | 0.15 | 44.34 | 0.078 | 100.83 | 83.01 |
| CLHE-2(6)-2 | 37.70 | 27.71 | 0.43 | 0.23 | 34.54 | 0.018 | 100.66 | 68.95 |
| CLHE-2(20)-1 | 38.61 | 20.99 | 0.35 | 0.17 | 40.57 | 0.038 | 100.76 | 77.50 |
| CLHE-2(20)-2 | 37.73 | 26.20 | 0.44 | 0.24 | 35.82 | 0.006 | 100.45 | 70.90 |
| CLHE-2(19)-1 | 39.46 | 18.30 | 0.28 | 0.16 | 42.31 | 0.025 | 100.56 | 80.47 |
| CLHE-2(19)-2 | 38.01 | 24.92 | 0.41 | 0.22 | 36.42 | 0.003 | 100.01 | 72.26 |
| CLHE-2(15)-1 | 39.76 | 14.51 | 0.21 | 0.13 | 46.21 | 0.121 | 100.96 | 85.02 |
| CLHE-2(15)-2 | 38.88 | 21.87 | 0.35 | 0.19 | 39.42 | 0.053 | 100.77 | 76.26 |
| CLHE-2(15)-3 | 38.19 | 23.71 | 0.41 | 0.22 | 37.26 | 0.028 | 99.83 | 73.69 |
| CLHE-2(8)-1 | 39.59 | 15.82 | 0.23 | 0.17 | 44.54 | 0.075 | 100.44 | 83.38 |
| CLHE-2(8)-2 | 39.69 | 16.12 | 0.24 | 0.17 | 44.51 | 0.070 | 100.83 | 83.11 |
| CLHE-2(8)-3 | 39.83 | 15.80 | 0.20 | 0.15 | 44.88 | 0.107 | 100.99 | 83.50 |
| CLHE-2(8)-4 | 37.80 | 25.23 | 0.43 | 0.24 | 36.58 | 0.044 | 100.34 | 72.10 |
| CLHE-2(11)-1 | 40.07 | 15.93 | 0.23 | 0.15 | 45.23 | 0.106 | 101.73 | 83.50 |
| CLHE-2(11)-2 | 38.29 | 25.11 | 0.43 | 0.21 | 37.12 | 0.023 | 101.19 | 72.49 |
| CLHE-2(12)-1 | 40.01 | 14.36 | 0.20 | 0.14 | 46.15 | 0.139 | 101.02 | 85.14 |
| CLHE-2(12)-2 | 38.20 | 24.11 | 0.40 | 0.21 | 37.43 | 0.021 | 100.40 | 73.45 |
| CLHE-2(13)-1 | 39.30 | 14.88 | 0.21 | 0.15 | 45.34 | 0.108 | 100.00 | 84.45 |
| CLHE-2(13)-2 | 38.52 | 20.78 | 0.33 | 0.18 | 40.51 | 0.037 | 100.38 | 77.65 |
| CLHE-2(17)-1 | 39.47 | 15.57 | 0.22 | 0.14 | 44.82 | 0.095 | 100.33 | 83.69 |
| ***QZP Tephra*** | | | | | | | | |
| QZP_OL10.1 | 37.93 | 24.09 | 0.39 | 0.25 | 36.27 | 0.000 | 98.94 | 72.85 |
| QZP_OL10.2 | 38.06 | 24.48 | 0.41 | 0.22 | 36.11 | 0.050 | 99.32 | 72.44 |
| QZP_OL11.1 | 38.39 | 22.46 | 0.37 | 0.20 | 37.77 | 0.018 | 99.21 | 74.98 |
| QZP_OL11.2 | 38.72 | 20.67 | 0.35 | 0.18 | 39.34 | 0.082 | 99.34 | 77.23 |
| QZP_OL11.3 | 38.80 | 21.08 | 0.35 | 0.23 | 39.02 | 0.005 | 99.49 | 76.74 |
| QZP_OL12.1 | 38.24 | 22.88 | 0.37 | 0.24 | 37.39 | 0.048 | 99.17 | 74.44 |
| QZP_OL12.2 | 38.15 | 22.86 | 0.38 | 0.24 | 37.66 | 0.020 | 99.32 | 74.59 |
| QZP_OL12.3 | 37.40 | 22.85 | 0.36 | 0.24 | 35.18 | 0.043 | 96.09 | 73.29 |
| QZP_OL13.1 | 37.82 | 24.73 | 0.43 | 0.26 | 36.02 | 0.000 | 99.26 | 72.19 |
| QZP_OL14.1 | 37.99 | 24.98 | 0.44 | 0.23 | 35.66 | 0.034 | 99.33 | 71.79 |
| QZP_OL15.1 | 38.08 | 25.48 | 0.40 | 0.21 | 35.73 | 0.000 | 99.89 | 71.42 |
| QZP_OL16.1 | 37.91 | 24.83 | 0.43 | 0.23 | 36.22 | 0.023 | 99.65 | 72.22 |
| QZP_OL17.2 | 38.10 | 25.00 | 0.44 | 0.25 | 35.49 | 0.056 | 99.32 | 71.67 |
| QZP_OL18.1 | 38.26 | 21.79 | 0.35 | 0.23 | 38.6 | 0.000 | 99.22 | 75.95 |
| QZP_OL18.2 | 38.18 | 22.49 | 0.38 | 0.22 | 37.5 | 0.069 | 98.85 | 74.82 |
| QZP_OL2.1 | 37.73 | 25.83 | 0.45 | 0.26 | 34.84 | 0.064 | 99.18 | 70.62 |
| QZP_OL2.2 | 37.92 | 24.44 | 0.42 | 0.24 | 36.04 | 0.010 | 99.07 | 72.44 |
| QZP_OL2.3 | 38.08 | 23.63 | 0.39 | 0.23 | 36.82 | 0.075 | 99.23 | 73.52 |
| QZP_OL3.1 | 38.19 | 23.55 | 0.39 | 0.20 | 36.61 | 0.013 | 98.95 | 73.48 |

| | $SiO_2$ | FeO | MnO | CaO | MgO | NiO | Total | Fo |
|---|---|---|---|---|---|---|---|---|
| | wt % | wt % | wt % | wt % | wt % | wt % | wt % | % |
| QZP_OL4.1 | 38.42 | 21.82 | 0.35 | 0.22 | 38.45 | 0.039 | 99.31 | 75.85 |
| QZP_OL5.1 | 38.80 | 19.54 | 0.28 | 0.17 | 40.46 | 0.000 | 99.26 | 78.68 |
| QZP_OL6.2 | 37.98 | 25.11 | 0.45 | 0.24 | 35.84 | 0.000 | 99.61 | 71.78 |
| QZP_OL7.1 | 38.29 | 23.88 | 0.41 | 0.25 | 32.38 | 0.072 | 95.29 | 70.73 |
| QZP_OL7.2 | 37.85 | 25.38 | 0.42 | 0.25 | 35.74 | 0.000 | 99.64 | 71.51 |
| QZP_OL9.1 | 38.08 | 23.20 | 0.38 | 0.25 | 37.39 | 0.078 | 99.37 | 74.18 |
| QZP_OL1 | 38.32 | 24.76 | 0.43 | 0.23 | 35.85 | 0.064 | 99.67 | 72.07 |
| QZP_OL51 | 39.48 | 17.84 | 0.26 | 0.15 | 41.41 | 0.106 | 99.25 | 80.53 |
| QZP_OL1.2 | 38.04 | 25.05 | 0.42 | 0.26 | 36.22 | 0.031 | 100.02 | 72.04 |
| QZP_OL10 | 38.97 | 20.84 | 0.33 | 0.19 | 39.3 | 0.063 | 99.70 | 77.07 |
| QZP_OL11 | 38.03 | 23.78 | 0.41 | 0.24 | 37.23 | 0.046 | 99.73 | 73.62 |
| QZP_OL12 | 38.41 | 23.92 | 0.41 | 0.22 | 37.06 | 0.067 | 100.08 | 73.41 |
| QZP_OL13 | 39.03 | 21.21 | 0.36 | 0.22 | 38.54 | 0.089 | 99.46 | 76.41 |
| QZP_OL15.1 | 39.10 | 20.13 | 0.33 | 0.17 | 40.31 | 0.094 | 100.13 | 78.11 |
| QZP_OL15.2 | 38.67 | 21.22 | 0.36 | 0.20 | 39.20 | 0.114 | 99.76 | 76.70 |
| QZP_OL17 | 38.35 | 24.88 | 0.44 | 0.24 | 36.36 | 0.031 | 100.29 | 72.26 |
| QZP_OL19 | 39.25 | 19.45 | 0.29 | 0.18 | 40.75 | 0.097 | 100.02 | 78.88 |
| QZP_OL2 | 38.13 | 23.57 | 0.37 | 0.24 | 37.30 | 0.082 | 99.69 | 73.83 |
| QZP_OL20 | 38.56 | 22.04 | 0.37 | 0.20 | 38.23 | 0.100 | 99.50 | 75.56 |
| QZP_OL21 | 38.35 | 23.47 | 0.39 | 0.20 | 37.21 | 0.053 | 99.67 | 73.86 |
| QZP_OL22 | 38.63 | 22.55 | 0.39 | 0.21 | 38.22 | 0.053 | 100.05 | 75.13 |
| QZP_OL23 | 38.43 | 23.36 | 0.38 | 0.24 | 37.54 | 0.062 | 100.01 | 74.12 |
| QZP_OL24 | 39.16 | 20.42 | 0.34 | 0.19 | 39.47 | 0.083 | 99.65 | 77.50 |
| QZP_OL25 | 39.46 | 18.49 | 0.29 | 0.16 | 41.86 | 0.125 | 100.38 | 80.14 |
| QZP_OL26 | 37.90 | 25.14 | 0.41 | 0.22 | 35.83 | 0.054 | 99.55 | 71.75 |
| QZP_OL27 | 38.19 | 23.28 | 0.38 | 0.22 | 37.73 | 0.073 | 99.87 | 74.28 |
| QZP_OL29 | 38.74 | 22.61 | 0.37 | 0.26 | 38.28 | 0.068 | 100.32 | 75.11 |
| QZP_OL3.1 | 39.08 | 20.75 | 0.33 | 0.17 | 39.68 | 0.132 | 100.13 | 77.32 |
| QZP_OL3.2 | 38.44 | 24.05 | 0.39 | 0.19 | 36.96 | 0.080 | 100.11 | 73.25 |
| QZP_OL30 | 36.22 | 28.44 | 0.46 | 0.22 | 31.16 | 0.000 | 96.51 | 66.13 |
| QZP_OL31 | 38.10 | 23.70 | 0.42 | 0.24 | 36.44 | 0.086 | 98.98 | 73.26 |
| QZP_OL32 | 38.53 | 22.56 | 0.39 | 0.26 | 37.75 | 0.074 | 99.56 | 74.89 |
| QZP_OL33 | 38.46 | 23.13 | 0.42 | 0.19 | 37.32 | 0.092 | 99.61 | 74.20 |
| QZP_OL34 | 38.24 | 25.32 | 0.43 | 0.24 | 36.05 | 0.064 | 100.35 | 71.73 |
| QZP_OL35 | 37.90 | 25.60 | 0.45 | 0.23 | 35.40 | 0.044 | 99.62 | 71.14 |
| QZP_OL36 | 38.54 | 23.16 | 0.40 | 0.21 | 37.80 | 0.034 | 100.14 | 74.42 |
| QZP_OL37 | 37.94 | 25.60 | 0.46 | 0.21 | 35.39 | 0.049 | 99.65 | 71.13 |
| QZP_OL38 | 39.20 | 21.16 | 0.31 | 0.19 | 39.44 | 0.058 | 100.35 | 76.86 |
| QZP_OL39 | 38.52 | 23.46 | 0.39 | 0.23 | 37.08 | 0.052 | 99.73 | 73.80 |
| QZP_OL4 | 37.62 | 26.27 | 0.44 | 0.22 | 35.05 | 0.025 | 99.63 | 70.40 |
| QZP_OL40 | 38.73 | 21.96 | 0.36 | 0.20 | 38.53 | 0.098 | 99.87 | 75.77 |
| QZP_OL42 | 38.50 | 22.83 | 0.39 | 0.21 | 37.67 | 0.072 | 99.67 | 74.62 |
| QZP_OL43 | 38.56 | 22.71 | 0.37 | 0.18 | 38.03 | 0.052 | 99.91 | 74.90 |
| QZP_OL44 | 38.82 | 22.27 | 0.38 | 0.22 | 38.19 | 0.033 | 99.92 | 75.35 |
| QZP_OL46 | 37.94 | 25.09 | 0.44 | 0.22 | 36.28 | 0.052 | 100.03 | 72.04 |
| QZP_OL48 | 38.77 | 21.46 | 0.35 | 0.22 | 39.01 | 0.074 | 99.89 | 76.41 |
| QZP_OL49 | 38.43 | 21.52 | 0.34 | 0.23 | 39.10 | 0.074 | 99.68 | 76.41 |
| QZP_OL5 | 38.14 | 22.34 | 0.00 | 0.00 | 36.39 | 0.043 | 96.92 | 74.38 |
| QZP_OL5 | 37.58 | 24.30 | 0.00 | 0.00 | 36.66 | 0.076 | 98.62 | 72.89 |
| QZP_OL50 | 38.44 | 23.16 | 0.39 | 0.20 | 37.29 | 0.000 | 99.49 | 74.16 |
| QZP_OL51 | 39.39 | 18.03 | 0.25 | 0.14 | 41.76 | 0.121 | 99.70 | 80.50 |
| QZP_OL52 | 37.19 | 30.51 | 0.46 | 0.23 | 31.40 | 0.039 | 99.83 | 64.72 |
| QZP_OL53 | 39.76 | 17.22 | 0.24 | 0.17 | 42.31 | 0.122 | 99.82 | 81.41 |
| QZP_OL54 | 38.60 | 25.26 | 0.45 | 0.25 | 35.02 | 0.012 | 99.60 | 71.19 |
| QZP_OL55 | 38.24 | 25.91 | 0.45 | 0.25 | 35.25 | 0.057 | 100.16 | 70.80 |
| QZP_OL56 | 38.29 | 24.32 | 0.38 | 0.24 | 36.54 | 0.040 | 99.81 | 72.81 |
| QZP_OL57 | 38.18 | 23.65 | 0.40 | 0.25 | 37.29 | 0.081 | 99.84 | 73.75 |

| | $SiO_2$ | FeO | MnO | CaO | MgO | NiO | Total | Fo |
|---|---|---|---|---|---|---|---|---|
| | wt % | wt % | wt % | wt % | wt % | wt % | wt % | % |
| QZP_OL58 | 39.11 | 21.21 | 0.34 | 0.21 | 39.49 | 0.040 | 100.40 | 76.84 |
| QZP_OL59 | 38.80 | 21.07 | 0.34 | 0.17 | 39.55 | 0.048 | 99.99 | 76.99 |
| QZP_OL6 | 38.85 | 22.33 | 0.34 | 0.18 | 38.31 | 0.015 | 100.02 | 75.36 |
| QZP_OL7 | 38.29 | 22.20 | 0.35 | 0.26 | 38.64 | 0.069 | 99.81 | 75.62 |
| QZP_OL8 | 38.50 | 22.82 | 0.41 | 0.19 | 38.25 | 0.039 | 100.20 | 74.92 |
| ***LRMC NORTH*** | | | | | | | | |
| CLRN3-Test | 39.19 | 17.93 | 0.26 | 0.13 | 41.93 | 0.119 | 99.55 | 80.65 |
| CLRN3-gmTEST2 | 37.09 | 27.43 | 0.50 | 0.24 | 33.77 | 0.009 | 99.05 | 68.69 |
| CLRN3_OL1.2 | 38.08 | 21.30 | 0.36 | 0.16 | 38.83 | 0.073 | 98.81 | 76.47 |
| CLRN3_OL1.2 | 38.37 | 21.82 | 0.37 | 0.16 | 38.42 | 0.053 | 99.19 | 75.83 |
| CLRN3_OL10 | 39.78 | 15.65 | 0.23 | 0.12 | 43.15 | 0.154 | 99.09 | 83.09 |
| CLRN3_OL11 | 39.82 | 15.63 | 0.23 | 0.13 | 43.56 | 0.123 | 99.5 | 83.24 |
| CLRN3_OL12.2 | 39.59 | 16.97 | 0.24 | 0.14 | 42.76 | 0.139 | 99.84 | 81.79 |
| CLRN3_OL12.3 | 39.72 | 16.75 | 0.23 | 0.12 | 42.72 | 0.133 | 99.68 | 81.97 |
| CLRN3_OL12.4 | 39.62 | 16.24 | 0.23 | 0.13 | 43.08 | 0.097 | 99.39 | 82.54 |
| CLRN3_OL13.1 | 39.53 | 17.64 | 0.26 | 0.15 | 42.19 | 0.120 | 99.88 | 81.00 |
| CLRN3_OL13.2 | 39.19 | 17.28 | 0.25 | 0.13 | 42.42 | 0.124 | 99.39 | 81.40 |
| CLRN3_OL13.3 | 38.87 | 19.10 | 0.28 | 0.17 | 40.97 | 0.058 | 99.44 | 79.27 |
| CLRN3_OL14.1 | 38.52 | 21.58 | 0.38 | 0.16 | 38.47 | 0.034 | 99.14 | 76.06 |
| CLRN3_OL2.10 | 39.55 | 17.77 | 0.26 | 0.14 | 41.6 | 0.090 | 99.42 | 80.67 |
| CLRN3_OL2.11 | 38.70 | 21.15 | 0.38 | 0.16 | 38.49 | 0.083 | 98.96 | 76.43 |
| CLRN3_OL2.12 | 38.33 | 24.20 | 0.47 | 0.21 | 35.56 | 0.025 | 98.80 | 72.37 |
| CLRN3_OL2.2 | 38.30 | 22.97 | 0.42 | 0.20 | 37.05 | 0.056 | 98.99 | 74.19 |
| CLRN3_OL2.3 | 38.90 | 20.04 | 0.31 | 0.16 | 40.03 | 0.054 | 99.49 | 78.07 |
| CLRN3_OL2.4 | 39.75 | 16.82 | 0.26 | 0.14 | 42.54 | 0.087 | 99.60 | 81.84 |
| CLRN3_OL2.5 | 39.68 | 17.10 | 0.24 | 0.13 | 42.29 | 0.101 | 99.55 | 81.51 |
| CLRN3_OL2.6 | 39.53 | 17.60 | 0.26 | 0.16 | 41.84 | 0.078 | 99.47 | 80.91 |
| CLRN3_OL2.7 | 39.64 | 18.04 | 0.29 | 0.14 | 41.29 | 0.074 | 99.46 | 80.31 |
| CLRN3_OL2.8 | 39.26 | 18.24 | 0.30 | 0.15 | 41.11 | 0.071 | 99.13 | 80.07 |
| CLRN3_OL2.9 | 39.85 | 16.85 | 0.25 | 0.13 | 42.56 | 0.113 | 99.75 | 81.82 |
| CLRN3_OL3.2 | 39.51 | 16.67 | 0.23 | 0.12 | 42.88 | 0.106 | 99.52 | 82.09 |
| CLRN3_OL3.3 | 39.32 | 17.36 | 0.27 | 0.15 | 42.37 | 0.104 | 99.58 | 81.31 |
| CLRN3_OL4.1 | 39.47 | 17.79 | 0.26 | 0.13 | 42.03 | 0.094 | 99.78 | 80.81 |
| CLRN3_OL4.2 | 39.49 | 17.78 | 0.26 | 0.15 | 41.88 | 0.110 | 99.67 | 80.76 |
| CLRN3_OL5.1 | 39.53 | 17.82 | 0.26 | 0.13 | 41.59 | 0.081 | 99.41 | 80.62 |
| CLRN3_OL6.1 | 38.02 | 25.90 | 0.48 | 0.21 | 34.41 | 0.032 | 99.05 | 70.31 |
| CLRN3_OL6.2 | 39.02 | 20.37 | 0.34 | 0.16 | 39.23 | 0.012 | 99.13 | 77.44 |
| CLRN3_OL7.1 | 38.01 | 24.52 | 0.45 | 0.25 | 35.42 | 0.010 | 98.67 | 72.02 |
| CLRN3_OL7.2 | 39.33 | 18.59 | 0.30 | 0.16 | 40.98 | 0.042 | 99.41 | 79.71 |
| CLRN3_OL7.3 | 39.00 | 18.28 | 0.28 | 0.17 | 40.71 | 0.071 | 98.51 | 79.88 |
| CLRN3_OL8 | 39.92 | 15.75 | 0.24 | 0.13 | 43.11 | 0.135 | 99.28 | 82.99 |
| CLRN3_OL9 | 39.62 | 17.27 | 0.25 | 0.12 | 41.11 | 0.123 | 98.49 | 80.93 |
| CLRN5_OL1.1 | 37.77 | 25.39 | 0.49 | 0.13 | 35.15 | 0.020 | 98.96 | 71.16 |
| CLRN5_OL1.2 | 39.22 | 18.16 | 0.30 | 0.14 | 41.26 | 0.058 | 99.14 | 80.20 |
| CLRN5_OL1.3 | 39.54 | 16.89 | 0.23 | 0.13 | 42.32 | 0.109 | 99.22 | 81.70 |
| CLRN5_OL1.4 | 39.71 | 16.24 | 0.23 | 0.13 | 43.05 | 0.114 | 99.47 | 82.53 |
| CLRN5_OL2.1 | 37.54 | 26.99 | 0.55 | 0.21 | 33.57 | 0.040 | 98.89 | 68.91 |
| CLRN5_OL2.2 | 38.90 | 20.16 | 0.30 | 0.15 | 40.15 | 0.060 | 99.72 | 78.02 |
| CLRN5_OL3.1 | 36.96 | 29.56 | 0.66 | 0.22 | 31.26 | 0.039 | 98.70 | 65.34 |
| CLRN5_OL3.2 | 37.96 | 24.11 | 0.46 | 0.12 | 36.03 | 0.014 | 98.69 | 72.70 |
| CLRN5_OL3.3 | 37.83 | 23.72 | 0.41 | 0.13 | 36.52 | 0.055 | 98.66 | 73.29 |
| CLRN5_OL4 | 39.40 | 20.17 | 0.33 | 0.15 | 38.5 | 0.072 | 98.62 | 77.28 |
| CLRN5_OL5.1 | 37.62 | 27.49 | 0.58 | 0.20 | 33.12 | 0.052 | 99.07 | 68.23 |
| CLRN5_OL5.2 | 39.07 | 19.84 | 0.31 | 0.12 | 39.52 | 0.065 | 98.93 | 78.02 |
| CLRN5_OL6.2 | 37.65 | 21.42 | 0.36 | 0.13 | 35.46 | 0.075 | 95.10 | 74.69 |
| CLRN5_OL6.3 | 39.38 | 19.24 | 0.33 | 0.14 | 40.78 | 0.087 | 99.95 | 79.07 |

| | $SiO_2$ | FeO | MnO | CaO | MgO | NiO | Total | Fo |
|---|---|---|---|---|---|---|---|---|
| | wt % | wt % | wt % | wt % | wt % | wt % | wt % | % |
| CLRN5_OL7.1 | 38.33 | 24.04 | 0.45 | 0.11 | 36.33 | 0.051 | 99.32 | 72.93 |
| CLRN5_OL7.2 | 39.10 | 19.03 | 0.31 | 0.15 | 40.58 | 0.085 | 99.25 | 79.17 |
| CLRN5_OL8 | 38.48 | 23.34 | 0.39 | 0.12 | 37.04 | 0.056 | 99.42 | 73.88 |
| CLRN5_OL9.1 | 38.58 | 24.99 | 0.47 | 0.16 | 34.4 | 0.033 | 98.63 | 71.04 |
| CLRN5_OL9.2 | 39.25 | 20.10 | 0.30 | 0.15 | 40.05 | 0.032 | 99.89 | 78.03 |
| ***LRMC SOUTH*** | | | | | | | | |
| CLRS_OL1.1 | 38.61 | 21.93 | 0.39 | 0.13 | 38.11 | 0.052 | 99.22 | 75.59 |
| CLRS_OL2 | 39.86 | 17.32 | 0.27 | 0.16 | 42.21 | 0.048 | 99.88 | 81.29 |
| CLRS_OL3.1 | 38.63 | 21.14 | 0.37 | 0.20 | 39.12 | 0.034 | 99.50 | 76.73 |
| CLRS_OL3.2 | 39.51 | 18.44 | 0.29 | 0.14 | 41.68 | 0.064 | 100.12 | 80.11 |
| CLRS_OL3.3 | 39.64 | 17.17 | 0.28 | 0.17 | 42.25 | 0.101 | 99.61 | 81.43 |
| CLRS_OL4 | 39.31 | 18.05 | 0.30 | 0.16 | 41.75 | 0.050 | 99.62 | 80.48 |
| CLRS_OL5 | 39.40 | 17.93 | 0.30 | 0.17 | 41.62 | 0.038 | 99.46 | 80.53 |
| CLRS_OL6 | 39.39 | 17.54 | 0.28 | 0.17 | 41.45 | 0.101 | 98.92 | 80.81 |
| CLRS_OL7.1 | 38.99 | 20.11 | 0.32 | 0.13 | 39.49 | 0.054 | 99.11 | 77.78 |
| CLRS_OL7.2 | 38.95 | 20.57 | 0.34 | 0.16 | 40.2 | 0.088 | 100.31 | 77.69 |
| CLRS_OL9.1 | 39.67 | 18.41 | 0.28 | 0.14 | 41.37 | 0.028 | 99.90 | 80.02 |
| CLRS_OL9.2 | 38.34 | 23.44 | 0.40 | 0.13 | 36.84 | 0.000 | 99.16 | 73.69 |

# Appendix Chapter 3

## Textural analysis of olivine hosts: avoiding/noticing growth textures out of equilibrium.

Manuscript title: The early structure of olivine from subduction zones and its missing zoning

Pablo Salas[1]*, Philipp Ruprecht[2], Laura Hernández[3], Osvaldo Rabbia[3]

[1]Departamento de Ciencias de la Tierra, Universidad de Concepción, Chile. **E-mail: pabsalas@udec.cl*

[2]Department of Geological Sciences and Engineering, University of Nevada, Reno, United States.

[3]Instituto de Geología Económica Aplicada GEA, Universidad de Concepción, Chile.

Table A.3.1.- Compositional data of olivine discussed through the text separated by textural classification.

| Location in profile (mm) | $SiO_2$ wt% | $Al_2O_3$ wt% | FeO wt% | MnO wt% | NiO wt% | MgO wt% | CaO wt% | Total wt% | Fo mol% | Ni ppm |
|---|---|---|---|---|---|---|---|---|---|---|
| Group 1 olivine OL_37 | | | | | | | | | | |
| 0,440 | 40,16 | n.m. | 10,02 | 0,144 | 0,199 | 48,70 | 0,176 | 99,39 | 89,64 | 1561 |
| 0,432 | 40,20 | n.m. | 9,50 | 0,161 | 0,262 | 48,98 | 0,159 | 99,26 | 90,18 | 2057 |
| 0,424 | 40,07 | n.m. | 9,15 | 0,145 | 0,296 | 49,23 | 0,155 | 99,06 | 90,55 | 2329 |
| 0,416 | 40,30 | n.m. | 9,37 | 0,146 | 0,277 | 49,55 | 0,145 | 99,79 | 90,40 | 2174 |
| 0,408 | 40,26 | n.m. | 9,52 | 0,146 | 0,278 | 48,95 | 0,144 | 99,30 | 90,15 | 2184 |
| 0,400 | 40,25 | n.m. | 9,34 | 0,146 | 0,302 | 49,33 | 0,131 | 99,50 | 90,39 | 2376 |
| 0,384 | 40,15 | n.m. | 8,88 | 0,137 | 0,378 | 49,59 | 0,137 | 99,27 | 90,86 | 2972 |
| 0,376 | 40,43 | n.m. | 8,45 | 0,143 | 0,366 | 50,43 | 0,145 | 99,97 | 91,40 | 2877 |
| 0,368 | 40,65 | n.m. | 8,44 | 0,133 | 0,345 | 49,80 | 0,134 | 99,51 | 91,31 | 2714 |
| 0,360 | 40,35 | n.m. | 8,46 | 0,104 | 0,383 | 50,56 | 0,128 | 99,99 | 91,41 | 3008 |
| 0,352 | 40,34 | n.m. | 8,30 | 0,134 | 0,403 | 50,65 | 0,129 | 99,95 | 91,57 | 3170 |
| 0,344 | 40,41 | n.m. | 8,25 | 0,140 | 0,412 | 49,96 | 0,129 | 99,30 | 91,51 | 3235 |
| 0,336 | 40,27 | n.m. | 8,27 | 0,141 | 0,422 | 50,08 | 0,131 | 99,31 | 91,51 | 3316 |
| 0,328 | 40,70 | n.m. | 8,10 | 0,138 | 0,430 | 50,45 | 0,131 | 99,95 | 91,73 | 3378 |
| 0,320 | 40,30 | n.m. | 7,95 | 0,141 | 0,436 | 50,44 | 0,124 | 99,39 | 91,87 | 3427 |
| 0,312 | 40,90 | n.m. | 7,73 | 0,133 | 0,435 | 50,13 | 0,132 | 99,45 | 92,03 | 3417 |
| 0,304 | 40,44 | n.m. | 7,99 | 0,154 | 0,438 | 51,26 | 0,133 | 100,42 | 91,95 | 3438 |
| 0,296 | 40,45 | n.m. | 7,87 | 0,127 | 0,449 | 50,24 | 0,128 | 99,27 | 91,91 | 3528 |
| 0,288 | 40,38 | n.m. | 7,83 | 0,104 | 0,421 | 50,27 | 0,131 | 99,13 | 91,96 | 3305 |
| 0,280 | 40,31 | n.m. | 7,95 | 0,121 | 0,416 | 50,37 | 0,124 | 99,30 | 91,86 | 3268 |
| 0,272 | 40,63 | n.m. | 7,82 | 0,133 | 0,445 | 50,78 | 0,124 | 99,93 | 92,04 | 3499 |
| 0,256 | 40,57 | n.m. | 7,77 | 0,113 | 0,448 | 51,40 | 0,117 | 100,42 | 92,18 | 3520 |
| 0,248 | 40,66 | n.m. | 7,84 | 0,117 | 0,442 | 50,31 | 0,116 | 99,49 | 91,95 | 3470 |
| 0,240 | 40,63 | n.m. | 7,69 | 0,149 | 0,434 | 50,05 | 0,118 | 99,07 | 92,06 | 3414 |
| 0,232 | 40,64 | n.m. | 7,66 | 0,111 | 0,431 | 50,20 | 0,127 | 99,17 | 92,11 | 3389 |
| 0,224 | 40,20 | n.m. | 7,66 | 0,114 | 0,437 | 50,86 | 0,127 | 99,38 | 92,20 | 3430 |
| 0,216 | 40,19 | n.m. | 7,71 | 0,146 | 0,440 | 50,49 | 0,132 | 99,10 | 92,10 | 3461 |
| 0,208 | 40,85 | n.m. | 7,75 | 0,136 | 0,452 | 50,15 | 0,127 | 99,48 | 92,02 | 3554 |
| 0,200 | 40,51 | n.m. | 7,76 | 0,149 | 0,416 | 50,08 | 0,121 | 99,04 | 92,00 | 3272 |
| 0,192 | 40,84 | n.m. | 7,76 | 0,135 | 0,446 | 50,69 | 0,126 | 100,00 | 92,08 | 3508 |
| 0,184 | 40,53 | n.m. | 7,71 | 0,134 | 0,457 | 50,99 | 0,125 | 99,95 | 92,17 | 3590 |
| 0,176 | 40,65 | n.m. | 7,69 | 0,109 | 0,442 | 50,61 | 0,120 | 99,62 | 92,14 | 3470 |
| 0,168 | 40,33 | n.m. | 7,84 | 0,124 | 0,453 | 50,16 | 0,127 | 99,03 | 91,93 | 3557 |
| 0,160 | 40,74 | n.m. | 7,84 | 0,113 | 0,440 | 50,37 | 0,132 | 99,63 | 91,96 | 3461 |
| 0,152 | 40,41 | n.m. | 7,95 | 0,119 | 0,428 | 50,12 | 0,133 | 99,16 | 91,82 | 3360 |
| 0,144 | 40,27 | n.m. | 8,20 | 0,153 | 0,423 | 50,53 | 0,128 | 99,71 | 91,65 | 3326 |
| 0,136 | 40,39 | n.m. | 8,18 | 0,122 | 0,416 | 50,05 | 0,136 | 99,29 | 91,59 | 3270 |
| 0,128 | 40,66 | n.m. | 8,32 | 0,155 | 0,387 | 50,14 | 0,133 | 99,79 | 91,48 | 3041 |
| 0,120 | 40,59 | n.m. | 8,29 | 0,141 | 0,389 | 49,78 | 0,134 | 99,32 | 91,45 | 3054 |
| 0,112 | 40,33 | n.m. | 8,37 | 0,146 | 0,353 | 50,09 | 0,134 | 99,42 | 91,42 | 2773 |
| 0,104 | 40,45 | n.m. | 8,54 | 0,159 | 0,373 | 49,95 | 0,127 | 99,61 | 91,24 | 2932 |
| 0,096 | 40,32 | n.m. | 8,57 | 0,125 | 0,371 | 49,84 | 0,141 | 99,37 | 91,19 | 2917 |
| 0,088 | 40,24 | n.m. | 8,64 | 0,156 | 0,379 | 50,18 | 0,141 | 99,73 | 91,18 | 2981 |
| 0,080 | 40,28 | n.m. | 8,59 | 0,121 | 0,360 | 49,87 | 0,140 | 99,35 | 91,18 | 2829 |
| 0,072 | 40,42 | n.m. | 8,77 | 0,140 | 0,346 | 50,02 | 0,130 | 99,84 | 91,04 | 2717 |
| 0,064 | 40,11 | n.m. | 8,65 | 0,158 | 0,325 | 49,76 | 0,134 | 99,14 | 91,11 | 2557 |
| 0,056 | 40,43 | n.m. | 9,13 | 0,142 | 0,325 | 49,53 | 0,133 | 99,69 | 90,62 | 2552 |

| Location in profile (mm) | $SiO_2$ wt% | $Al_2O_3$ wt% | FeO wt% | MnO wt% | NiO wt% | MgO wt% | CaO wt% | Total wt% | Fo mol% | Ni ppm |
|---|---|---|---|---|---|---|---|---|---|---|
| 0,040 | 39,98 | n.m. | 9,69 | 0,195 | 0,267 | 49,00 | 0,142 | 99,27 | 90,01 | 2095 |
| 0,032 | 40,33 | n.m. | 9,51 | 0,147 | 0,271 | 49,29 | 0,141 | 99,69 | 90,22 | 2126 |
| 0,024 | 40,44 | n.m. | 9,34 | 0,173 | 0,285 | 49,26 | 0,149 | 99,64 | 90,38 | 2240 |
| 0,016 | 40,30 | n.m. | 8,95 | 0,130 | 0,321 | 49,65 | 0,155 | 99,50 | 90,81 | 2522 |
| 0,008 | 40,33 | n.m. | 9,34 | 0,141 | 0,303 | 49,31 | 0,155 | 99,58 | 90,39 | 2384 |
| 0,000 | 40,16 | n.m. | 11,29 | 0,196 | 0,183 | 48,13 | 0,173 | 100,13 | 88,36 | 1437 |
| OL_39 | | | | | | | | | | |
| 0,000 | 40,07 | 0,0257 | 12,18 | 0,185 | 0,131 | 48,10 | 0,208 | 100,90 | 87,55 | 1031 |
| 0,007 | 39,94 | 0,0271 | 11,31 | 0,181 | 0,144 | 47,71 | 0,197 | 99,50 | 88,25 | 1133 |
| 0,014 | 40,45 | 0,0235 | 10,45 | 0,158 | 0,221 | 49,36 | 0,176 | 100,84 | 89,38 | 1734 |
| 0,021 | 40,25 | 0,0213 | 9,93 | 0,152 | 0,258 | 49,29 | 0,161 | 100,06 | 89,84 | 2028 |
| 0,028 | 40,46 | 0,0244 | 9,46 | 0,142 | 0,305 | 49,73 | 0,152 | 100,27 | 90,35 | 2398 |
| 0,035 | 40,56 | 0,0244 | 9,17 | 0,131 | 0,338 | 50,06 | 0,143 | 100,43 | 90,67 | 2658 |
| 0,042 | 40,45 | 0,0225 | 8,95 | 0,127 | 0,368 | 50,14 | 0,137 | 100,19 | 90,89 | 2894 |
| 0,049 | 40,72 | 0,0247 | 8,96 | 0,127 | 0,362 | 50,17 | 0,139 | 100,51 | 90,89 | 2843 |
| 0,056 | 40,41 | 0,0264 | 8,92 | 0,118 | 0,364 | 50,42 | 0,138 | 100,40 | 90,96 | 2861 |
| 0,063 | 40,58 | 0,0229 | 8,88 | 0,126 | 0,366 | 50,56 | 0,140 | 100,68 | 91,02 | 2873 |
| 0,070 | 40,63 | 0,0242 | 8,83 | 0,130 | 0,365 | 50,38 | 0,135 | 100,50 | 91,04 | 2867 |
| 0,077 | 40,45 | 0,0225 | 8,96 | 0,131 | 0,351 | 50,62 | 0,136 | 100,68 | 90,96 | 2759 |
| 0,084 | 40,43 | 0,0256 | 9,00 | 0,130 | 0,343 | 49,72 | 0,138 | 99,79 | 90,77 | 2695 |
| 0,091 | 40,60 | 0,0263 | 9,04 | 0,130 | 0,355 | 50,28 | 0,138 | 100,57 | 90,83 | 2789 |
| 0,098 | 40,44 | 0,0276 | 8,98 | 0,128 | 0,354 | 50,37 | 0,133 | 100,44 | 90,90 | 2779 |
| 0,105 | 40,49 | 0,0236 | 8,98 | 0,128 | 0,338 | 50,48 | 0,138 | 100,57 | 90,92 | 2655 |
| 0,112 | 40,30 | 0,0236 | 9,00 | 0,129 | 0,372 | 50,51 | 0,140 | 100,47 | 90,90 | 2925 |
| 0,119 | 40,80 | 0,0246 | 8,76 | 0,123 | 0,364 | 50,51 | 0,133 | 100,71 | 91,13 | 2857 |
| 0,126 | 40,35 | 0,0261 | 8,63 | 0,120 | 0,383 | 50,43 | 0,130 | 100,07 | 91,23 | 3012 |
| 0,133 | 40,26 | 0,0263 | 8,59 | 0,118 | 0,396 | 50,72 | 0,129 | 100,24 | 91,32 | 3114 |
| 0,140 | 40,62 | 0,0275 | 8,39 | 0,119 | 0,417 | 50,70 | 0,125 | 100,40 | 91,50 | 3275 |
| 0,147 | 40,25 | 0,0321 | 8,32 | 0,109 | 0,446 | 50,69 | 0,125 | 99,97 | 91,56 | 3506 |
| 0,161 | 40,35 | 0,0287 | 8,09 | 0,111 | 0,454 | 50,55 | 0,125 | 99,71 | 91,75 | 3567 |
| 0,175 | 40,61 | 0,0273 | 7,81 | 0,106 | 0,475 | 51,18 | 0,122 | 100,33 | 92,11 | 3733 |
| 0,182 | 40,27 | 0,0252 | 7,83 | 0,107 | 0,469 | 51,31 | 0,121 | 100,13 | 92,11 | 3688 |
| 0,189 | 40,41 | 0,0306 | 7,80 | 0,111 | 0,478 | 51,24 | 0,123 | 100,19 | 92,13 | 3757 |
| 0,196 | 40,37 | 0,029 | 7,82 | 0,109 | 0,472 | 51,12 | 0,124 | 100,04 | 92,09 | 3708 |
| 0,203 | 40,35 | 0,0248 | 7,84 | 0,110 | 0,457 | 50,91 | 0,123 | 99,82 | 92,04 | 3591 |
| 0,210 | 40,35 | 0,0318 | 7,84 | 0,111 | 0,461 | 51,30 | 0,126 | 100,22 | 92,10 | 3622 |
| 0,217 | 40,33 | 0,0337 | 7,90 | 0,112 | 0,458 | 51,05 | 0,126 | 100,01 | 92,01 | 3600 |
| 0,224 | 40,51 | 0,035 | 7,93 | 0,111 | 0,462 | 50,94 | 0,125 | 100,11 | 91,96 | 3630 |
| 0,231 | 40,08 | 0,0308 | 7,91 | 0,113 | 0,475 | 51,27 | 0,123 | 100,00 | 92,03 | 3730 |
| 0,238 | 40,31 | 0,0265 | 7,91 | 0,113 | 0,473 | 51,09 | 0,122 | 100,04 | 92,00 | 3717 |
| 0,245 | 40,36 | 0,0286 | 7,91 | 0,111 | 0,460 | 51,02 | 0,123 | 100,01 | 91,99 | 3611 |
| 0,252 | 40,34 | 0,0249 | 8,01 | 0,111 | 0,474 | 51,02 | 0,125 | 100,10 | 91,90 | 3725 |
| 0,259 | 40,26 | 0,0291 | 8,14 | 0,116 | 0,458 | 50,81 | 0,126 | 99,93 | 91,75 | 3602 |
| 0,266 | 40,24 | 0,0247 | 8,18 | 0,105 | 0,462 | 50,88 | 0,123 | 100,02 | 91,72 | 3628 |
| 0,273 | 40,07 | 0,0289 | 8,18 | 0,107 | 0,446 | 50,73 | 0,123 | 99,69 | 91,70 | 3507 |
| 0,280 | 39,79 | 0,0329 | 8,34 | 0,117 | 0,439 | 50,41 | 0,123 | 99,25 | 91,50 | 3453 |
| 0,287 | 40,51 | 0,0274 | 8,46 | 0,123 | 0,425 | 50,16 | 0,124 | 99,83 | 91,35 | 3341 |
| 0,294 | 39,98 | 0,0244 | 8,62 | 0,121 | 0,385 | 50,48 | 0,126 | 99,74 | 91,25 | 3028 |
| 0,301 | 40,04 | 0,0273 | 8,73 | 0,123 | 0,382 | 49,83 | 0,129 | 99,26 | 91,04 | 3004 |
| 0,308 | 40,33 | 0,0239 | 8,75 | 0,127 | 0,368 | 50,26 | 0,133 | 100,00 | 91,09 | 2890 |
| 0,315 | 39,92 | 0,0253 | 8,99 | 0,127 | 0,356 | 50,25 | 0,135 | 99,80 | 90,87 | 2795 |
| 0,322 | 39,90 | 0,0277 | 9,04 | 0,128 | 0,359 | 50,04 | 0,132 | 99,63 | 90,79 | 2821 |
| 0,329 | 40,01 | 0,0246 | 9,07 | 0,131 | 0,346 | 50,22 | 0,138 | 99,94 | 90,79 | 2716 |
| 0,336 | 39,80 | 0,0226 | 8,99 | 0,134 | 0,342 | 50,05 | 0,135 | 99,47 | 90,84 | 2691 |
| 0,343 | 40,32 | 0,0223 | 9,03 | 0,124 | 0,338 | 50,45 | 0,139 | 100,42 | 90,87 | 2659 |

| Location in profile (mm) | $SiO_2$ wt% | $Al_2O_3$ wt% | FeO wt% | MnO wt% | NiO wt% | MgO wt% | CaO wt% | Total wt% | Fo mol% | Ni ppm |
|---|---|---|---|---|---|---|---|---|---|---|
| 0,350 | 40,01 | 0,0266 | 9,03 | 0,129 | 0,363 | 49,91 | 0,131 | 99,60 | 90,78 | 2850 |
| 0,357 | 40,26 | 0,023 | 8,83 | 0,127 | 0,357 | 50,09 | 0,139 | 99,83 | 90,99 | 2809 |
| 0,364 | 39,88 | 0,0209 | 8,89 | 0,133 | 0,368 | 49,77 | 0,137 | 99,20 | 90,88 | 2890 |
| 0,371 | 39,99 | 0,0203 | 8,92 | 0,127 | 0,353 | 49,49 | 0,139 | 99,03 | 90,81 | 2775 |
| 0,378 | 39,97 | 0,0259 | 9,10 | 0,132 | 0,351 | 49,83 | 0,143 | 99,55 | 90,70 | 2754 |
| 0,389 | 40,78 | 0,0174 | 9,59 | 0,143 | 0,285 | 49,09 | 0,156 | 100,06 | 90,11 | 2240 |
| 0,396 | 40,76 | 0,023 | 9,46 | 0,143 | 0,267 | 48,77 | 0,157 | 99,59 | 90,18 | 2101 |
| 0,403 | 40,98 | 0,0209 | 9,98 | 0,154 | 0,246 | 48,73 | 0,164 | 100,27 | 89,69 | 1931 |
| OL_49 | | | | | | | | | | |
| 0,483 | 40,36 | 0,0201 | 10,96 | 0,167 | 0,238 | 48,11 | 0,145 | 100,00 | 88,66 | 1867 |
| 0,476 | 40,38 | 0,024 | 10,74 | 0,153 | 0,226 | 48,22 | 0,148 | 99,88 | 88,88 | 1774 |
| 0,469 | 40,17 | 0,0274 | 10,77 | 0,151 | 0,254 | 48,22 | 0,139 | 99,74 | 88,86 | 1995 |
| 0,462 | 40,13 | 0,0242 | 10,09 | 0,141 | 0,305 | 48,56 | 0,132 | 99,38 | 89,55 | 2398 |
| 0,455 | 40,61 | 0,0223 | 9,60 | 0,137 | 0,340 | 49,54 | 0,131 | 100,38 | 90,19 | 2670 |
| 0,448 | 40,10 | 0,0264 | 9,22 | 0,129 | 0,357 | 49,74 | 0,134 | 99,72 | 90,57 | 2809 |
| 0,441 | 40,23 | 0,0221 | 9,11 | 0,124 | 0,366 | 50,20 | 0,128 | 100,18 | 90,75 | 2873 |
| 0,434 | 40,65 | 0,0264 | 8,92 | 0,126 | 0,355 | 49,87 | 0,127 | 100,08 | 90,87 | 2792 |
| 0,427 | 40,78 | 0,0227 | 8,92 | 0,112 | 0,326 | 50,56 | 0,130 | 100,85 | 90,99 | 2560 |
| 0,420 | 40,57 | 0,0254 | 8,74 | 0,115 | 0,342 | 50,11 | 0,128 | 100,03 | 91,08 | 2684 |
| 0,413 | 40,70 | 0,0246 | 8,70 | 0,132 | 0,376 | 50,57 | 0,123 | 100,62 | 91,19 | 2955 |
| 0,406 | 40,63 | 0,0274 | 8,58 | 0,121 | 0,391 | 50,63 | 0,123 | 100,52 | 91,31 | 3072 |
| 0,399 | 40,26 | 0,0262 | 8,42 | 0,111 | 0,414 | 50,20 | 0,126 | 99,56 | 91,39 | 3252 |
| 0,392 | 40,61 | 0,0252 | 8,41 | 0,104 | 0,442 | 50,71 | 0,120 | 100,42 | 91,48 | 3470 |
| 0,385 | 40,60 | 0,0269 | 8,17 | 0,116 | 0,434 | 50,81 | 0,118 | 100,28 | 91,72 | 3412 |
| 0,378 | 40,85 | 0,0279 | 8,07 | 0,109 | 0,439 | 50,67 | 0,120 | 100,29 | 91,79 | 3446 |
| 0,371 | 40,97 | 0,0287 | 8,04 | 0,107 | 0,449 | 50,65 | 0,120 | 100,37 | 91,82 | 3526 |
| 0,364 | 40,43 | 0,0314 | 7,92 | 0,089 | 0,442 | 50,90 | 0,121 | 99,93 | 91,96 | 3475 |
| 0,357 | 40,67 | 0,0289 | 7,85 | 0,109 | 0,443 | 50,93 | 0,116 | 100,15 | 92,03 | 3481 |
| 0,350 | 40,60 | 0,0311 | 7,85 | 0,100 | 0,460 | 50,74 | 0,118 | 99,90 | 92,01 | 3613 |
| 0,343 | 40,55 | 0,0295 | 7,83 | 0,108 | 0,451 | 51,23 | 0,119 | 100,32 | 92,10 | 3543 |
| 0,336 | 40,39 | 0,0262 | 7,80 | 0,107 | 0,455 | 50,70 | 0,122 | 99,60 | 92,05 | 3578 |
| 0,329 | 40,41 | 0,0335 | 7,84 | 0,107 | 0,466 | 50,54 | 0,117 | 99,51 | 91,99 | 3661 |
| 0,322 | 40,43 | 0,032 | 7,75 | 0,105 | 0,456 | 50,71 | 0,119 | 99,60 | 92,10 | 3581 |
| 0,315 | 40,63 | 0,0267 | 7,81 | 0,101 | 0,448 | 51,14 | 0,116 | 100,27 | 92,10 | 3518 |
| 0,308 | 40,29 | 0,0243 | 7,80 | 0,101 | 0,446 | 50,82 | 0,119 | 99,60 | 92,07 | 3501 |
| 0,301 | 40,30 | 0,0265 | 7,77 | 0,100 | 0,449 | 50,65 | 0,116 | 99,41 | 92,07 | 3529 |
| 0,294 | 40,46 | 0,0273 | 7,94 | 0,100 | 0,453 | 50,81 | 0,116 | 99,91 | 91,93 | 3560 |
| 0,287 | 40,55 | 0,0238 | 7,81 | 0,110 | 0,444 | 51,10 | 0,114 | 100,14 | 92,10 | 3491 |
| 0,280 | 40,61 | 0,0229 | 7,86 | 0,106 | 0,457 | 50,85 | 0,118 | 100,02 | 92,01 | 3592 |
| 0,273 | 40,64 | 0,0251 | 7,87 | 0,094 | 0,453 | 51,29 | 0,118 | 100,48 | 92,07 | 3558 |
| 0,266 | 40,89 | 0,0262 | 7,81 | 0,097 | 0,451 | 51,40 | 0,120 | 100,79 | 92,14 | 3540 |
| 0,259 | 40,82 | 0,0279 | 7,80 | 0,112 | 0,446 | 51,03 | 0,118 | 100,36 | 92,10 | 3506 |
| 0,252 | 40,75 | 0,0234 | 7,96 | 0,112 | 0,458 | 51,16 | 0,130 | 100,60 | 91,97 | 3602 |
| 0,224 | 40,54 | 0,0214 | 8,00 | 0,109 | 0,449 | 50,92 | 0,128 | 100,17 | 91,89 | 3529 |
| 0,217 | 40,78 | 0,0262 | 7,96 | 0,106 | 0,452 | 50,83 | 0,117 | 100,27 | 91,92 | 3554 |
| 0,210 | 40,81 | 0,0231 | 7,98 | 0,112 | 0,438 | 50,64 | 0,119 | 100,12 | 91,87 | 3440 |
| 0,203 | 40,91 | 0,0259 | 7,94 | 0,108 | 0,456 | 50,97 | 0,120 | 100,53 | 91,96 | 3580 |
| 0,196 | 40,56 | 0,0229 | 7,98 | 0,109 | 0,453 | 50,80 | 0,118 | 100,05 | 91,89 | 3556 |
| 0,189 | 40,57 | 0,0201 | 8,06 | 0,113 | 0,436 | 51,24 | 0,122 | 100,57 | 91,88 | 3423 |
| 0,182 | 40,91 | 0,0268 | 8,06 | 0,112 | 0,440 | 50,80 | 0,119 | 100,46 | 91,82 | 3455 |
| 0,175 | 40,58 | 0,0243 | 8,14 | 0,108 | 0,441 | 50,79 | 0,119 | 100,20 | 91,74 | 3466 |
| 0,161 | 40,58 | 0,0256 | 8,19 | 0,117 | 0,415 | 51,09 | 0,117 | 100,54 | 91,74 | 3264 |
| 0,154 | 40,58 | 0,0314 | 8,26 | 0,101 | 0,431 | 50,21 | 0,121 | 99,74 | 91,54 | 3385 |
| 0,147 | 40,63 | 0,0271 | 8,45 | 0,120 | 0,415 | 50,24 | 0,123 | 100,00 | 91,37 | 3261 |
| 0,140 | 40,57 | 0,0335 | 8,49 | 0,115 | 0,399 | 50,16 | 0,121 | 99,89 | 91,32 | 3137 |

| Location in profile (mm) | $SiO_2$ wt% | $Al_2O_3$ wt% | FeO wt% | MnO wt% | NiO wt% | MgO wt% | CaO wt% | Total wt% | Fo mol% | Ni ppm |
|---|---|---|---|---|---|---|---|---|---|---|
| 0,133 | 40,66 | 0,0262 | 8,57 | 0,120 | 0,396 | 50,50 | 0,119 | 100,40 | 91,30 | 3109 |
| 0,126 | 40,61 | 0,0250 | 8,84 | 0,120 | 0,388 | 50,26 | 0,123 | 100,36 | 91,01 | 3052 |
| 0,119 | 40,37 | 0,0288 | 8,91 | 0,122 | 0,391 | 50,62 | 0,130 | 100,58 | 91,01 | 3073 |
| 0,112 | 40,15 | 0,0246 | 8,95 | 0,117 | 0,366 | 50,15 | 0,126 | 99,89 | 90,89 | 2878 |
| 0,105 | 40,09 | 0,0233 | 8,99 | 0,117 | 0,341 | 50,66 | 0,124 | 100,35 | 90,94 | 2677 |
| 0,098 | 40,43 | 0,0251 | 9,09 | 0,128 | 0,318 | 50,16 | 0,129 | 100,28 | 90,76 | 2502 |
| 0,091 | 40,27 | 0,0211 | 9,14 | 0,136 | 0,312 | 50,27 | 0,128 | 100,28 | 90,74 | 2453 |
| 0,077 | 40,27 | 0,0234 | 9,16 | 0,135 | 0,348 | 50,01 | 0,128 | 100,07 | 90,67 | 2734 |
| 0,070 | 40,26 | 0,0212 | 9,16 | 0,129 | 0,353 | 49,86 | 0,131 | 99,91 | 90,65 | 2775 |
| 0,063 | 40,51 | 0,0212 | 9,30 | 0,126 | 0,343 | 49,91 | 0,130 | 100,34 | 90,53 | 2699 |
| 0,056 | 40,42 | 0,0243 | 9,66 | 0,139 | 0,336 | 49,68 | 0,137 | 100,39 | 90,16 | 2637 |
| 0,049 | 40,11 | 0,0213 | 10,04 | 0,136 | 0,309 | 49,62 | 0,137 | 100,37 | 89,80 | 2424 |
| 0,042 | 39,94 | 0,0199 | 10,76 | 0,147 | 0,248 | 48,66 | 0,135 | 99,92 | 88,95 | 1949 |
| 0,035 | 40,02 | 0,0201 | 11,32 | 0,155 | 0,232 | 48,39 | 0,135 | 100,26 | 88,39 | 1823 |
| 0,028 | 40,15 | 0,0215 | 11,42 | 0,163 | 0,214 | 48,30 | 0,143 | 100,42 | 88,28 | 1683 |
| 0,021 | 39,90 | 0,0204 | 11,15 | 0,165 | 0,223 | 48,79 | 0,155 | 100,40 | 88,63 | 1751 |
| 0,014 | 39,96 | 0,0218 | 11,37 | 0,170 | 0,192 | 48,22 | 0,160 | 100,09 | 88,31 | 1510 |
| 0,007 | 39,97 | 0,0202 | 11,86 | 0,164 | 0,179 | 48,07 | 0,168 | 100,43 | 87,83 | 1407 |
| 0,000 | 39,38 | 0,0193 | 12,92 | 0,195 | 0,113 | 47,33 | 0,198 | 100,15 | 86,71 | 890 |
| OL_50 | | | | | | | | | | |
| 0,000 | 39,75 | n.m. | 14,28 | 0,216 | 0,157 | 45,84 | 0,170 | 100,41 | 85,11 | 1237 |
| 0,008 | 39,74 | n.m. | 11,37 | 0,166 | 0,185 | 47,96 | 0,156 | 99,57 | 88,25 | 1455 |
| 0,016 | 40,37 | n.m. | 10,71 | 0,179 | 0,226 | 48,18 | 0,133 | 99,80 | 88,90 | 1778 |
| 0,024 | 40,28 | n.m. | 9,61 | 0,157 | 0,262 | 48,81 | 0,135 | 99,25 | 90,04 | 2062 |
| 0,032 | 40,45 | n.m. | 9,45 | 0,121 | 0,332 | 49,64 | 0,124 | 100,11 | 90,34 | 2610 |
| 0,040 | 40,23 | n.m. | 9,24 | 0,124 | 0,286 | 49,40 | 0,138 | 99,43 | 90,50 | 2247 |
| 0,048 | 40,61 | n.m. | 9,15 | 0,143 | 0,311 | 49,78 | 0,128 | 100,12 | 90,64 | 2442 |
| 0,056 | 40,31 | n.m. | 9,07 | 0,140 | 0,344 | 50,47 | 0,121 | 100,46 | 90,83 | 2706 |
| 0,064 | 40,28 | n.m. | 8,52 | 0,131 | 0,362 | 49,74 | 0,132 | 99,16 | 91,23 | 2842 |
| 0,072 | 40,54 | n.m. | 8,51 | 0,129 | 0,331 | 50,80 | 0,127 | 100,44 | 91,40 | 2604 |
| 0,080 | 40,85 | n.m. | 8,27 | 0,126 | 0,357 | 50,19 | 0,123 | 99,92 | 91,53 | 2807 |
| 0,088 | 40,73 | n.m. | 8,25 | 0,114 | 0,376 | 51,03 | 0,128 | 100,62 | 91,68 | 2958 |
| 0,096 | 40,92 | n.m. | 8,14 | 0,127 | 0,393 | 50,64 | 0,127 | 100,35 | 91,72 | 3086 |
| 0,104 | 40,95 | n.m. | 7,89 | 0,127 | 0,391 | 50,47 | 0,108 | 99,94 | 91,93 | 3073 |
| 0,112 | 40,88 | n.m. | 7,69 | 0,147 | 0,428 | 51,03 | 0,126 | 100,29 | 92,20 | 3361 |
| 0,120 | 40,82 | n.m. | 7,93 | 0,126 | 0,435 | 50,67 | 0,103 | 100,09 | 91,92 | 3420 |
| 0,128 | 40,72 | n.m. | 7,73 | 0,123 | 0,441 | 50,91 | 0,121 | 100,04 | 92,14 | 3467 |
| 0,136 | 40,72 | n.m. | 7,69 | 0,137 | 0,437 | 50,85 | 0,113 | 99,94 | 92,17 | 3436 |
| 0,144 | 40,57 | n.m. | 7,76 | 0,113 | 0,456 | 51,16 | 0,113 | 100,18 | 92,15 | 3581 |
| 0,152 | 40,83 | n.m. | 7,54 | 0,120 | 0,445 | 51,15 | 0,116 | 100,20 | 92,36 | 3499 |
| 0,160 | 40,89 | n.m. | 7,64 | 0,116 | 0,448 | 50,99 | 0,120 | 100,20 | 92,24 | 3518 |
| 0,168 | 40,52 | n.m. | 7,62 | 0,116 | 0,455 | 51,03 | 0,109 | 99,86 | 92,26 | 3573 |
| 0,184 | 40,69 | n.m. | 7,49 | 0,131 | 0,456 | 50,31 | 0,117 | 99,20 | 92,29 | 3585 |
| 0,192 | 40,85 | n.m. | 7,82 | 0,117 | 0,427 | 51,19 | 0,117 | 100,53 | 92,10 | 3359 |
| 0,200 | 40,52 | n.m. | 8,02 | 0,118 | 0,441 | 51,37 | 0,128 | 100,60 | 91,94 | 3462 |
| 0,208 | 40,61 | n.m. | 8,07 | 0,123 | 0,391 | 51,08 | 0,122 | 100,41 | 91,85 | 3070 |
| 0,216 | 40,47 | n.m. | 8,03 | 0,150 | 0,408 | 50,59 | 0,117 | 99,77 | 91,82 | 3202 |
| 0,224 | 40,65 | n.m. | 8,20 | 0,125 | 0,375 | 50,64 | 0,131 | 100,12 | 91,67 | 2943 |
| 0,232 | 40,24 | n.m. | 8,34 | 0,149 | 0,358 | 50,68 | 0,117 | 99,88 | 91,54 | 2813 |
| 0,240 | 40,57 | n.m. | 8,32 | 0,145 | 0,360 | 50,54 | 0,120 | 100,06 | 91,54 | 2825 |
| 0,248 | 40,48 | n.m. | 8,59 | 0,124 | 0,354 | 50,07 | 0,129 | 99,74 | 91,21 | 2784 |
| 0,256 | 40,25 | n.m. | 8,30 | 0,111 | 0,352 | 50,73 | 0,124 | 99,86 | 91,59 | 2764 |
| 0,264 | 40,84 | n.m. | 8,23 | 0,131 | 0,351 | 49,91 | 0,120 | 99,58 | 91,53 | 2758 |
| 0,272 | 40,34 | n.m. | 8,55 | 0,150 | 0,351 | 50,53 | 0,123 | 100,04 | 91,32 | 2757 |
| 0,280 | 40,24 | n.m. | 8,68 | 0,135 | 0,383 | 49,89 | 0,127 | 99,45 | 91,10 | 3007 |

| Location in profile (mm) | $SiO_2$ wt% | $Al_2O_3$ wt% | FeO wt% | MnO wt% | NiO wt% | MgO wt% | CaO wt% | Total wt% | Fo mol% | Ni ppm |
|---|---|---|---|---|---|---|---|---|---|---|
| 0,288 | 40,48 | n.m. | 8,73 | 0,153 | 0,351 | 50,05 | 0,137 | 99,90 | 91,08 | 2760 |
| 0,296 | 40,29 | n.m. | 9,02 | 0,131 | 0,317 | 49,92 | 0,132 | 99,80 | 90,79 | 2492 |
| 0,304 | 40,65 | n.m. | 9,11 | 0,142 | 0,310 | 49,22 | 0,141 | 99,58 | 90,59 | 2435 |
| 0,312 | 40,10 | n.m. | 9,28 | 0,150 | 0,258 | 49,28 | 0,122 | 99,19 | 90,44 | 2028 |
| 0,320 | 40,28 | n.m. | 9,29 | 0,142 | 0,269 | 50,26 | 0,129 | 100,37 | 90,60 | 2113 |
| 0,328 | 40,37 | n.m. | 9,16 | 0,131 | 0,332 | 49,73 | 0,128 | 99,85 | 90,63 | 2611 |
| 0,336 | 40,17 | n.m. | 9,62 | 0,154 | 0,340 | 49,89 | 0,134 | 100,31 | 90,23 | 2669 |
| 0,344 | 40,16 | n.m. | 10,09 | 0,173 | 0,295 | 48,77 | 0,142 | 99,63 | 89,59 | 2316 |
| 0,352 | 39,65 | n.m. | 13,24 | 0,207 | 0,227 | 45,81 | 0,150 | 99,28 | 86,04 | 1784 |
| 0,360 | 39,22 | n.m. | 15,23 | 0,279 | 0,134 | 44,05 | 0,183 | 99,10 | 83,74 | 1051 |
| Group 2 olivines OL_32 | | | | | | | | | | |
| 0,000 | 40,14 | 0,021 | 12,72 | 0,192 | 0,123 | 46,66 | 0,211 | 100,07 | 86,72 | 965 |
| 0,007 | 40,18 | 0,023 | 11,68 | 0,177 | 0,145 | 46,96 | 0,199 | 99,36 | 87,75 | 1136 |
| 0,014 | 40,10 | 0,023 | 11,22 | 0,177 | 0,192 | 48,06 | 0,179 | 99,95 | 88,41 | 1506 |
| 0,021 | 40,32 | 0,023 | 10,56 | 0,163 | 0,214 | 47,86 | 0,173 | 99,31 | 88,98 | 1679 |
| 0,035 | 40,19 | 0,021 | 10,12 | 0,156 | 0,263 | 48,95 | 0,157 | 99,86 | 89,60 | 2067 |
| 0,042 | 40,17 | 0,022 | 10,24 | 0,154 | 0,280 | 48,34 | 0,155 | 99,36 | 89,37 | 2204 |
| 0,049 | 40,40 | 0,022 | 10,12 | 0,150 | 0,289 | 48,87 | 0,152 | 100,00 | 89,58 | 2273 |
| 0,056 | 40,11 | 0,024 | 10,03 | 0,145 | 0,286 | 48,58 | 0,151 | 99,33 | 89,61 | 2247 |
| 0,070 | 40,66 | 0,019 | 9,96 | 0,139 | 0,281 | 48,66 | 0,143 | 99,86 | 89,69 | 2207 |
| 0,077 | 40,32 | 0,028 | 9,76 | 0,138 | 0,295 | 48,99 | 0,144 | 99,67 | 89,94 | 2318 |
| 0,084 | 40,23 | 0,024 | 9,55 | 0,133 | 0,325 | 48,59 | 0,147 | 99,00 | 90,06 | 2552 |
| 0,091 | 40,76 | 0,027 | 9,54 | 0,137 | 0,336 | 48,73 | 0,140 | 99,67 | 90,10 | 2642 |
| 0,098 | 40,43 | 0,025 | 9,35 | 0,127 | 0,356 | 49,33 | 0,142 | 99,75 | 90,38 | 2801 |
| 0,112 | 40,48 | 0,025 | 9,10 | 0,133 | 0,357 | 49,10 | 0,139 | 99,33 | 90,57 | 2805 |
| 0,126 | 40,50 | 0,027 | 9,30 | 0,125 | 0,336 | 48,86 | 0,140 | 99,29 | 90,34 | 2641 |
| 0,133 | 40,54 | 0,023 | 9,21 | 0,136 | 0,319 | 49,03 | 0,137 | 99,40 | 90,46 | 2510 |
| 0,140 | 40,33 | 0,021 | 9,31 | 0,129 | 0,313 | 49,45 | 0,143 | 99,69 | 90,44 | 2459 |
| 0,147 | 40,43 | 0,024 | 9,43 | 0,131 | 0,325 | 48,68 | 0,136 | 99,15 | 90,19 | 2552 |
| 0,154 | 40,31 | 0,024 | 9,36 | 0,120 | 0,331 | 48,85 | 0,132 | 99,13 | 90,29 | 2599 |
| 0,161 | 40,18 | 0,028 | 9,22 | 0,129 | 0,344 | 49,39 | 0,133 | 99,42 | 90,51 | 2705 |
| 0,175 | 40,59 | 0,024 | 9,19 | 0,127 | 0,337 | 49,44 | 0,135 | 99,85 | 90,55 | 2651 |
| 0,182 | 40,13 | 0,028 | 9,23 | 0,126 | 0,361 | 49,20 | 0,128 | 99,20 | 90,47 | 2835 |
| 0,189 | 40,38 | 0,027 | 9,19 | 0,128 | 0,356 | 49,31 | 0,134 | 99,53 | 90,53 | 2799 |
| 0,196 | 40,38 | 0,026 | 9,06 | 0,123 | 0,366 | 49,62 | 0,132 | 99,71 | 90,70 | 2879 |
| 0,203 | 40,68 | 0,030 | 8,76 | 0,126 | 0,366 | 49,22 | 0,130 | 99,31 | 90,91 | 2878 |
| 0,210 | 40,10 | 0,028 | 8,90 | 0,115 | 0,372 | 49,51 | 0,133 | 99,15 | 90,83 | 2924 |
| 0,217 | 40,38 | 0,028 | 8,84 | 0,122 | 0,380 | 49,16 | 0,130 | 99,04 | 90,83 | 2984 |
| 0,231 | 40,53 | 0,026 | 8,64 | 0,114 | 0,391 | 49,89 | 0,125 | 99,72 | 91,14 | 3071 |
| 0,238 | 40,66 | 0,028 | 8,61 | 0,114 | 0,409 | 49,41 | 0,126 | 99,36 | 91,09 | 3216 |
| 0,245 | 40,59 | 0,031 | 8,54 | 0,113 | 0,407 | 49,32 | 0,125 | 99,13 | 91,14 | 3200 |
| 0,252 | 40,81 | 0,026 | 8,23 | 0,114 | 0,422 | 49,78 | 0,126 | 99,51 | 91,51 | 3316 |
| 0,266 | 40,60 | 0,028 | 8,02 | 0,110 | 0,415 | 49,85 | 0,123 | 99,15 | 91,71 | 3263 |
| 0,273 | 40,41 | 0,029 | 8,29 | 0,117 | 0,426 | 49,63 | 0,119 | 99,03 | 91,42 | 3348 |
| 0,280 | 40,75 | 0,028 | 8,23 | 0,111 | 0,430 | 49,89 | 0,126 | 99,56 | 91,52 | 3376 |
| 0,294 | 40,59 | 0,030 | 8,30 | 0,107 | 0,425 | 49,72 | 0,125 | 99,31 | 91,43 | 3339 |
| 0,308 | 40,59 | 0,028 | 8,25 | 0,113 | 0,435 | 49,90 | 0,120 | 99,44 | 91,50 | 3417 |
| 0,315 | 40,46 | 0,033 | 8,29 | 0,112 | 0,441 | 50,13 | 0,124 | 99,59 | 91,50 | 3467 |
| 0,329 | 40,47 | 0,033 | 8,20 | 0,112 | 0,415 | 49,99 | 0,126 | 99,35 | 91,57 | 3263 |
| 0,343 | 40,69 | 0,031 | 8,14 | 0,118 | 0,426 | 49,68 | 0,129 | 99,22 | 91,57 | 3345 |
| 0,350 | 40,79 | 0,029 | 8,47 | 0,121 | 0,425 | 49,86 | 0,123 | 99,82 | 91,29 | 3343 |
| 0,357 | 40,57 | 0,027 | 8,18 | 0,112 | 0,432 | 49,68 | 0,127 | 99,13 | 91,54 | 3397 |
| 0,364 | 40,77 | 0,026 | 8,53 | 0,113 | 0,423 | 49,79 | 0,122 | 99,77 | 91,22 | 3326 |
| 0,371 | 40,72 | 0,028 | 8,58 | 0,113 | 0,414 | 49,92 | 0,126 | 99,91 | 91,20 | 3256 |

| Location in profile (mm) | $SiO_2$ wt% | $Al_2O_3$ wt% | FeO wt% | MnO wt% | NiO wt% | MgO wt% | CaO wt% | Total wt% | Fo mol% | Ni ppm |
|---|---|---|---|---|---|---|---|---|---|---|
| 0,378 | 40,41 | 0,026 | 8,63 | 0,119 | 0,405 | 50,12 | 0,127 | 99,84 | 91,18 | 3186 |
| 0,385 | 40,94 | 0,028 | 8,57 | 0,123 | 0,397 | 49,24 | 0,128 | 99,43 | 91,10 | 3123 |
| 0,392 | 41,27 | 0,026 | 8,85 | 0,128 | 0,396 | 49,46 | 0,128 | 100,26 | 90,87 | 3109 |
| 0,399 | 40,95 | 0,026 | 8,75 | 0,121 | 0,379 | 49,23 | 0,128 | 99,58 | 90,93 | 2977 |
| 0,406 | 41,06 | 0,026 | 8,97 | 0,120 | 0,387 | 48,38 | 0,132 | 99,08 | 90,57 | 3041 |
| 0,413 | 40,72 | 0,026 | 8,89 | 0,122 | 0,370 | 49,04 | 0,131 | 99,30 | 90,76 | 2911 |
| 0,420 | 40,69 | 0,028 | 9,14 | 0,123 | 0,367 | 48,90 | 0,125 | 99,38 | 90,50 | 2883 |
| 0,427 | 40,89 | 0,024 | 9,23 | 0,122 | 0,362 | 49,45 | 0,129 | 100,21 | 90,51 | 2847 |
| 0,441 | 40,71 | 0,026 | 9,29 | 0,133 | 0,354 | 49,04 | 0,130 | 99,68 | 90,39 | 2782 |
| 0,448 | 40,68 | 0,025 | 9,19 | 0,129 | 0,336 | 49,31 | 0,132 | 99,81 | 90,53 | 2639 |
| 0,455 | 41,15 | 0,026 | 9,37 | 0,127 | 0,352 | 48,84 | 0,132 | 99,99 | 90,27 | 2769 |
| 0,462 | 40,62 | 0,027 | 9,41 | 0,126 | 0,343 | 49,14 | 0,132 | 99,81 | 90,29 | 2698 |
| 0,469 | 40,90 | 0,023 | 9,41 | 0,133 | 0,337 | 49,44 | 0,138 | 100,38 | 90,34 | 2651 |
| 0,476 | 40,58 | 0,025 | 9,35 | 0,129 | 0,332 | 48,76 | 0,137 | 99,32 | 90,28 | 2611 |
| 0,483 | 40,64 | 0,027 | 9,34 | 0,130 | 0,329 | 48,91 | 0,137 | 99,52 | 90,32 | 2588 |
| 0,490 | 40,55 | 0,023 | 9,35 | 0,138 | 0,322 | 48,87 | 0,136 | 99,39 | 90,30 | 2533 |
| 0,497 | 40,70 | 0,021 | 9,23 | 0,134 | 0,318 | 49,28 | 0,134 | 99,82 | 90,48 | 2503 |
| 0,504 | 40,84 | 0,030 | 8,62 | 0,132 | 0,357 | 49,39 | 0,139 | 99,50 | 91,07 | 2802 |
| 0,511 | 40,55 | 0,025 | 9,15 | 0,132 | 0,358 | 49,01 | 0,131 | 99,35 | 90,51 | 2815 |
| 0,532 | 40,34 | 0,025 | 9,07 | 0,125 | 0,362 | 49,37 | 0,135 | 99,43 | 90,65 | 2844 |
| 0,539 | 40,63 | 0,026 | 9,26 | 0,137 | 0,339 | 48,50 | 0,140 | 99,03 | 90,32 | 2665 |
| 0,546 | 40,47 | 0,026 | 9,33 | 0,137 | 0,342 | 49,56 | 0,137 | 100,00 | 90,44 | 2691 |
| 0,553 | 39,68 | 0,023 | 9,60 | 0,129 | 0,329 | 49,14 | 0,143 | 99,04 | 90,11 | 2585 |
| 0,560 | 40,12 | 0,023 | 9,82 | 0,148 | 0,312 | 49,12 | 0,141 | 99,68 | 89,91 | 2451 |
| 0,567 | 40,46 | 0,023 | 9,80 | 0,146 | 0,301 | 49,02 | 0,143 | 99,89 | 89,91 | 2366 |
| 0,574 | 40,21 | 0,020 | 10,00 | 0,141 | 0,283 | 48,46 | 0,153 | 99,27 | 89,62 | 2228 |
| 0,581 | 40,06 | 0,019 | 10,27 | 0,155 | 0,242 | 48,56 | 0,155 | 99,45 | 89,38 | 1904 |
| 0,588 | 40,10 | 0,021 | 10,60 | 0,159 | 0,229 | 47,91 | 0,161 | 99,17 | 88,95 | 1796 |
| 0,595 | 40,07 | 0,023 | 10,87 | 0,160 | 0,205 | 47,78 | 0,164 | 99,27 | 88,67 | 1612 |
| 0,602 | 39,65 | 0,024 | 11,14 | 0,177 | 0,176 | 47,98 | 0,178 | 99,33 | 88,47 | 1383 |
| 0,609 | 39,53 | 0,022 | 12,17 | 0,187 | 0,128 | 46,81 | 0,189 | 99,03 | 87,26 | 1008 |
| OL_34 | | | | | | | | | | |
| 0,000 | 39,89 | n.m. | 9,72 | 0,178 | 0,246 | 50,28 | 0,159 | 100,47 | 90,21 | 1935 |
| 0,008 | 40,07 | n.m. | 9,06 | 0,151 | 0,314 | 50,17 | 0,154 | 99,92 | 90,79 | 2464 |
| 0,016 | 40,49 | n.m. | 8,72 | 0,134 | 0,320 | 50,13 | 0,149 | 99,94 | 91,10 | 2518 |
| 0,024 | 40,61 | n.m. | 8,59 | 0,140 | 0,335 | 51,15 | 0,135 | 100,96 | 91,38 | 2635 |
| 0,032 | 40,58 | n.m. | 8,44 | 0,157 | 0,393 | 50,72 | 0,146 | 100,43 | 91,45 | 3088 |
| 0,040 | 40,28 | n.m. | 8,17 | 0,142 | 0,396 | 50,42 | 0,140 | 99,55 | 91,66 | 3109 |
| 0,048 | 40,32 | n.m. | 8,48 | 0,128 | 0,379 | 50,64 | 0,129 | 100,08 | 91,41 | 2978 |
| 0,056 | 40,59 | n.m. | 8,51 | 0,153 | 0,364 | 50,65 | 0,135 | 100,40 | 91,38 | 2860 |
| 0,064 | 40,67 | n.m. | 8,46 | 0,141 | 0,339 | 50,06 | 0,139 | 99,81 | 91,33 | 2662 |
| 0,072 | 40,38 | n.m. | 8,80 | 0,132 | 0,341 | 50,04 | 0,140 | 99,84 | 91,01 | 2683 |
| 0,080 | 40,42 | n.m. | 8,63 | 0,152 | 0,321 | 50,13 | 0,142 | 99,79 | 91,19 | 2519 |
| 0,088 | 40,12 | n.m. | 8,81 | 0,140 | 0,344 | 49,87 | 0,136 | 99,41 | 90,98 | 2705 |
| 0,096 | 40,51 | n.m. | 8,62 | 0,148 | 0,354 | 49,28 | 0,127 | 99,04 | 91,06 | 2779 |
| 0,104 | 40,26 | n.m. | 8,66 | 0,149 | 0,347 | 50,08 | 0,125 | 99,62 | 91,15 | 2723 |
| 0,112 | 40,14 | n.m. | 8,83 | 0,145 | 0,357 | 49,54 | 0,133 | 99,15 | 90,90 | 2806 |
| 0,120 | 40,47 | n.m. | 8,76 | 0,142 | 0,371 | 50,40 | 0,135 | 100,28 | 91,11 | 2915 |
| 0,128 | 40,05 | n.m. | 8,79 | 0,167 | 0,384 | 50,69 | 0,122 | 100,20 | 91,13 | 3014 |
| 0,136 | 40,47 | n.m. | 8,45 | 0,126 | 0,375 | 50,52 | 0,127 | 100,07 | 91,41 | 2950 |
| 0,144 | 40,62 | n.m. | 8,56 | 0,121 | 0,364 | 50,50 | 0,130 | 100,30 | 91,31 | 2863 |
| 0,152 | 40,38 | n.m. | 8,43 | 0,139 | 0,389 | 50,35 | 0,134 | 99,82 | 91,41 | 3056 |
| 0,160 | 40,64 | n.m. | 8,68 | 0,143 | 0,351 | 50,25 | 0,138 | 100,21 | 91,16 | 2756 |
| 0,168 | 40,60 | n.m. | 8,58 | 0,127 | 0,385 | 50,26 | 0,137 | 100,08 | 91,25 | 3029 |
| 0,176 | 40,45 | n.m. | 8,50 | 0,138 | 0,379 | 50,14 | 0,126 | 99,73 | 91,31 | 2976 |

| Location in profile (mm) | $SiO_2$ wt% | $Al_2O_3$ wt% | FeO wt% | MnO wt% | NiO wt% | MgO wt% | CaO wt% | Total wt% | Fo mol% | Ni ppm |
|---|---|---|---|---|---|---|---|---|---|---|
| 0,184 | 40,55 | n.m. | 8,60 | 0,149 | 0,360 | 50,68 | 0,116 | 100,46 | 91,30 | 2833 |
| 0,192 | 40,55 | n.m. | 8,61 | 0,138 | 0,378 | 50,06 | 0,129 | 99,87 | 91,19 | 2970 |
| 0,200 | 40,49 | n.m. | 8,52 | 0,134 | 0,369 | 49,46 | 0,124 | 99,09 | 91,18 | 2899 |
| 0,208 | 40,79 | n.m. | 8,66 | 0,121 | 0,364 | 50,17 | 0,122 | 100,22 | 91,16 | 2859 |
| 0,216 | 41,07 | n.m. | 8,75 | 0,142 | 0,379 | 49,93 | 0,128 | 100,40 | 91,04 | 2981 |
| 0,224 | 40,68 | n.m. | 8,75 | 0,142 | 0,366 | 49,79 | 0,126 | 99,86 | 91,02 | 2877 |
| 0,232 | 40,32 | n.m. | 8,77 | 0,152 | 0,344 | 49,67 | 0,131 | 99,39 | 90,98 | 2704 |
| 0,240 | 40,52 | n.m. | 9,01 | 0,141 | 0,358 | 50,10 | 0,138 | 100,27 | 90,83 | 2817 |
| 0,248 | 40,98 | n.m. | 8,62 | 0,140 | 0,339 | 50,24 | 0,138 | 100,45 | 91,21 | 2668 |
| 0,256 | 40,45 | n.m. | 8,95 | 0,122 | 0,326 | 49,67 | 0,136 | 99,65 | 90,81 | 2558 |
| 0,264 | 40,74 | n.m. | 8,64 | 0,142 | 0,332 | 50,03 | 0,135 | 100,02 | 91,16 | 2607 |
| 0,272 | 40,59 | n.m. | 8,45 | 0,139 | 0,343 | 50,40 | 0,130 | 100,06 | 91,40 | 2694 |
| 0,280 | 40,43 | n.m. | 8,19 | 0,131 | 0,364 | 49,83 | 0,145 | 99,09 | 91,55 | 2862 |
| 0,288 | 40,62 | n.m. | 8,24 | 0,151 | 0,409 | 50,42 | 0,134 | 99,98 | 91,59 | 3216 |
| 0,296 | 40,51 | n.m. | 8,24 | 0,153 | 0,384 | 50,45 | 0,129 | 99,87 | 91,60 | 3014 |
| 0,304 | 40,78 | n.m. | 8,80 | 0,146 | 0,377 | 50,14 | 0,144 | 100,38 | 91,03 | 2959 |
| 0,312 | 40,85 | n.m. | 8,83 | 0,137 | 0,336 | 49,30 | 0,138 | 99,59 | 90,86 | 2643 |
| 0,320 | 40,70 | n.m. | 9,06 | 0,169 | 0,295 | 49,33 | 0,135 | 99,69 | 90,65 | 2321 |
| 0,328 | 41,00 | n.m. | 9,09 | 0,149 | 0,321 | 49,11 | 0,159 | 99,82 | 90,59 | 2519 |
| 0,336 | 40,97 | n.m. | 9,24 | 0,162 | 0,301 | 49,12 | 0,168 | 99,96 | 90,45 | 2362 |
| 0,344 | 40,71 | n.m. | 9,65 | 0,165 | 0,233 | 49,30 | 0,156 | 100,22 | 90,10 | 1832 |
| 0,352 | 40,82 | n.m. | 10,18 | 0,185 | 0,228 | 48,84 | 0,172 | 100,42 | 89,52 | 1794 |
| 0,360 | 40,75 | n.m. | 10,73 | 0,184 | 0,169 | 48,15 | 0,185 | 100,17 | 88,88 | 1331 |
| 0,368 | 40,29 | n.m. | 11,86 | 0,236 | 0,125 | 47,52 | 0,217 | 100,25 | 87,71 | 983 |
| 0,376 | 40,77 | n.m. | 13,34 | 0,242 | 0,072 | 45,62 | 0,212 | 100,25 | 85,90 | 563 |
| OL_35 | | | | | | | | | | |
| 0,000 | 41,02 | n.m. | 10,13 | 0,128 | 0,237 | 48,55 | 0,182 | 100,25 | 89,51 | 1860 |
| 0,015 | 40,54 | n.m. | 9,23 | 0,146 | 0,276 | 49,35 | 0,155 | 99,70 | 90,50 | 2165 |
| 0,023 | 41,11 | n.m. | 9,00 | 0,133 | 0,280 | 49,06 | 0,170 | 99,76 | 90,66 | 2204 |
| 0,033 | 40,77 | n.m. | 8,97 | 0,135 | 0,353 | 50,13 | 0,148 | 100,50 | 90,87 | 2777 |
| 0,043 | 40,85 | n.m. | 8,75 | 0,134 | 0,375 | 49,68 | 0,143 | 99,92 | 91,00 | 2944 |
| 0,063 | 41,18 | n.m. | 9,01 | 0,125 | 0,374 | 49,46 | 0,147 | 100,30 | 90,72 | 2936 |
| 0,083 | 41,13 | n.m. | 9,23 | 0,129 | 0,403 | 49,37 | 0,148 | 100,41 | 90,50 | 3169 |
| 0,093 | 40,65 | n.m. | 9,54 | 0,131 | 0,394 | 49,34 | 0,140 | 100,19 | 90,21 | 3099 |
| 0,103 | 40,65 | n.m. | 9,19 | 0,134 | 0,373 | 49,62 | 0,140 | 100,11 | 90,58 | 2929 |
| 0,113 | 41,22 | n.m. | 8,75 | 0,117 | 0,401 | 49,21 | 0,142 | 99,84 | 90,92 | 3154 |
| 0,123 | 40,95 | n.m. | 8,46 | 0,135 | 0,389 | 50,10 | 0,140 | 100,17 | 91,34 | 3061 |
| 0,133 | 41,30 | n.m. | 8,54 | 0,161 | 0,392 | 50,05 | 0,141 | 100,59 | 91,26 | 3083 |
| 0,143 | 40,96 | n.m. | 8,40 | 0,115 | 0,389 | 50,07 | 0,132 | 100,07 | 91,39 | 3058 |
| 0,153 | 41,04 | n.m. | 8,25 | 0,116 | 0,423 | 49,89 | 0,141 | 99,86 | 91,50 | 3328 |
| 0,163 | 41,05 | n.m. | 8,23 | 0,122 | 0,371 | 50,53 | 0,134 | 100,43 | 91,62 | 2913 |
| 0,173 | 40,88 | n.m. | 8,32 | 0,122 | 0,417 | 50,06 | 0,134 | 99,93 | 91,46 | 3274 |
| 0,183 | 40,51 | n.m. | 8,29 | 0,123 | 0,393 | 50,41 | 0,128 | 99,84 | 91,55 | 3091 |
| 0,193 | 40,88 | n.m. | 8,18 | 0,109 | 0,437 | 50,59 | 0,143 | 100,33 | 91,68 | 3434 |
| 0,203 | 41,09 | n.m. | 8,14 | 0,121 | 0,376 | 49,89 | 0,138 | 99,75 | 91,61 | 2958 |
| 0,000 | 41,02 | n.m. | 10,13 | 0,128 | 0,237 | 48,55 | 0,182 | 100,25 | 89,51 | 1860 |
| 0,015 | 40,54 | n.m. | 9,23 | 0,146 | 0,276 | 49,35 | 0,155 | 99,70 | 90,50 | 2165 |
| 0,023 | 41,11 | n.m. | 9,00 | 0,133 | 0,280 | 49,06 | 0,170 | 99,76 | 90,66 | 2204 |
| 0,033 | 40,77 | n.m. | 8,97 | 0,135 | 0,353 | 50,13 | 0,148 | 100,50 | 90,87 | 2777 |
| 0,043 | 40,85 | n.m. | 8,75 | 0,134 | 0,375 | 49,68 | 0,143 | 99,92 | 91,00 | 2944 |
| 0,063 | 41,18 | n.m. | 9,01 | 0,125 | 0,374 | 49,46 | 0,147 | 100,30 | 90,72 | 2936 |
| 0,083 | 41,13 | n.m. | 9,23 | 0,129 | 0,403 | 49,37 | 0,148 | 100,41 | 90,50 | 3169 |
| 0,093 | 40,65 | n.m. | 9,54 | 0,131 | 0,394 | 49,34 | 0,140 | 100,19 | 90,21 | 3099 |
| 0,103 | 40,65 | n.m. | 9,19 | 0,134 | 0,373 | 49,62 | 0,140 | 100,11 | 90,58 | 2929 |
| 0,113 | 41,22 | n.m. | 8,75 | 0,117 | 0,401 | 49,21 | 0,142 | 99,84 | 90,92 | 3154 |

| Location in profile (mm) | $SiO_2$ wt% | $Al_2O_3$ wt% | FeO wt% | MnO wt% | NiO wt% | MgO wt% | CaO wt% | Total wt% | Fo mol% | Ni ppm |
|---|---|---|---|---|---|---|---|---|---|---|
| 0,123 | 40,95 | n.m. | 8,46 | 0,135 | 0,389 | 50,10 | 0,140 | 100,17 | 91,34 | 3061 |
| 0,133 | 41,30 | n.m. | 8,54 | 0,161 | 0,392 | 50,05 | 0,141 | 100,59 | 91,26 | 3083 |
| 0,143 | 40,96 | n.m. | 8,40 | 0,115 | 0,389 | 50,07 | 0,132 | 100,07 | 91,39 | 3058 |
| 0,153 | 41,04 | n.m. | 8,25 | 0,116 | 0,423 | 49,89 | 0,141 | 99,86 | 91,50 | 3328 |
| 0,163 | 41,05 | n.m. | 8,23 | 0,122 | 0,371 | 50,53 | 0,134 | 100,43 | 91,62 | 2913 |
| 0,173 | 40,88 | n.m. | 8,32 | 0,122 | 0,417 | 50,06 | 0,134 | 99,93 | 91,46 | 3274 |
| 0,183 | 40,51 | n.m. | 8,29 | 0,123 | 0,393 | 50,41 | 0,128 | 99,84 | 91,55 | 3091 |
| 0,193 | 40,88 | n.m. | 8,18 | 0,109 | 0,437 | 50,59 | 0,143 | 100,33 | 91,68 | 3434 |
| 0,203 | 41,09 | n.m. | 8,14 | 0,121 | 0,376 | 49,89 | 0,138 | 99,75 | 91,61 | 2958 |
| Group 3 olivines | | | | | | | | | | |
| OL_38 | | | | | | | | | | |
| 0,000 | 41,03 | n.m. | 12,31 | 0,206 | 0,093 | 46,75 | 0,240 | 100,63 | 87,12 | 730 |
| 0,003 | 40,85 | n.m. | 12,41 | 0,186 | 0,096 | 46,77 | 0,235 | 100,55 | 87,03 | 751 |
| 0,006 | 40,86 | n.m. | 12,40 | 0,180 | 0,121 | 47,04 | 0,230 | 100,84 | 87,11 | 949 |
| 0,009 | 40,55 | n.m. | 12,26 | 0,201 | 0,146 | 46,93 | 0,221 | 100,31 | 87,21 | 1150 |
| 0,012 | 40,07 | n.m. | 12,19 | 0,204 | 0,117 | 46,52 | 0,271 | 99,37 | 87,17 | 918 |
| 0,018 | 40,51 | n.m. | 12,21 | 0,207 | 0,130 | 47,65 | 0,216 | 100,92 | 87,42 | 1022 |
| 0,021 | 40,60 | n.m. | 11,92 | 0,196 | 0,129 | 47,64 | 0,208 | 100,69 | 87,68 | 1015 |
| 0,027 | 40,99 | n.m. | 11,51 | 0,164 | 0,171 | 47,85 | 0,205 | 100,89 | 88,10 | 1345 |
| 0,030 | 40,67 | n.m. | 11,43 | 0,161 | 0,153 | 47,92 | 0,209 | 100,54 | 88,19 | 1203 |
| 0,036 | 40,68 | n.m. | 11,15 | 0,170 | 0,161 | 48,46 | 0,195 | 100,82 | 88,56 | 1261 |
| 0,039 | 40,76 | n.m. | 11,17 | 0,177 | 0,158 | 47,91 | 0,206 | 100,39 | 88,42 | 1245 |
| 0,054 | 41,03 | n.m. | 11,00 | 0,162 | 0,197 | 48,19 | 0,187 | 100,76 | 88,64 | 1547 |
| 0,057 | 40,72 | n.m. | 10,77 | 0,148 | 0,179 | 48,36 | 0,201 | 100,38 | 88,88 | 1407 |
| 0,075 | 40,76 | n.m. | 10,84 | 0,158 | 0,183 | 48,45 | 0,186 | 100,59 | 88,84 | 1434 |
| 0,096 | 40,49 | n.m. | 10,85 | 0,179 | 0,194 | 48,84 | 0,201 | 100,76 | 88,91 | 1528 |
| OL_38b | | | | | | | | | | |
| 0,000 | 39,19 | n.m. | 16,77 | 0,266 | 0,101 | 43,23 | 0,271 | 99,83 | 82,11 | 790 |
| 0,007 | 39,71 | n.m. | 16,76 | 0,252 | 0,040 | 43,11 | 0,270 | 100,14 | 82,08 | 312 |
| 0,014 | 39,82 | n.m. | 15,08 | 0,231 | 0,112 | 44,19 | 0,235 | 99,67 | 83,92 | 883 |
| 0,021 | 40,49 | n.m. | 12,11 | 0,188 | 0,168 | 46,43 | 0,210 | 99,60 | 87,23 | 1322 |
| 0,028 | 40,44 | n.m. | 11,28 | 0,154 | 0,187 | 47,64 | 0,206 | 99,91 | 88,26 | 1472 |
| 0,042 | 40,45 | n.m. | 10,91 | 0,169 | 0,177 | 48,47 | 0,202 | 100,38 | 88,78 | 1393 |
| 0,049 | 40,33 | n.m. | 11,03 | 0,175 | 0,181 | 47,73 | 0,189 | 99,64 | 88,51 | 1422 |
| 0,056 | 40,93 | n.m. | 11,23 | 0,172 | 0,168 | 47,72 | 0,200 | 100,43 | 88,33 | 1319 |
| 0,063 | 40,61 | n.m. | 11,41 | 0,186 | 0,181 | 47,7 | 0,200 | 100,28 | 88,16 | 1422 |
| 0,070 | 39,84 | n.m. | 12,92 | 0,218 | 0,154 | 46,47 | 0,201 | 99,80 | 86,50 | 1210 |
| 0,077 | 39,98 | n.m. | 14,86 | 0,220 | 0,094 | 45,43 | 0,219 | 100,80 | 84,48 | 735 |
| 0,084 | 39,42 | n.m. | 15,46 | 0,248 | 0,059 | 44,19 | 0,228 | 99,61 | 83,58 | 464 |
| OL_67 | | | | | | | | | | |
| * | 41,04 | n.m. | 8,43 | 0,124 | 0,387 | 50,16 | 0,148 | 100,29 | 91,38 | 3041 |
| * | 41,46 | n.m. | 8,57 | 0,145 | 0,351 | 50,19 | 0,161 | 100,88 | 91,25 | 2760 |
| * | 41,13 | n.m. | 8,46 | 0,131 | 0,358 | 50,27 | 0,141 | 100,48 | 91,37 | 2815 |
| * | 41,05 | n.m. | 8,70 | 0,127 | 0,334 | 50,48 | 0,145 | 100,84 | 91,18 | 2626 |
| OL_106 | | | | | | | | | | |
| * | 40,43 | n.m. | 9,93 | n.m. | 0,261 | 49,57 | 0,142 | 100,33 | 89,89 | 2050 |

* this data represent local analyzed points instead of crystal profiles

Table A.3.2.- Clinopyroxene and glass composition

| Sample | Grain | $SiO_2$ wt% | $TiO_2$ wt% | $Al_2O_3$ wt% | FeO wt% | MnO wt% | MgO wt% | CaO wt% | $Na_2O$ wt% | $K_2O$ wt% | $Cr_2O_3$ wt% | Total wt% | #Mg mol% |
|---|---|---|---|---|---|---|---|---|---|---|---|---|---|
| CLHE-TF4 | Cpx-2-a | 49,09 | 0,529 | 4,29 | 5,52 | 0,117 | 15,32 | 21,98 | 0,230 | 0,000 | 0,819 | 97,89 | 83,18 |
| CLHE-TF4 | Cpx-2-b | 49,11 | 0,672 | 4,85 | 5,97 | 0,102 | 15,38 | 21,73 | 0,230 | 0,000 | 0,728 | 98,78 | 82,12 |
| CLHE-TF4 | Cpx-2-c | 49,17 | 0,700 | 4,93 | 5,79 | 0,101 | 15,41 | 21,47 | 0,231 | 0,004 | 0,692 | 98,50 | 82,59 |
| CLHE-TF4 | Cpx-3 | 48,72 | 0,635 | 4,59 | 5,71 | 0,098 | 15,91 | 22,10 | 0,250 | 0,000 | 0,697 | 98,50 | 83,24 |
| CLHE-TF4 | Cpx-4 | 49,39 | 0,477 | 3,94 | 5,25 | 0,095 | 15,97 | 21,90 | 0,226 | 0,000 | 0,951 | 98,21 | 84,43 |
| CLHE-TF4 | Cpx-7 | 49,35 | 0,574 | 4,99 | 6,40 | 0,121 | 15,93 | 21,18 | 0,253 | 0,000 | 0,331 | 99,13 | 81,60 |
| CLHE-TF4 | Cpx-8 | 49,53 | 0,434 | 3,52 | 4,95 | 0,123 | 16,34 | 22,07 | 0,216 | 0,000 | 0,628 | 97,81 | 85,47 |
| CLHE-TF4 | Cpx-9 | 49,12 | 0,601 | 4,48 | 5,50 | 0,087 | 15,78 | 21,87 | 0,240 | 0,000 | 0,914 | 98,58 | 83,64 |
| CLHE-TF4 | Cpx-10 | 49,53 | 0,588 | 4,25 | 5,72 | 0,118 | 15,75 | 22,08 | 0,231 | 0,000 | 0,597 | 98,88 | 83,07 |
| CLHE-TF4 | Cpx-15 | 50,82 | 0,493 | 3,69 | 6,22 | 0,117 | 16,16 | 21,30 | 0,267 | 0,000 | 0,495 | 99,56 | 82,24 |
| CLHE-TF4 | Cpx-18 | 49,38 | 0,618 | 4,95 | 6,00 | 0,096 | 16,33 | 21,35 | 0,215 | 0,000 | 0,772 | 99,71 | 82,91 |
| CLHE-TF4 | Cpx-19 | 50,99 | 0,425 | 3,43 | 5,49 | 0,128 | 16,77 | 21,21 | 0,227 | 0,014 | 0,443 | 99,13 | 84,48 |
| CLHE-TF4 | Cpx-22 | 48,81 | 0,515 | 4,60 | 5,84 | 0,103 | 15,67 | 22,09 | 0,276 | 0,000 | 0,612 | 98,51 | 82,70 |
| CLHE-TF4 | Cpx-23 | 49,49 | 0,458 | 4,19 | 5,29 | 0,104 | 15,81 | 22,00 | 0,252 | 0,002 | 0,866 | 98,46 | 84,19 |
| CLHE-TF4 | Cpx-24 | 49,69 | 0,602 | 4,66 | 6,33 | 0,134 | 15,94 | 20,98 | 0,266 | 0,000 | 0,305 | 98,91 | 81,78 |
| CLHE-TF4 | Cpx-28 | 49,16 | 0,676 | 4,59 | 6,17 | 0,098 | 15,54 | 21,89 | 0,221 | 0,000 | 0,404 | 98,74 | 81,78 |
| CLHE-TF4 | Cpx-29 | 49,17 | 0,622 | 4,55 | 6,04 | 0,118 | 15,50 | 22,06 | 0,234 | 0,000 | 0,397 | 98,69 | 82,06 |
| CLHE-TF4 | Cpx-31 | 49,59 | 0,681 | 5,00 | 6,41 | 0,107 | 15,78 | 21,20 | 0,246 | 0,000 | 0,461 | 99,48 | 81,44 |
| CLHE-TF4 | Cpx-32 | 49,36 | 0,699 | 4,87 | 6,40 | 0,133 | 15,82 | 21,20 | 0,232 | 0,000 | 0,551 | 99,28 | 81,50 |
| CLHE-TF4 | Cpx-35 | 48,63 | 0,539 | 4,29 | 6,29 | 0,103 | 15,63 | 21,96 | 0,259 | 0,000 | 0,554 | 98,25 | 81,58 |
| CLHE-TF4 | Cpx-38 | 49,16 | 0,508 | 3,97 | 5,44 | 0,083 | 16,06 | 22,26 | 0,236 | 0,000 | 0,659 | 98,38 | 84,03 |
| CLHE-TF1 | Cpx-41 | 48,17 | 0,612 | 3,90 | 6,49 | 0,131 | 15,83 | 21,43 | 0,249 | 0,004 | 0,353 | 97,16 | 81,30 |
| CLHE-TF1 | Cpx-44 | 48,85 | 0,603 | 4,57 | 6,09 | 0,094 | 16,00 | 21,69 | 0,241 | 0,000 | 0,646 | 98,78 | 82,40 |
| CLHE-TF1 | Cpx-53 | 48,72 | 0,557 | 4,64 | 5,85 | 0,093 | 15,22 | 22,40 | 0,236 | 0,000 | 0,648 | 98,36 | 82,26 |
| CLHE-TF1 | Cpx-54 | 49,61 | 0,639 | 4,51 | 6,43 | 0,139 | 15,85 | 21,50 | 0,262 | 0,000 | 0,353 | 99,29 | 81,46 |
| CLHE-TF1 | Cpx-55 | 49,64 | 0,609 | 4,41 | 6,24 | 0,138 | 15,84 | 21,65 | 0,249 | 0,002 | 0,242 | 99,02 | 81,90 |
| CLHE-TF1 | Cpx-56 | 48,35 | 0,595 | 4,66 | 6,13 | 0,095 | 15,64 | 21,95 | 0,248 | 0,004 | 0,589 | 98,26 | 81,97 |
| CLHE-TF1 | Cpx-60 | 48,44 | 0,595 | 4,66 | 5,70 | 0,119 | 15,66 | 21,52 | 0,239 | 0,000 | 0,515 | 97,45 | 83,04 |
| CLHE-TF1 | Cpx-61 | 49,05 | 0,587 | 4,14 | 6,16 | 0,132 | 15,47 | 21,61 | 0,256 | 0,002 | 0,567 | 97,98 | 81,74 |
| CLHE-TF1 | Cpx-62 | 48,75 | 0,748 | 5,09 | 6,28 | 0,094 | 15,36 | 22,54 | 0,253 | 0,000 | 0,368 | 99,49 | 81,34 |
| CLHE-TF1 | Cpx-66 | 49,82 | 0,477 | 4,20 | 5,61 | 0,083 | 15,77 | 22,20 | 0,255 | 0,000 | 0,777 | 99,20 | 83,36 |
| CLHE-TF1 | Cpx-69 | 48,70 | 0,708 | 5,31 | 6,45 | 0,123 | 15,88 | 21,24 | 0,242 | 0,000 | 0,460 | 99,12 | 81,44 |

Glass composition

| Sample | Grain | $SiO_2$ wt% | $TiO_2$ wt% | $Al_2O_3$ wt% | FeO wt% | MnO wt% | MgO wt% | CaO wt% | $Na_2O$ wt% | $K_2O$ wt% | $P_2O_5$ wt% | $SO_3$ wt% | Cl wt% | Total wt% |
|---|---|---|---|---|---|---|---|---|---|---|---|---|---|---|
| CLHE-TF4 | OL_119 | 51.18 | 0.800 | 15.50 | 8.74 | 0.146 | 5.92 | 10.87 | 2.920 | 0.891 | 0.136 | 0.023 | 0.093 | 97.10 |

Table A.3.3a.- Spinel composition by WDS.

| Host | OL # | Grain | SiO2 wt% | TiO2 wt% | Al2O3 wt% | Cr2O3 wt% | V2O3 wt% | FeO wt% | MnO wt% | MgO wt% | CaO wt% | NiO wt% | ZnO wt% | #Cr mol% | #Mg mol% | Total |
|---|---|---|---|---|---|---|---|---|---|---|---|---|---|---|---|---|
| Sample CLHE-TF-4 | | | | | | | | | | | | | | | | |
| Olivine | OL-49 | Sp-49a | 0,230 | 0,349 | 13,15 | 48,21 | 0,109 | 25,58 | 0,309 | 10,10 | 0,068 | 0,082 | 0,077 | 71,08 | 41,29 | 98,26 |
| Olivine | OL-49 | Sp-49b | 0,242 | 0,249 | 13,16 | 49,64 | 0,097 | 24,58 | 0,315 | 10,16 | 0,028 | 0,144 | 0,042 | 71,68 | 42,42 | 98,66 |
| Olivine | OL-49 | Sp-49c | 0,200 | 0,205 | 12,33 | 53,79 | 0,096 | 22,32 | 0,249 | 11,01 | 0,037 | 0,126 | 0,118 | 74,54 | 46,79 | 100,48 |
| Olivine | OL-49 | Sp-49d | 0,185 | 0,384 | 12,79 | 51,64 | 0,097 | 21,99 | 0,311 | 11,54 | 0,052 | 0,114 | 0,071 | 73,04 | 48,32 | 99,17 |
| Olivine | OL-39 | Sp-39a | 0,282 | 0,186 | 12,79 | 53,21 | 0,072 | 18,84 | 0,235 | 13,67 | 0,044 | 0,166 | 0,025 | 73,62 | 56,38 | 99,52 |
| Olivine | OL-39 | Sp-39b | 0,277 | 0,179 | 12,57 | 53,55 | 0,084 | 18,93 | 0,214 | 13,71 | 0,014 | 0,178 | 0,068 | 74,08 | 56,36 | 99,77 |
| Olivine | OL-39 | Sp-39c | 0,290 | 0,170 | 12,27 | 54,03 | 0,102 | 18,93 | 0,224 | 13,61 | 0,051 | 0,167 | 0,082 | 74,70 | 56,17 | 99,94 |
| Olivine | OL-39 | Sp-39d | 0,250 | 0,434 | 16,33 | 46,41 | 0,125 | 20,27 | 0,216 | 14,33 | 0,011 | 0,204 | 0,031 | 65,59 | 55,74 | 98,61 |
| Olivine | OL-32 | Sp-32a | 0,442 | 0,685 | 18,57 | 41,21 | 0,191 | 23,61 | 0,250 | 13,69 | 0,050 | 0,161 | 0,078 | 59,82 | 50,82 | 98,94 |
| Olivine | OL-32 | Sp-32b | 0,204 | 0,572 | 18,11 | 42,37 | 0,191 | 24,24 | 0,243 | 13,44 | 0,016 | 0,172 | 0,098 | 61,09 | 49,69 | 99,66 |
| Olivine | OL-32 | Sp-32c | 0,296 | 0,633 | 17,74 | 41,13 | 0,205 | 23,72 | 0,222 | 13,79 | 0,014 | 0,184 | 0,098 | 60,86 | 50,89 | 98,05 |
| Olivine | OL-50 | Sp-50a | 0,222 | 0,200 | 12,07 | 55,31 | 0,062 | 18,18 | 0,236 | 13,78 | 0,008 | 0,146 | 0,000 | 75,46 | 57,47 | 100,21 |
| Olivine | OL-50 | Sp-50b | 0,224 | 0,260 | 12,12 | 55,67 | 0,091 | 18,36 | 0,234 | 13,71 | 0,005 | 0,143 | 0,076 | 75,50 | 57,10 | 100,89 |
| Olivine | OL-50 | Sp-50c | 0,438 | 0,258 | 13,47 | 50,37 | 0,095 | 19,61 | 0,209 | 13,68 | 0,041 | 0,203 | 0,086 | 71,49 | 55,42 | 98,46 |
| Olivine | OL-50 | Sp-50c | 0,752 | 0,190 | 13,93 | 49,05 | 0,108 | 19,91 | 0,214 | 13,74 | 0,014 | 0,174 | 0,061 | 70,25 | 55,15 | 98,15 |
| Olivine | OL-50 | Sp-50d | 0,174 | 0,286 | 14,01 | 48,48 | 0,092 | 26,19 | 0,359 | 8,94 | 0,085 | 0,114 | 0,142 | 69,89 | 37,82 | 98,87 |
| Olivine | OL-37 | Sp-37a | 0,302 | 0,138 | 14,24 | 47,55 | 0,075 | 16,99 | 0,218 | 14,57 | 0,005 | 0,234 | 0,084 | 69,14 | 60,45 | 94,41 |

Table A.3.3b.- Spinel composition by EDS.

| Host | Grain | MgO wt% | Al2O3 wt% | CaO wt% | TiO2 wt% | Cr2O3 wt% | FeO wt% | #Cr mol% | #Mg mol% | Total wt% |
|---|---|---|---|---|---|---|---|---|---|---|
| Sample CLHE-TF-4 | | | | | | | | | | |
| Cpx | Sp-983 | 9,52 | 12,38 | 0,481 | 0,000 | 52,73 | 24,88 | 74,07 | 40,55 | 100 |
| Cpx | Sp-984 | 9,74 | 13,54 | 0,377 | 0,000 | 50,24 | 26,11 | 71,34 | 39,93 | 100 |
| Cpx | Sp-987 | 9,86 | 12,94 | 1,164 | 1,327 | 41,40 | 33,30 | 68,22 | 34,55 | 100 |
| Cpx | Sp-999 | 6,34 | 7,89 | 0,000 | 0,592 | 41,93 | 43,25 | 78,10 | 20,73 | 100 |
| Cpx | Sp-1003 | 10,00 | 12,90 | 1,178 | 0,000 | 46,95 | 28,97 | 70,95 | 38,09 | 100 |
| Cpx | Sp-1004 | 10,13 | 13,52 | 0,500 | 0,347 | 47,27 | 28,24 | 70,11 | 38,99 | 100 |
| Cpx | Sp-1005 | 9,72 | 12,14 | 0,000 | 0,000 | 51,41 | 26,72 | 73,96 | 39,34 | 100 |
| Cpx | Sp-1006 | 9,70 | 12,53 | 0,568 | 0,000 | 49,19 | 28,01 | 72,48 | 38,18 | 100 |
| Cpx | Sp-1007 | 8,82 | 12,77 | 0,000 | 0,000 | 49,69 | 28,72 | 72,31 | 35,38 | 100 |
| Cpx | Sp-1012 | 9,68 | 14,12 | 0,000 | 0,752 | 44,31 | 31,14 | 67,79 | 35,65 | 100 |
| Cpx | Sp-1013 | 8,37 | 12,51 | 0,266 | 0,000 | 47,02 | 31,84 | 71,60 | 31,90 | 100 |
| Cpx | Sp-1014 | 9,44 | 11,50 | 0,435 | 0,000 | 49,57 | 29,06 | 74,29 | 36,67 | 100 |
| Cpx | Sp-1023 | 8,45 | 12,04 | 0,246 | 0,304 | 47,22 | 31,74 | 72,46 | 32,18 | 100 |
| Cpx | Sp-1024 | 11,35 | 15,51 | 0,000 | 0,749 | 44,74 | 27,65 | 65,93 | 42,25 | 100 |
| Cpx | Sp-1027 | 8,94 | 10,28 | 0,000 | 0,000 | 45,06 | 35,72 | 74,62 | 30,85 | 100 |
| Cpx | Sp-1028 | 7,74 | 9,42 | 0,000 | 0,000 | 52,42 | 30,42 | 78,87 | 31,19 | 100 |
| Cpx | Sp-1029 | 8,81 | 10,30 | 0,000 | 0,000 | 54,98 | 25,91 | 78,17 | 37,73 | 100 |
| Cpx | Sp-1030 | 9,20 | 11,25 | 0,269 | 0,000 | 52,38 | 26,90 | 75,74 | 37,86 | 100 |
| Olivine | Sp-990 | 12,19 | 14,37 | 0,000 | 0,000 | 52,66 | 20,78 | 71,08 | 51,13 | 100 |
| Olivine | Sp-991 | 12,49 | 12,69 | 0,000 | 0,000 | 54,56 | 20,25 | 74,25 | 52,38 | 100 |
| Olivine | Sp-992 | 13,01 | 12,76 | 0,074 | 0,463 | 57,32 | 16,38 | 75,09 | 58,61 | 100 |
| Olivine | Sp-993 | 14,04 | 12,48 | 0,000 | 0,000 | 55,83 | 17,64 | 75,01 | 58,66 | 100 |
| Olivine | Sp-994 | 11,76 | 13,24 | 0,000 | 0,000 | 56,90 | 18,11 | 74,25 | 53,66 | 100 |
| Olivine | Sp-1034 | 11,72 | 12,17 | 0,000 | 0,000 | 55,51 | 20,60 | 75,37 | 50,35 | 100 |
| Olivine | Sp-1035 | 13,20 | 14,14 | 0,000 | 0,000 | 52,02 | 20,65 | 71,17 | 53,27 | 100 |
| Olivine | Sp-1036 | 12,11 | 12,42 | 0,000 | 0,000 | 53,24 | 22,22 | 74,19 | 49,28 | 100 |
| Olivine | Sp-1037 | 11,96 | 12,58 | 0,000 | 0,000 | 54,22 | 21,24 | 74,31 | 50,10 | 100 |
| Olivine | Sp-1038 | 13,18 | 14,80 | 0,000 | 0,000 | 49,50 | 22,51 | 69,17 | 51,07 | 100 |
| Olivine | Sp-1039 | 7,67 | 13,53 | 0,000 | 0,000 | 49,13 | 29,68 | 70,90 | 31,53 | 100 |
| Olivine | Sp-1040 | 13,64 | 15,72 | 0,000 | 0,000 | 51,03 | 19,61 | 68,53 | 55,35 | 100 |
| Olivine | Sp-1051 | 8,73 | 10,80 | 0,000 | 0,000 | 47,44 | 33,04 | 74,67 | 32,01 | 100 |
| Olivine | Sp-1052 | 11,23 | 12,74 | 0,000 | 0,000 | 52,27 | 23,76 | 73,36 | 45,71 | 100 |

| Host | Grain | MgO wt% | Al2O3 wt% | CaO wt% | TiO2 wt% | Cr2O3 wt% | FeO wt% | #Cr mol% | #Mg mol% | Total wt% |
|---|---|---|---|---|---|---|---|---|---|---|
| Olivine | Sp-1053 | 11,22 | 12,09 | 0,000 | 0,000 | 52,81 | 23,88 | 74,55 | 45,58 | 100 |
| Olivine | Sp-1054 | 11,57 | 12,68 | 0,000 | 0,000 | 54,45 | 21,30 | 74,22 | 49,21 | 100 |
| Olivine | Sp-1055 | 11,99 | 12,94 | 0,000 | 0,000 | 52,65 | 22,41 | 73,18 | 48,81 | 100 |
| Olivine | Sp-1056 | 11,41 | 12,37 | 0,000 | 0,000 | 55,77 | 20,45 | 75,15 | 49,87 | 100 |
| Olivine | Sp-1057 | 12,89 | 14,89 | 0,000 | 0,000 | 52,63 | 19,60 | 70,34 | 53,96 | 100 |
| Olivine | Sp-1058 | 11,80 | 13,49 | 0,000 | 0,000 | 51,58 | 23,12 | 71,95 | 47,64 | 100 |
| Olivine | Sp-1080 | 12,71 | 11,96 | 0,000 | 0,000 | 54,39 | 20,94 | 75,31 | 51,97 | 100 |
| Olivine | Sp-1081 | 14,63 | 12,81 | 0,000 | 0,000 | 55,55 | 17,00 | 74,41 | 60,53 | 100 |
| Olivine | Sp-1082 | 12,18 | 12,78 | 0,000 | 0,000 | 55,96 | 19,09 | 74,61 | 53,22 | 100 |
| Olivine | Sp-1083 | 11,71 | 12,07 | 0,000 | 0,000 | 53,40 | 22,82 | 74,80 | 47,78 | 100 |
| Olivine | Sp-1084 | 12,63 | 12,16 | 0,000 | 0,000 | 55,00 | 20,21 | 75,21 | 52,68 | 100 |
| Olivine | Sp-1085 | 13,27 | 12,12 | 0,000 | 0,000 | 53,98 | 20,63 | 74,92 | 53,40 | 100 |
| Olivine | Sp-1086 | 11,59 | 11,03 | 0,000 | 0,000 | 54,68 | 22,70 | 76,88 | 47,65 | 100 |
| Olivine | Sp-1087 | 13,67 | 12,44 | 0,000 | 0,000 | 56,14 | 17,74 | 75,16 | 57,88 | 100 |
| Olivine | Sp-1088 | 12,32 | 16,29 | 0,000 | 0,000 | 49,70 | 21,69 | 67,18 | 50,31 | 100 |

Table A.3.4.- Summary of thermobarometry results

| | Kd | T(°C) | P (Eqn. 31) (kbar) | Depth (km) | P (Eqn. 32c) (kbar) | Depth (km) |
|---|---|---|---|---|---|---|
| PX1_SEL1(1) | 0.33 | 1144 | 4.11 | 15 | 4.85 | 17 |
| PX1_SEL1(1a) | 0.35 | 1151 | 4.28 | 15 | 5.67 | 20 |
| PX1_SEL1(2) | 0.34 | 1153 | 4.37 | 16 | 5.57 | 20 |
| PX1_SEL1(3) | 0.32 | 1154 | 4.50 | 16 | 6.47 | 23 |
| PX1_SEL1(4) | 0.30 | 1146 | 3.82 | 14 | 4.87 | 17 |
| PX1_SEL1(8) | 0.27 | 1140 | 3.35 | 12 | 4.24 | 15 |
| PX2_SEL1(9) | 0.31 | 1152 | 4.35 | 16 | 5.76 | 21 |
| PX2_SEL1(10) | 0.33 | 1146 | 4.00 | 14 | 5.05 | 18 |
| PX3_SEL1(15) | 0.35 | 1161 | 4.56 | 16 | 4.62 | 17 |
| PX4_SEL1(18) | 0.33 | 1155 | 3.85 | 14 | 6.24 | 22 |
| PX6_SEL1(19) | 0.30 | 1151 | 3.55 | 13 | 3.78 | 14 |
| PX6_SEL1(22) | 0.34 | 1158 | 5.07 | 18 | 6.44 | 23 |
| PX6_SEL1(23) | 0.30 | 1151 | 4.51 | 16 | 5.21 | 19 |
| PX6_SEL1(24) | 0.36 | 1167 | 4.98 | 18 | 5.92 | 21 |
| PX35_SEL1(28) | 0.36 | 1147 | 3.88 | 14 | 5.36 | 19 |
| PX35_SEL1(29) | 0.35 | 1148 | 4.16 | 15 | 5.38 | 19 |
| PX51_SEL1(38) | 0.31 | 1146 | 3.95 | 14 | 5.30 | 19 |
| PX59_CLHE-S1a(44) | 0.34 | 1156 | 4.31 | 15 | 6.39 | 23 |
| PX84_CLHE-S1a(53) | 0.35 | 1145 | 4.30 | 15 | 5.58 | 20 |
| PX88_CLHE-S1a(55) | 0.36 | 1156 | 4.42 | 16 | 5.44 | 19 |
| PX94_CLHE-S1a(56) | 0.35 | 1155 | 4.50 | 16 | 6.57 | 24 |
| PX102_CLHE-S1a(60) | 0.33 | 1154 | 4.41 | 16 | 5.99 | 21 |
| PX109_CLHE-S1a(61) | 0.36 | 1155 | 4.58 | 16 | 5.49 | 20 |
| PX126_CLHE-S1a(66) | 0.32 | 1151 | 4.50 | 16 | 5.16 | 18 |

## A.3.- Methods

### Samples

Tephra samples were collected in the fallout deposit at ~300 m from the vent. Bulk rock analysis of individual tephra layers that cover the full thickness of the fallout show broadly similar contents of major and minor elements (~12 to ~15 wt% of MgO; ~51 to ~53 wt% $SiO_2$; ~400 to ~500 ppm of NiO). We selected two representative tephra layers of fine granulometry where olivines were found as loose grains. Those samples are CLHE-TF4 (IGSN: PPRAI1021) and CLHE-TF1 (IGSN: PPRAI101Y). Samples were sieved at 25 mesh size and magnetic phases were removed out. Olivine separates were obtained by the use of LST (lithium heteropolytungstate) at room temperature of 25°C. Further, aliquots of olivine separates were mounted in epoxy as bulk grains. In addition, selected crystals were individually mounted oriented normal to the chosen crystallographic axis.

### Mineral textures

Olivine separates embedded in mineral oil were texturally analyzed and documented under the binocular lenses. Most of the crystals are imperfectly broken along one or two combined planes, most commonly parallel to (010) and (001). Crystals preserving recognizable orientation features were hand-picked and grouped in three categories: early skeletal (i.e. preserving dendritic features in the innermost part of the crystal; Group 3), advanced skeletal (Group 2) and polyhedral (Group 1).

### Mineral and glass compositions

Electron microprobe analyses of olivine, pyroxene, spinel and matrix glass were performed using a JEOL JXA-8600M Superprobe with 5 wavelength-dispersive spectrometers at Instituto GEA, Universidad de Concepción, Chile. Analyzed samples were prepared by the conventional technique as epoxy blocks with mounted mineral grains. The polished surface of the samples was covered with a conducting carbon coating ~25 nm thick using a vacuum evaporator JEOL JEE-4X. All analyses were performed under 15 kV using K□ lines for all elements. Natural and synthetic minerals, simple oxides and glasses were used as reference samples, and the set of these samples varied depending on the object of analysis. Those with USNM code were donated by the Smithsonian Institution, USA (ref. [44]): diopside USNM 117733 (Si), USNM 137041 anorthite (Al), fayalite USNM 85276 (Fe), microcline USNM 143966 (K), chromite USNM 117075 (Cr), MnTiO3 (Ti and Mn), forsterite (Mg), jadeite (Na), wollastonite (Ca). Specific analytical conditions applied

for different minerals and glass are described below. In all cases, corrections for the matrix effect were calculated by the ZAF method.

*Rim to rim profiles in olivine*

High contrast backscattered electron images were obtained in single olivine crystals. Rim to rim spot analyses were performed in selected olivine grains using a beam current of 20 nA (for Si and Mg) and 60nA (for Al, Fe, Mn, Ni and Ca). On-peak counting times were 20 s (Si, Mg), 100 s (Fe), and 120 s (Al, Mn, Ni and Ca); high and low background count times were half the peak times for Si, Mg and Fe, and twice for Al, Mn, Ni and Ca. Under these conditions the 1□ detection limits were estimated to be 143 ppm Ni, 38 ppm Ca, 94 ppm Mn and 25 ppm Al. Analytical error for Si and Mg is less than 1% relative, it is <1.5% for Fe, <3% for Ni, <4.5% for Ca and <11% for Al and Mn. Replicate analyses of the olivine standard (San Carlos olivine NMNH111312-44) were collected and averaged, and compared to reported values to evaluate the accuracy; $SiO_2$, MgO and FeO varied from reported values by <1.5% relative. NiO varied from reported values by <6% and MnO <9%. $Al_2O_3$ and CaO are not reported for this standard therefore we are unable to assess the variation in our analyses for these elements. Olivines of Group 3 and OL_35 of Group 2 were measured using 20nA for all elements. On-peak counting times were 20 s (Si, Mg) and 60 s for the remaining elements; high and low background count times were half the peak times for all elements. Under these conditions analytical error for Ni is better than 23% for all measurements except for two point with low Ni contents.

*Clinopyroxene*

Clinopyroxene was analyzed using a beam current of 20 nA. On-peak counting times were 20 s (Si, Mg and Ca), 40 s (Al, Mn), and 60 s (Ti, Cr, Fe and Na); high and low background count times were half the peak times for all elements. Analytical error (1□) for Si, Mg, Ca, Fe and Al is less than 1.5% relative, it is <5% for Na and Ti, <8% for Cr and <15% for Mn. Replicate analyses of the clinopyroxene standard (Kakanui Augite NMNH122142) were collected and averaged, and compared to reported values to evaluate the accuracy. $SiO_2$, $TiO_2$, $Al_2O_3$, CaO and $Na_2O$ varied from reported values by <1.5% relative. MgO varied from reported values by <2.5% and FeO <7%. $Cr_2O_3$ is not reported for this standard therefore we are unable to assess the variation in our analyses for this element.

*Spinel*

Spinel was analyzed using a beam current of 20 nA. On-peak counting times were 60 s for all elements; high and low background count times were half the peak times also for all elements. Chromium, V and Ti were measured using LIF crystal to minimize Ti K□ overlap on V K□. Analytical error (1□) for Al, Cr, Fe and Mg is less than 1% relative, it is <10% for Si and Mn, <20% for Ti, V and Ni, <40% for Ca and <50% for Zn. Replicate analyses of the spinel standard (chromite

NMNH117075) were collected and averaged, and compared to reported values to evaluate the accuracy; $Al_2O_3$, $Cr_2O_3$ and MgO varied from reported values by <1% relative. FeO varied by <1.6%, and Mn <55%. Manganese oxide and $TiO_2$ accuracy was determined using Fe-Ti oxide (ilmenite NMNH 96189), being both below 5% relative. $SiO_2$, CaO, NiO and ZnO are not reported for neither of used internal standard therefore we are unable to assess the variation in our analyses for these elements.

Few clinopyroxene and spinel quantitative analyses were performed using a TESCAN VEGA II LSH scanning electron microscope installed in the same institution. Data was collected with a Quantax EDS system with a Bruker Nano LN2-free XFLASH® 6|3 silicon drift detector energy dispersive spectrometer (126 eV resolution for Mn K□) and the Esprit 1.9 software. The analytical setting was 15 kV accelerating voltage and 5 nA probe current. A pure Cu standard was used for calibrating the EDS. Analyses were done under the standardless mode using PB-ZAF matrix correction method. Results are expressed as normalized wt%.

*Matrix glass*

Major and minor element composition (Si, Ti, Al, Fe, Mn, Mg, Ca, Na, K, P, S and Cl) of glasses were determined using an accelerating voltage of 15 kV and a defocused 10 µm beam probe current. Sodium was measured first with a beam current of 4 nA to reduce alkali migration (cf., [45]). Other elements were measured with 10 nA. Peak counting time was 10 s for Na, 60 s for S and Cl, and 30 s, for remaining elements. High and low background count times were half the peak times also for all elements. Smithsonian Institution A99 basalt glass (NMNH113498-1) was used for standardization for Mg, Ca, Ti and Fe, rhyolitic VG568 glass for Si, Al and K and Corning Glass (NMNH 117218-3) for P[44]. Sodium was standardized on jadeite, Cl on tugtupite and Mn on $MnTiO_3$. Sulfur was measured on the sulfate peak position and was standardized on $CaSO_4$. Related precision (1σ) based on repeat analysis of standard MRND7001 is better than 1% for Si, Al, Mg, Ca, and Na; 1.5% for Ti, about 2.5% for Fe, <3.5% for P, <9% for K, and <15% for Mn. Accuracy is less than 1% for Si and Al, about 1.5% for Fe, <3.5% for Ti and Mg, <11% for Mn and Ca, <6 for Na, <9% for K and <36% for P. Sulfur accuracy was determined on A99 glass to be <15%. Chlorine is not reported for the analyzed standards therefore we are unable to assess the variation in our analyses for this element.

**Diffusion protocol**

The images were individually processed in ImageJ. Each gray value image was calibrated using EPMA spot analyses. In a strongly zoned crystal accurate gray value calibration is difficult due to the substantial changes and gray scale over short distances. The compositional gradients are largest at the rims where normal zoning exceeds >5 mol% Fo content over less than 20 µm and

edge effects further convolute the gray scale signal. In some cases, these effects lead to less accurate calibration curves for the crystal interiors with a narrow compositional range (< 2 mol% Fo), which is the main focus of the diffusion modeling. Therefore, we limited for OL_50 the calibration to microprobe spot analyses with olivine major element compositions >$Fo_{90}$. Good linear fits are recovered for the cores so that compositional profiles at accurate absolute Fo contents are extracted in ImageJ.

The diffusion modeling was performed on zoning profiles extracted from parts of the crystal where a one-dimensional (1D) profile is appropriate (center of crystal face). A region of interest significantly wider than measurement spot sizes were defined in ImageJ to smooth zoning profiles, while not altering the overall lengthscales of the zoning. We limit our timescale calculations to three crystals for which orientations are easily determined by measuring angles within the crystal and those three crystals are cut parallel to major crystallographic axes (Figure 2). Fe-Mg interdiffusion is faster along the *c*-axis[46] and the Los Hornitos crystals show that oscillatory zoning is almost removed || c, retaining only flat shoulders instead of reverse zoning, and therefore limits its use for timescale estimates. All timescales are calculated from profiles perpendicular to *c*.

We make a number of simplifications in our diffusion calculations. The major element reversals are small (~0.2 Fo units) justifying the choice a constant average Fo content of 90.5 when calculating Fe-Mg interdiffusion. We use a temperature range of 1150 to 1200°C, an oxygen fugacity estimate from the nearby Quizapu volcano[47] (mafic magmas are at NNO+0.5; for T=1150°C → $fO_2 = 3.5 \times 10^{-3}$ Pa and for T=1200°C → $fO_2 = 1.4 \times 10^{-2}$ Pa) and the model of Dohmen and Chakraborty[46] to determine Fe-Mg interdiffusion coefficients of $9.76 \times 10^{-17}$ $m^2/s$ (1150˚C and || 001) and $2.19 \times 10^{-16}$ $m^2/s$ (1200˚C and || 001). Pressure was set to $5 \times 10^5$ Pa as an average crustal pressure, but it has no significant implications for the calculations.

For simplicity and given the fact that exact boundary and growth conditions cannot be extracted as well as temperature constraints introduce the largest uncertainties, we estimate timescales using an analytical solution for step function of semi-infinite constant Fo content; a choice that is made to obtain order of magnitude estimates. Note that given the short diffusion lengthscales and the limited knowledge of exact starting conditions and boundary conditions resulted from our overall olivine growth model a more detailed model is considered here to be misleading in its accuracy. Even the uncertainties related to temperature are negligible for our final conclusions and by making numerous simplifications our overall timescale estimates are constrained to within a factor of 2.

**Glass volatile contents (SIMS)**

SIMS data were collected with a Cameca IMS 7f-Geo at the Institute of Materials Science and Engineering (IMSE) in the Washington University of St. Louis (WUSTL), Louisiana. A single SIMS session were devoted to volatile abundance measurements on the glass surrounding olivine crystals. The sample holder with the olivine-glass pairs were coated with a -40 nm thick- layer of gold. The samples were pre-sputtered for 5 min. The $Cs^+$ ion beam configured using a 5-10 nA current and 10kV of acceleration voltage was used to create a 15 µm spot size. Calibration curves were constructed using the standard glasses ALV1833-11, ALV519-4-1, ND7001 and ND6001. $H_2O$ values measured on 22 external glasses range between 0,3 to 0,7 wt%.

**Cpx-melt thermobarometry**

We applied the thermobarometric approach of Putirka et al.[48] based in the jadeite-diopside/hedenbergite exchange between clinopyroxene and the associated melt, which account a standard error of estimate (SEE) of ±1.7 kbar for the barometer and ±33°C for the temperature determination. A re-calibration of Putirka[27] includes $H_2O$ as an input parameter allowing a more suitable application to hydrous systems. These models correspond to Eq. 31 and Eq. 33 for pressure and temperature, respectively[27].

Another barometric approach that consider the partitioning of Al between clinopyroxene and melt (Eq.32c; ref. [27]) was applied to the data. This model has a SEE of ±1.5 kbar and requires temperature and $H_2O$ as input parameters, with the former being provided by Eq.33 to every mineral melt pair.

Based on SIMS measurements, we used a medium value of 0.5 wt% of $H_2O$ as input for barometry calculations.

We tested the chemical equilibrium conditions for clinopyroxene and the associated melt by two methods. The Fe-Mg exchange in the selected mineral-melt pairs fall into the $K_D$(Fe-Mg) = 0,28 ± 0,08 envelope[27]. As this approach does not consider equilibria between others exchange components, we also compared the predicted versus the observed DiHd component between the melt and mineral, respectively. A close match between these components validate the required cpx-liquid equilibrium for robust pressure and temperature calculations (e.g., ref. [49]).

During the calculations, we considered a $Fe^{3+}/\Sigma Fe$ ratio equals to 0.25. This value is representative of the redox conditions measured in basaltic melt inclusions of arc environment at global scale, that range between 0.18 to 0.32 (refs. [50–52]).

In order to convert the obtained values into depth, a mean value of 2.85 g $cm^{-3}$ was used for a simplified crustal rock density (e.g., ref. [53]).

# Appendix Chapter 4

## The redox state and metal/volatile budget of primitive arc magmas

Table A.4.1: Calculated volume of melt inclusion and related bubble.

| Label | Volumen MI ($\mu m^3$) | Volume bubble ($\mu m^3$) |
|---|---|---|
| OL_30 | 18850 | 1150 |
| OL_37 | 28274 | 9203 |
| OL_40 | 16032 | 905 |
| OL_44 | 1309 | 65 |
| OL_47 | 71995 | 4189 |
| OL_50 | 2945 | 65 |
| OL_58 | 106029 | 8181 |
| OL_61 | 33510 | 2145 |
| OL_64 | 3592 | 524 |
| OL_66 | 11451 | 905 |
| OL_69 | 44899 | 8181 |
| OL_70 | 4021 | 697 |
| OL_81 | 46077 | 905 |
| OL_82 | 14866 | 1437 |
| OL_83 | 83776 | 8181 |
| OL_85 | 27816 | 2572 |
| OL_86 | 18850 | 1437 |
| OL_87 | 65450 | 5575 |
| OL_90 | 12566 | 1437 |
| OL_91 | 13090 | 4189 |
| OL_98 | 11454 | 905 |
| OL_100 | 50265 | 4189 |
| OL_106 | 38485 | 1437 |
| OL_106_b | 56549 | 3054 |
| OL_107 | 28274 | 1150 |
| OL_110 | 18850 | 4189 |
| OL_112 | 2566 | 65 |
| OL_112b | 1885 | 113 |
| OL_115 | 10472 | 1767 |
| OL_119 | 37699 | 2145 |
| OL_120 | 19635 | 1437 |
| OL_122 | 37699 | 2145 |
| OL_123 | 41888 | 1437 |
| OL_124 | 184307 | 17157 |
| OL_124b | 359189 | 22449 |
| OL_125 | 54454 | 1767 |
| OL_127 | 10472 | 697 |
| OL_128 | 87114 | 3591 |
| OL_128b | 58316 | 3591 |
| OL_129 | 67021 | 7238 |
| OL_130 | 50265 | 3054 |
| OL_131 | 18850 | 697 |
| OL_131b | 2566 | 65 |
| OL_133 | 226195 | 33510 |
| OL_135 | 11454 | 1150 |
| OL_136 | 13090 | 905 |
| OL_137 | 28863 | 1437 |

Table A.4.2.- Analisys of standards by SIMS probe.

| Standard | $CO_2$ 12C/30Si | $H_2O$ 16OH/30Si | P 31P/30Si | F 19F/30Si | Cl 35Cl/30Si | S 32S/30Si |
|---|---|---|---|---|---|---|
| ALV1833-11 | | 2,4836 | 0,1074 | 0,5029 | 0,3814 | 1,3405 |
| ALV1833-11 | | 2,4784 | 0,1075 | 0,4874 | 0,3507 | 1,3426 |
| ALV1833-11 | | 2,4851 | 0,1070 | 0,5339 | 0,3949 | 1,3377 |
| ALV519-4-1 | | 0,3834 | 0,0572 | 0,2852 | 0,0792 | 1,4075 |
| ALV519-4-1 | | 0,3788 | 0,0576 | 0,2849 | 0,0758 | 1,3991 |
| ALV519-4-1 | | 0,3825 | 0,0572 | 0,2881 | 0,0761 | 1,4117 |
| SynFo | | 0,0094 | 0,0003 | 0,0816 | 0,0269 | 0,0131 |
| SynFo | | 0,0096 | 0,0003 | 0,0735 | 0,0249 | 0,0163 |
| ALV1833-1 | | 4,1754 | 0,2240 | 0,9942 | 0,9315 | 1,0509 |
| ALV1833-1 | | 4,1933 | 0,2245 | 1,0008 | 0,9358 | 1,0624 |
| ALV1833-1 | | 4,2175 | 0,2245 | 1,0020 | 0,9391 | 1,0661 |
| ND7001@1 | | 2,0016 | 0,0732 | 0,4785 | 0,2832 | 1,3234 |
| ND7001@2 | | 2,0877 | 0,0725 | 0,4711 | 0,2823 | 1,3252 |
| ND7001@3 | | 2,1247 | 0,0727 | 0,4673 | 0,2737 | 1,3234 |
| ND7001@10 | 0,0105 | 1,9967 | 0,0716 | 0,3935 | 0,2651 | 1,2713 |
| ND7001@11 | 0,0096 | 1,8588 | 0,0717 | 0,3721 | 0,2609 | 1,2566 |
| ND7001@12 | 0,0083 | 1,7660 | 0,0728 | 0,3500 | 0,2640 | 1,2723 |
| ND7001@13 | 0,0096 | 2,5037 | 0,0724 | 0,3631 | 0,2633 | 1,2671 |
| ND7001@14 | 0,0109 | 2,5104 | 0,0724 | 0,4638 | 0,2779 | 1,2811 |
| ND7001@15 | 0,0122 | 2,4468 | 0,0722 | 0,3782 | 0,2660 | 1,2606 |
| ND7001@16 | 0,0103 | 1,7502 | 0,0725 | 0,3854 | 0,2606 | 1,2486 |
| ND7001@17 | 0,0096 | 1,9119 | 0,0719 | 0,4342 | 0,2658 | 1,2448 |
| ND7001@18 | 0,0076 | 1,7638 | 0,0744 | 0,3850 | 0,2945 | 1,3506 |
| ND7001@19 | 0,0093 | 2,3567 | 0,0724 | 0,4179 | 0,2657 | 1,2524 |
| ND6001@8 | 0,0035 | 2,3498 | 0,0864 | 0,7245 | 0,9313 | 0,0733 |
| ND6001@9 | 0,0031 | 1,7567 | 0,0860 | 0,4815 | 0,9420 | 0,0676 |
| ND6001@10 | 0,0028 | 2,4927 | 0,0892 | 0,5998 | 1,0241 | 0,0710 |
| ND6001@11 | 0,0053 | 1,8796 | 0,0874 | 0,4571 | 0,9755 | 0,0791 |
| ND6001@12 | 0,0040 | 2,6158 | 0,0854 | 0,4532 | 0,8983 | 0,0706 |
| ND6001@13 | 0,0029 | 2,1808 | 0,0876 | 0,8210 | 0,9662 | 0,0737 |
| ND6001@14 | 0,0033 | 1,6173 | 0,0854 | 0,5011 | 0,9234 | 0,0663 |
| ND6001@15 | 0,0029 | 1,7939 | 0,0884 | 0,4886 | 0,9819 | 0,0684 |
| ND6001@16 | 0,0045 | 2,5470 | 0,0865 | 0,4956 | 0,9449 | 0,0709 |

Table A.4.3.- Compositions of standards

| Standard | $CO_2$ (ppm) | $H_2O$ (ppm) | F (ppm) | P (ppm) | S (ppm) | Cl (ppm) |
|---|---|---|---|---|---|---|
| ALV1833-11 | 0 | 11700 | 195 | 786 | 0 | 0 |
| ALV1833-1 | 10 | 19800 | 446 | 1095 | 643 | 747 |
| ALV519-4-1 | 165 | 1700 | 95 | 302 | 950 | 53 |
| SynFo | 0 | 0 | 0 | 0 | 0 | 0 |
| ND7001 | 80 | 10000 | 150 | 382 | 888 | 198 |
| ND6001 | 2,7 | 14200 | 208 | 461 | 42,1 | 720 |

Figure A.4.1

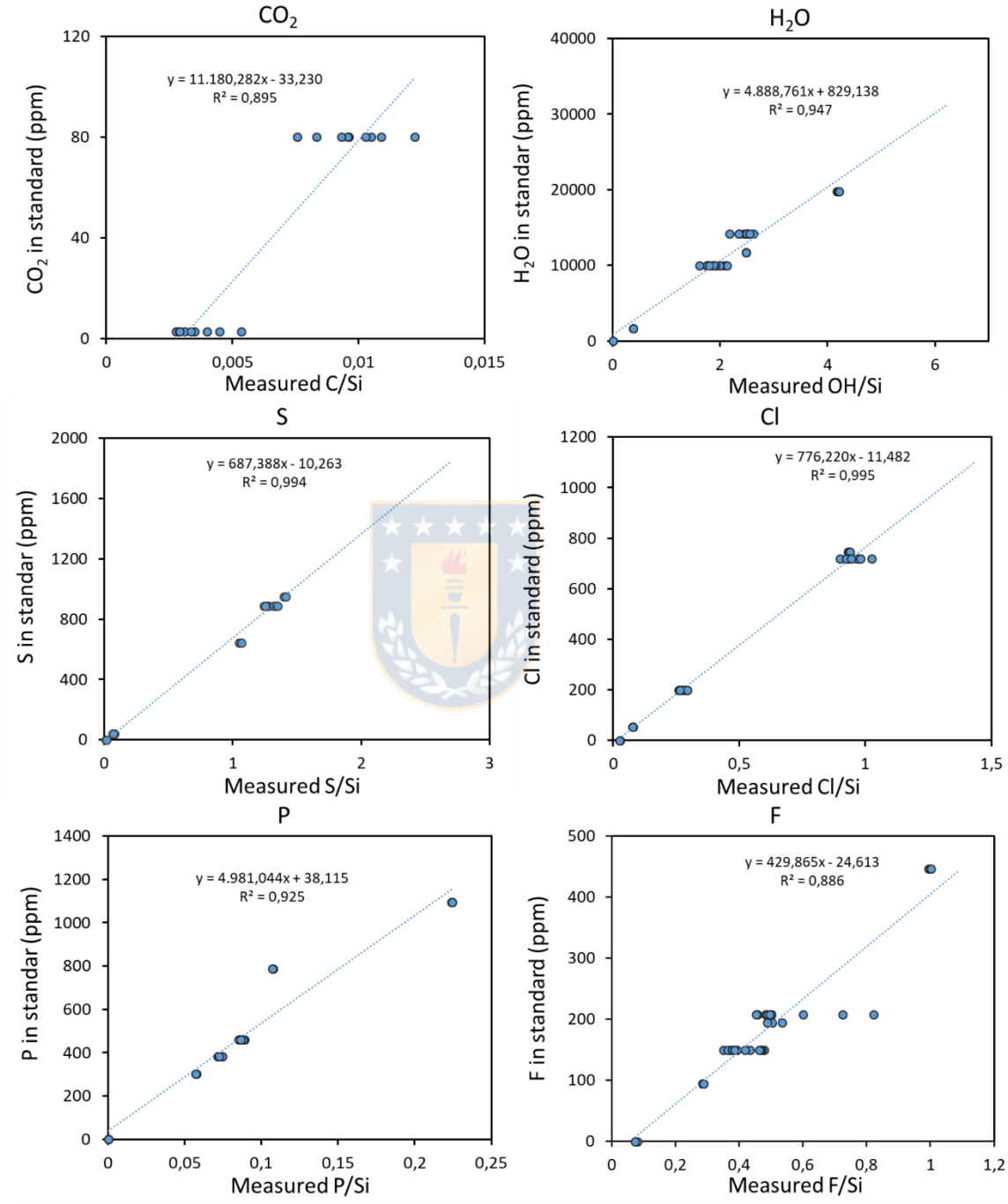


Figure A.4.1.- Standardization curves retrieved during the SIMS analytical session

Table A.4.4.- Volatile data measured in melt inclusions by SIMS (*n*=25)

| Label | Sample type | $CO_2$ ppm | $H_2O$ wt % | F ppm | P ppm | S ppm | Cl ppm |
|---|---|---|---|---|---|---|---|
| OL_ 100 inc.1 | Melt inclusion | 38 | 2,54 | 420 | 675 | 1823 | 1003 |
| OL_ 130 inc.1 | Melt inclusion | 242 | 2,00 | 402 | 722 | 3352 | 1390 |
| OL_ 124inc.1 | Melt inclusion | 311 | 2,93 | 475 | 645 | 3212 | 1248 |
| OL_ 133inc.1 | Melt inclusion | 294 | 3,44 | 509 | 786 | 2784 | 1085 |
| OL_ 128inc.1_B | Melt inclusion | 402 | 3,14 | 429 | 627 | 3296 | 1136 |
| OL_ 128inc.2 | Melt inclusion | 2855 | 3,47 | 499 | 627 | 3637 | 1138 |
| OL_ 122inc.1 | Melt inclusion | 46 | 2,76 | 341 | 683 | 2132 | 1108 |
| OL_ 120inc.1 | Melt inclusion | 2285 | 2,35 | 574 | 648 | 3945 | 1184 |
| OL_ 110inc.1 | Melt inclusion | 271 | 2,03 | 431 | 655 | 3500 | 1355 |
| OL_ 107inc.1 | Melt inclusion | 50 | 1,63 | 442 | 702 | 1645 | 1002 |
| OL_ 82inc.1 | Melt inclusion | 227 | 3,17 | 413 | 670 | 3260 | 1274 |
| OL_ 86inc.1 | Melt inclusion | 226 | 2,29 | 421 | 823 | 3429 | 1347 |
| OL_ 58inc.1 | Melt inclusion | 244 | 2,68 | 401 | 675 | 3456 | 1371 |
| OL_ 91inc.1 | Melt inclusion | 5707 | 2,58 | 745,64 | 775 | 3595 | 1488 |
| OL_ 129inc.1 | Melt inclusion | 375 | 2,67 | 499 | 660 | 3894 | 1443 |
| OL_ 66inc.2 | Melt inclusion | 24325 | 2,58 | 345 | 870 | 3117 | 1191 |
| OL_ 127inc.1 | Melt inclusion | 195 | 1,76 | 386 | 734 | 3077 | 1345 |
| OL_ 119inc.1 | Melt inclusion | 26062 | 3,23 | 688 | 622 | 3787 | 1413 |
| OL_ 112inc.1 | Melt inclusion | 6900 | 2,89 | 765 | 703 | 5305 | 1281 |
| OL_ 64inc.1 | Melt inclusion | 9401 | 3,09 | 806 | 698 | 2729 | 1416 |
| OL_ 82inc.2 | Melt inclusion | 258 | 2,00 | 381 | 719 | 3034 | 1257 |
| OL_ 85inc.1 | Melt inclusion | 145 | 1,96 | 353 | 752 | 3163 | 1279 |
| OL_ 85inc.2 | Melt inclusion | 116 | 1,63 | 366 | 728 | 3350 | 1296 |
| OL_ 87inc.1 | Melt inclusion | 333 | 3,35 | 427 | 621 | 4302 | 1265 |
| OL_ 58inc.2 | Melt inclusion | 1883 | 2,83 | 787 | 571 | 4698 | 1016 |

Table A.4.5.- Volatile data measured in external glasses by SIMS (*n*=24)

| Label | Sample type | $CO_2$ ppm | $H_2O$ wt % | F ppm | P ppm | S ppm | Cl ppm |
|---|---|---|---|---|---|---|---|
| OL_ 47@1 | Groundmass | 62 | 0,74 | 274 | 698 | 417 | 993 |
| OL_ 64@2 | Groundmass | 50 | 0,62 | 357 | 661 | 518 | 823 |
| OL_ 130@2 | Groundmass | 15920 | 0,54 | 381 | 776 | 44 | 728 |
| OL_ 131@1 | Groundmass | 9 | 0,29 | 500 | 847 | 9 | 740 |
| OL_ 131@2 | Groundmass | 178 | 0,41 | 508 | 813 | 55 | 871 |
| OL_ 66@1 | Groundmass | 44 | 0,58 | 316 | 638 | 82 | 687 |
| OL_ 122@2 | Groundmass | 144 | 0,54 | 341 | 841 | 57 | 852 |
| OL_ 110@2 | Groundmass | 80 | 0,67 | 418 | 845 | 19 | 811 |
| OL_ 106@2 | Groundmass | 4303 | 0,69 | 402 | 656 | 245 | 754 |
| OL_ 81@2 | Groundmass | 27 | 0,62 | 515 | 690 | 90 | 820 |
| OL_ 47@2 | Groundmass | 124 | 0,53 | 258 | 778 | 127 | 998 |
| OL_ 90@3 | Groundmass | 26 | 0,31 | 161,80 | 413 | 27 | 272 |
| OL_ 130@3 | Groundmass | 35 | 0,43 | 361 | 965 | 45 | 971 |
| OL_ 112@3 | Groundmass | 72 | 0,68 | 455 | 720 | 178 | 883 |
| OL_ 106@3 | Groundmass | 101 | 0,57 | 497 | 684 | 26 | 730 |
| OL_ 106@4 | Groundmass | 540 | 0,65 | 345 | 736 | 24 | 716 |
| OL_ 106@5 | Groundmass | 141 | 0,45 | 462 | 846 | 19 | 748 |
| OL_ 106@6 | Groundmass | 222 | 0,66 | 392 | 754 | 82 | 743 |
| OL_ 106@7 | Groundmass | 159 | 0,68 | 371 | 706 | 112 | 756 |
| OL_ 90@2 | Groundmass | 4 | 0.76 | 465 | 801 | 4 | 542 |
| OL_ 112@2 | Groundmass | 242 | 0.72 | 436 | 842 | 66 | 902 |
| OL_ 81@1 | Groundmass | 35 | 0.45 | 453 | 777 | 10 | 782 |
| OL_ 87@2 | Groundmass | 339 | 0.57 | 455 | 938 | 38 | 1092 |
| OL_ 106@8 | Groundmass | 124 | 0,69 | 389 | 665 | 141 | 738 |

Table A.4.6.- Measured composition on 27 MI's. The subset of 6 MI's at the bottom were discarded by low MgO, whereas the subset of 4 MI's that continue upward were discarded by high FeO. The upper 17 MI's were used.

| Sample | $SiO_2$ wt % | $TiO_2$ wt % | $Al_2O_3$ wt % | FeO* wt % | MnO wt % | MgO wt % | CaO wt % | $Na_2O$ wt % | $K_2O$ wt % | $P_2O_5$ wt % | $SO_3$ wt % | Cl wt % | Total wt % |
|---|---|---|---|---|---|---|---|---|---|---|---|---|---|
| OL_58inc.1 | 46,83 | 0,74 | 15,93 | 6,70 | 0,066 | 8,18 | 12,18 | 2,42 | 0,609 | 0,115 | 0,580 | 0,066 | 94,46 |
| OL_82inc.1 | 48,55 | 0,76 | 16,04 | 6,36 | 0,090 | 7,82 | 11,91 | 2,56 | 0,619 | 0,152 | 0,509 | 0,128 | 95,49 |
| OL_82inc.2 | 47,78 | 0,71 | 15,58 | 7,03 | 0,052 | 7,51 | 12,40 | 2,40 | 0,596 | 0,154 | 0,526 | 0,120 | 94,86 |
| OL_86inc.1 | 47,34 | 0,77 | 17,21 | 7,20 | 0,080 | 6,21 | 12,62 | 2,49 | 0,705 | 0,162 | 0,551 | 0,138 | 95,48 |
| OL_87inc.1 | 47,53 | 0,72 | 15,25 | 6,38 | 0,135 | 6,07 | 13,07 | 2,32 | 0,527 | 0,131 | 0,668 | 0,130 | 92,94 |
| OL_100inc.1 | 49,94 | 0,72 | 15,87 | 7,18 | 0,067 | 7,75 | 11,33 | 2,48 | 0,682 | 0,073 | 0,321 | 0,091 | 96,51 |
| OL_106inc.1 | 46,86 | 0,74 | 16,35 | 7,86 | 0,139 | 7,45 | 12,18 | 2,86 | 0,678 | 0,098 | 0,545 | 0,132 | 95,89 |
| OL_107inc.1 | 48,77 | 0,79 | 16,77 | 6,73 | 0,111 | 7,01 | 12,20 | 3,00 | 0,789 | 0,131 | 0,323 | 0,102 | 96,73 |
| OL_110inc.2 | 46,04 | 0,71 | 17,29 | 5,93 | 0,061 | 7,03 | 13,94 | 2,55 | 0,620 | 0,143 | 0,640 | 0,154 | 95,11 |
| OL_115inc.1 | 46,56 | 0,76 | 16,79 | 6,77 | 0,127 | 7,01 | 12,94 | 2,95 | 0,659 | 0,173 | 0,552 | 0,104 | 95,39 |
| OL_119inc.1 | 48,5 | 0,74 | 16,58 | 6,59 | 0,054 | 6,97 | 11,87 | 2,78 | 0,668 | 0,134 | 0,350 | 0,107 | 95,35 |
| OL_120inc.1 | 47,66 | 0,79 | 17,36 | 6,12 | 0,054 | 7,55 | 12,41 | 2,93 | 0,723 | 0,109 | 0,582 | 0,126 | 96,41 |
| OL_122inc.1 | 48,45 | 0,64 | 15,26 | 7,39 | 0,137 | 7,71 | 11,00 | 2,49 | 0,647 | 0,138 | 0,325 | 0,097 | 94,29 |
| OL_124inc.3 | 47,04 | 0,70 | 16,54 | 7,17 | 0,122 | 7,31 | 13,02 | 2,51 | 0,540 | 0,122 | 0,562 | 0,121 | 95,76 |
| OL_125inc.1 | 48,75 | 0,67 | 15,84 | 6,80 | 0,125 | 6,86 | 12,94 | 2,26 | 0,539 | 0,132 | 0,520 | 0,117 | 95,55 |
| OL_130inc.1 | 46,92 | 0,78 | 17,82 | 6,43 | 0,140 | 7,32 | 13,62 | 2,74 | 0,658 | 0,120 | 0,568 | 0,129 | 46,92 |
| OL_135inc.1 | 47,32 | 0,73 | 17,90 | 6,20 | 0,069 | 6,24 | 13,77 | 2,90 | 0,671 | 0,116 | 0,622 | 0,145 | 96,68 |
| OL_66inc.2 | 48,06 | 0,82 | 16,09 | 9,37 | 0,135 | 7,4 | 10,37 | 2,65 | 0,920 | 0,151 | 0,512 | 0,115 | 96,59 |
| OL_133inc.1 | 47,14 | 0,73 | 15,14 | 8,63 | 0,113 | 8,52 | 10,96 | 2,45 | 0,632 | 0,099 | 0,432 | 0,104 | 94,95 |
| OL_137inc.1 | 49,74 | 0,72 | 14,71 | 8,19 | 0,145 | 7,94 | 10,9 | 2,34 | 0,642 | 0,125 | 0,461 | 0,121 | 96,03 |
| OL_137binc.1 | 48,23 | 0,66 | 14,68 | 8,59 | 0,138 | 7,29 | 10,98 | 2,05 | 0,671 | 0,168 | 0,452 | 0,122 | 94,03 |
| OL_98inc.1 | 47,76 | 0,84 | 18,75 | 5,59 | 0,071 | 4,6 | 13,55 | 2,82 | 0,727 | 0,156 | 0,689 | 0,139 | 95,69 |
| OL_128inc.1 | 48,76 | 0,72 | 16,85 | 6,18 | 0,047 | 4,98 | 13,35 | 2,70 | 0,626 | 0,112 | 0,590 | 0,147 | 95,06 |
| OL_128inc.2 | 48,46 | 0,71 | 16,6 | 6,35 | 0,147 | 5,18 | 13,12 | 2,49 | 0,644 | 0,134 | 0,614 | 0,132 | 94,59 |
| OL_131inc.3 | 47,58 | 0,85 | 16,56 | 7,79 | 0,107 | 4,98 | 13,59 | 2,58 | 0,619 | 0,112 | 0,573 | 0,145 | 95,49 |
| OL_137inc.2 | 49,49 | 0,78 | 16 | 8,64 | 0,093 | 5,65 | 12,16 | 2,63 | 0,695 | 0,136 | 0,485 | 0,103 | 96,86 |
| OL_137binc.2 | 48,6 | 0,77 | 15,94 | 7,76 | 0,160 | 5,42 | 12,31 | 2,75 | 0,764 | 0,179 | 0,520 | 0,122 | 95,30 |

Table A.4.7: Major and minor elements measured in external glasses by EPMA

| Sample | $SiO_2$ (wt%) | $TiO_2$ (wt%) | $Al_2O_3$ (wt%) | FeO (wt%) | MnO (wt%) | MgO (wt%) | CaO (wt%) | $Na_2O$ (wt%) | $K_2O$ (wt%) | $P_2O_5$ (wt%) | S (ppm) | Cl (ppm) | Total (wt%) |
|---|---|---|---|---|---|---|---|---|---|---|---|---|---|
| OL_ 30@1 | 53,56 | 0,99 | 14,71 | 8,53 | 0,11 | 5,51 | 9,88 | 2,91 | 1,12 | 0,20 | 38 | 803 | 97,62 |
| OL_ 47@1 | 51,35 | 0,74 | 16,07 | 7,31 | 0,11 | 6,18 | 11,16 | 2,83 | 0,83 | 0,14 | 394 | 988 | 96,90 |
| OL_ 47@2 | 52,83 | 0,83 | 15,98 | 7,58 | 0,18 | 5,92 | 10,71 | 2,90 | 0,88 | 0,12 | 70 | 947 | 98,03 |
| OL_ 58@2 | 53,29 | 0,93 | 14,35 | 8,73 | 0,16 | 5,61 | 10,00 | 2,88 | 1,04 | 0,13 | 108 | 890 | 97,23 |
| OL_ 64@1 | 53,90 | 0,96 | 14,84 | 8,84 | 0,14 | 5,08 | 9,67 | 3,16 | 1,12 | 0,21 | 0 | 910 | 98,00 |
| OL_ 66@1 | 53,48 | 0,79 | 15,76 | 6,81 | 0,18 | 5,90 | 10,94 | 3,13 | 0,93 | 0,14 | 0 | 1051 | 98,18 |
| OL_ 66@3 | 52,39 | 0,91 | 14,35 | 8,74 | 0,16 | 5,52 | 9,94 | 3,07 | 1,02 | 0,16 | 26 | 825 | 96,36 |
| OL_ 81@1 | 53,31 | 0,79 | 15,34 | 7,86 | 0,15 | 5,84 | 10,48 | 2,72 | 0,93 | 0,15 | 152 | 960 | 97,70 |
| OL_ 81@2 | 54,02 | 0,94 | 14,68 | 8,86 | 0,09 | 5,52 | 10,01 | 2,82 | 1,08 | 0,17 | 6 | 633 | 98,25 |
| OL_ 81@3 | 54,37 | 1,00 | 14,68 | 8,70 | 0,13 | 5,60 | 9,80 | 3,16 | 1,05 | 0,24 | 0 | 689 | 98,82 |
| OL_ 85@1 | 54,11 | 1,04 | 14,45 | 8,38 | 0,22 | 5,13 | 9,39 | 3,18 | 1,17 | 0,23 | 50 | 1100 | 97,43 |
| OL_ 85@2 | 53,89 | 0,97 | 14,53 | 8,65 | 0,20 | 5,30 | 9,49 | 3,34 | 1,14 | 0,22 | 76 | 956 | 97,86 |
| OL_ 90@1 | 55,55 | 0,97 | 15,09 | 8,24 | 0,09 | 5,26 | 9,52 | 3,24 | 1,16 | 0,19 | 61 | 1142 | 99,45 |
| OL_ 106@2 | 51,60 | 0,82 | 16,21 | 8,11 | 0,16 | 5,79 | 11,00 | 2,89 | 0,90 | 0,14 | 298 | 870 | 97,77 |
| OL_ 107@2 | 53,89 | 0,99 | 14,66 | 8,82 | 0,09 | 5,44 | 10,12 | 3,18 | 1,06 | 0,16 | 18 | 783 | 98,50 |
| OL_ 110@1 | 54,30 | 0,91 | 15,18 | 7,30 | 0,10 | 5,62 | 10,20 | 2,95 | 1,09 | 0,17 | 3 | 1068 | 97,94 |
| OL_ 112@1 | 54,27 | 0,97 | 14,67 | 8,60 | 0,15 | 5,48 | 10,00 | 3,08 | 1,04 | 0,17 | 70 | 979 | 98,54 |
| OL_ 115@2 | 53,16 | 1,03 | 14,26 | 9,03 | 0,13 | 5,51 | 10,12 | 2,92 | 1,05 | 0,17 | 0 | 838 | 97,48 |
| OL_ 119@2 | 51,18 | 0,80 | 15,50 | 8,74 | 0,15 | 5,92 | 10,87 | 2,92 | 0,89 | 0,14 | 93 | 934 | 97,22 |
| OL_ 120@2 | 52,93 | 0,88 | 14,61 | 8,39 | 0,18 | 5,73 | 10,21 | 3,00 | 0,96 | 0,21 | 97 | 929 | 97,22 |
| OL_ 122@2 | 52,94 | 0,96 | 14,50 | 8,78 | 0,14 | 5,51 | 10,13 | 3,06 | 1,01 | 0,19 | 14 | 981 | 97,32 |
| OL_ 127b@1 | 53,94 | 0,96 | 14,96 | 8,74 | 0,15 | 5,71 | 10,03 | 2,74 | 1,01 | 0,20 | 0 | 797 | 98,54 |
| OL_ 128@3 | 53,67 | 1,00 | 14,33 | 8,97 | 0,10 | 5,21 | 9,57 | 2,98 | 1,14 | 0,20 | 0 | 531 | 97,23 |
| OL_ 130 @2 | 54,50 | 1,02 | 14,88 | 8,58 | 0,06 | 5,38 | 9,92 | 3,16 | 1,14 | 0,21 | 28 | 1070 | 98,97 |
| OL_ 131@1 | 54,70 | 0,94 | 14,96 | 7,55 | 0,15 | 5,42 | 10,52 | 3,11 | 1,09 | 0,13 | 28 | 1002 | 98,66 |
| OL_ 131@2 | 54,31 | 1,05 | 14,98 | 7,40 | 0,13 | 5,50 | 11,03 | 3,06 | 1,04 | 0,20 | 33 | 916 | 98,81 |
| OL_ 137b@3 | 53,13 | 0,93 | 15,00 | 8,85 | 0,15 | 5,45 | 10,09 | 2,94 | 1,02 | 0,24 | 105 | 995 | 97,93 |

Table A.4.8: Standard glasses used during µ-XANES measurements

| Standard | $Fe^{3+}/\Sigma Fe$ | Measurement #1 eV | Measurement #2 eV | Average eV | Standard deviation | Fiege et al. (2017) |
|---|---|---|---|---|---|---|
| H2O-52 | 54,9 | 7112,96264 | 7112,96300 | 7112,9628 | 0,000254365 | 7112,797 |
| H2O-53 | 50,1 | 7112,93930 | 7112,94004 | 7112,9397 | 0,000527125 | 7112,747 |
| H2O-54 | 56,2 | 7113,10703 | 7113,12717 | 7113,1171 | 0,014244052 | 7112,846 |
| H2O-55 | 57,2 | 7112,91488 | 7112,91896 | 7112,9169 | 0,002883605 | 7112,725 |
| H2O-66 | 53,5 | 7112,97492 | 7112,97494 | 7112,9749 | 0,000018076 | 7112,788 |
| H2O-67 | 59,7 | No data | 7113,09209 | | | 7112,799 |
| PD2K3-a | 27 | 7112,53261 | 7112,51616 | 7112,5244 | 0,011626184 | 7112,400 |
| PD2K3-b | 27 | 7112,53261 | 7112,51616 | 7112,5244 | 0,011626184 | 7112,383 |
| PD2K4-a | 23 | 7112,47578 | 7112,49159 | 7112,4837 | 0,011175671 | 7112,354 |
| PD2K4-b | 23 | 7112,47578 | 7112,49159 | 7112,4837 | 0,011175671 | 7112,328 |

Table A.4.9.- Centroid positions, $Fe^{3+}/\Sigma Fe$ values for melt inclusions and groundmass glasses.

| Sample | Type [1] | Centroid position [2] | $Fe^{3+}/\Sigma Fe$ [3] | Averaged error [4] |
|---|---|---|---|---|
| Fe_XANES_ol81inc2.1 | MI | 7112,456 | 0,40 | 0,013 |
| Fe_XANES_ol82inc1.1 | MI | 7112,355 | 0,34 | 0,029 |
| Fe_XANES_ol82inc2.1 | MI | 7112,351 | 0,34 | 0,029 |
| Fe_XANES_ol100_inc1.1 | MI | 7112,332 | 0,33 | 0,032 |
| Fe_XANES_ol100_inc1.2 | MI | 7112,348 | 0,34 | 0,030 |
| Fe_XANES_ol107inc1.1 | MI | 7112,307 | 0,32 | 0,036 |
| Fe_XANES_ol122inc1.1 | MI | 7112,313 | 0,32 | 0,035 |
| Fe_XANES_ol122inc3.1 | MI | 7112,339 | 0,33 | 0,031 |
| Fe_XANES_ol124inc1.1 | MI | 7112,233 | 0,28 | 0,045 |
| Fe_XANES_ol125inc1.1 | MI | 7112,435 | 0,39 | 0,016 |
| Fe_XANES_ol128inc2.2 | MI | 7112,375 | 0,35 | 0,026 |
| Fe_XANES_ol133inc1.1 | MI | 7112,295 | 0,31 | 0,037 |
| Fe_XANES_olxx137inc1.1 | MI | 7112,401 | 0,37 | 0,022 |
| Fe_XANES_ol47mat1.1 | EG | 7112,142 | 0,23 | 0,056 |
| Fe_XANES_ol58mat1.1 | EG | 7112,230 | 0,28 | 0,046 |
| Fe_XANES_ol81mat1.1 | EG | 7112,164 | 0,24 | 0,053 |
| Fe_XANES_ol81mat3.1 | EG | 7112,129 | 0,23 | 0,057 |
| Fe_XANES_ol82mat1.1 | EG | 7112,203 | 0,26 | 0,049 |
| Fe_XANES_ol86mat2.1 | EG | 7112,161 | 0,24 | 0,054 |
| Fe_XANES_ol106mat2.2 | EG | 7112,104 | 0,22 | 0,060 |
| Fe_XANES_ol106mat3.1 | EG | 7112,095 | 0,21 | 0,061 |
| Fe_XANES_ol106mat3.2 | EG | 7112,082 | 0,21 | 0,062 |
| Fe_XANES_ol106mat6.1 | EG | 7112,181 | 0,25 | 0,051 |
| Fe_XANES_ol107mat1.1 | EG | 7112,130 | 0,23 | 0,057 |
| Fe_XANES_ol112mat1.1 | EG | 7112,108 | 0,22 | 0,060 |
| Fe_XANES_ol112mat2.1 | EG | 7112,157 | 0,24 | 0,054 |
| Fe_XANES_ol112mat3.1 | EG | 7112,126 | 0,23 | 0,058 |
| Fe_XANES_ol115mat2.1 | EG | 7112,143 | 0,23 | 0,056 |
| Fe_XANES_ol120mat2.1 | EG | 7112,200 | 0,26 | 0,049 |
| Fe_XANES_ol122mat2.2 | EG | 7112,129 | 0,23 | 0,057 |
| Fe_XANES_ol125mat1.1 | EG | 7112,274 | 0,30 | 0,040 |
| Fe_XANES_ol127mat1.2 | EG | 7112,330 | 0,33 | 0,032 |
| Fe_XANES_ol135mat1.1 | EG | 7112,210 | 0,27 | 0,048 |
| Fe_XANES_ol135mat1.2 | EG | 7112,317 | 0,32 | 0,034 |
| Fe_XANES_olxx137mat3.2 | EG | 7112,156 | 0,24 | 0,054 |

[1] MI = melt inclusions; EG = external glass

[2] Centroid position calculated after de application of the correction values of 0,1078 eV to measured data. See text for details.

[3] Fe speciation calculated from Eq.6 Fiege et al. (2017); $CFe[eV] = 7111,6\ (\pm 0,034497) + 0,025722\ (\pm 0,0019192) \times Fe^{3+}/\Sigma Fe - 0,00010624\ (\pm 2,0847e^{-5}) \times (Fe^{3+}/\Sigma Fe)^2$.

[4] Averaged error calculated from Eq.6 Fiege et al. (2017)

Table A.4.10.- Trace element concentrations by LA-ICP-MS for reconstructed melt inclusions (*n*=15)

| | Sc ppm | Cu ppm | Rb ppm | Sr ppm | Y ppm | Zr ppm | Nb ppm | Ba ppm | La ppm | Ce ppm | Pr ppm | Nd ppm | Sm ppm | Eu ppm | Gd ppm | Dy ppm | Er ppm | Yb ppm | Hf ppm | Pb ppm | Th ppm | U ppm |
|---|---|---|---|---|---|---|---|---|---|---|---|---|---|---|---|---|---|---|---|---|---|---|
| OL_58inc.1 | 38 | 102 | 10 | 619 | 16 | 54 | 0,8 | 171 | 7,1 | 17 | 2,3 | 11 | 1,4 | 0,8 | 3,0 | 2,5 | 1,6 | 1,2 | 1,5 | 7,2 | 2,5 | 0,6 |
| OL_82inc.1 | 37 | 102 | 9 | 593 | 14 | 55 | 0,8 | 164 | 7,0 | 17 | 2,1 | 11 | 2,4 | 0,8 | 2,2 | 2,7 | 2,1 | 1,7 | 1,4 | 7,3 | 2,2 | 0,6 |
| OL_82inc.2 | 49 | 124 | 11 | 629 | 18 | 72 | 1,1 | 192 | 8,5 | 20 | 2,6 | 11 | 2,2 | 1,2 | 3,2 | 2,2 | 2,6 | 2,2 | 2,3 | 7,8 | 2,6 | 0,6 |
| OL_86inc.1 | 57 | 81 | 13 | 727 | 19 | 69 | 1,2 | 222 | 8,7 | 23 | 2,9 | 14 | 3,1 | 1,0 | 2,8 | 3,2 | 2,1 | 1,7 | 2,1 | 10,1 | 2,7 | 0,8 |
| OL_87inc.1b | 48 | 100 | 10 | 626 | 17 | 63 | 0,7 | 173 | 7,4 | 18 | 2,3 | 11 | 2,9 | 0,8 | 3,3 | 2,7 | 1,9 | 1,4 | 1,6 | 8,2 | 2,2 | 0,6 |
| OL_100 inc.1 | 43 | 107 | 12 | 585 | 17 | 65 | 1,4 | 193 | 7,4 | 19 | 2,4 | 12 | 2,5 | 0,6 | 2,9 | 3,5 | 1,6 | 1,1 | 2,1 | 7,7 | 3,0 | 0,8 |
| OL_107inc.1 | 43 | 107 | 12 | 585 | 17 | 65 | 1,4 | 193 | 7,4 | 19 | 2,4 | 12 | 2,5 | 0,6 | 2,9 | 3,5 | 1,6 | 1,1 | 2,1 | 7,7 | 3,0 | 0,8 |
| OL_110inc.2 | 56 | 220 | 29 | 766 | 34 | 130 | 2,5 | 370 | 14,7 | 39 | 4,5 | 24 | 7,0 | 1,9 | 4,1 | 6,4 | 2,7 | 3,3 | 3,9 | 15,9 | 5,0 | 1,3 |
| OL_115inc.1 | 56 | 134 | 14 | 632 | 18 | 70 | 1,1 | 199 | 7,1 | 23 | 2,9 | 12 | 2,7 | 1,0 | 2,6 | 2,2 | 1,9 | 2,5 | 2,2 | 9,2 | 2,2 | 0,7 |
| OL_119inc.1 | 43 | 116 | 9 | 583 | 16 | 57 | 0,8 | 155 | 6,4 | 16 | 2,1 | 10 | 2,9 | 0,6 | 2,5 | 2,3 | 1,8 | 1,5 | 2,1 | 7,7 | 2,4 | 0,5 |
| OL_120inc.1 | 51 | 114 | 12 | 614 | 19 | 72 | 1,0 | 186 | 7,8 | 19 | 2,2 | 12 | 0,6 | 1,1 | 2,1 | 3,0 | 2,5 | 2,6 | 2,9 | 8,9 | 2,1 | 0,5 |
| OL_122inc.1 | 40 | 114 | 14 | 582 | 16 | 63 | 1,5 | 188 | 7,7 | 20 | 2,4 | 10 | 2,6 | 0,9 | 2,7 | 4,2 | 1,7 | 1,6 | 2,1 | 8,7 | 2,4 | 0,7 |
| OL_125 inc.1 | 42 | 123 | 9 | 630 | 15 | 56 | 0,9 | 159 | 6,8 | 15 | 2,3 | 10 | 2,8 | 0,8 | 3,8 | 2,1 | 1,5 | 1,2 | 1,7 | 6,9 | 2,1 | 0,6 |
| OL_130 inc.1 | 40 | 104 | 10 | 663 | 17 | 59 | 0,8 | 171 | 7,2 | 17 | 2,2 | 10 | 3,2 | 1,1 | 2,8 | 3,1 | 1,9 | 1,9 | 1,5 | 7,6 | 2,6 | 0,5 |
| OL_135inc.1 | 70 | 150 | 13 | 678 | 21 | 74 | 1,5 | 206 | 7,5 | 24 | 2,8 | 17 | 4,2 | 1,6 | 4,4 | 3,0 | 2,0 | 3,1 | 2,6 | 8,7 | 1,3 | 0,9 |

Table A.4.11.- Trace element concentrations by LA-ICP-MS for MI's not analyzed by EPMA (*n*=58)

| | Sc ppm | Cu ppm | Rb ppm | Sr ppm | Y ppm | Zr ppm | Nb ppm | Ba ppm | La ppm | Ce ppm | Pr ppm | Nd ppm | Sm ppm | Eu ppm | Gd ppm | Dy ppm | Er ppm | Yb ppm | Hf ppm | Pb ppm | Th ppm | U ppm |
|---|---|---|---|---|---|---|---|---|---|---|---|---|---|---|---|---|---|---|---|---|---|---|
| OL_90inc.3 | 52 | 171 | 22 | 754 | 21 | 98 | 2,2 | 266 | 10,0 | 26 | 3,2 | 13 | 2,1 | 0,9 | 2,7 | 4,3 | 2,3 | 1,5 | 1,9 | 9,4 | 3,2 | 0,9 |
| OL_90inc.2 | 79 | 230 | 33 | 689 | 31 | 146 | 2,4 | 372 | 14,2 | 37 | 4,6 | 22 | 4,7 | 1,0 | 5,3 | 4,0 | 3,0 | 3,7 | 3,9 | 14,7 | 5,2 | 1,1 |
| OL_91inc.1 | 44 | 99 | 10 | 654 | 17 | 61 | 1,1 | 181 | 7,4 | 17 | 2,3 | 12 | 3,2 | 0,9 | 2,8 | 3,0 | 1,5 | 2,0 | 2,1 | 7,8 | 1,9 | 0,5 |
| OL_137inc.1 | 49 | 114 | 18 | 668 | 19 | 92 | 1,6 | 224 | 9,3 | 20 | 2,5 | 13 | 3,4 | 1,0 | 1,8 | 3,3 | 2,2 | 2,0 | 2,6 | 9,7 | 3,1 | 0,7 |
| OL_137inc.2 | 73 | 172 | 22 | 632 | 24 | 97 | 1,9 | 223 | 7,8 | 26 | 2,9 | 13 | 3,4 | N.D | 4,2 | 3,1 | 2,2 | 2,8 | 2,7 | 11,4 | 3,0 | 0,5 |
| OL_130inc.2 | 31 | 124 | 17 | 737 | 16 | 65 | 1,5 | 218 | 7,9 | 19 | 2,5 | 12 | 3,0 | 0,9 | 2,1 | 2,3 | 1,9 | 1,6 | 2,1 | 8,6 | 2,7 | 0,7 |
| OL_137binc.1 | 51 | 117 | 19 | 659 | 19 | 88 | 1,6 | 223 | 8,5 | 25 | 3,0 | 13 | 2,5 | 0,9 | 4,0 | 3,4 | 1,1 | 2,0 | 1,3 | 10,3 | 3,1 | 0,8 |
| OL_137binc.2 | 57 | 210 | 29 | 699 | 28 | 132 | 2,6 | 337 | 13,8 | 34 | 4,4 | 20 | 4,8 | 1,6 | 3,1 | 4,4 | 3,6 | 2,8 | 3,6 | 16,5 | 4,5 | 1,4 |
| OL_137inc.3 | 66 | 139 | 12 | 681 | 19 | 67 | 1,1 | 191 | 7,8 | 21 | 2,3 | 15 | 2,0 | 0,9 | 2,4 | 3,5 | 1,8 | 2,3 | 2,1 | 9,2 | 2,9 | 0,8 |
| OL_135inc.2 | 49 | 219 | 29 | 705 | 26 | 118 | 2,5 | 319 | 13,9 | 34 | 4,3 | 21 | 4,8 | 1,6 | 5,4 | 5,1 | 2,9 | 2,8 | 2,7 | 14,7 | 4,2 | 1,3 |
| OL_133inc.1 | 40 | 171 | 20 | 725 | 19 | 79 | 1,5 | 256 | 11,0 | 24 | 2,9 | 13 | 3,3 | 1,3 | 3,6 | 3,7 | 2,4 | 2,2 | 2,8 | 12,1 | 2,6 | 1,0 |
| OL_131inc.1 | 69 | 110 | 10 | 613 | 19 | 67 | 0,6 | 181 | 7,5 | 19 | 2,4 | 11 | N.D | 0,7 | N.D | 2,5 | 1,8 | 2,7 | 2,3 | 7,4 | 1,8 | 0,8 |
| OL_131inc.2 | 49 | 139 | 12 | 582 | 17 | 61 | 0,6 | 162 | 7,0 | 17 | 2,3 | 9 | 2,0 | 0,8 | 2,6 | 2,4 | 2,3 | 1,6 | 1,7 | 8,7 | 2,5 | 0,8 |
| OL_131inc.3 | 47 | 141 | 13 | 619 | 17 | 58 | 0,4 | 167 | 7,2 | 19 | 2,4 | 11 | 2,9 | 1,1 | 2,7 | 2,4 | 1,2 | 1,5 | 1,7 | 9,0 | 2,4 | 0,7 |
| OL_129inc.1 | 40 | 115 | 9 | 604 | 17 | 69 | 0,9 | 161 | 6,9 | 20 | 2,3 | 13 | 2,7 | 0,9 | 2,2 | 2,4 | 1,9 | 2,1 | 2,1 | 8,6 | 2,5 | 0,8 |
| OL_128inc.1 | 43 | 138 | 16 | 660 | 18 | 76 | 1,3 | 227 | 8,4 | 20 | 2,7 | 12 | 3,4 | 1,0 | 3,1 | 3,4 | 1,9 | 2,2 | 2,6 | 8,6 | 2,5 | 0,6 |
| OL_128inc.2 | 43 | 141 | 19 | 674 | 18 | 88 | 1,7 | 232 | 10,2 | 22 | 2,8 | 15 | 3,7 | 0,9 | 3,6 | 3,8 | 2,1 | 2,1 | 2,4 | 9,0 | 3,3 | 0,8 |
| OL_66inc.1 | 82 | 259 | 28 | 727 | 23 | 132 | 2,4 | 276 | 11,5 | 32 | 3,5 | 16 | 5,5 | 1,1 | 4,4 | 4,5 | 1,8 | 2,5 | 2,8 | 10,4 | 5,4 | 0,9 |
| OL_100inc.1 | 47 | 180 | 26 | 706 | 24 | 116 | 2,3 | 317 | 13,5 | 31 | 4,1 | 17 | 4,1 | 1,4 | 4,0 | 4,1 | 2,6 | 2,6 | 3,2 | 14,7 | 5,1 | 1,3 |
| OL_66inc.2 | 37 | 145 | 19 | 729 | 22 | 91 | 1,8 | 265 | 11,2 | 25 | 3,6 | 17 | 3,7 | 0,9 | 3,2 | 4,0 | 2,6 | 2,5 | 2,5 | 10,0 | 3,6 | 0,9 |
| OL_66inc.3 | 61 | 134 | 20 | 487 | 20 | 78 | 1,6 | 223 | 9,6 | 24 | 2,9 | 11 | 2,4 | 1,0 | 2,9 | 3,3 | 2,2 | 1,6 | 2,9 | 8,6 | 2,9 | 0,8 |
| OL_127inc.2 | 71 | 113 | 16 | 635 | 20 | 82 | 1,4 | 213 | 9,7 | 25 | 2,7 | 12 | 2,4 | 0,9 | 3,4 | 3,4 | 2,2 | 1,8 | 2,3 | 7,6 | 2,9 | 0,6 |
| OL_122inc.2 | 69 | 199 | 21 | 666 | 25 | 98 | 1,9 | 300 | 11,9 | 31 | 3,6 | 15 | 2,9 | 1,5 | 3,1 | 4,1 | 3,2 | 2,1 | 3,6 | 11,0 | 3,4 | 1,3 |
| OL_120inc.2 | 47 | 165 | 25 | 669 | 25 | 113 | 2,4 | 309 | 13,3 | 29 | 4,0 | 19 | 4,5 | 1,3 | 4,3 | 5,0 | 2,8 | 2,9 | 2,2 | 12,3 | 4,4 | 1,1 |
| OL_119inc.2 | 48 | 92 | 11 | 616 | 18 | 66 | 1,0 | 169 | 7,3 | 18 | 2,4 | 13 | 3,1 | 0,7 | 2,2 | 3,6 | 1,8 | 1,4 | 2,1 | 7,8 | 2,1 | 0,6 |
| OL_119inc.3 | 75 | 209 | 27 | 705 | 32 | 139 | 2,4 | 343 | 14,6 | 42 | 4,7 | 19 | 1,6 | 2,2 | 3,7 | 4,2 | 3,9 | 2,8 | 2,9 | 13,8 | 4,7 | 1,4 |
| OL_115inc.2 | 53 | 198 | 24 | 699 | 25 | 113 | 2,4 | 316 | 12,9 | 33 | 4,5 | 19 | 6,0 | 1,5 | 3,9 | 4,3 | 3,1 | 2,8 | 3,5 | 13,3 | 4,3 | 0,9 |
| OL_112inc.1 | 50 | 207 | 36 | 683 | 24 | 118 | 2,7 | 355 | 13,1 | 37 | 4,1 | 19 | 4,7 | 1,6 | 3,5 | 3,7 | 2,6 | 2,1 | 3,1 | 20,8 | 4,1 | 1,7 |
| OL_112inc.2 | 41 | 137 | 11 | 601 | 18 | 59 | 1,0 | 167 | 6,6 | 20 | 2,1 | 13 | 2,2 | 0,9 | 2,6 | 1,9 | 1,8 | 2,1 | 1,3 | 7,7 | 2,4 | 1,0 |

| | Sc ppm | Cu ppm | Rb ppm | Sr ppm | Y ppm | Zr ppm | Nb ppm | Ba ppm | La ppm | Ce ppm | Pr ppm | Nd ppm | Sm ppm | Eu ppm | Gd ppm | Dy ppm | Er ppm | Yb ppm | Hf ppm | Pb ppm | Th ppm | U ppm |
|---|---|---|---|---|---|---|---|---|---|---|---|---|---|---|---|---|---|---|---|---|---|---|
| OL_112inc.3 | 54 | 241 | 34 | 693 | 25 | 115 | 2,4 | 342 | 14,5 | 34 | 4,6 | 18 | 7,0 | 1,2 | 3,9 | 4,4 | 2,1 | 1,9 | 2,7 | 18,4 | 4,4 | 1,7 |
| OL_112inc.4 | 43 | 171 | 20 | 682 | 20 | 85 | 1,8 | 257 | 10,9 | 24 | 3,2 | 16 | 3,2 | 1,0 | 2,6 | 3,3 | 3,0 | 2,6 | 2,6 | 10,9 | 3,5 | 1,0 |
| OL_110inc.1 | 48 | 176 | 23 | 671 | 20 | 91 | 2,4 | 279 | 11,9 | 28 | 3,8 | 15 | 3,6 | 1,1 | 3,7 | 2,2 | 2,7 | 1,9 | 2,6 | 13,7 | 3,7 | 1,1 |
| OL_107inc.2 | 51 | 176 | 28 | 685 | 26 | 107 | 2,1 | 311 | 13,3 | 31 | 4,2 | 16 | 3,4 | 1,3 | 3,7 | 3,6 | 1,9 | 1,7 | 3,5 | 11,3 | 3,8 | 1,3 |
| OL_106inc.2 | 47 | 129 | 11 | 650 | 18 | 67 | 1,5 | 192 | 7,7 | 21 | 3,0 | 10 | 2,1 | 0,9 | 2,9 | 2,7 | 2,6 | 2,0 | 2,2 | 9,5 | 2,5 | 0,8 |
| OL_106inc.7 | 49 | 192 | 30 | 713 | 24 | 123 | 2,3 | 327 | 14,3 | 35 | 4,0 | 21 | 3,6 | 1,4 | 4,6 | 4,2 | 2,7 | 2,8 | 4,2 | 14,6 | 4,9 | 1,4 |
| OL_106inc.6 | 41 | 180 | 26 | 715 | 21 | 99 | 2,3 | 275 | 11,5 | 27 | 3,7 | 16 | 2,8 | 1,3 | 3,8 | 5,1 | 2,2 | 2,1 | 2,4 | 12,4 | 4,2 | 1,1 |
| OL_106inc.9 | 64 | 155 | 12 | 620 | 19 | 72 | 0,9 | 180 | 6,6 | 22 | 2,4 | 14 | 2,4 | 0,8 | 1,3 | 2,5 | 1,6 | 0,9 | 1,7 | 9,0 | 2,7 | 0,6 |
| OL_106inc.5 | 54 | 158 | 26 | 754 | 25 | 115 | 2,1 | 329 | 14,2 | 34 | 4,2 | 22 | 3,5 | 1,6 | 3,7 | 3,9 | 2,2 | 2,9 | 3,0 | 14,9 | 4,5 | 1,1 |
| OL_106inc.4 | 41 | 134 | 13 | 637 | 19 | 66 | 1,1 | 199 | 8,3 | 20 | 2,7 | 11 | 2,9 | 0,9 | 3,0 | 2,6 | 1,6 | 2,0 | 1,9 | 8,6 | 2,3 | 0,8 |
| OL_98inc.1 | 55 | 237 | 41 | 716 | 35 | 158 | 3,1 | 420 | 17,9 | 49 | 5,3 | 24 | 4,3 | 1,9 | 5,8 | 5,6 | 4,0 | 2,1 | 4,1 | 19,2 | 6,4 | 2,3 |
| OL_87inc.2 | 72 | 275 | 40 | 710 | 33 | 160 | 2,7 | 398 | 17,0 | 48 | 5,1 | 22 | 3,8 | 1,7 | 5,6 | 5,1 | 3,3 | 1,9 | 3,6 | 15,8 | 6,1 | 1,8 |
| OL_85inc.2 | 41 | 90 | 11 | 638 | 15 | 66 | 1,0 | 189 | 7,8 | 19 | 2,2 | 11 | 2,4 | 0,9 | 2,2 | 2,1 | 1,9 | 1,8 | 1,6 | 7,2 | 2,2 | 0,6 |
| OL_85inc.3 | 40 | 144 | 22 | 751 | 19 | 90 | 2,3 | 263 | 10,3 | 27 | 2,9 | 16 | 3,1 | 1,4 | 3,8 | 3,5 | 1,9 | 2,8 | 2,7 | 11,1 | 3,4 | 0,9 |
| OL_85inc.4 | 44 | 197 | 28 | 779 | 25 | 118 | 2,4 | 348 | 14,1 | 35 | 4,2 | 21 | 4,4 | 1,4 | 3,3 | 3,9 | 2,7 | 3,1 | 3,4 | 15,3 | 4,5 | 1,3 |
| OL_82inc.3 | 49 | 170 | 25 | 712 | 22 | 90 | 2,1 | 302 | 11,7 | 30 | 4,0 | 17 | 3,8 | 1,2 | 3,6 | 3,5 | 2,6 | 1,9 | 2,5 | 11,0 | 3,7 | 0,9 |
| OL_81inc.1 | 41 | 160 | 24 | 721 | 24 | 112 | 2,4 | 335 | 15,0 | 29 | 4,1 | 19 | 4,3 | 1,2 | 2,7 | 4,0 | 2,0 | 2,6 | 3,6 | 11,8 | 4,6 | 1,1 |
| OL_81inc.3 | 59 | 143 | 32 | 755 | 23 | 109 | 2,5 | 294 | 12,9 | 32 | 4,0 | 18 | 3,4 | 0,9 | 2,8 | 4,4 | 2,0 | 2,0 | 2,3 | 14,5 | 4,2 | 1,2 |
| OL_81inc.2 | 59 | 176 | 18 | 693 | 24 | 83 | 1,2 | 276 | 11,5 | 29 | 3,5 | 16 | 3,6 | 1,1 | 3,5 | 3,6 | 2,6 | 2,3 | 1,3 | 10,2 | 3,3 | 1,0 |
| OL_81inc.4 | 45 | 181 | 26 | 726 | 22 | 109 | 2,2 | 326 | 13,7 | 36 | 4,6 | 18 | 5,2 | 1,3 | 4,7 | 4,0 | 2,7 | 3,3 | 2,9 | 14,0 | 4,1 | 1,3 |
| OL_64inc.1 | 32 | 135 | 21 | 810 | 19 | 87 | 2,0 | 284 | 11,0 | 28 | 3,3 | 15 | 3,7 | 1,3 | 3,3 | 3,8 | 2,0 | 1,6 | 2,9 | 10,3 | 3,9 | 1,1 |
| OL_64inc.2 | 69 | 123 | 10 | 619 | 19 | 68 | 0,7 | 178 | 7,9 | 20 | 2,2 | 13 | 3,9 | 0,7 | 4,6 | 3,6 | 1,9 | 2,5 | 2,4 | 8,1 | 2,8 | 0,8 |
| OL_64inc.3 | 39 | 138 | 16 | 696 | 20 | 77 | 1,6 | 249 | 10,2 | 23 | 3,1 | 13 | 2,6 | 0,9 | 1,9 | 3,2 | 1,9 | 1,9 | 2,4 | 8,9 | 2,8 | 0,7 |
| OL_30inc.1 | 46 | 139 | 19 | 712 | 24 | 98 | 1,9 | 272 | 10,1 | 28 | 3,5 | 18 | 3,2 | 1,1 | 4,2 | 4,0 | 1,9 | 2,6 | 2,1 | 9,6 | 4,1 | 1,0 |
| OL_40inc.1 | 37 | 103 | 9 | 628 | 16 | 59 | 0,9 | 167 | 7,2 | 17 | 2,1 | 11 | 2,2 | 0,9 | 2,5 | 2,7 | 1,2 | 1,6 | 1,6 | 7,7 | 2,1 | 0,6 |
| OL_47inc.1 | 45 | 97 | 16 | 630 | 19 | 83 | 1,6 | 225 | 9,2 | 21 | 3,0 | 14 | 3,1 | 0,9 | 3,3 | 3,0 | 1,8 | 1,8 | 2,2 | 7,7 | 3,0 | 0,7 |
| OL_47inc.2 | 52 | 171 | 22 | 754 | 21 | 98 | 2,2 | 266 | 10,0 | 26 | 3,2 | 13 | 2,1 | 0,9 | 2,7 | 4,3 | 2,3 | 1,5 | 1,9 | 9,4 | 3,2 | 0,9 |
| OL_58inc.2 | 79 | 230 | 33 | 689 | 31 | 146 | 2,4 | 372 | 14,2 | 37 | 4,6 | 22 | 4,7 | 1,0 | 5,3 | 4,0 | 3,0 | 3,7 | 3,9 | 14,7 | 5,2 | 1,1 |
| OL_58inc.3 | 44 | 99 | 10 | 654 | 17 | 61 | 1,1 | 181 | 7,4 | 17 | 2,3 | 12 | 3,2 | 0,9 | 2,8 | 3,0 | 1,5 | 2,0 | 2,1 | 7,8 | 1,9 | 0,5 |

*Continued Table A.11.*

Table A.4.12. Trace element composition obtained in whole-rock analysis of tephras from Los Hornitos

| Sample | Rb ppm | Ba ppm | Th ppm | U ppm | Nb ppm | La ppm | Ce ppm | Pb ppm | Pr ppm | Nd ppm | Sr ppm | Sm ppm | Zr ppm | Ti ppm | Eu ppm | Gd ppm | Dy ppm | Y ppm | Er ppm | Rb ppm | Ba ppm | Th ppm |
|---|---|---|---|---|---|---|---|---|---|---|---|---|---|---|---|---|---|---|---|---|---|---|
| LHWC-S1a | 18 | 199 | 2,4 | 0,7 | 1,8 | 8,9 | 20 | 8,2 | 2,7 | 11,7 | 457 | 2,8 | 66 | 3884 | 0,9 | 2,7 | 2,7 | 13,9 | 1,5 | 18 | 199 | 2,4 |
| LHWC-S1b | 13 | 149 | 1,9 | 0,6 | 1,2 | 6,5 | 15 | 6,5 | 2,1 | 9,0 | 453 | 2,3 | 53 | 3569 | 0,8 | 2,2 | 2,3 | 11,9 | 1,3 | 13 | 149 | 1,9 |
| LHWC-S1d | 13 | 147 | 2,0 | 0,6 | 1,2 | 6,7 | 15 | 6,2 | 2,1 | 9,4 | 441 | 2,4 | 55 | 3748 | 0,8 | 2,4 | 2,4 | 12,8 | 1,4 | 13 | 147 | 2,0 |
| LHCE-S1a | 20 | 218 | 2,6 | 0,8 | 2,0 | 9,6 | 21 | 8,8 | 2,9 | 12,7 | 496 | 3,1 | 71 | 4185 | 1,0 | 3,0 | 2,8 | 15,0 | 1,6 | 20 | 218 | 2,6 |
| LHCE-S1b | 15 | 174 | 2,1 | 0,7 | 1,4 | 7,6 | 17 | 7,2 | 2,4 | 10,5 | 483 | 2,6 | 62 | 3874 | 0,8 | 2,5 | 2,5 | 13,1 | 1,4 | 15 | 174 | 2,1 |
| LHCE-S1c | 17 | 185 | 2,3 | 0,7 | 1,6 | 8,2 | 18 | 7,3 | 2,5 | 11,0 | 451 | 2,8 | 63 | 3750 | 0,8 | 2,6 | 2,6 | 13,4 | 1,5 | 17 | 185 | 2,3 |
| LHCE-S1d | 15 | 155 | 2,0 | 0,6 | 1,2 | 6,8 | 15 | 6,5 | 2,1 | 9,4 | 465 | 2,4 | 55 | 3734 | 0,8 | 2,3 | 2,4 | 12,4 | 1,3 | 15 | 155 | 2,0 |
| LHEC-S1e | 14 | 155 | 2,0 | 0,6 | 1,2 | 6,7 | 15 | 6,5 | 2,1 | 9,3 | 466 | 2,4 | 55 | 3728 | 0,8 | 2,4 | 2,4 | 12,6 | 1,4 | 14 | 155 | 2,0 |
| LHCE-S1f | 14 | 157 | 2,1 | 0,7 | 1,3 | 7,1 | 16 | 6,6 | 2,2 | 9,7 | 468 | 2,4 | 58 | 3823 | 0,8 | 2,4 | 2,5 | 13,1 | 1,4 | 14 | 157 | 2,1 |

Table A.4.13.- Pearson coefficients showing the correlation values for major-minor elements measured by EPMA contrasted with the Fe speciation measured by µ-XANES. Note that the warmer colors show the highest positive correlations whereas green show the highest negative correlations.

| | $SiO_2$ | $TiO_2$ | $Al_2O_3$ | FeO* | MnO | MgO | CaO | $Na_2O$ | $K_2O$ | $P_2O_5$ | $SO_3$ | Cl | $SO_3$/MgO | Fo | $Fe^{3+}/\Sigma Fe$ |
|---|---|---|---|---|---|---|---|---|---|---|---|---|---|---|---|
| $SiO_2$ | 1,00 | | | | | | | | | | | | | | |
| $TiO_2$ | 0,09 | 1,00 | | | | | | | | | | | | | |
| $Al_2O_3$ | 0,47 | 0,75 | 1,00 | | | | | | | | | | | | |
| FeO* | -0,51 | -0,38 | -0,82 | 1,00 | | | | | | | | | | | |
| MnO | -0,18 | -0,44 | -0,35 | 0,41 | 1,00 | | | | | | | | | | |
| MgO | -0,42 | 0,12 | -0,38 | 0,44 | -0,19 | 1,00 | | | | | | | | | |
| CaO | 0,15 | 0,23 | 0,62 | -0,72 | -0,30 | -0,65 | 1,00 | | | | | | | | |
| $Na_2O$ | 0,19 | 0,77 | 0,83 | -0,52 | -0,21 | -0,02 | 0,19 | 1,00 | | | | | | | |
| $K_2O$ | 0,27 | 0,52 | 0,38 | 0,05 | 0,07 | -0,08 | -0,32 | 0,64 | 1,00 | | | | | | |
| $P_2O_5$ | -0,36 | -0,27 | -0,20 | -0,08 | 0,26 | -0,42 | 0,22 | -0,25 | -0,16 | 1,00 | | | | | |
| $SO_3$ | -0,45 | -0,14 | -0,21 | -0,09 | -0,18 | -0,09 | 0,49 | -0,51 | -0,76 | 0,52 | 1,00 | | | | |
| Cl | -0,38 | -0,07 | -0,17 | -0,11 | -0,01 | -0,22 | 0,38 | -0,42 | -0,48 | 0,78 | 0,89 | 1,00 | | | |
| $SO_3$/MgO | -0,29 | -0,19 | -0,10 | -0,20 | -0,09 | -0,38 | 0,65 | -0,49 | -0,71 | 0,58 | 0,95 | 0,87 | 1,00 | | |
| Fo | 0,59 | 0,10 | 0,68 | -0,93 | -0,37 | -0,64 | 0,77 | 0,31 | -0,13 | 0,13 | 0,09 | 0,08 | 0,27 | 1,00 | |
| $Fe^{3+}/\Sigma Fe$ | 0,16 | -0,47 | -0,20 | -0,10 | 0,20 | -0,62 | 0,48 | -0,67 | -0,57 | 0,44 | 0,63 | 0,62 | 0,79 | 0,30 | 1,00 |

Fig. A.4.2

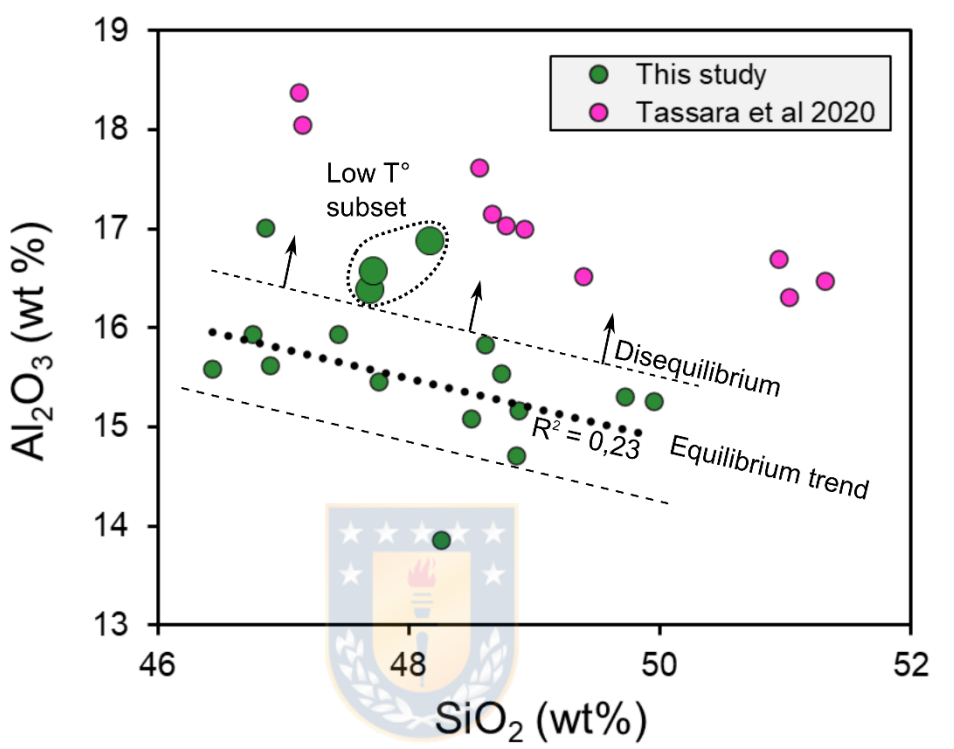


Figure A.4.2.- Comparison of $Al_2O_3$ contents versus $SiO_2$ measured in MI's from Los Hornitos by this study and Tassara et al. (2020).